ABSTRACT

Title of dissertation: ACTIVE SPANWISE LIFT CONTROL:
A DISTRIBUTED PARAMETER APPROACH

Joaquim Neto Dias
Doctor of Philosophy, 2019

Dissertation directed by: James E. Hubbard, Jr.
Professor Emeritus
Department of Aerospace Engineering

Structural load alleviation has been a very active research topic since the 1950s for many reasons. By mitigating the effect of gusts on the wing, the maximum loads can be effectively reduced. This capability would lead to substantial benefits, such as reduced structural weight, better fuel burn performance, and improved passenger ride comfort. Instead of controlling the structural response, however, it can be argued that the aerodynamic behavior of the wing should be primarily controlled. Since the gust loads are caused by disturbances in the lift distribution, it is possible to mitigate the gust loads by controlling the shape of the lift distribution profile along the span. In contrast to previous approaches, this research builds on concepts from Distributed Parameter Systems (DPS), which is indeed the case of aerodynamic surfaces. The unsteady aerodynamic behavior of the 3D flow around a wing is modeled using two approaches: the Unsteady Lifting-Line Theory (ULLT) and the Unsteady Vortex-Lattice Method (UVLM). Then, modal identification techniques are used to identify spanwise aerodynamic mode shapes in terms of local lift coefficient along the span.

These shapes provide an optimal basis for model order reduction and also for spatial control. The lift distribution is decomposed as a linear superposition of these shapes, with each weighted by a shape coefficient. By controlling a set of shape coefficients, the overall lift profile can be effectively controlled. In this work, the shape control problem is addressed using a Linear Quadratic Tracker to dynamically follow any desired reference lift profile. The gust alleviation problem is investigated using a similar controller with a special observer, able to decouple the state estimation from the gust input.

ACTIVE SPANWISE LIFT CONTROL: A DISTRIBUTED PARAMETER APPROACH

by

Joaquim Neto Dias

Dissertation submitted to the Faculty of the Graduate School of the
University of Maryland, College Park in partial fulfillment
of the requirements for the degree of
Doctor of Philosophy
2019

Advisory Committee:

Professor James E. Hubbard, Jr., Chair/Advisor
Professor James Baeder
Professor Amr Baz
Professor Alison Flatau
Professor Robert Sanner

Preface

When I decided to pursue a doctoral degree, I was interested in many research topics, all within flight dynamics. Having a background in Flight Test Engineering, I was used to applying system identification techniques to actual flight test data, in order to obtain aerodynamic models for aircraft simulation and control. For most conditions tested, the natural frequencies related to rigid body dynamics (short period, phugoid, etc) were much lower than the structural natural frequencies, so that a rigid body assumption was applicable. That naturally lead to purely temporal, lumped parameter models, in the sense that the system states have no spatial dependence whatsoever.

In this context, I met my advisor, Dr. James E. Hubbard Jr., and became aware of his research on Distributed Parameter Systems (DPS), smart structures, and design of spatial filters. He taught me that, in reality, all systems in nature exhibit spatial dynamics at some level, being therefore *spatial-temporal* systems. Then, Dr. Hubbard showed me his perspective about the problem of spatial control of spanwise lift distribution, and all the challenges involved, while I observed with skepticism. I took his course on Advanced Structural Dynamics, and slowly became a believer of the spatial-temporal world myself.

This work presents a novel methodology to apply spatial control techniques to aerodynamic systems. It was largely motivated by his book *Spatial Filtering for the Control of Smart Structures: An Introduction* [1], which deals with shape control techniques for self-adjoint systems, such as structural, acoustic, thermal. However,

aerodynamic systems are non-self-adjoint. For this reason, the very definition of "modes" must be revisited for this class of systems, and the modeling techniques required to obtain system eigenfunctions also differs from those in the book. For a relatively simple self-adjoint system with simple boundary conditions, the eigenfunctions can be obtained directly from the analytical solutions of the Partial Differential Equation (PDE) that govern that system. For an aerodynamic system involving 3D flow around a wing, analytical solutions for the governing PDE equations are not available, thus requiring numerical approaches in order to obtain the aerodynamic eigenfunctions. Interestingly, after overcoming these difficulties, the same shape control techniques from Dr. Hubbard's book could be applied to the case of lift profile along the wingspan. The spatial-temporal controller synthesis technique provides a powerful framework to control DPS using a low-order controller. Special attention is given to the fact that quasi-steady aerodynamic models do not suffice for shape control.

In this work, the spatial control of lift distribution is demonstrated for the problem of gust load alleviation, although other problems that require control of the lift profile can also benefit from the technique, such as flutter suppression, maneuver load alleviation, and in-flight drag minimization. On a larger scale, the methodology can also be applied to non-self-adjoint systems in general, such as structural systems that require Finite Element modeling or feature complicated boundary conditions.

Joaquim N. Dias

Hampton, Virginia, July 2019

Dedication

For my family.

Acknowledgments

I would like to thank my wife, Michele, for everything she has done over the years. She provided emotional support when things seem too difficult or unbearable, and gave me the personal motivation required to get this work done. I also thank my son Daniel, who often reminds me of what really matters in life, and my soon to be born daughter Amanda, who is already a source of inspiration and love. I would also like to express my gratitude to my parents, brother and sisters, who are silently cheering for me from thousands of miles away.

I am in debt with Dr. James E. Hubbard Jr., who did much more than what was required from a doctoral advisor. His passion for Engineering gave me the motivation to pursue problems that seemed unsolvable. Thanks for the countless hours of discussions, and for teaching me how to trust my intuition. I also appreciate the time and effort that my committee has dedicated to this work. The comments and suggestions helped improve the quality of this work.

The unconditional support of lab mates and friends in the Morpheus Lab is greatly appreciated. Thank you, Michael Cunningham, Jose Mondragon, and Rose Weinstein for your help during these four years of graduate school. All of you have contributed to this work.

Finally, I am grateful to the Brazilian Air Force for providing financial support during my doctorate, and to the National Council of Scientific and Technological Development (CNPq) of the Brazilian Government, for the academic scholarship under grant number 202714/2015-2.

Contents

List of Tables

List of Figures

Chapter 1

Introduction

This chapter begins with the relevance of the topic *Active Control of Spanwise Loads* for current and also future aircraft generations. A reduction in structural loads can lead to substantial weight savings, which improves fuel efficiency. For transport aircraft, the most demanding condition is typically under gust inputs, which largely explains why gust load alleviation (GLA) is still a very active research subject. A literature review on active load alleviation is presented, focusing on GLA. Based on the limitations identified in the previous studies, a novel approach is proposed to perform GLA by controlling the spanwise distribution of aerodynamic loads. Then, the research hypothesis is formulated and the main contributions of the present work are listed. This chapter is concluded with a dissertation outline, containing a brief description of the subsequent chapters.

1.1 Motivation: the quest for increasingly efficient aircraft

The aviation industry is constantly pursuing more fuel efficient airplanes to reduce operating costs. Today, a lower fuel consumption is also required to reduce pollutant emissions, due to increasing concerns about aviation impacts on environment. In order to address these concerns, organizations like NASA and the Advisory Council for Aviation Research and Innovation in Europe (ACARE) have proposed aggressive fuel-burn reduction goals for the next decades. NASA stablished goals for the future aircraft generations with respect to the current generation N. The $N+1$, $N+2$ and $N+3$ generations incorporate technologies that will be approaching maturity (i.e. roughly Technology Readiness Level 6), by 2015, 2020, and 2025, respectively [2]. NASA envisions that future aircraft generations $N+2$ (service-entry 2025) and $N+3$ (service-entry 2030-35) should exhibit 50% and 60% reduction in fuel-burn, respectively, as compared to year-2005 best-in-class aircraft [3].

In 2011, ACARE published the document *FlightPath 2050*, replacing its *Vision 2020* [4] published in 2001 and setting a new 75% fuel-burn reduction as a target for 2050, relative to year-2000 aircraft [5]. Besides goals for fuel reduction, targets for noise reduction and nitrogen oxides (NOx) were also set. A summary of goals from NASA and ACARE are presented in Table 1.1. More information about these values and the nomenclature can be found in [3].

For the purposes of this work, a comparison with the current trends in fuel burn and noise reduction provides a better picture of how ambitious these goals are. Figure

Table 1.1: Fuel-burn and emissions reduction goals put forward by ACARE and NASA. (Source: [3])

Category	ACARE		NASA		
	Vision 2020	FlightPath 2050	N+1 (2020)	N+2 (2025)	N+3 (2030-2035)
Fuel	50%	75%	33%	50%	60%
	Relative to year-2000 aircraft		Relative to year-2005 best-in-class		
NOx	80%	90%	60%	75%	80%
	Relative to year-2000 aircraft		Relative to CAEP 6		
Noise	50%	65%	32 EPNdB	42 EPNdB	71 EPNdB
	Relative to year-2000 aircraft		Cumulative, relative to Stage 4		

1.1 shows the fuel burn reduction trend for modern single-aisle aircraft, whereas Fig. 1.2 presents the trend in noise reduction, along with corresponding NASA and ACARE goals from Table 1.1.

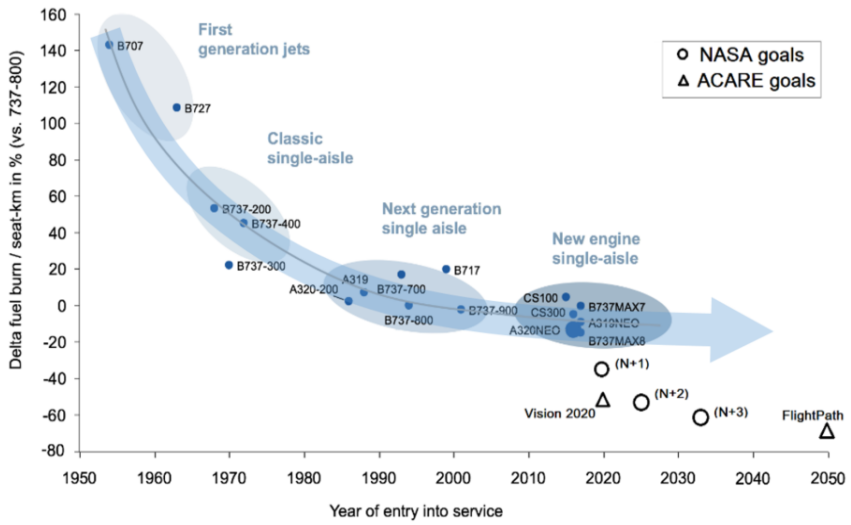

Figure 1.1: Trend of fuel-burn per seat-km over time. (Adapted from: [6])

Most of the fuel burn and noise reductions shown in these trends were obtained from engine improvements, by increasing the turbofan by-pass ratio (BPR), whereas the airplane configuration remained basically unchanged in the last 60 years (the so-

called tube and wing configuration). Higher BPR requires a larger nacelle diameter, which inevitably increases the engine weight and frontal area. At some point, the weight and drag penalties outweigh the benefits in fuel consumption and noise. The diminishing returns in both trends indicate that it is getting increasingly more difficult to extract substantial performance gains. Therefore, by using the current approaches for aircraft design, one should not expect to obtain a substantial performance upgrade. [3, 6].

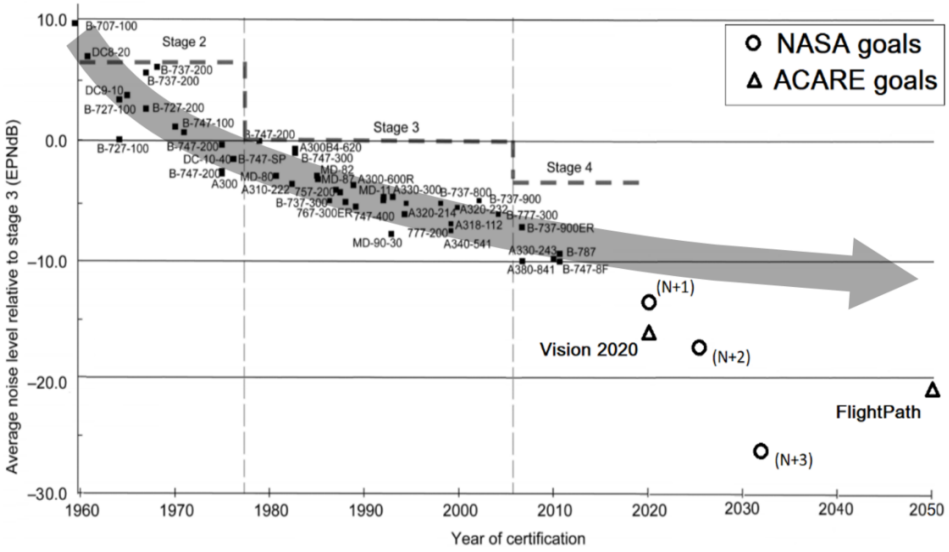

Figure 1.2: Trend of aircraft noise levels over time. (Adapted from: [7])

In [8], an optimization study analyzed the impact of future technologies on fuel burn of a conventional configuration (tube and wing). The results indicated that, even with implementation of technologies that will only be available in the next decades, the conventional configurations would not achieve the FlightPath 2050 for fuel efficiency.

The new goals set by NASA and ACARE clearly represent a departure from the

current trends and, if these reductions goals are to be met, some radical changes in aircraft design are required. In other words, improvement of current technology alone will not provide the step changes required to fill the gaps between the current trends and desired goals [3, 9].

In fact, these stringent goals motivated the development of new configurations during the last decade, which might be able to break the paradigm of a tube and wing configuration, first introduced with the Boeing 707 almost 60 years ago. A summarized description of such configurations and a comparison of their predicted improvements in fuel burn and noise reduction is provided in [3]. According to this study, the two most promising designs are the NASA (N+3) configurations (service-entry 2030-35), namely the Boeing Subsonic Ultra Green Aircraft Research (SUGAR Volt) truss-braced wing with hybrid-electric engines [10] and the MIT D8.5 transport configuration, with a *double-bubble* fuselage cross-section [11]. Both designs are shown in Fig. 1.3.

Figure 1.3: Boeing SUGAR (left) and the MIT D8 configurations. (Image credits: NASA)

The Boeing SUGAR relies on Laminar Flow Control (LFC) to reduce viscous drag and also depends on a hybrid electric engine to reduce fuel consumption. The

LFC consists in applying suction via porous along the surface, in order to postpone transition from laminar to turbulent flow. While the concept is well understood and validated in experiments, there is uncertainty about its applicability onboard an aircraft. The hybrid electric turbofans burn jet fuel during takeoff, then use electric motors to run the fans for flying, when low levels of thrust are required. A detailed description can be found in [10, 12].

On the other hand, the MIT D8.5 assumes a Natural Laminar Flow (NLF) at the bottom surface of the wing, which is a form of laminar flow obtained in a passive way. Also, the D8 requires ultra-high by-pass ratio turbofans, with a distortion-tolerant fan to accomplish boundary layer ingestion (BLI). The BLI technology is supposed to feed the engines with the low-energy flow at the rear part of the fuselage. By using the engines to re-energize this flow, the fuselage wake and the engine wakes are merged, reducing the total kinetic energy wasted in the form of wake shed into the atmosphere. Additional design features are available in [11].

Interestingly, the two designs rely on very distinct, disruptive technologies, but have one point in common. In an attempt to maximize aerodynamic efficiency, they exhibit a very large wing aspect ratio (AR). While most current passenger jets have aspect ratios between 8 and 10, the Boeing SUGAR features AR around 19 [10] and the MIT D8.5 design (comparable to a Boeing 737-800) has AR around 25 [13]. ***This is only possible because both configurations rely on active load alleviation systems to reduce the design loads, which ultimately size the wing structure***. Otherwise, the structural weight of the wing would become prohibitive.

These new configurations promise significant fuel and noise reductions, based on:

1) A synergistic approach in aircraft design, in the sense that there is much more interaction between the aerodynamic configuration, structures and propulsive system in the aircraft design process than in a conventional configuration (fuselage tube, cantilever wing, wing-mounted engines);

2) Incorporation of new technologies that will only be operationally available in 2030, such as:

- Laminar Flow Control
- **Active Load Alleviation**
- Boundary Layer Ingestion
- Advanced propulsion
- Advanced materials

These technologies were selected as the most promising for improving aircraft fuel efficiency by NASA studies [9, 14] and also by the International Air Transport Association (IATA), which published in 2013 a technology roadmap with a list of such technologies [15]. Moreover, this same list is presented in a recent independent study as game-changing technologies for fuel efficiency [8].

Following the trend in the last decades, it is somewhat expected that all future aircraft employ some degree of advanced propulsion and materials. Other than that, the one technology that is added in all future aircraft configurations is the *active load alleviation*, because of its potential to provide structural weight savings and relatively high maturity level.

1.1.1 Quantification of fuel efficiency benefits from active load alleviation

In order to reduce fuel burn, the most immediate measure is to reduce the engine fuel consumption, which has been the major source of fuel-burn improvements in the last decades. However, other aircraft parameters also impact fuel efficiency, such as aerodynamic efficiency and weight. This is more clearly seen from the Breguet equation (or range equation), which is valid for the dominant cruise portion [11]:

$$W_{fuel} = W_{zf}\left[\exp\left(\frac{TSFC}{V}\frac{D}{L}R\right) - 1\right] \cong W_{zf} \times \frac{TSFC}{V} \times \frac{D}{L} \times R \qquad (1.1)$$

The linearized approximation on the right is valid for short and medium range aircraft, for which the fuel fraction (fuel weight over maximum takeoff weight) is not very large. This equation shows that, for a fixed range R and velocity V, the amount of fuel required (W_{fuel}) depends on:

- The aerodynamic efficiency (Lift/Drag);
- Engine thrust specific fuel consumption (TSFC);
- The aircraft zero-fuel weight W_{zf} (i.e. payload + operational empty weight)

By using an active load alleviation system, the reduction in the design loads can be used to decrease the wing stiffness, thus reducing the aircraft empty weight. Alternatively, these gains can allow an increase in the wing span, while keeping the same weight, which increases the aspect ratio and leads to higher lift-over-drag ratios. Therefore, it can be seen that the addition of a load alleviation feature can significantly change the final optimum design.

Quantification of the full potential benefits due exclusively to load alleviation is very challenging, because it requires development and evaluation of an active load alleviation system early in the design phase of the aircraft [16]. This means that the performance of an active load alleviation system is also used to drive the Multi-disciplinary Design Optimization (MDO) of the aircraft, along with other factors.

In [17], fuel savings of 11.2% were obtained when adding an active load alleviation system in the design of an aircraft comparable to a Boeing 737-800 (i.e. similar size and mission). These gains originated from an 8.2% increase in L/D combined with a 12.1% reduction in wing weight, relative to the baseline model (without load alleviation). The NASA SUGAR Volt preliminary design report assumed that a 25% reduction in wing weight could be obtained via active load alleviation [18]. In [19], load alleviation also would allow a 25% wing weight reduction, which is associated to a 7% fuel burn improvement. More recently, in [8], an optimization study of the impact of future technologies on aircraft design was conducted. The results indicate that a load alleviation system alone would be able to reduce the fuel burn by 11.8%, for a medium-range aircraft comparable to an Airbus A320. These previous works suggest that active load alleviation offers significant potential for improving aircraft fuel efficiency.

1.2 Literature review on active load alleviation

This section provides an overview of the relevant aspects of gust load alleviation in the literature. Although passive techniques have also been studied, this review is

focused on active gust alleviation. Initially, a historical overview of the evolution of the field is given, culminating with the first model-based control synthesis developed for accurate aeroelastic models [20]. From the selected references, it will be clear that a wide variety of control approaches have been tested in simulation environments since the early 80s, employing different degrees of model fidelity. Next, the implementations of gust alleviation in production aircraft are summarized, in order to quantify what has been accomplished in practical applications. In the case of passenger transports, the industry standard so far has been to incorporate such system when the aircraft is already designed, usually to improve passenger comfort. Finally, recent developments in sensors and novel control synthesis approaches are presented, including simulation results for the current state-of-the-art in gust load alleviation for passenger jets.

A separate branch of this review is dedicated to large aspect ratio, highly flexible Unmanned Aerial Vehicles (UAV). For these aircraft, the usual separation in frequency between rigid-body modes and structural modes does not hold. Consequently, significant coupling exist between aeroelastic effects and flight dynamics, which has motivated a significant research effort in the literature of gust alleviation specific for this class of aircraft.

1.2.1 Historical developments and early approaches

The building blocks required for active load alleviation are: an aeroelastic model (structural dynamics plus unsteady aerodynamics), and a model-based controller, which includes sensors and actuators. However, the early developments in aeroelastic

modelling were obtained for flutter prediction, and not for load alleviation. Until the 1960s, accurate dynamic structural models for aircraft still relied on experimentally measured mode shapes (Ground Vibration Tests), but the Finite Element Method (FEM) was quickly evolving. The first panel flutter results obtained from FEM were published in 1967 [21, 22], and assumed quasi-steady aerodynamics. Regarding unsteady aerodynamics, the problem of unsteady loads on an oscillating flat plate (2D flow) was solved analytically by Theodorsen in 1935 [23], but flutter predictions for a finite wing (3D flow) could only be obtained for very simple geometries, or by significantly simplifying the problem (e.g. via strip theory) [24]. Preferable approaches were: wind tunnel testing of inertially scaled models, use of empirical equations based on similar designs, or flight testing the prototype itself [24].

This trend continued until 1969, when the Doublet Lattice Method (DLM) was published in a seminal paper [25]. The DLM provided unsteady aerodynamic loads for complex geometries, at a given frequency of interest, including compressibility effects, and became the industry standard for numerical flutter predictions. Since the data from DLM is sampled at specific frequencies, it is perfectly amenable to flutter analysis (one frequency of interest), but not to aeroelastic simulations, which require a continuous model in the frequency domain, i.e. a transfer function model. The DLM data can be interpolated by a Rational Function Approximation (RFA), and a number of methods are suitable for this task, such as Roger's Approximation [26]. This approach provides an accurate aeroelastic model, which can then be used for simulation of gust inputs. Using this continuous model, closed-loop behavior of simple controllers (such as PID) could be analyzed before actual implementation.

However, the state-space realization of such a model contained a large number of states, precluding synthesis of model-based controllers. For more accurate representation of aerodynamic data from DLM, higher degree polynomials were required in the approximating transfer functions, resulting in even more states in a state-space realization.

In a seminal paper in 1982, Karpel [20] presented the minimum-state method for aeroelastic model realization. For a given desired accuracy, this method provided the minimum number of augmented states, which allowed synthesis of an output feedback controller for flutter suppression and gust alleviation. While the paper demonstrates the methodology for a typical section, more complex geometries are presented in [27]. These studies showed that low-order models could be obtained at an acceptable accuracy level, at a time when the model-order reduction techniques from controls engineering were still being developed (e.g. balanced truncation [28]).

The seminal work by Karpel [20] set the state-of-the-art at the time. However, for preliminary studies, many works on gust alleviation still relied on much simpler models. Particularly, the unsteady aerodynamics required most of the computation effort. In [29], a gust load alleviation (GLA) system was devised for the Airbus A300, based on classical single input single output (SISO) techniques. The authors evaluated the two typical control approaches for GLA: 1) feedforward control, based on local measurements of the gust (using a vane for angle of attack, at the aircraft nose) and the time interval required for the gust disturbance to reach the wing; and 2) feedback scheme, based on data from three accelerometers (fuselage, left and right wing tips). The results indicated that the feedback approach was more effective in

reducing the gust loads than the feedforward scheme. The combination of the two schemes (feedback + feedforward) was not tested. For controller design, the analysis included a flexible structural model, but the aerodynamic effects were assumed quasi-steady. Other works applied optimal controllers for gust alleviation. In [30], a Linear Quadratic Regulator (LQR) was applied to a B-52E model to reduce vertical accelerations during gusts, whereas [31, 32] used a Linear Quadratic Gaussian (LQG) controller to reduce the bending moment of a C-5A model. In both cases, the model featured structural flexibility, but the unsteady aerodynamics effects were approximated using Wagner and Küssner indicial functions. In [33], a multivariable controller based on eigenspace techniques was designed for gust load alleviation on a flexible half-wing model. In this case, the unsteady aerodynamics model was obtained from the Doublet Lattice Method (DLM) and additional complexity was added by controlling up to three surfaces (two at the trailing edge, one at the leading edge), as opposed to one single aileron.

1.2.2 Applications in operational aircraft

While the previous section presented the early simulated approaches in GLA, this section focuses on actual applications. Before proceeding, a short discussion on structural load types and airworthiness certification is beneficial.

Undesired structural loads acting on an airframe are usually of two types: maneuvering loads and gust loads. In the first case, the transient loads are caused by intentionally pitching or rolling the aircraft, for example. If the command input is

too large and no limitation is enforced by the Flight Control System (FCS), the load peaks achieved might be higher than initially expected in the aircraft structural design, leading to undesirable flying qualities and reducing the structural fatigue life. In order to reduce these loads, a Maneuver Load Alleviation (MLA) system can be employed.

The second cause of undesired structural loads is due to atmospheric disturbances, which can be further divided into discrete and continuous gusts. Discrete gusts have lower temporal frequencies and are evaluated as isolated events in time-domain for a relatively short period of time. They are usually referred to as the '1-cos' (*one-minus-cosine*) gust [34]. The Federal Aviation Administration (FAA) requires certification of aircraft structural loads with respect to the critical discrete gust profile, i.e. the one associated to the critical gust length and which causes the highest loads in the airframe response. Continuous gusts, on the other hand, have much higher frequencies and are usually referred to as turbulence. The two main turbulence models commonly employed for turbulence assessment are the Dryden and von Karman models, both formulated in the frequency-domain [35]. Together, the discrete and continuous gust evaluations allow the designer to obtain loads under unsteady conditions, which might be considerably different than the quasi-steady predictions. The design of a Gust Load Alleviation (GLA) is more demanding than that of MLA. While a MLA system only needs to react to the pilots commands, which are known (i.e. measurable onboard), a GLA system must react to dynamic and exogenous (unknown) gust inputs as well.

The highest critical loads (maneuver or gust) ultimately define the structural design. Therefore, an airframe can be structurally defined by maneuver loads or by

gust loads [36, 37, 38]. For military jet fighters, which are designed to withstand high-g maneuvers, the critical loading conditions are usually given by the maneuvering loads. Transport aircraft, on the other hand, are usually designed to withstand a lower load factor of 2.5g, with a safety factor of 1.5 [16]. Thus, the maneuvering loads are relatively lower. Typical transport aircraft have moderate to high wing aspect ratios, which makes them more susceptible to gust disturbances. As a result, their structural design is sized by gust loads and thus the maximum benefit from a GLA system can be achieved for this type of aircraft.

Structural load alleviation has been investigated since the 1950s (see [30] and the references therein), but interest was renewed in 1964 due to an incident with a B-52H bomber. After encountering severe turbulence (estimated peak intensity of 35 m/s, [39]), the aircraft lost 80% of its vertical tail. The crew was able to land the aircraft and data analysis motivated the development of an active control system, under the Load Alleviation and Mode Stabilization (LAMS) program [40, 41], which demonstrated load alleviation without degrading aircraft stability and flying qualities.

In the 1970s, an Active Lift Distribution Control System (ALDCS) was developed for the C-5A aircraft to reduce the wing stress during turbulence and normal maneuvering, thus improving fatigue life [42]. The ailerons were deflected upwards symmetrically, in order to concentrate the lift towards the wing root, as shown in Fig. 1.4. This is the most common approach to reduce the bending moment at the wing root. In this case, the bending moment was reduced by 30%, with an increase of only 5% in torsional moment at wing root. The system used forward and aft vertical accelerometers at the wingtips and the existing inertial reference to measure bending

and torsional motion, and structural weight savings of 5.5% (18,000 lb) were achieved. [36]

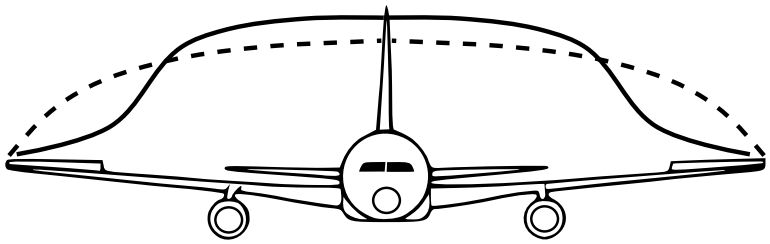

Figure 1.4: Change in lift distribution by symmetric deflection of ailerons during an upward gust.

A similar system was designed to the Lockheed L-1011, providing both MLA and GLA capabilities. It allowed the wingspan to be increased by 5.8% and avoided an increase of 1.25% in the aircraft empty weight [43, 44]. As another example of operational aircraft with GLA, the bomber B-1 Lancer suppresses structural vibrations that are aggravated by gust disturbances. The weight savings attributed to this system are 9,100 lb or 4.7% of its empty weight [45]. Differently from the previous examples, the B-2 Spirit uses a GLA that is based not only on inertial measurements, but also on aerodynamic sensors. Based on the difference between the measured angle of attack and the angle of attack derived from the inertial navigation system (INS) onboard, the control surfaces are deflected, allowing gust load reductions of up to 50% [46]. MLA has also been incorporated into commercial aircraft, such as Airbus 320, 330 and 340, whereas the Airbus 380 and the Boeing 787 feature a GLA system [36]. However, the main objective is to increase passenger ride comfort during turbulence and not to improve the aircraft efficiency. Numerous experimental works on gust alleviation

and ride comfort were also conducted in experimental aircraft and in wind tunnels. A summary of these studies is given in [36], which presents a historical survey and also a state-of-the-art assessment of active GLA systems, but only for experimental applications.

In summary, these GLA examples were implemented when the aircraft was already flying, as a method to fix or improve some undesirable aeroelastic characteristic that was only uncovered after the design phase. In order to be realizable, these approaches only employed simple accelerometers as sensors and used the existing control surfaces as actuators, which somewhat limited the GLA capability. Therefore, one could argue that if sensors and actuators specifically designed for gust alleviation were used, better performances could be achieved. In fact, *the performance of GLA systems can be strongly constrained by sensor and actuator bandwidth capabilities* [17].

1.2.3 Recent developments in sensors, actuators and control techniques

Most of the GLA applications presented so far are based on feedback of the structural response, as measured by accelerometer and/or strain gages. The disadvantage of a feedback controller lies in a delayed compensation, because the disturbance signal must propagate through the system before the control effects are applied. Moreover, this control application will likely require high actuation rates. Such disadvantages can be overcome by using a feedforward controller, if a reference signal is available [47]. On the other hand, the performance of feedforward controllers is very sensitive

to plant variations (e.g. weight, flight condition), which has motivated the use of adaptive feedforward control lately. Another possibility is a combination of feedback and feedforward controls for improved performance, also known as hybrid approach [48] or 2-DOF (degree-of-freedom) control strategy [49].

In order to provide a lead-time reference signal for feedforward control, a number of techniques have been proposed for gust measurement, including using local angle of attack (AOA) measurements, local flow sensors on the wing surface, and a forward-looking light detection and ranging (LIDAR) system.

In recent studies using feedforward controller for load alleviation, it was assumed that the AOA at the aircraft nose can be measured using vanes [50, 51] or a five-hole pressure probe [49]. The vertical gust component can be resolved by coupling the local flow angles with the inertial components of the aircraft velocity (i.e. with respect to the Earth, obtained via inertial system onboard). In practice, high quality instrumentation onboard is required for gust estimation with low standard deviations. Also, this approach is more suitable for large aircraft, for which the AOA sensor can be placed well ahead of the wing, providing a larger lead-time. In [52], an adaptive feedforward controller was designed for a large transport aircraft, using preview information of the gust sensed by an onboard alpha probe. The structural model was obtained from FEM, whereas the unsteady aerodynamic effects was modeled by DLM. The simulation results showed significant reductions in the wing root bending moment, as compared to the open-loop plant. The root-mean-square (RMS) values were reduced by 60% in a continuous (Dryden) gust environment, whereas the peak value of the critical discrete ('1-cos' profile) gust was reduced by 66%. The

authors assumed that the flight control laws can be simply superimposed on the GLA controller. Therefore, inner control loops were not considered in that study.

Another approach to reduce the gust-sensing delay is to use special sensors for direct measurement of local unsteady flow, such as the leading edge stagnation point (LESP) sensor, which consists of an array of hot films [53] and artificial hair sensors (AHS) developed by the Air Force Research Laboratory (AFRL) [54]. These devices provide a very short response time, with high-sensitivity and low power consumption. The LESP has been tested in flight in 2015 [55], whereas the AHS was tested in wind tunnel [56]. In addition to the calibration issues associated to hot films, the largest challenge is operational. Since these sensors are exposed to the flow, they are susceptible to damage by external agents such as rain, ice, and even insects.

Finally, some researchers have attempted to measure the gust disturbance ahead of the aircraft by using a forward-looking LIDAR (Light Detection and Ranging) system. A coherent Doppler LIDAR was developed in [57], with flight test results presented afterwards [58, 59]. However, in order to work properly, it required high aerosol densities in the atmosphere, which motivated a new type of LIDAR to overcome this limitation. In [60], preliminary flight test results with a short-pulse UV Doppler LIDAR were able to measure wind at altitudes with no appreciable aerosol concentrations, but the standard deviations were too high (about 10 m/s). With further developments [61], the standard deviation was reduced to 1.5 m/s during the flight tests. By measuring the gust velocity at a plane 50 meters ahead of the aircraft (perpendicular to its flight path), a lead-time of 200-300 ms was obtained [61]. These, however, were assessments of the LIDAR in open-loop conditions, i.e. its

performance in measuring the gust field ahead of the aircraft, without integration to the flight control system. LIDAR technology has evolved significantly, but still face challenges, such as physical installation in the aircraft [61] and robustness against uncertainties in the gust measurement [62], since the LIDAR system would be critical for structural integrity.

Nevertheless, some recent works simply assume that a LIDAR system is available. In [63], it is assumed that the gust field ahead of the aircraft can be measured by a light detection and ranging (LIDAR) system, and an adaptive feedforward control is designed for the F/A-18 active aeroelastic wing (AAW) model. Ref. [64] also assumes that LIDAR measurements are available for a GLA system designed with H_∞-synthesis.

The performance of the actuators will also affect the reaction time of a GLA system. For example, a typical aileron actuator in a large transport aircraft has a maximum rate of 35-40 deg/s in cruise conditions [17, 61, 65]. For gusts of relatively high temporal frequency, the limited deflection rate of the surface might constrain the GLA performance. In order to take into account the saturations in surface deflection angle and rate, a Model Predictive Control (MPC) approach can be adopted [62, 66]. Additionally, the preview gust information from the LIDAR system can be used to synthesize the control law. In [62], four different control configurations were evaluated: basic aircraft (no GLA), feedback control based on accelerometer data, MPC with nose measurements of gusts, and MPC with LIDAR (50 m ahead of nose). Significant load reductions occur for all cases, but MPC with LIDAR performed better. However, it was observed that the performance limitations of the MPC schemes are due to the

deflection rate constraints on the actuators. The authors also did not consider the interactions between control laws and the GLA functionality.

Closed-loop flight tests with a LIDAR system have not been performed yet. However, a complete simulation of this LIDAR system with a high-fidelity aircraft model was performed in [67], which used a combined feedback and feedforward approach for GLA. This study is the first assessment of GLA synthesis using LIDAR and integration with the typical functions from the flight control system (FCS). Thus, it represents the current state-of-the-art within the published literature. The model used was based on the Airbus XRF1 configuration, a generic long-range aircraft model designed by Airbus, which incorporates the nonlinear equations of motion coupled with the aeroelastic model, as well as actuator and sensor models. Also, FCS functions were developed to closely represent the typical behavior of a modern Airbus fly-by-wire system. On top of these control laws, two load alleviation functions were designed: a feedback loop (FB, based on inertial measurements) and a feedforward loop (FF, based on LIDAR measurements). Each alleviation function was obtained independently, using an optimization-based multi-objective robust control synthesis. Among the many design criteria, it was enforced that the load alleviation should not deteriorate flying qualities nor passenger ride comfort (as compared to FCS alone), and the load reductions in the wing root should not cause load increases at other points of the structure (such as horizontal tail) beyond allowable limits. Also, since the nonlinear plant behavior is considered in the optimization, no linearizations were necessary. The GLA performance was evaluated against different '1-cos' discrete gust profile, and three cases were considered: FCS alone, FCS + FB law, and FCS + FB

+ FF law.

It was found that the existing flight control system already provides some degree of load alleviation. When the feedback alleviation function is added (i.e. FCS + FB), some extra reduction is obtained (e.g. 9% in peak bending moment at the wing root). However, when the gust measurements from LIDAR were included via a feedforward control (i.e. FCS + FB + FF), the load reduction was only minimally improved, in terms of wing root bending moment. Specifically in this case (FCS + FB + FF), it can be seen that the controller tries to pitch the aircraft in anticipation to the gust, in order to reach a better angle of attack for gust entry. However, this procedure is slower than deflecting a control surface and, as observed by the authors in that study, it basically shifts the current load levels before entering the gust. Therefore, in order to minimize the load peak overshoot during the gust, the control law causes an undershoot before the gust. A typical result, for one specific gust length (300 ft), is shown in Fig. 1.5. The peak is slightly reduced, but the overall behavior becomes more oscillatory.

Perhaps this fact indicates insufficient control authority to change the aerodynamic loads distributions along the wing. Like in all of the previous works, only the existing control surfaces for GLA (ailerons, spoilers and elevators) were employed in [67]. Therefore, even if a high-fidelity model simulation is employed and the gust disturbance is known (i.e. measured by LIDAR with a small standard deviation), the load reductions achievable will most likely be constrained by the control authority.

As pointed out by [49], forward-looking control techniques can be used to react to the disturbance before it arrives, but it requires substantial control authority to

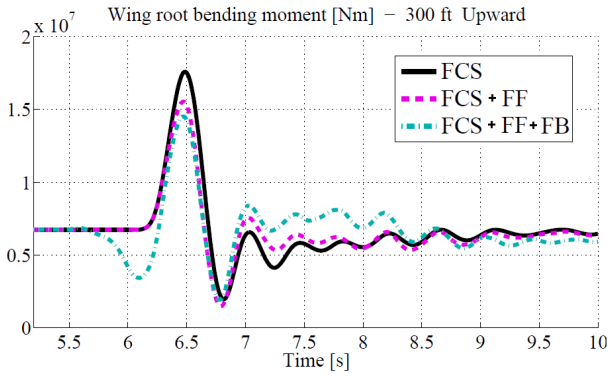

Figure 1.5: Comparison of gust responses using different flight control laws.

(Source: [67])

modify the lift distribution over the entire aircraft. In that study, it was shown that using the elevator to modify the wing lift distribution (by pitching the aircraft) was too slow for load alleviation during wake vortex encounters. Moreover, the ailerons lost efficiency at higher frequencies, due to aeroelastic couplings, and a solution was proposed by using two inboard flaps to improve control authority over the load distribution.

In conventional transport aircraft, while ailerons can change the local lift at the wingtip regions by quickly moving up and down (35-40 deg/s), the other wing sections (middle and root) feature slow-moving flaps, that only deflect downwards at a rate of 2 deg/s, being therefore unsuitable for GLA [16]. Spoilers can only be used to reduce or dump lift in the middle and root sections, but not to increase it. Load control in the inner sections of the wing is usually achieved by pitching the aircraft up or down (which increases or decreases the wing lift globally, respectively), while deflecting the ailerons symmetrically to modify the lift locally at the regions near the wingtips. If

the aircraft pitches up, while both ailerons deflect down, the net effect is an increase in local lift in the inner sections. According to [64], pitching the aircraft allows the controller to achieve higher levels of load variations, as compared to deflecting trailing edge control surfaces. The problem is that pitching the aircraft takes more time than simply deflecting a surface, because of the aircraft inertia around the longitudinal axis.

One way to increase the control authority over the wing loading distribution consists in having multiple trailing edge control surfaces along the entire wingspan, capable of deflecting up and down. The wing loads would be alleviated by these control surfaces, whereas the elevator would only be used to cancel any residual pitching moment resulting from flap deflection, thus avoiding pitching the fuselage.

In [50], a GLA system was designed for a blended wing body (BWB) aircraft, which is particularly sensitive to gust disturbances due to its low wing loading ratio (weight over reference area). In order to achieve sufficient control authority, the GLA system used 12 trailing edge flaps, yielding reductions of 20% in the wing root bending moment.

Multiple trailing edge flaps along the span could be implemented with conventional actuation systems, but also with novel approaches, such as the variable camber continuous trailing edge flap (VCCTEF) [68], which continuously deflects the trailing edge along the wingspan. This is achieved by having a high number of flap sections (e.g. 20) along the semi-span, interconnected by a transition material (elastomer). By avoiding gaps between the several surfaces, viscous drag is also reduced, while enabling optimal lift distributions for minimum induced drag. Initially designed for

drag reduction in cruise, the VCCTEF has also been considered for flutter suppression, wing morphing and dynamic load alleviation. In [69], the concept is applied to the Boeing SUGAR (truss-braced wing configuration), with a rigid wing assumption (Fig. 1.6(a)). The deflections of 20 spanwise flap sections, uniformly sized, were optimized to reduce the bending moment at the wing-truss joint by 36% during a 2.5g pull-up flight maneuver. In [70], the VCCTEF was applied to a flexible-wing configuration based on the NASA Generic Transport Model (GTM), featuring 16 flap sections on each side of the wing (Fig. 1.6(b)). The load alleviation results were simulated against continuous gusts, which were assumed unknown and estimated using an Extended State Observer (ESO). The reduction in the wing root bending moment obtained by a LQG controller varied between 18% and 59%, depending on turbulence intensity, but no rate limitation was enforced to the actuators. In both studies, no specific reason was given for the number of flap sections selected (16 and 20, respectively, along each side of the wing). These examples in the literature show that multiple trailing edge surfaces might be required in future aircraft for several purposes, such as drag minimization, flutter suppression, and higher control authority for active load alleviation.

1.2.4 Gust load alleviation in very flexible HALE aircraft

From section 1.1, it is clear that the future passenger aircraft will have higher aspect ratio wings for aerodynamic efficiency, and will employ increasingly higher percentages of composite materials for structural weight savings. Such a combination

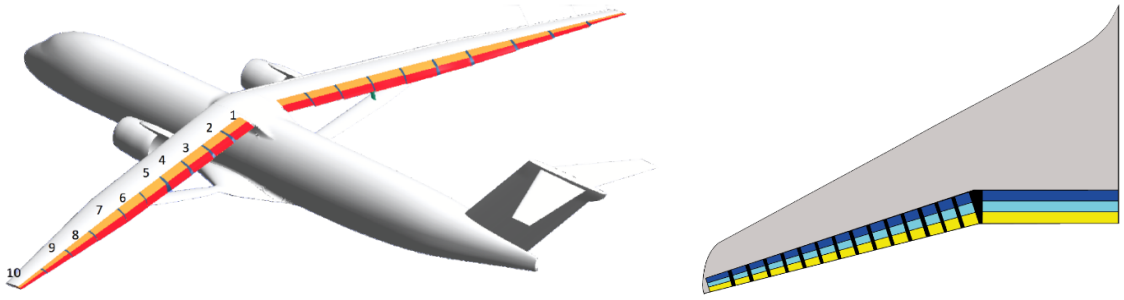

(a) Truss-braced wing aircraft with VCCTEF. (Source: [69])

(b) GTM wing with VCCTEF. (Source: [70])

Figure 1.6: Preliminary studies of the VCCTEF system.

yields aircrafts with more flexible wings (such as Boeing 787 and Airbus A350) and thus lower structural natural frequencies. In this case, the flight dynamics analysis becomes more complicated, because the usual separation in the frequency domain between rigid-body modes and structural modes vanishes.

While this extreme scenario might still take a few decades to reach transport aircraft, it has been a reality for Unmanned Aerial Vehicles (UAV), particularly for the high-altitude, long-endurance (HALE) vehicles, such as the MQ-1 Predator (wing aspect ratio 19) and RQ-4 Global Hawk (wing aspect ratio 25). Within HALE, there are lighter and more flexible aircrafts that are designed to stay airborne for several days, relying on electric propulsion and solar cell batteries, such as the NASA solar vehicles (Pathfinder, Centurion and Helios) and the Airbus Zephyr. These Very Flexible Aircraft (VFA) can be used for military applications (intelligence, surveillance and reconnaissance ISR) or as a pseudo-satellite to offer temporary coverage over an area of interest.

Due to the large aspect ratio of the wing and relatively low weight, VFA aircraft are

particularly sensitive to gust loads. This fact was sadly confirmed in 2003, when the NASA Helios vehicle crashed during a flight test (Fig. 1.7), after suffering unstable, diverging pitch oscillations triggered by turbulence [71].

(a) Helios prototype in flight.

(b) Helios disintegrates as it falls towards the Pacific.

Figure 1.7: NASA solar vehicle Helios. (Source: [71])

As one of the causes of the accident, the mishap report stated "lack of adequate analysis methods led to an inaccurate risk assessment of the effects of configuration changes, leading to an inappropriate decision to fly an aircraft configuration highly sensitive to disturbances" [71]. As a recommendation, the report suggested the development of more advanced, multidisciplinary time-domain analysis methods, appropriate to highly flexible aircraft [71, 72], which provided additional motivation for new methodologies dedicated to VFA, including gust alleviation.

Over the last two decades, a significant effort has been dedicated to aeroelastic modeling of VFA. The early efforts in aeroelastic modeling consisted of rigid-body equations augmented by second-order differential equations representing the structural modes [30, 31, 32]. A more detailed formulation of flight dynamics for flexible

aircraft is provided by the mean-axes method [73], but it relies on strip theory and small structural deformation. Hence, this approach is less appropriate for highly flexible aircraft, which motivated the development of more rigorous formulations based on body-fixed frame. [66, 74, 75]

Due to large structural deformations, non-negligible model nonlinearities arise in both structural and aerodynamic models [76, 77]. Structurally, these aircraft deform beyond the limits that can be correctly captured by simple linear finite element representations. For example, wingtip deflections as high as 43% of the wing semi-span were reported in [78], as shown in Fig. 1.8(b). Aerodynamically, large deformations require nonplanar wake modeling. A recent review on nonlinear aeroelasticity of high aspect ratio wings is given in Ref. [79]. In general, previous works on VFA rely on nonlinear finite element method (FEM) for structural modeling and some type of unsteady aerodynamic theory capable of dealing with nonplanar geometries. However, even with modest discretizations, the final linearized model may contain thousands of states. While this format is suitable for simulations and flight dynamic analysis, it is not appropriate for control synthesis.

Still, different control approaches have been applied to alleviate gust loads on VFA. In [80], a Proportional-Integral-Derivative (PID) controller was used to generate control inputs to the surfaces (aileron, elevator and rudder), based on the aircraft rotation rates (roll, pitch, yaw, respectively). The aircraft model was a VFA with a wingspan of 25 m, similar to the Airbus Zephyr 8, shown in Fig. 1.8(a). Reductions in bending strains at the wing root of up to 66% were obtained. For this very basic, non-model-based controller, the large number of states was not critical. Model-

based control synthesis approaches, on the other hand, usually require model-order reduction techniques. In [81], balanced truncation was used to reduce the model of the X-HALE vehicle, shown in Fig. 1.8(b), to 50 states. Then, a Linear Quadratic Gaussian (LQG) controller was applied to keep the wing curvature while flying in turbulence. Reductions in the peaks of wing curvature of about 47% in average were obtained, as compared to open-loop tests. Balanced truncation was also used in [82] to obtain a reduced-order model with 169 states, which was then used to generate a controller via H_∞-synthesis. As a result, the bending moment at the wing root was reduced by 9%, for the critical '1-cos' discrete gust profile. The gust alleviation performance achieved in these works, however, depend largely on the number of sensors assumed available and the bandwidth of the control surface actuators.

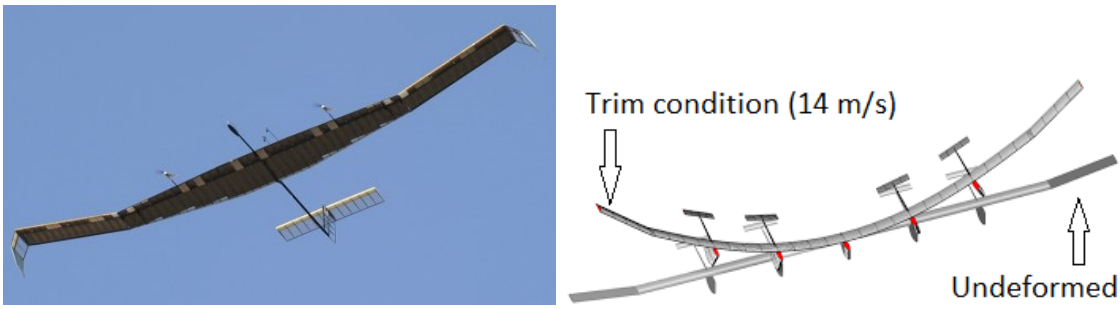

(a) Zephyr 8. (Credits: Airbus). (b) X-HALE UAV. (Source: [78])

Figure 1.8: Examples of Very Flexible Aircraft (VFA).

In order to take into account saturations in actuator rate and surface deflection, Model Predictive Control (MPC) has been used. In [83], MPC provided better load alleviation capability than a Linear Quadratic Regulator (LQR) designed with similar weighting matrices, during a '1-cos' discrete gust. The LQR reached the saturation levels for surface deflection, whereas the MPC managed to avoid them. However,

the performance of predictive controllers depends on the accuracy of the model employed. In [66], a prediction enhancement (PE) technique was proposed to improve the prediction accuracy of the MPC. In the simulation results, the performance of the MPC+PE was less sensitive to the loss of control surface effectiveness than the usual MPC formulation.

For all of the approaches above, the baseline models were linearized around a trimmed condition (structurally deformed), but the actual nonlinear plant can quickly deviate from this linear behavior. This is especially applicable to VFA. Therefore, nonlinear control techniques have also been investigated. [84]

1.2.5 Summary of Gust Load Alleviation developments along a timeline

From the previous sections, it is clear that gust load alleviation continues to attract attention from researchers, mainly because of the potential for significant structural weight savings. At this point, it is helpful to draw a big picture of GLA along a timeline, schematically shown in Fig. 1.9, where the developments were divided in three phases:

Phase 1, until early 90s, represents the developmental stage for the prediction techniques based on aeroelastic modeling. During this period, most practical applications of GLA were intended to correct some aspect of the structural response that was not anticipated in the design. The objectives included structural fatigue life extension, structural vibration suppression or even to allow a wingspan extension with

minimal weight penalties.

In **Phase 2**, the aeroelastic modeling was well stablished in industry by using FEM for structural modeling and DLM for unsteady aerodynamic loads. GLA has been demonstrated in different airframes, but the passenger jet industry was limited to use the system to improve ride quality for comfort, which is a non-critical feature. Perhaps the largest obstacle comes from airworthiness regulations. Currently, the Federal Aviation Regulations (FAR, in the USA) and the Joint Aviation Requirements (JAR, in Europe) do not allow a reduction in the design loads due to the fact that the GLA system will be active at all times [85]. However, as technology matures and the need for more efficient aircraft intensifies, the gust loads design requirements for transport aircraft might change. In fact, these requirements have naturally evolved with aviation itself [86].

Finally, **Phase 3** deals precisely with this change in paradigms regarding the industry and the airworthiness authorities. From section 1.1, the future aircraft will feature large aspect ratios and will need to actively manage spanwise loads for structural efficiency. In order to achieve substantial fuel savings and lower structural weight, it is expected that GLA will be one of many criteria driving the aircraft design. This projection is already a reality in the design of very flexible aircraft since the early 2000s.

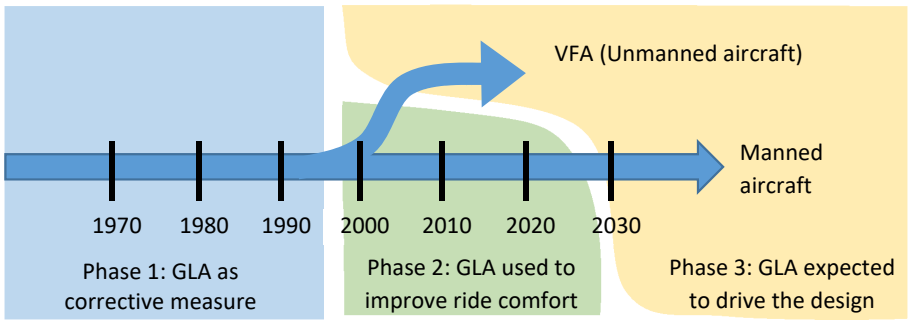

Figure 1.9: Timeline of gust load alleviation role in aircraft design.

1.2.6 Limitations of previous approaches

The literature review showed that the three main elements for a GLA system are: model, sensors and actuators, and recent developments have been achieved in all of them. However, it also revealed a number of limitations of previous approaches, such as:

1. **The spatially distributed behavior of spanwise loads is disregarded.** Most controllers aim at reducing loads (bending, torsion moments, and shear force) at discrete points of the wing (e.g. the wing root). However, because the control synthesis is based on a single point, it can cause detrimental loads at other points of the structure in closed-loop. Controlling the loads at several discrete points might improve overall gust alleviation results along the structure, but it overly complicates the controller synthesis. This type of limitation is typical of treating a Distributed Parameter System (DPS) as a Lumped Parameter System (LPS). In order to take into account the distributed nature of unsteady spanwise loads, the load distribution must be controlled along its entire profile,

and not only at some of its points. In the present work, this is accomplished by applying shape control and modal decomposition concepts to the spanwise aerodynamic loads distribution.

2. **Lack of control authority over spanwise loads,** which severely limits the GLA performance. This is due to the fact that only conventional control surfaces are employed (ailerons, spoilers and elevators). While ailerons provide local load control, modifying the entire spanwise profile requires to change the aircraft angle of attack by pitching up/down. Due to longitudinal inertia, this strategy is too slow to counteract the critical gusts. In an attempt to mitigate this time lag, very high actuation rates in the control surfaces are typically required. In this work, multiple abutted trailing edge surfaces are used along the entire wingspan, which provides higher control authority and naturally reduces the deflection rate requirements.

3. **Use of control surfaces not designed for gust load alleviation.** Intuitively, one can expect that better GLA performance could be obtained by optimizing the control surfaces for such. In fact, it is shown in [17] that the control surface optimization in the preliminary design should incorporate GLA performance, but that involved a Multi-Disciplinary Optimization (MDO). As will be seen in Chapter 5, the present work applies a methodology for sizing the control surfaces that maximizes the controllability of each of the modal components in the load profile decomposition. This will result in higher accuracy reduced-order models and lower flap deflection rate requirements.

1.3 Proposed approach

The limitations discussed in the previous section motivated the technical approach employed in the present work. In this dissertation, a novel approach is presented in order to tackle the gust alleviation problem. Instead of controlling the structural response at discrete points along the wingspan, it is argued that the aerodynamic behavior of the wing is what should be primarily controlled. Since the gust loads (namely bending moment and shear force) are caused by disturbances in the lift, *the objective is to control the shape of the lift distribution profile along the wingspan.* The distribution of other aerodynamic loads, such as drag and pitching moment, would be associated to other structural loads (in-plane bending moment and torsion moment, respectively). However, this work is focused on lift distribution, which is usually the most relevant loading condition. Henceforth, whenever *aerodynamic load* distribution profile is mentioned, it should be understood as *lift* distribution profile. The complete modeling approach is summarized in Fig. 1.10.

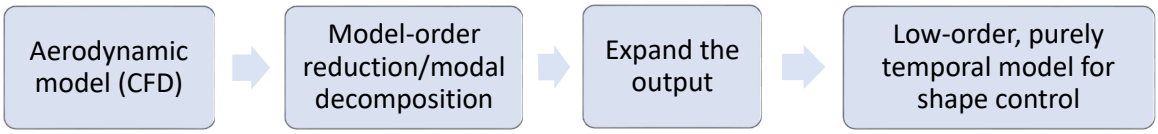

Figure 1.10: Roadmap for shape control of the spanwise lift distribution.

Initially, it is necessary to properly model the spanwise dynamic behavior of the lift on a wing featuring multiple control surfaces. In this work, the control effectors are trailing edge surfaces, able to move up and down in realistically fast rates (e.g. 100 deg/s), but these will be simply referred to as *flaps* hereafter, even though

conventional wing flaps are slow actuated surfaces (e.g. 2 deg/s) that only deflect down.

Rigorously, the aerodynamic behavior of a wing is fundamentally a Distributed Parameter System (DPS), i.e. its state-space representation is infinite-dimensional, governed by Partial Differential Equations (PDE) and associated boundary conditions. In the viscous case, it is governed by the Navier-Stokes equations, whereas for potential (i.e. inviscid, irrotational and incompressible) flows, these are reduced to the simpler Laplace equation. This work deals with the second case (potential flow) and, although the Laplace equation is relatively simple, the time-varying boundaries in unsteady conditions forbid analytical solutions (i.e. continuous in space and time). In order to make the problem solvable, the problem is numerically discretized in space, reducing the PDE to a system of Ordinary Differential Equations (ODE), which has temporal dependence only.

Following this strategy, two CFD (Computational Fluid Dynamics) models capable of dealing with unsteady aerodynamics are developed, namely the Unsteady Lifting-Line Theory (ULLT) and the Unsteady Vortex-Lattice Method (UVLM). With some reasonable assumptions, both models yield linear, time-invariant state-space representations for the wing, with flap deflections as inputs and local lift coefficients at discrete points as outputs. While these models capture the necessary unsteady features of the flow, the large number of states typically obtained from CFD prevent using such models for control synthesis.

Therefore, it becomes necessary to reduce the order of the aerodynamic models. In this work, balanced truncation techniques are employed, which ensure that the trun-

cated model still captures the features of the full-order model in an optimal manner (i.e. the lowest number of states required for a given desired accuracy). Specifically, two model-order reduction methods are applied: the Eigensystem Realization Algorithm (ERA) and the balanced POD, which is derived from the classical Proper Orthogonal Decomposition technique. From the reduced-order models, the dominant eigenvalues and associated mode shapes can be obtained, hence allowing modal identification of aerodynamic models. (A reasonable amount of research has been dedicated to eigenanalysis of flows and a literature survey on the topic is provided in Chapter 4).

In the last box of Fig. 1.10, the output of the resulting reduced-order model is expanded in terms of basis functions (or basis shapes), properly scaled by shape coefficients. In other words, the local lift distribution is represented as a superposition of aerodynamic basis shapes. In principle, any set of basis shapes could be chosen. For example, if the set of basis shapes is a complete set in the sense of Parseval, then any desired lift profile can be approximated by a finite summation of basis functions. However, choosing the previously identified mode shapes as the basis functions provides convenient results: if the reduced-order system is put in modal canonical form, then the modal coordinates (system states) become equal to the shape coefficients (system outputs). In other words, the DPS representation is expanded in terms of a truncated superposition of basis shapes, in order to yield a low order system whose outputs are the shape coefficients.

This MIMO system, mapping flap inputs into aerodynamic shape coefficients is purely temporal, i.e. the spatial dependence has been treated as basis shapes. This

approach allows application of all conventional control tools for the gust alleviation problem, which is cast in the framework of lift distribution control. By controlling the shape coefficients, we are effectively controlling the overall lift profile. Moreover, this approach provides direct relationships between every aerodynamic surface available for GLA and the basis functions used to expand the lift distribution, in the form of a Transfer Function Matrix (TFM). Therefore, additional control surfaces can be easily added to the formulation and, more importantly, their spatial aperture can be designed to maximize their effects over the aerodynamic mode shapes of interest. As will be discussed in Chapter 5, there is one specific set of flap apertures for which the condition number of the TFM evaluated at some frequency of interest (e.g. $s = 0$) can be minimized (i.e. as close to one as possible). This specific spatial design reduces plant directionality and ensures that all mode shapes of interest are achieved with similar control effort, reducing actuator rate requirements, as compared to ordinary set of apertures. It will be shown that, even for a fixed number of control surfaces, control authority can be improved by properly sizing the flaps, such that they best *couple* to the aerodynamic mode shape of interest. Other metrics can also be used and will be explored in Chapter 5.

In this work, this methodology is used to synthesize regulators, to drive lift disturbance caused by exogenous inputs (gusts) to zero, and also trackers, to dynamically follow any desired reference lift profile. The problem of estimation of shape coefficients under the influence of external disturbances (gust) is addressed using observers, and will also be presented in Chapter 5.

1.4 Research hypothesis

In most works regarding aeroelastic models for gust alleviation, the structural portion is obtained from FEM, and the modal expansion treatment is typically employed. However, proper evaluation of dynamic gust loads requires unsteady aerodynamics, which is achieved by some numerical model of the flow (CFD). When the unsteady aerodynamic model is added, many more states are required, which not only complicates simulation and control synthesis, but also breaks the symmetry (self-adjointness) that the purely structural system exhibited (assuming no damping, or proportional damping). As a consequence, the resulting aeroelastic mode shapes are not orthogonal. This happens because fluid systems are, in general, non-self-adjoint [87], [88, Chapter 5]. When combined with the structural system (typically assumed self-adjoint), it renders the aeroelastic system non-self-adjoint. In order to properly model the spanwise load distribution with gust inputs, i.e. to give a treatment from the point of view of DPS, it is required to deal with the non-self-adjointness of unsteady flows. If one is able to apply spatial control to the aerodynamics, then the addition of structural dynamics via modal expansion is relatively simple. In the present work, the main objective is to extend shape control techniques from [1] to aerodynamic systems (non-self-adjoint), although application of such techniques are typically restricted to self-adjoint systems (e.g. structural, acoustic, thermal, etc.). This work addresses the following research hypothesis:

Since the problem lies with aerodynamics systems, this work will focus precisely on the spatial treatment of the aerodynamic part of the problem. The structural part

- The unsteady spanwise lift distribution admits modal decomposition in terms of aerodynamic mode shapes, thereby enabling the design of efficient spatial-temporal controllers for improved gust load alleviation performance.

is well-known and can be treated under the framework of self-adjoint systems. The real contribution lies in how to do a similar procedure to the non-self-adjoint part of the problem.

For this reason, in this work the wing structure is assumed to be rigid, so that the characteristics of the modal behavior can be attributed to the aerodynamics alone. Of course, the structural dynamics can be added later on. Alternatively, the same methodology can be applied to the aeroelastic system (non-self-adjoint), but then the effects of contributions to modal behavior from structures or aerodynamics would become indiscernible.

1.5 Contributions of this work

As observed in the literature review, GLA performance is affected by three main factors: model, sensors, and actuators. This work proposes contributions to all of these fields. First, a new modeling of aerodynamic loads is pursued based on modal superposition concepts. By exploring a modal representation of the spanwise lift distribution, a low-order system Multi-Input Multi-Output (MIMO) representation is obtained, suitable for control synthesis. Regarding actuators, it will be shown

that the control of spanwise loads depends largely on the spatial distribution of control surfaces. Finally, regarding sensors, the present work does not rely on full-state feedback, nor on availability of measurements of gust field ahead of the aircraft (i.e. LIDAR). Instead, the relevant aerodynamic states are estimated via observers. Moreover, the gust magnitude is not assumed known *a priori* and may also be obtained in the estimation process, if desired. The main contributions of the present work can be summarized as:

- Development of a novel approach for spanwise load control using concepts from Distributed Parameter Systems;
- Modal identification of aerodynamic modes from unsteady CFD models;
- Application of a technique for spatial design of flaps that maximizes control authority and reduces the deflection rate requirements for actuators;
- Development of a purely temporal framework for shape control of the lift profile, which is readily amenable to modern MIMO control techniques; and
- Application of real-time state estimation techniques in the presence of exogenous inputs (i.e. gust) using the Unknown Input Observer (UIO).

Although the problem of gust load alleviation provided most of the motivation for this work, the methodology is much more general, in the sense that it can be applied to dynamic management of aerodynamic loads along the wingspan. Therefore, other tasks could also benefit from this methodology, such as flutter suppression, maneuver load alleviation, structural health monitoring and in-flight drag minimization. On a

much larger scale, this work also exemplifies the general problem of spatial control of non-self-adjoint systems based on a truncated plant representation, given by its most relevant modes.

1.6 Dissertation outline

This dissertation is organized as follows:

Chapter 2 contains the details about the unsteady aerodynamic models. A review about thin airfoil unsteady aerodynamics is presented, which is used to augment the classical Prandtl's Lifting-Line, yielding the Unsteady Lifting-Line Theory (ULLT). The second aerodynamic model used is the Unsteady Vortex Lattice Method (UVLM), which is the typical Vortex Lattice Method (VLM) augmented with a finite wake history. The limitations of each method are also explored. Despite being low-order aerodynamic methods (i.e. based on potential flow theory), the number of states in the resulting state-space formulations is too large for practical control synthesis. Therefore, both models require model-order reduction methods.

Chapter 3 reviews the model order reduction methods used in this work, namely the Eigensystem Realization Algorithm (ERA) and the Proper Orthogonal Decomposition (POD). Both methods yield balanced truncated realizations, from which eigenvalues and eigenvectors (mode shapes) can be obtained. Before applying these methods to the aerodynamic models (ULLT and UVLM), a simple Finite Element Model (FEM) of a cantilever beam in bending and torsion is considered. Because the eigenvalues and mode shapes are available from analytical solutions, this test

case serves to validate the ERA and POD routines before applying to aerodynamic models, whose modal parameters are unknown.

Chapter 4 presents the aerodynamic reduced-order models (ROM) obtained via application of the techniques from Chapter 3 to the aerodynamic models formulated in Chapter 2. The eigenvalues and the associated mode shapes obtained from ULLT and UVLM are presented. Both models yield remarkably similar mode shapes, but the model obtained from UVLM has some advantages if compared to that from ULLT. The challenges involved in the identification of modal parameters are discussed, and a physical interpretation of aerodynamic mode shapes is presented. Finally, the mode shapes for other wing planforms are presented and compared to those from a rectangular wing, which is the baseline model used in this work.

Chapter 5 explores the controllers synthesized for gust alleviation. First, the model synthesis is finalized by expanding the system output in terms of mode shapes, and also by defining a truncation level, i.e. how many modes are kept in the reduced-order representation. Then, the size and location of actuators (flaps) are defined, so that the controllability over the modes of interest is maximized. The resulting state-space model is used to synthesize a tracker using full state feedback, in order to track a desired lift distribution and alleviate gust loads. For more practical applications, different observer designs are employed to provide state estimations from feasible measurements. Moreover, the Unknown Input Observer (UIO) is used to decouple the state estimation from the gust inputs, thereby removing the requirement for gust measurements ahead of the wing.

Finally, a summary of the main conclusions and directions for future research are

addressed in Chapter 6.

Chapter 2

Unsteady aerodynamic modeling of a multi-flap wing

In order to perform efficient control, it is necessary to obtain a model that represents the system dynamics. However, most aerodynamic models for airfoils, wings, and also complete configurations are quasi-steady representations, obtained from local linearizations using Taylor series. For example, the lift coefficient for a flapped airfoil can be represented as a function of angle of attack (α) and flap deflection δ_f:

$$C_L = C_L(\alpha, \delta_f) \tag{2.1}$$

Using Taylor series, truncated at the first term for each independent variable, one can obtain:

$$C_L = C_{L0} + \frac{\partial C_L}{\partial \alpha}(\alpha - \alpha_0) + \frac{\partial C_L}{\partial \delta_f}(\delta_f - \delta_{f0}) \tag{2.2}$$

where the subscript *0* represents the nominal condition, i.e. the condition around which the linearization is performed. Merging all constant terms under a new constant

(C'_{L0}), yields:

$$C_L = \left(C_{L0} - \alpha_0 \frac{\partial C_L}{\partial \alpha} - \delta_{f0} \frac{\partial C_L}{\partial \delta_f} \right) + \frac{\partial C_L}{\partial \alpha} \alpha + \frac{\partial C_L}{\partial \delta_f} \delta_f \tag{2.3}$$

$$C_L = C'_{L0} + \frac{\partial C_L}{\partial \alpha} \alpha + \frac{\partial C_L}{\partial \delta_f} \delta_f \tag{2.4}$$

The nominal condition is generally known, so that the model is used to provide variations around this condition:

$$\Delta C_L = \frac{\partial C_L}{\partial \alpha} \Delta\alpha + \frac{\partial C_L}{\partial \delta_f} \Delta\delta_f \tag{2.5}$$

The derivatives can be obtained using finite differences with simulation or experimental data, for example. The inputs are (α, δ_f), whereas the output is C_L. This approach considers a quasi-steady assumption, according to which the rate of change of the inputs is considered small enough, as compared to the forward velocity, so that unsteady effects are negligible. Usually, this is determined using the non-dimensional reduced frequency parameter (k):

$$k = \frac{\omega c}{2V} \tag{2.6}$$

where ω is the oscillation frequency (of angle of attack or flap inputs), c is a reference length (the chord, for the case of airfoil) and V is the freestream velocity. For steady-state applications, ω is zero. As the model inputs are varied more rapidly, the reduced frequency increases and the results provided by the model above deviate from reality, since the quasi-steady assumption breaks down.

From the point of view of controls, the model above is equivalent to a direct gain

relationship. In a transfer-function representation, one would have:

$$\frac{C_L(s)}{\alpha(s)} = \frac{\partial C_L}{\partial \alpha} = C_{L\alpha}(\text{constant}) \tag{2.7}$$

$$\frac{C_L(s)}{\delta_f(s)} = \frac{\partial C_L}{\partial \delta_f} = C_{L\delta_f}(\text{constant}) \tag{2.8}$$

Equivalently, in a state-space representation, the quasi-steady model is simply a direct transmission matrix D, with A, B and C being null matrices of appropriate dimensions:

$$x = Ax + Bu \tag{2.9}$$

$$y = Cx + Du \tag{2.10}$$

The output y is the variation in lift coefficient, the inputs are variations in (α, δ_f):

$$y = Du \tag{2.11}$$

$$\Delta C_L = \begin{bmatrix} C_{L\alpha} & C_{L\delta_f} \end{bmatrix} \begin{bmatrix} \Delta\alpha \\ \\ \Delta\delta_f \end{bmatrix} \tag{2.12}$$

Despite the fact that the quasi-steady model does not contain any states, it usually suffices for most aerodynamic modeling requirements. For classical flight mechanics, for example, the frequencies related to rigid-body motion are much lower than those required to excite unsteady aerodynamics effects, which then become negligible. Moreover, this quasi-steady model could even suffice for long-term lift control applications (i.e. that involve sufficiently low reduced frequencies), such as lift control during the cruise phase of flight.

In this work, however, the primary interest is in short-term lift control. It will be shown that efficient load alleviation requires modeling of unsteady lift behavior, such

as that observed shortly after a sharp gust encounter, or during turbulence. Such variations in lift will most likely require fast control inputs (flap deflections), which is why it is necessary to model lift unsteadiness caused by flap motions as well.

In the next sections, this quasi-steady aerodynamic model is initially presented for a wing featuring multiple trailing edge flaps along the entire span. Then, unsteady models from two different approaches are developed, namely the Unsteady Lifting-Line Theory (ULLT) and Unsteady Vortex Lattice Method (UVLM). These 3D potential flow methods are considered low-order methods from the point of view of aerodynamics, because they are based on solutions of Laplace equation, as opposed to numerical solutions of higher-order PDEs, such as the Navier-Stokes equations. However, the final models obtained from these so-called low-order aerodynamic methods are still relatively complex, and their linear representations in state-space form may require hundreds or thousands of states. From the point of view of controls, this is a high-order model. The large number of states precludes application of model-based control techniques, leading naturally to the necessity of model-order reduction, which will be covered in Chapter 3.

2.1 Quasi-steady aerodynamic model

The reference model used throughout this work is a rectangular wing, with geometric parameters and operating conditions provided in Table 2.1. Also, the wing features 8 trailing edge flaps, spanning 25% of the local chord (0.75c to 1.0c), uniformly distributed along the wingspan, as shown in Fig. 2.1.

Table 2.1: Geometric parameters and operating condition for the wing model used

Geometric parameters	Wingspan	1.80 m
	Chord (c)	0.30 m
	Reference area ($S = b\,c$)	0.54 m^2
	Aspect ratio ($AR = b^2/S$)	6
Operating condition	Airspeed (V)	10 m/s
	Angle of attack (α)	3.0 deg

Figure 2.1: Baseline wing planform and flap distribution.

A discussion on the number of flaps chosen and their spanwise apertures is provided in Chapter 5, Section 5.2. The most basic model for lift distribution as a result of flap deflections is given by a constant matrix M, similarly to the airfoil lift model given previously. However, for the case of a wing, the lift coefficient is now given by an output vector, which represents the lift coefficient distribution along the wingspan. Considering the effects of flap deflections only, one can obtain:

$$\underset{64\times1}{\Delta C_L} = \underbrace{\begin{bmatrix} C_{L\delta f_1} & C_{L\delta f_2} & \dots & C_{L\delta f_8} \end{bmatrix}}_{\text{Matrix M, } 64\times8} \underbrace{\begin{bmatrix} \Delta\delta f_1 \\ \Delta\delta f_2 \\ \vdots \\ \Delta\delta f_8 \end{bmatrix}}_{u,\ 8\times1} = Mu \tag{2.13}$$

Each flap deflection in the input vector u multiplies a column of lift slope vector ($C_{L\delta f_i}$), which quantifies how the i-th flap causes variations in the spanwise lift profile (ΔC_L).

Figure 2.2(a) presents distributions of local lift coefficient as a function of nor-

malized wingspan, such that $y/(b/2) = -1, 0, 1$ are left wingtip, wing root and right wingtip stations, respectively. It shows lift coefficient distributions associated to each flap individually deflected by 5 deg, as well as the baseline distribution for the rectangular wing at 3 deg AOA (i.e. no flaps deflected). The spanwise location and size of each flap is also indicated by arrows. The lift slope vectors $C_{L\delta f_i}$ are obtained by subtracting the baseline distribution from the distributions associated to each flap, and dividing by the flap deflection employed (in this example, 5 deg), and were plotted in Figure 2.2(b). These results were generated using a Vortex Lattice Method (VLM) routine, and the lift profile is sampled at 64 uniformly distributed spanwise stations.

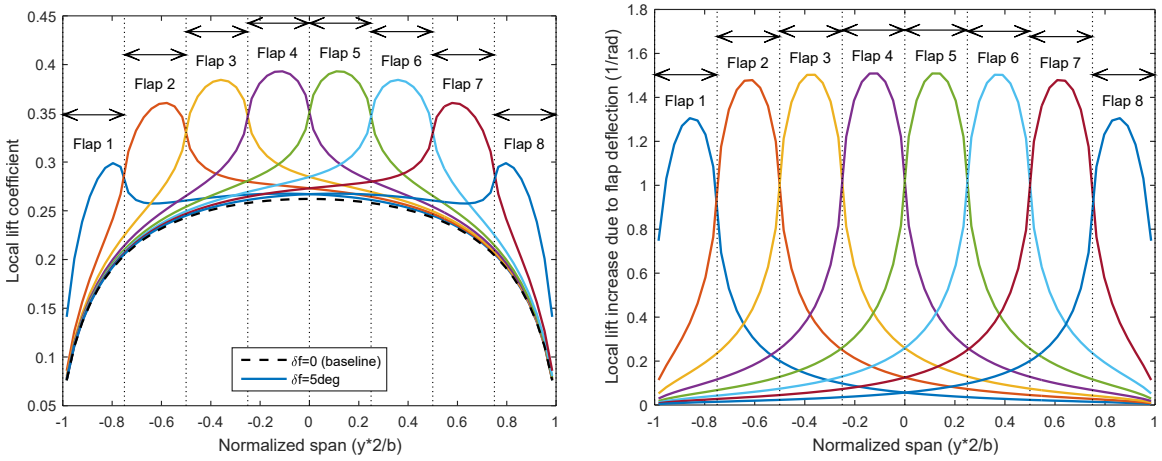

(a) (b)

Figure 2.2: Influence functions for 8 flaps uniformly distributed.

It is clear that the variations in spanwise lift can be readily obtained by simply multiplying (scaling) each curve in Figure 2.2(b) by the corresponding flap deflection and summing the results. Therefore, the quasi-steady model is completely described by the matrix M. It is also clear that flaps near the wingtips have lower lift slope

peaks, due to 3D flow effects. Each curve crosses zero at the wingtips, where the pressure differential between the top and bottom wing surfaces necessarily becomes zero. In the context of this work, these curves will be addressed as *influence functions* of the system, or *static Green's functions*, since they represent the steady-state behavior of the plant under constant inputs.

The natural question that rises is: can this simplified model be used for lift distribution control? At least in steady-state conditions? Assume that the current lift distribution profile ($C_{L,\text{actual}}$) is somehow measured (e.g. using pressure taps around the airfoil, along several spanwise stations), but a different lift profile is desired ($C_{L,\text{desired}}$). It is possible to deflect flaps to generate a change in local lift coefficient ΔC_L, such that the current lift profile becomes the desired profile:

$$\underbrace{C_{L,\text{actual}}}_{\text{output, } y} + \Delta C_L = \underbrace{C_{L,\text{desired}}}_{\text{reference, } r} \tag{2.14}$$

Combining the two previous equations:

$$\Delta C_L = Mu = r - y \tag{2.15}$$

Because the columns of the matrix M are always linearly independent (the matrix M is always full-rank), it is possible to obtain the optimal flap inputs u that best approximate the desired profile, in a least squares sense. The control inputs can be also obtained using the Moore-Penrose pseudoinverse of the matrix (M^+), which provides the same solution as the least squares regression when M is full-rank:

$$u = \underbrace{M^+}_{8\times 64}(\Delta C_L) = M^+ \underbrace{(r - y)}_{\text{error, } e} \tag{2.16}$$

From the point of view of controls, let the aerodynamic system be represented by a 64×8 Transfer Function Matrix (TFM) called $G(s)$, whose entries are rational, proper transfer functions, but are unknown at this point. Then, at low frequencies (i.e. as s tends to zero), $G(s)$ must replicate the quasi-steady model, given by the matrix M :

$$\lim_{s \to 0} G(s) = G_0 = M \tag{2.17}$$

In block diagram form, the controller approach proposed so far is given in Figure 2.3, where r, y and e are 64×1 vectors, and u is the 8×1 input vector.

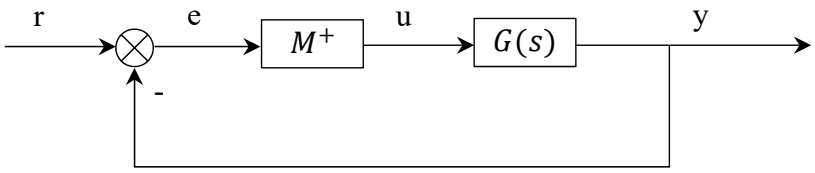

Figure 2.3: Block diagram for lift distribution control using a quasi-steady aerodynamic model.

It can be seen that such control law is simply a proportional gain controller (K_p), given precisely by the 8×64 matrix M^+. Therefore, it will always exhibit non-zero steady-state error in tracking a desired lift distribution. The transfer function matrix between the reference command (r) and the error (e) is given by:

$$\begin{aligned} e(s) &= r(s) - y(s) = r(s) - G(s)M^+e(s) \\ e(s) &= \frac{I}{I + G(s)M^+} r(s) \end{aligned} \tag{2.18}$$

Now, consider that the system is required to achieve a reference lift distribution $r = C_{L,\text{desired}}$, given by a 64×1 vector. Assuming that the aerodynamic system $G(s)$ is open-loop stable, the Final Value Theorem for a step input (in all 64 channels) can

be used to obtain the steady-state error:

$$e_{ss} = \lim_{s\to 0} s \underbrace{\left(\frac{I}{I + G(s)M^{+}}\right)}_{64\times 64} \underbrace{\left(\frac{1}{s}r\right)}_{64\times 1} = \frac{I}{I + G_0 M^{+}} r = \frac{I}{I + MM^{+}} r = \underbrace{\frac{1}{2}r}_{64\times 1} \tag{2.19}$$

Therefore, using the quasi-steady model as depicted above, one should expect steady-state errors of 50% when tracking a desired lift distribution. Similarly to a Single-Input Single-Output (SISO) case, increasing the gain reduces the steady-state error, but may also induce instability at some point.

Differently from a SISO case, however, augmenting the controller with damping and integral action (i.e. PID controller) would be no simple task, because this is a large MIMO system (64×8), whose internal dynamics are unknown at this point. Even if the internal dynamics were known, assuming a fully coupled system, it would be necessary to simultaneously tune the entries of two 8×64 matrices, for the derivative and integral gains. Reducing the number of system outputs from 64 to 32 or 16 spanwise stations would simplify the gains matrices, but would also degrade the discretization of the lift profile being modeled. This discussion makes it clear that ***the quasi-steady model is not suitable for reference tracking in feedback control***. A better representation of the system dynamics is necessary to allow proper controller synthesis.

2.2 Unsteady Lifting-Line Theory (ULLT)

From the previous section, it became clear that the quasi-steady model yields a very limited representation of the actual system. It is known from classical unsteady

2D airfoil theory that the lift response to a unit step input in flap deflection cannot be represented by a simple gain. In other words, there are internal dynamics that can only be properly addressed with a state-space or transfer-function representation. Theodorsen's function represents the unsteady airfoil behavior in the frequency-domain [23], whereas Wagner's function is formulated in time-domain [89] and provides the lift response to a unit step input in angle of attack. In fact, these two representations are related by means of a Fourier transform [90].

However, lift distribution control requires a model that represents the unsteady 3D behavior of the lift along the wingspan. While Theodorsen's theory is analytically exact (within its assumptions and constraints) for thin airfoils, there is no such analytical solution to the unsteady aerodynamics of wings, which have tip effects that induce the 3D flow behavior along the wingspan. Therefore, numerical approaches are usually employed, generally referred to as Computational Fluid Dynamics (CFD).

Perhaps the simplest model for finite wings is provided by Prandtl's classical Lifting-Line Theory (LLT), according to which the bounded vorticity along the wing is represented by a superposition of horseshoe vortices [91]. The traditional form, however, is only able to provide quasi-steady results. This is because the method assumes a quasi-steady airfoil behavior, and also employs a quasi-steady version of the Kutta-Joukowski theorem. In the present work, Prandtl's LLT is augmented with unsteady 2D airfoil behavior (Wagner's function, in the time domain) and also with the unsteady version of the Kutta-Joukowski theorem.

2.2.1 Potential flow

When the potential-flow assumption is made, the flow is considered incompressible, irrotational and inviscid. Moreover, the continuity equation is reduced to the Laplace's equation, which is a much simpler, well-known, linear Partial Differential Equation (PDE) that governs potential flows:

$$\nabla^2 \varphi = 0 \tag{2.20}$$

where φ is a scalar function whose gradient is equal to the flow velocity vector. This equation admits a number of fundamental flows as solutions, namely source, doublet, vortex and uniform flow. Since the equation is linear, any combination of these fundamental solutions is also a solution. The different flow solutions are a consequence of the boundary conditions for each problem. The two sets of boundary conditions (B.C.) required are:

1. Infinity B.C.: the flow velocity far away from the body must be equal to the uniform freestream value (V_∞);

2. Wall B.C. (flow tangency condition): the flow must not penetrate the body surface, therefore the flow component perpendicular to the body surface is zero.

2.2.2 Prandtl's classical Lifting-Line Theory

The development and nomenclature shown here follow closely the derivation from [91, Chapter 5] and [92, Chapter 7]. In the Lifting-Line approach, a uniform flow is combined with a superposition of horseshoe vortex filaments, in order to satisfy the

boundary conditions and also represent the bound vorticity and the wingtip vortices observed experimentally. From the Biot-Savart law, one can obtain the flow velocity induced by a vortex filament:

$$\mathrm{d}V = \frac{\Gamma}{4\pi}\frac{\mathrm{d}l \times r}{|r|^3} \tag{2.21}$$

where Γ is the circulation (strength) of the vortex filament (Fig. 2.4). Integrating along the filament, which extends from $-\infty$ to $+\infty$, yields the velocity vector induced by the entire vortex filament at a point P:

$$V = \int_{-\infty}^{+\infty} \frac{\Gamma}{4\pi}\frac{\mathrm{d}l \times r}{|r|^3} \tag{2.22}$$

Then, the magnitude of the velocity (scalar quantity) is given by:

$$V = \frac{\Gamma}{4\pi}\int_{-\infty}^{+\infty} \frac{\sin\theta}{r^2}\mathrm{d}l = \frac{\Gamma}{2\pi h} \tag{2.23}$$

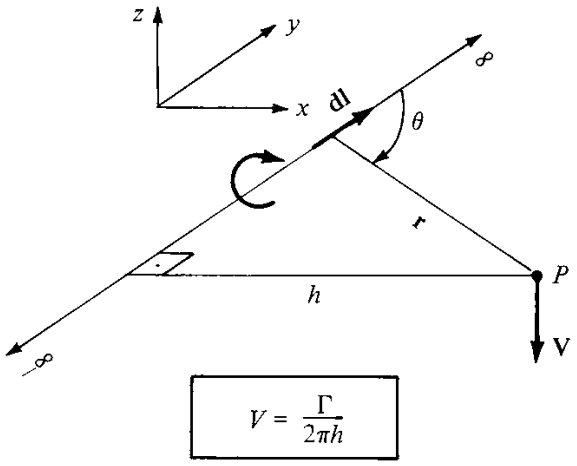

Figure 2.4: Velocity induced at point P by an infinite, straight vortex filament.

(Source: [91])

Similarly, the velocity (magnitude) induced by a half-infinite filament is given by $V = \Gamma/4\pi h$. Now, change the variable V to downwash w (out of the plane defined by

the filament and the point P), take $h = (y_0 - y)$, i.e. the distance between point of interest y_0 and the vortex filament location y, according to Figure 2.5, and consider an infinitesimally small vortex strength:

$$\mathrm{d}w = -\frac{\left(\frac{\mathrm{d}\Gamma}{\mathrm{d}y}\right)\mathrm{d}y}{4\pi\left(y_0 - y\right)} \tag{2.24}$$

where the negative sign is added for consistency with the figure. Integrating along the wingspan, from wingtip to wingtip, yields:

$$w\left(y_0\right) = -\frac{1}{4\pi}\int_{-b/2}^{b/2}\frac{\left(\frac{\mathrm{d}\Gamma}{\mathrm{d}y}\right)\mathrm{d}y}{y_0 - y} \tag{2.25}$$

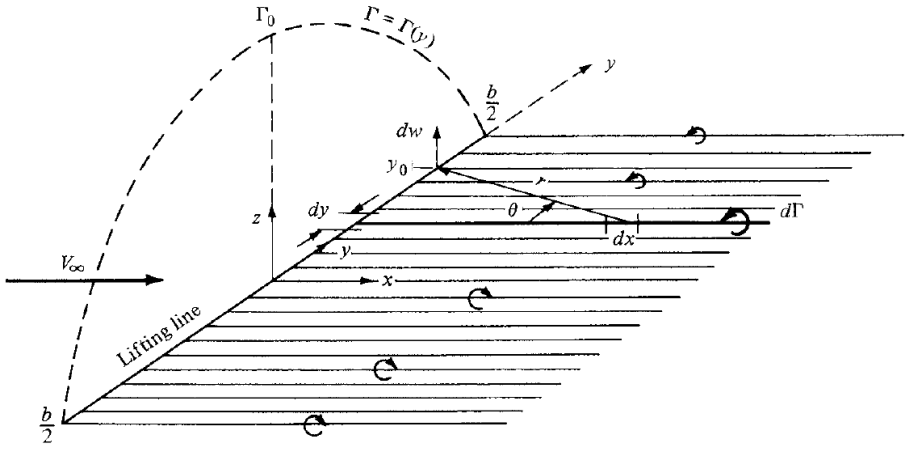

Figure 2.5: Superposition of an infinite number of horseshoe vortices along the lifting line. (Source: [91])

This is the equation relating the distributed induced downwash with circulation along wingspan. For a given function $\Gamma\left(y\right)$, the induced downwash (w) and induced angle of attack (α_i) can be obtained using a small angle approximation:

$$\alpha_i\left(y_0\right) = \tan^{-1}\left(\frac{-w\left(y_0\right)}{V_\infty}\right) \cong -\frac{w\left(y_0\right)}{V_\infty} = \frac{1}{4\pi V_\infty}\int_{-b/2}^{b/2}\frac{\left(\frac{\mathrm{d}\Gamma}{\mathrm{d}y}\right)\mathrm{d}y}{y_0 - y} \tag{2.26}$$

Now, some basic aerodynamic considerations are applied:

1. The effective angle of attack (α_{eff}) at each wing section is given by the geometric angle of attack (α), minus the induced angle of attack (α_i):

$$\alpha_{eff}(y_0) = \alpha(y_0) - \alpha_i(y_0) \tag{2.27}$$

2. The 2D lift model for the airfoil is given by a simple linear relation, as a function of the local effective angle of attack:

$$c_l = c_{l,0} + c_{l,\alpha}\alpha_{eff} = c_{l,\alpha}\left(\frac{c_{l,0}}{c_{l,\alpha}} + \alpha_{eff}\right) = c_{l,\alpha}(\alpha_{eff} - \alpha_0) \tag{2.28}$$

where lowercase notation indicates parameters for the airfoil: $c_{l,0}$ is lift coefficient at zero angle of attack, which is zero for symmetric airfoils; $c_{l,\alpha}$ denotes the lift slope, usually assumed 2π (from thin airfoil theory); α_0 is the angle of attack for zero lift.

Any geometric or aerodynamic torsion along the wing can be incorporated into these parameters, which become functions of the spanwise location (y_0). The model for flap deflection (δ_f) can also be added:

$$c_l = c_{l,0} + c_{l,\alpha}\alpha_{eff} + c_{l,\delta f}\delta_f \tag{2.29}$$

At low angles of attack, the effect of positive flap deflection (i.e. trailing edge down) is simply to increase the lift generated by the section. This can be interpreted as an increase in $c_{l,0}$, or a decrease in α_0. In either way, the variation of flap deflection along the wingspan can be easily incorporated into $c_{l,0}(y_0)$ or $\alpha_0(y_0)$.

3. Kutta-Joukowski theorem, which relates the local lift per unit span (L') to the circulation $\Gamma(y)$:

$$L'(y_0) = \rho_\infty V_\infty \Gamma(y_0) \tag{2.30}$$

where ρ_∞ and V_∞ represent flow density and velocity in freestream conditions, respectively. Hence, if the distribution of circulation is known, the local (dimensional) lift per unit span can be readily obtained. In non-dimensional form, one can obtain:

$$c_l(y_0) = \frac{L'(y)}{\frac{1}{2}\rho_\infty V_\infty^2 c(y_0)} = \frac{2\rho_\infty V_\infty \Gamma(y_0)}{\rho_\infty V_\infty^2 c(y_0)} = \frac{2\Gamma(y_0)}{V_\infty c(y_0)} \tag{2.31}$$

where the airfoil chord c is also allowed to vary as a function of spanwise coordinate (y_0). Substituting (3) into (2) yields:

$$c_l = c_{l,\alpha}(\alpha_{eff} - \alpha_0) = \frac{2\Gamma(y_0)}{V_\infty c(y_0)} \tag{2.32}$$

$$\alpha_{eff} = \frac{2\Gamma(y_0)}{c_{l,\alpha} V_\infty c(y_0)} + \alpha_0 \tag{2.33}$$

Substituting the expression for α_{eff} gives:

$$\alpha_{eff} = \frac{2\Gamma(y_0)}{c_{l,\alpha} V_\infty c(y_0)} + \alpha_0 = \alpha(y_0) - \alpha_i(y_0) \tag{2.34}$$

Substituting the expression for $\alpha_i(y_0)$ as a function of circulation $\Gamma(y_0)$ yields the Prandtl's Lifting-Line equation:

$$\alpha(y_0) = \frac{2\Gamma(y_0)}{c_{l,\alpha} V_\infty c(y_0)} + \alpha_0(y_0) + \frac{1}{4\pi V_\infty} \int_{-b/2}^{b/2} \frac{\left(\frac{\mathrm{d}\Gamma}{\mathrm{d}y}\right) \mathrm{d}y}{y_0 - y} \tag{2.35}$$

Note that the geometric angle of attack $\alpha(y_0)$ is also allowed to vary along the span. This is particularly useful for simulating quasi-steady effects, such as locally induced velocity components due to wing motion (pitch, roll, yaw rates).

Despite the apparent simplicity in its derivation, there is no general analytical solution to this integral-differential equation. However, it can be verified that it

admits an elegant solution for the specific case of elliptical circulation distribution (hence, elliptical lift distribution as well):

$$\Gamma(y) = \Gamma_0 \sqrt{1 - \left(\frac{2y}{b}\right)^2} \tag{2.36}$$

$$L'(y) = \rho_\infty V_\infty \Gamma_0 \sqrt{1 - \left(\frac{2y}{b}\right)^2} \tag{2.37}$$

There are some important aspects about the elliptical distribution:

1. It generates a constant downwash along the wingspan;

2. It can be proved that the constant downwash is also associated to a minimum induced drag;

3. An elliptical planform is required to generate an exact elliptical lift distribution.

However, for the purposes of this work, the main aspect of the elliptical circulation distribution is that it can be represented by a sine function, under the following change of variables:

$$y = -\frac{b}{2}\cos\theta \qquad , \qquad \mathrm{d}y = \frac{b}{2}\sin\theta\,\mathrm{d}\theta \tag{2.38}$$

The coordinate in the spanwise direction is given by θ, with $0 \leq \theta \leq \pi$. Therefore, the circulation is now given by:

$$\Gamma(\theta) = \Gamma_0 \sin\theta \tag{2.39}$$

This formulation suggests that other circulation distributions can be represented by a Fourier sine series. An approximated but general solution can be obtained using

Fourier sine series expansion for $\Gamma(\theta)$:

$$\Gamma(\theta) = 2bV_\infty \sum_{n=1}^{N} A_n \sin n\theta \tag{2.40}$$

Using this expanded form, it is possible to obtain new expressions for $\mathrm{d}\Gamma/\mathrm{d}y$ and α_i as functions of the new variable θ:

$$\frac{\mathrm{d}\Gamma}{\mathrm{d}y} = \frac{\mathrm{d}\Gamma}{\mathrm{d}\theta}\frac{\mathrm{d}\theta}{\mathrm{d}y} = 2bV_\infty \sum_{n=1}^{N} n\, A_n \cos n\theta \, \frac{\mathrm{d}\theta}{\mathrm{d}y} \tag{2.41}$$

$$\alpha_i(\theta) = \sum_{n=1}^{N} n\, A_n \frac{\sin n\theta}{\sin\theta} \tag{2.42}$$

Substituting equations for $\Gamma(\theta)$ and $\alpha_i(\theta)$ into the original equation yields:

$$\alpha(\theta_0) = \frac{4b}{c_{l,\alpha}\, c(\theta_0)} \sum_{n=1}^{N} A_n \sin(n\theta_0) + \alpha_{L=0}(\theta_0) + \sum_{n=1}^{N} nA_n \frac{\sin(n\theta_0)}{\sin(\theta_0)} \tag{2.43}$$

This is the general Lifting-Line equation for arbitrary circulation distributions. All parameters are prescribed, except for the N Fourier coefficients A_n. In order to obtain these coefficients, it is required to evaluate the equation at N prescribed spanwise stations, providing a system of N algebraic equations and N unknowns (A_n). After some manipulation, the matrix format $(A\,a = B)$ for this linear system of equations can be obtained:

$$\underbrace{\sin(\theta_0\, \underline{n})}_{N\times N} \circ \left\{ \underbrace{\begin{bmatrix} \sin(\theta_0) & \cdots & \sin(\theta_0) \end{bmatrix}}_{N\times N} + \frac{c_{l,\alpha}}{4b} \underbrace{c(\theta_0)\, \underline{n}}_{N\times N} \right\} \underbrace{\begin{bmatrix} A_1 \\ \vdots \\ A_N \end{bmatrix}}_{a} =$$

$$\underbrace{(\alpha(\theta_0) - \alpha_{L=0}(\theta_0)) \circ \frac{c_{l,\alpha}}{4b} c(\theta_0) \circ \sin(\theta_0)}_{B\text{: column vector, } N\times 1} \tag{2.44}$$

where:

$\circ$ denotes element-wise multiplication (or Hadamard product);

θ_0 is a $N \times 1$ column vector of spanwise stations (cosine distribution);

$\underline{n}$ is a $1 \times N$ row vector of Fourier series indexes, $\underline{n} = [1, 2, \ldots, N]$;

a is a $N \times 1$ column vector of unknown Fourier coefficients A_n.

All quantities depending on θ_0 vary from one spanwise location to another. Therefore, these quantities vary along the columns of the A matrix, whereas the Fourier series indexes (n) vary along its rows. Therefore, a simple matrix inversion yields the Fourier coefficients for the circulation distribution $\Gamma(\theta)$, from which all other parameters can be obtained: local lift, local downwash, effective angle of attack, induced drag, for example. Because of its simplicity, Prandtl's Lifting-Line is still used today as a preliminary design tool, before higher fidelity methods are applied. [91].

2.2.3 Unsteady 2D Thin Airfoil Theory

Perhaps the most widely used model for an oscillating airfoil in incompressible flow is the one developed by Theodorsen [23]. In his approach, the unsteady lift caused by airfoil harmonic motion is represented in the frequency-domain by a complex-valued function, such that any variation in its magnitude and phase as a function of the reduced-frequency represent the deviations with respect to the steady-state case (zero frequency). Although very useful in rotary-wing and fixed-wing (e.g. for flutter analysis), Theodorsen's function is rigorously applicable only for purely oscillatory inputs.

For general inputs, a time-domain approach was conducted by Wagner [89], who obtained the indicial lift response function to a step input in angle of attack. If the indicial (step) response is known, then any arbitrary input can be obtained by means of Duhamel's superposition integral:

$$y(t) = f(0)A(t) + \int_0^t \frac{\mathrm{d}f(\tau)}{\mathrm{d}\tau} A(t-\tau)\mathrm{d}\tau \tag{2.45}$$

where $f(t)$ is an arbitrary input, $A(t)$ is the indicial (step) response of the system, and $y(t)$ is the calculated output. Duhamel's integral is closely related to the convolution integral, which employs the system's impulse response $h(t)$ to generate the output and is given by:

$$y(t) = \int_0^t f(\tau)h(t-\tau)\mathrm{d}\tau \tag{2.46}$$

The convolution integral is commonly represented as a function of the impulse response $h(t)$. In Appendix A, it is proved that both approaches (convolution and Duhamel's integrals) are equivalent. Although Wagner's function is known exactly in terms of Bessel functions (see [93, Section 5-7]), an exponential approximation is typically used for practical applications:

$$\phi(s) = 1 - A_1 \exp(-b_1 s) - A_2 \exp(-b_2 s) \tag{2.47}$$

where $A_1 = 0.2048$, $b_1 = 0.0557$, $A_2 = 0.2952$, $b_2 = 0.333$ and s is the distance traveled in semichords ($s = 2Vt/c$). These coefficients are from Leishman (1994)[90], although other sets were published by R. T. Jones (1938) [94] and W. P. Jones (1945) [95]. Further discussion is available in [96, Section 8.10]. These approximations yield an error of less than 1% of the exact solution, as can be observed in Fig. 2.6.

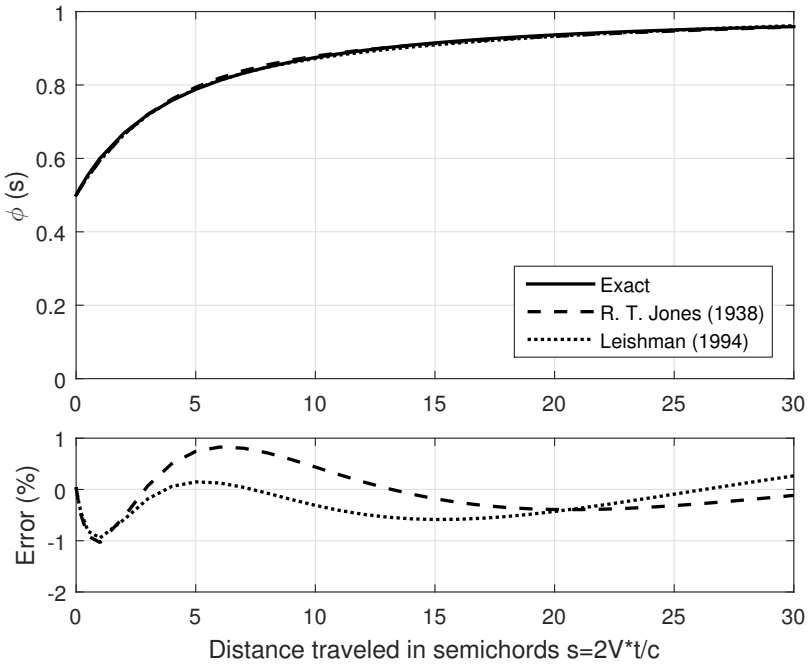

Figure 2.6: Comparison of Wagner's function approximation with exact values.

The mechanism of generation of circulatory lift due to changes in AOA is the same as that for changes in flap deflection. Therefore, Wagner's function is also used to obtain the airfoil lift response to arbitrary flap inputs, for a given flap geometry. Using the approximation of Wagner's function (Eq. 2.47), it is possible to obtain a state-space formulation equivalent to the Duhamel's integral, given by:

$$\begin{bmatrix} \dot{z}_1 \\ \dot{z}_2 \end{bmatrix} = \begin{bmatrix} 0 & 1 \\ -b_1 b_2 \left(2V/c\right)^2 & -\left(b_1 + b_2\right)\left(2V/c\right) \end{bmatrix} \begin{bmatrix} z_1 \\ z_2 \end{bmatrix} + \begin{bmatrix} 0 \\ 1 \end{bmatrix} \delta_{qs}\left(t\right) \tag{2.48}$$

where V is the freestream velocity, c is the airfoil chord and δ_{qs} is the quasi-steady flap input, given by a combination of flap deflection (δ_f) and its time-derivative ($\dot{\delta}_f$):

$$\delta_{qs}(t) = \frac{F_{10}\delta_f(t)}{\pi} + \frac{cF_{11}\dot{\delta}_f(t)}{4\pi V} \tag{2.49}$$

where F_{10} and F_{11} are geometric constants that depend only on the percentage of the airfoil chord occupied by the flap. More details are provided in [90]. For this

state-space formulation, the output equation is given by:

$$C^{c}_{L,\delta f}(t) = 2\pi \begin{bmatrix} b_1 b_2 \left(2V/c\right)^2 & \left(A_1 b_1 + A_2 b_2\right)\left(2V/c\right) \end{bmatrix} \begin{bmatrix} z_1 \\ \\ z_2 \end{bmatrix} + \pi \delta_{qs}(t) \tag{2.50}$$

which provides the circulatory portion of the airfoil lift due to flap inputs.

2.2.4 Non-circulatory terms and the relation to actuator dynamics

The total unsteady lift due to flaps is obtained by adding this circulatory model (Eq. 2.50) to the non-circulatory portion, which is given by:

$$C^{nc}_{L,\delta f}(t) = \frac{c}{2V^2}\left[-VF_4\dot{\delta}_f(t) - \frac{c}{2}F_1\ddot{\delta}_f(t)\right] \tag{2.51}$$

where F_4 and F_1 are geometric constants that depend only on the size of the flap relative to the airfoil chord, as given in [90]. This non-circulatory part is proportional to the instantaneous displacements and require no states to be represented. Also called *apparent mass effect*, this term accounts for the acceleration of the fluid around the airfoil, and becomes increasingly more important for higher values of reduced frequency (k). For low reduced frequencies ($k < 0.1$) the unsteady lift is dominated by the circulatory component [96, page 435]. For fixed wing applications, the values of k involved are usually well below 0.1 because of the relatively large forward velocity V (as compared to a flapping wing vehicle, for example):

$$k = \omega c/2V \tag{2.52}$$

In this work, it is necessary to represent the unsteady lift due to dynamic flap inputs. For the reference model and operating conditions from Table 2.1, one can

compute the required flap actuation rate such that $k = 0.1$:

$$\omega = k\frac{2V}{c} = (0.1)\frac{2\,(10)}{0.3} = 6.66 \text{ rad/s} = 380 \text{ deg/s} \tag{2.53}$$

For a typical airliner, with mean aerodynamic chord $c = 3$ m, cruise speed $V = 200$ m/s, the requirement would be twice that value:

$$\omega = k\frac{2V}{c} = (0.1)\frac{2\,(200)}{3} = 13.3 \text{ rad/s} = 760 \text{ deg/s} \tag{2.54}$$

For a realistic actuator, it is very unlikely that the maximum attainable rates would reach these limits. As an example in small scale vehicles, a typical digital servo-motor can achieve nominal deflection rates up to 300-400 deg/s under zero external load conditions. When loaded, the rates naturally become smaller, becoming a function of the external torque applied. For large-scale aircraft, conventional electro-hydraulic actuators (EHA) typically operate at rates up to 100 deg/s or lower, depending on the dynamic pressure. For example, maximum aileron rates from 60 to 100 deg/s were observed in typical flight conditions with a F-18 fighter jet [97]. Also, a frequency bandwidth of 4 rad/s (230 deg/s) was observed in flight tests. After this frequency, the actuator response rolls-off. In large commercial passenger aircraft, a typical aileron actuator has a maximum rate of 35-40 deg/s in cruise conditions [17, 65, 61]. Therefore, the application of inputs in fixed wing aircraft generally yields a reduced frequency well below 0.1.

Such actuator rates are still high enough, so that an unsteady model is required to account for the circulatory effects (i.e. influence of the shed wake vorticity). On the other hand, trailing edge actuators realistically have limitations that preclude achieving very high deflection rates and accelerations, thus the non-circulatory term

is relatively small. In this work, its contribution to the unsteady lift is not explicitly considered in the final model, which can be justified for relatively low reduced frequencies.

2.2.5 Modeling of arbitrary gust inputs

In the state-space formulation provided for the circulatory lift due to flap deflections in Eq. (2.48), z_1 and z_2 are simply auxiliary states, without immediate physical interpretation. Similarly, the effect of arbitrary downwash inputs on lift (e.g. for gust simulation) can be obtained by using the Küssner gust entry indicial function, along with Duhamel's integral [90]. The Küssner function provides the lift response due to a step input in vertical gust, such as a sharp gust entry, and can be approximated by:

$$\psi(s) = 1 - A_3 \exp\left(-b_3 s\right) - A_4 \exp\left(-b_4 s\right) \tag{2.55}$$

where $A_3 = 0.5792$, $b_3 = 0.1393$, $A_4 = 0.4208$, $b_4 = 1.802$ and s is the distance traveled in semichords ($s = 2Vt/c$). After applying Duhamel's integral, the state-space formulation of lift due to arbitrary gust inputs is given by:

$$\begin{bmatrix} \dot{z}_3 \\ \\ \dot{z}_4 \end{bmatrix} = \begin{bmatrix} 0 & 1 \\ \\ -b_3 b_4 \left(2V/c\right)^2 & -\left(b_3 + b_4\right)\left(2V/c\right) \end{bmatrix} \begin{bmatrix} z_3 \\ \\ z_4 \end{bmatrix} + \begin{bmatrix} 0 \\ \\ 1 \end{bmatrix} \frac{w_g(t)}{V} \tag{2.56}$$

$$C_L^g(t) = 2\pi \begin{bmatrix} b_3 b_4 \left(2V/c\right)^2 & \left(A_3 b_3 + A_4 b_4\right)\left(2V/c\right) \end{bmatrix} \begin{bmatrix} z_3 \\ \\ z_4 \end{bmatrix} \tag{2.57}$$

Other terms could be added to the formulation, such as those due to airfoil pitching and plunging, as well as the unsteady pitching moment and flap hinge moment, including non-circulatory terms [90, 96]. However, for the purposes of this work,

only the influence of flaps and gust inputs are taken into account, so that 4 states ($z_i,\ i = 1, 2, 3, 4$) are sufficient for modeling unsteady lift in 2D conditions.

2.2.6 Analysis and simulation of the unsteady 2D lift model

The original formulation from Leishman [90, 96] requires a so-called quasi-steady flap input $\delta_{qs}(t)$ composed of both flap deflections and flap rates (Eq. 2.49). However, this formulation makes time-domain simulations less intuitive. For example, when a unit step input in $\delta_{qs}(t)$ is simulated, it is not clear how much flap deflection and flap rate is being applied. One additional state is needed to make flap rate the sole input:

$$\begin{bmatrix} \dot{z}_1 \\ \dot{z}_2 \\ \dot{\delta}_f \end{bmatrix} = \begin{bmatrix} 0 & 1 & 0 \\ -b_1 b_2 \left(2V/c\right)^2 & -\left(b_1 + b_2\right)\left(2V/c\right) & \frac{F_{10}}{\pi} \\ 0 & 0 & 0 \end{bmatrix} \begin{bmatrix} z_1 \\ z_2 \\ \delta_f \end{bmatrix} + \begin{bmatrix} 0 \\ \frac{cF_{11}}{4\pi V} \\ 1 \end{bmatrix} \dot{\delta}_f \tag{2.58}$$

$$C^c_{L,\delta f}(t) = 2\pi \begin{bmatrix} b_1 b_2 \left(2V/c\right)^2 & \left(A_1 b_1 + A_2 b_2\right)\left(2V/c\right) & \frac{F_{10}}{(2\pi)} \end{bmatrix} \begin{bmatrix} z_1 \\ z_2 \\ \delta_f \end{bmatrix} + \left[\frac{cF_{11}}{4V}\right] \dot{\delta}_f \tag{2.59}$$

Using this formulation, an impulse applied to this system (i.e. as flap rate) can be interpreted as a unit step input applied to flap deflection, which produces more intuitive results than the combined input $\delta_{qs}(t)$, even though both approaches are mathematically consistent. The system response to an impulse input is shown in Fig. 2.7). It can be seen that a unit step input on flap deflection (i.e. 1 radian = 57.3 deg) causes a variation of 3.82 in C_L, yielding a steady-state gain of 3.82/rad. This result could also be obtained using the Final Value Theorem. Even though the impulse is

applied with zero initial conditions, the model output does not start from zero at $t = 0$ s. This is fundamentally due to the fact that Wagner's indicial (step) function does not have zero initial conditions as well (see Fig. 2.6).

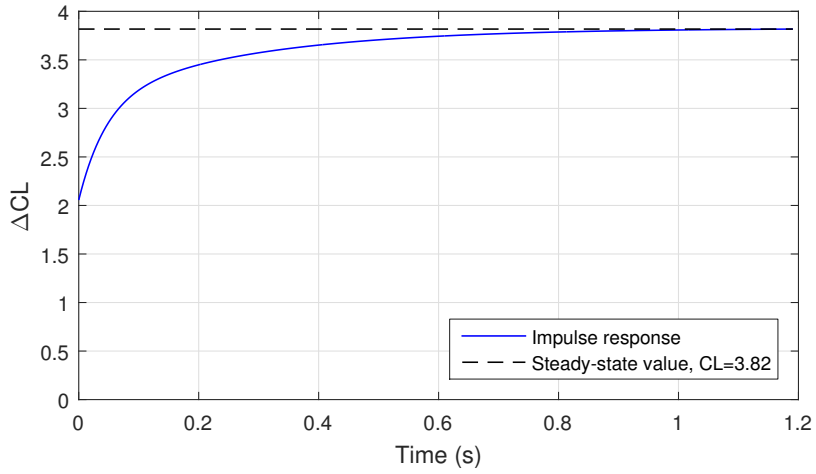

Figure 2.7: Lift response to an impulse input on flap rate.

Bode plots can also be promptly generated with the augmented formulation. Let $G(s)$ denote the transfer function of the system, i.e. between flap rate input $U(s)$ and output $Y(s)$:

$$G(s) = \frac{Y(s)}{U(s)} \tag{2.60}$$

However, it is more intuitive to obtain a transfer function between flap deflection $\Delta_f(s)$ and output $Y(s)$:

$$U(s) = \mathcal{L}\left\{\dot{\delta}_f(t)\right\} = s\Delta_f(s) - \delta_f(0) = s\Delta_f(s) \tag{2.61}$$

Hence:

$$\frac{Y(s)}{\Delta_f(s)} = s\,G(s) \tag{2.62}$$

Bode plots generated for this system are presented next. In Figure 2.8, the frequencies are given in terms of the reduced frequency k, which is the relevant parameter

for unsteady aerodynamics. Since k is non-dimensionalized by the airfoil chord (c) and the freestream velocity (V), it allows comparisons for different model scales and operating conditions. For better physical insight, the dimensional flap actuator frequencies ω (in Hz) associated to $c = 0.3$ m and $V = 10$ m/s (see Table 2.1) are also provided in the plot. It should be noted that the scales are all linear. As discussed in Section 2.3.4.1, flap actuators are expected to operate in a narrow range of k (specifically, $0 < k < 0.1$). However, it can be seen that variations in magnitude and phase occur even at these low reduced frequencies, thereby requiring an unsteady model, as opposed to a quasi-steady one.

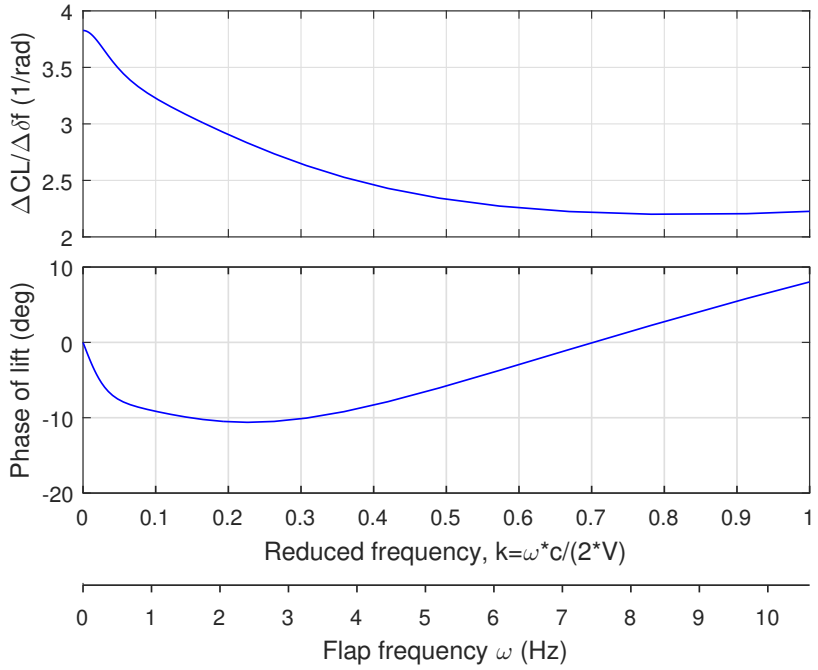

Figure 2.8: Bode plot as a function of the reduced frequency k.

The same information from Figure 2.8 is also provided in Figure 2.9, with magnitudes now in dB and frequencies on a logarithmic scale, as typically represented in Bode plots. This plot provides more details at lower frequencies. As k approaches

zero, the gain is 11.6 dB (or 3.82 rad^{-1}, in absolute units), which is exactly the steady-state value of ΔC_L for a unit step input in flap deflection (see Fig. 2.7). Also, there is no phase difference at very low frequencies, so the model behaves in a quasi-steady fashion, as expected. As the frequency increases (up to 10 Hz or $k = 1$), the magnitude reduces to almost half of the steady-state value. This means that, under unsteady conditions, the airfoil becomes less efficient in generating lift. Regarding the phase, it initially decreases due to the effects of the shed wake vorticity, reaching a minimum of -11 degrees (phase lag) around 2 Hz (or $k = 0.2$). Then, it increases again, returning to zero at 7.5 Hz (or $k = 0.7$) and developing positive values (phase lead) beyond, where the non-circulatory effects start to dominate. Above $k = 1$, special care must be taken. Such high aerodynamic frequencies are most likely not reached in fixed-wing flight, but it might be achieved in flapping-wing or rotary-wing vehicles, for example. The problem is that the flow under such conditions might be dominated by leading-edge vortices, hence violating the attached flow assumption of Theodorsen's theory. For this reason, the plots are limited to 10 Hz (approximately $k = 1$).

2.2.7 Unsteady Kutta-Joukowski theorem

The formulation developed in the previous section can be used to extend the classical Lifting-Line to unsteady conditions. However, additional care must be taken when calculating lift from the circulation under unsteady conditions. Since now the circulation (Γ) at each spanwise station is changing along time, the associated local lift

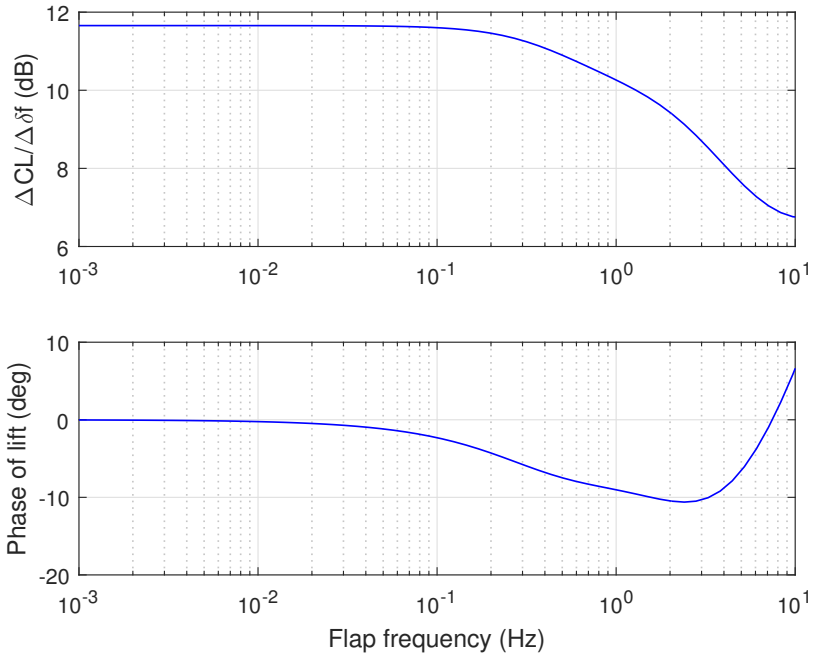

Figure 2.9: Same Bode plot as before, with magnitudes in dB and frequencies on a logarithmic scale.

per unit span (L') is not given by the simpler form of the Kutta-Joukowski theorem:

$$L'(y) = \rho_\infty V_\infty \Gamma(y) \tag{2.63}$$

where the circulation and the local (dimensional) lift per unit span are functions of the spanwise location (y), and (ρ_∞, V_∞) represent freestream density and velocity, respectively. Following the methodology in Katz and Plotkin [98], the unsteady version of the Kutta-Joukowski theorem is given by:

$$L'(t) = \int_0^c \Delta p(x,t)\mathrm{d}x = \rho_\infty V_\infty(t)\Gamma(t) + \rho_\infty \int_0^c \dot{\Gamma}(x,t)\mathrm{d}x \tag{2.64}$$

Assuming $\dot{\Gamma}(x,t)$ constant along the chord, and assuming (ρ_∞, V_∞) time-invariant:

$$L'(t) = \rho_\infty V_\infty \Gamma(t) + \rho_\infty c\dot{\Gamma}(t) \tag{2.65}$$

In non-dimensional form, the associated lift coefficient C_L is given by:

$$C_L = \frac{2\Gamma(t)}{V_\infty c} + \frac{2\dot{\Gamma}(t)}{V_\infty^2} \tag{2.66}$$

In the literature, some authors refer to Eq. (2.65) as the unsteady Kutta-Joukowski theorem [99, 100], while others address the two terms in the RHS separately, as Kutta-Joukowski lift and the apparent-mass lift [101]. A detailed derivation is given in [98, page 496]). The unsteady component $\rho_\infty c\dot{\Gamma}(t)$ in Eq. (2.65) derives from the apparent-mass term in the unsteady Bernoulli equation, and consequently accounts for non-circulatory effects [98, 102]. This fact leads to two observations:

1. This formulation provides a second approach to model non-circulatory lift, but it is computationally simpler than Theodorsen's equations for non-circulatory lift (such as Eq. 2.51) because it does not require second temporal derivative of inputs (e.g. δ_f); and

2. The unsteady Kutta-Joukowski theorem must not be applied if the non-circulatory effects are already being modeled using Theodorsen's equations, which would effectively double the apparent-mass effects.

2.2.8 Augmenting the Lifting-Line Theory

At this point, the unsteady thin airfoil theory and the unsteady Kutta-Joukowski theorem can be used to augment the classical Lifting-Line Theory, yielding a linear time-invariant (LTI) model in state-space format. First, consider the general expression for spanwise circulation, given by a Fourier sine series with unknown constant

coefficients A_n:

$$\Gamma(\theta) = 2bV_\infty \sum_{n=1}^{N} A_n \sin n\theta \tag{2.67}$$

In unsteady conditions, the Fourier coefficients are assumed to vary with time, such that the time derivative of $\Gamma(\theta)$ is given by:

$$\dot{\Gamma}(\theta) = 2bV_\infty \sum_{n=1}^{N} \dot{A}_n \sin n\theta \tag{2.68}$$

Applying this result in the derivation of the classical Lifting-Line yields the unsteady version of the Lifting-Line equation:

$$\alpha(\theta) = \frac{4b}{c_{l,\alpha} c(\theta)} \sum_{n=1}^{N} A_n \sin(n\theta) + \frac{4b}{c_{l,\alpha} V_\infty} \sum_{n=1}^{N} \dot{A}_n \sin(n\theta) + \alpha_{L=0}(\theta) + \sum_{n=1}^{N} n\, A_n \frac{\sin(n\theta)}{\sin(\theta)} \tag{2.69}$$

All parameters are known or prescribed, except A_n and $\dot{A}_n$. Therefore, applying the same equation at N different spanwise stations yields a system of N first-order Ordinary Differential Equations (ODE). Rearranging the terms, yields:

$$\underbrace{(\alpha - \alpha_0)\, c_{l,\alpha}}_{C_{L,2D}} \frac{c}{4b} \sin(\theta) = \sum_{n=1}^{N} A_n \sin(n\theta) \left[\sin(\theta) + \frac{c_{l,\alpha} c}{4b} n\right] + \sum_{n=1}^{N} \dot{A}_n \sin(n\theta) \frac{c}{V_\infty} \sin(\theta) \tag{2.70}$$

This system of ODE can be rearranged into matrix format:

$$C_{L,2D} \circ \frac{c(\theta)}{4b} \circ \sin(\theta) = \sin(\theta\, \underline{n}) \circ \left\{ \begin{bmatrix} \sin(\theta) & \cdots & \sin(\theta) \end{bmatrix} + \frac{c_{l,\alpha}}{4b} c(\theta)\, \underline{n} \right\} \times \begin{bmatrix} A_1 \\ \vdots \\ A_N \end{bmatrix} + \frac{1}{V_\infty} \sin(\theta\, \underline{n}) \circ \begin{bmatrix} c(\theta)\sin(\theta) & \cdots & c(\theta)\sin(\theta) \end{bmatrix} \begin{bmatrix} \dot{A}_1 \\ \vdots \\ \dot{A}_N \end{bmatrix} \tag{2.71}$$

where the symbol " $\circ$ " represents element-wise multiplication (Hadamard product). This equation has the format:

$$B = A\,a + C\,\dot{a}, \quad a = \begin{bmatrix} A_1 \\ \vdots \\ A_N \end{bmatrix}, \quad \dot{a} = \begin{bmatrix} \dot{A}_1 \\ \vdots \\ \dot{A}_N \end{bmatrix} \tag{2.72}$$

where a, A and B are the same as in the classical formulation, given in Eq. (2.44). The C matrix ($N \times N$) accounts for the unsteady circulation. Further manipulation yields:

$$\begin{aligned} \dot{a} &= -C^{-1}A\,a + C^{-1}B \\ &= -C^{-1}A\,a + C^{-1}\left[\frac{c\,(\theta)}{4b} \circ \sin\,(\theta) \circ C_{L,2D}\right] \end{aligned} \tag{2.73}$$

The dynamic inputs to the system are quasi-steady flap deflections δ_{qs} (Eq. 2.49), and vertical gust w_g. These inputs are embedded in the vector $C_{L,2D}$, which represents the lift that each airfoil section along the wing would exhibit, without 3D (finite wing) effects. It should be noted that *each* i-th entry in $C_{L,2D}$ has two components, due to flap deflection (Eq. 2.50) and gust inputs (Eq. 2.57):

$$\begin{aligned} \left(C_{L,2D}\right)_i &= C^c_{L,\delta f} + C^g_L \\ &= C_\delta \begin{bmatrix} z_1 \\ \\ z_2 \end{bmatrix} + D_\delta \delta_{qs}(t) + C_g \begin{bmatrix} z_3 \\ \\ z_4 \end{bmatrix}, \quad i = 1, \ldots, N \end{aligned} \tag{2.74}$$

where:

$$C_\delta = 2\pi \begin{bmatrix} b_1 b_2 \left(2V/c\right)^2 & \left(A_1 b_1 + A_2 b_2\right)\left(2V/c\right) \end{bmatrix} \tag{2.75}$$

$$D_\delta = \pi \tag{2.76}$$

$$C_g = 2\pi \begin{bmatrix} b_3 b_4 \left(2V/c\right)^2 & \left(A_3 b_3 + A_4 b_4\right)\left(2V/c\right) \end{bmatrix} \tag{2.77}$$

The state-space formulations for the auxiliary states ($z_i,\ i = 1, 2, 3, 4$) are also known from Eqs. (2.48) and (2.56):

$$\begin{bmatrix} \dot{z}_1 \\ \dot{z}_2 \end{bmatrix}_i = A_\delta \begin{bmatrix} z_1 \\ z_2 \end{bmatrix}_i + B_\delta \delta_{qs,i}\left(t\right) \ , \quad i = 1, \ldots, N \tag{2.78}$$

$$\begin{bmatrix} \dot{z}_3 \\ \dot{z}_4 \end{bmatrix}_i = A_g \begin{bmatrix} z_3 \\ z_4 \end{bmatrix}_i + B_g \frac{w_{g,i}\left(t\right)}{V} \ , \quad i = 1, \ldots, N \tag{2.79}$$

where:

$$A_\delta = \begin{bmatrix} 0 & 1 \\ -b_1 b_2 \left(2V/c\right)^2 & -\left(b_1 + b_2\right)\left(2V/c\right) \end{bmatrix} \ , \quad B_\delta = \begin{bmatrix} 0 \\ 1 \end{bmatrix} \tag{2.80}$$

$$A_g = \begin{bmatrix} 0 & 1 \\ -b_3 b_4 \left(2V/c\right)^2 & -\left(b_3 + b_4\right)\left(2V/c\right) \end{bmatrix} \ , \quad B_g = \begin{bmatrix} 0 \\ 1 \end{bmatrix} \tag{2.81}$$

Equations (2.73)-(2.79) form a system of N coupled, linear, first order ODE. By suitable manipulations, this system can be put into a state-space representation. However, a set of four auxiliary states is required for *each* spanwise station modeled in the lifting-line. The state-space formulation for all spanwise stations is given in Eq. (2.82), where the underline notation indicates that the associated variables are

now vector quantities.

$$\begin{bmatrix} \dot{a} \\ \dot{\underline{z}}_1 \\ \dot{\underline{z}}_2 \\ \dot{\underline{z}}_3 \\ \dot{\underline{z}}_4 \end{bmatrix} = \begin{bmatrix} -C^{-1}A & GC_\delta^{(1,1)} & GC_\delta^{(1,2)} & GC_g^{(1,1)} & GC_g^{(1,2)} \\ 0 & I_n A_\delta^{(1,1)} & I_n A_\delta^{(1,2)} & 0 & 0 \\ 0 & I_n A_\delta^{(2,1)} & I_n A_\delta^{(2,2)} & 0 & 0 \\ 0 & 0 & 0 & I_n A_g^{(1,1)} & I_n A_g^{(1,2)} \\ 0 & 0 & 0 & I_n A_g^{(2,1)} & I_n A_g^{(2,2)} \end{bmatrix} \begin{bmatrix} a \\ \underline{z}_1 \\ \underline{z}_2 \\ \underline{z}_3 \\ \underline{z}_4 \end{bmatrix} + \begin{bmatrix} GD_\delta & 0 \\ I_n B_\delta^{(1,1)} & 0 \\ I_n B_\delta^{(2,1)} & 0 \\ 0 & I_n B_g^{(1,1)} \\ 0 & I_n B_g^{(2,1)} \end{bmatrix} \begin{bmatrix} \underline{\delta}_{qs}(t) \\ \underline{w}_g(t)/V \end{bmatrix} \tag{2.82}$$

where the zero entries are $N \times N$ null matrices, and the notation I_n represents a $N \times N$ identity matrix. $A_\delta^{(i,j)}$ represents the (i,j) entry of the 2×2 matrix A_δ, and similarly for the other matrices A_g, B_δ, B_g, C_δ, C_g and D_δ used to model the 2D unsteady lift due to flap and gust inputs. The G matrix ($N \times N$) is given by:

$$G = C^{-1}\text{diag}\left(\frac{c(\theta)}{4b} \circ \sin\theta\right) \tag{2.83}$$

The notation diag(v) indicates a square diagonal matrix with the elements of vector v on the main diagonal. This is simply another way to guarantee the element-wise multiplications from Eq. (2.73) in matrix format.

For N stations discretized along the wingspan, there must be N Fourier coefficients in the vector a, and N elements in each auxiliary vector $\underline{z}_i, i = 1,2,3,4$, totalizing $5N$ states. The inputs vectors $\underline{\delta}_{qs}(t)$ and $\underline{w}_g(t)$ have dimensions $N \times 1$, since now

each local station admits individual flap and gust inputs. In practice, the number of moving flaps n will be much smaller than N, with each flap spanning several stations. For example, if $n = 8$, then the 8×1 vector with 8 flap deflections needs to be pre-multiplied by a $N \times 8$ sparse matrix consisting of zeros and ones, in order to generate the $N \times 1$ input vector $\underline{\delta}_{qs}$. Similarly, if a constant gust input is desired across all stations, then a pre-multiplication by a $N \times N$ identity matrix is required to create the $N \times 1$ vector $\underline{w}_g$.

Since the Fourier coefficients a and their temporal derivatives $\dot{a}$ are available for each spanwise station, $\Gamma(\theta)$ and $\dot{\Gamma}(\theta)$ can be obtained from Eqs. 2.67 and 2.68, respectively. The system output can be formulated as the $N \times 1$ vector of local C_L along the span using Eq. 2.66:

$$C_L = \frac{2}{V_\infty c}\Gamma + \frac{2}{V_\infty^2}\dot{\Gamma} = \frac{4b}{c}\underbrace{\sin(\theta n)}_{N\times N} a + \frac{4b}{V_\infty}\underbrace{\sin(\theta n)}_{N\times N}\dot{a} = E\,a + F\,\dot{a} \tag{2.84}$$

In case the airfoil chord is variable along the span, $c = c(\theta)$ and the formulation for matrix E becomes:

$$E = 4b\underbrace{\begin{bmatrix} \frac{1}{c(\theta)} & \cdots & \frac{1}{c(\theta)} \end{bmatrix}}_{N\times N}\underbrace{\sin(\theta n)}_{N\times N} \tag{2.85}$$

Substituting the expressions for a and $\dot{a}$, the vector of spanwise distribution of C_L

is obtained:

$$C_L = \begin{bmatrix} (E - FC^{-1}A) & FGC_{\delta}^{(1,1)} & FGC_{\delta}^{(1,2)} & FGC_{g}^{(1,1)} & FGC_{g}^{(1,2)} \end{bmatrix} \times \begin{bmatrix} a \\ \underline{z}_1 \\ \underline{z}_2 \\ \underline{z}_3 \\ \underline{z}_4 \end{bmatrix} + \begin{bmatrix} FGD_{\delta} & 0 \end{bmatrix} \begin{bmatrix} \underline{\delta}_{qs}(t) \\ \underline{w}_g(t)/V \end{bmatrix} \tag{2.86}$$

Finally, it should be pointed out that the first input is still given in terms of δ_{qs}, which is a combination of δ_f and $\dot{\delta}_f$ (Eq. 2.49). Proceeding similarly to section 2.2.6, it is possible to augment the states with a $N \times 1$ vector of flap deflections $\underline{\delta}_f$ and

leave $\underline{\dot{\delta}}_f$ as the sole input.

$$\begin{bmatrix} \dot{a} \\ \underline{\dot{z}}_1 \\ \underline{\dot{z}}_2 \\ \underline{\dot{z}}_3 \\ \underline{\dot{z}}_4 \\ \underline{\dot{\delta}}_f \end{bmatrix} = \begin{bmatrix} -C^{-1}A & GC_\delta^{(1,1)} & GC_\delta^{(1,2)} & GC_g^{(1,1)} & GC_g^{(1,2)} & GD_\delta F_{10}/\pi \\ 0 & I_n A_\delta^{(1,1)} & I_n A_\delta^{(1,2)} & 0 & 0 & I_n B_\delta^{(1,1)} F_{10}/\pi \\ 0 & I_n A_\delta^{(2,1)} & I_n A_\delta^{(2,2)} & 0 & 0 & I_n B_\delta^{(2,1)} F_{10}/\pi \\ 0 & 0 & 0 & I_n A_g^{(1,1)} & I_n A_g^{(1,2)} & 0 \\ 0 & 0 & 0 & I_n A_g^{(2,1)} & I_n A_g^{(2,2)} & 0 \\ 0 & 0 & 0 & 0 & 0 & 0 \end{bmatrix} \times \begin{bmatrix} a \\ \underline{z}_1 \\ \underline{z}_2 \\ \underline{z}_3 \\ \underline{z}_4 \\ \underline{\delta}_f \end{bmatrix} + \begin{bmatrix} GD_\delta \mathrm{diag}\,(c)\, F_{11}/(4\pi V) & 0 \\ I_n B_\delta^{(1,1)} \mathrm{diag}\,(c)\, F_{11}/(4\pi V) & 0 \\ I_n B_\delta^{(2,1)} \mathrm{diag}\,(c)\, F_{11}/(4\pi V) & 0 \\ 0 & I_n B_g^{(1,1)} \\ 0 & I_n B_g^{(2,1)} \\ I_{n\times n} & 0 \end{bmatrix} \begin{bmatrix} \underline{\dot{\delta}}_f\,(t) \\ \underline{w}_g\,(t)\,/V \end{bmatrix} \tag{2.87}$$

Note that $\mathrm{diag}(c)$ was used instead of c, in order to allow variations of airfoil chord along the wingspan. With these augmented states, the output equation is now given

by:

$$C_L = \left[\begin{array}{ccccccc} (E - FC^{-1}A) & FGC_{\delta}^{(1,1)} & FGC_{\delta}^{(1,2)} & FGC_{g}^{(1,1)} & FGC_{g}^{(1,2)} & FGD_{\delta}F_{10}/\pi \end{array} \right]$$
$$\times \left[\begin{array}{c} a \\ \underline{z}_1 \\ \underline{z}_2 \\ \underline{z}_3 \\ \underline{z}_4 \\ \underline{\delta}_f \end{array} \right] + \left[\begin{array}{cc} FGD_{\delta}\mathrm{diag}\,(c)\,F_{11}/(4\pi V) & 0 \end{array} \right] \left[\begin{array}{c} \dot{\underline{\delta}}_f\,(t) \\ \underline{w}_g\,(t)\,/V \end{array} \right] \tag{2.88}$$

For a discretization with N spanwise stations, this state-space realization requires a total of $6N$ states and provides the unsteady spanwise distribution of local C_L, for arbitrary flap deflection rates and vertical gust inputs.

In this work, the number of stations used to discretize the wing along the span is $N = 200$, which requires 1200 states. It should be noted that the gust and flap inputs are uncoupled. Therefore, if one is interested in flap rate inputs only (no gusts), then the rows and columns associated to gust inputs can be excluded, reducing the system to 800 states. The model could also be augmented to handle rotational and vertical translation of the sections (i.e. pitching and plunging). However, for the sole purpose of modeling the dynamics between flap inputs and lift distribution, under a rigid wing assumption, this model suffices.

2.3 Unsteady Vortex Lattice Method (UVLM)

In this section, the fundamentals of the Vortex Lattice Method (VLM) are presented, as well as its assumptions and constraints. Initially, the classical VLM is presented, which is the basis for the unsteady extension. Then, the nonlinear discrete-time equations for the unsteady VLM are developed. It is shown that, under the assumption of a frozen (or prescribed) wake, the formulation yields a system of discrete-time linear time-invariant (LTI) equations, which is presented in state-space form.

2.3.1 Classical VLM

Similarly to the Lifting-Line approach, VLM is also a potential method and also uses vortices as fundamental solutions of Laplace's equation to fulfill the wall boundary conditions of the problem. The main difference is that now the vortices are not superimposed along the spanwise direction, but placed adjacently, and not only spanwise but also in the chordwise direction. Therefore, a 2D array of vortices is used. In fact, VLM is a specific case of a more general class of so-called Lifting-Surface methods [98]. Since the wing is now discretized along the chord, the model predicts how lift and circulation change in the chordwise direction as well.

The derivation used in this work follows closely the nomenclature from [103]. The method involves the following steps (Fig. 2.10):

1. Divide the planform up into a lattice of quadrilateral panels, and put a horseshoe vortex on each panel;

2. Place the bound vortex of the horseshoe vortex on the 1/4 chord element line of each panel;

3. Place a collocation point on the 3/4 chord point of each panel at the midpoint in the spanwise direction (sometimes the lateral panel centroid location is used);

4. Assume a flat wake in the usual classical method;

5. Determine the strengths of each Γ_n required to satisfy the boundary conditions by solving a system of linear equations;

6. Calculate the forces and moments by using the Kutta-Joukowski theorem.

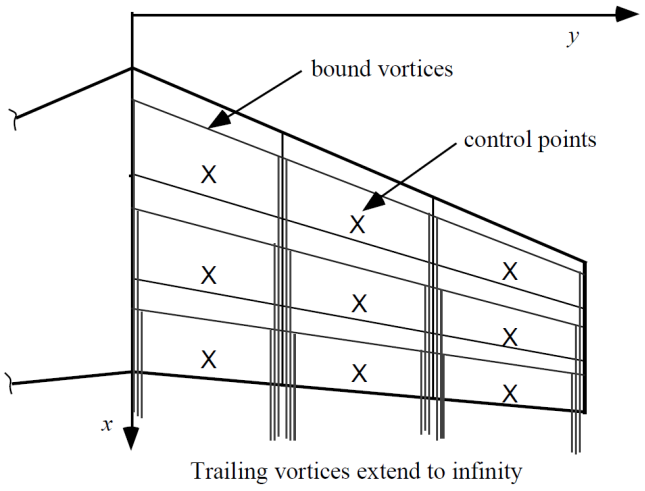

Figure 2.10: The horseshoe vortex layout for the classical vortex lattice method. (Source: [103])

In this formulation, the wake is assumed flat and, ideally, is aligned to the freestream velocity. For low angles of attack, the wake can be assumed to be in the same xy-plane of the lifting surface. Now, it is possible to obtain a mathe-

matical formulation of the problem described above. The general expression for the velocity induced at a point $P = P(x, y, z)$ by a horseshoe vortex placed at points $A = A(x_{1n}, y_{1n}, z_{1n})$ and $B = B(x_{2n}, y_{2n}, z_{2n})$, with trailing vortices parallel to the x-axis, is the sum of the contributions from the three separate straight line vortex segments making up the horseshoe vortex (Fig. 2.11):

$$V = V_{AB} + V_{A\infty} + V_{B\infty} \tag{2.89}$$

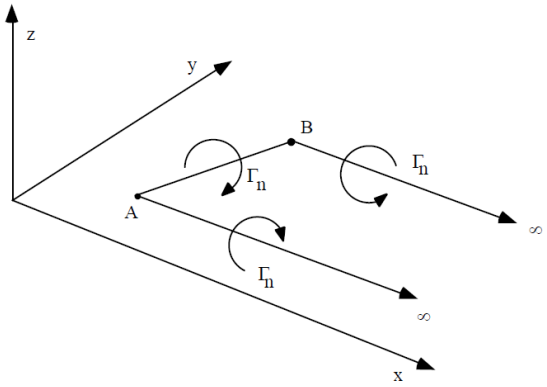

Figure 2.11: Definitions for notation used in induced velocity expressions. (Source: [103])

For each segment of the horseshoe vortex, the induced velocity at an arbitrary point is a function of the geometry between the vortex and the point of interest, multiplied linearly by the vortex intensity Γ_n. Since the grid geometry is constant, this matrix $C_{m,n}$ of aerodynamic influence coefficients (AIC) can be calculated once and then stored. The derivation of the equations for $C_{m,n}$ is given in [92, Chapter 7]. Therefore, the velocity induced at the m-th collocation point by the n-th horseshoe vortex is given by:

$$\underset{3N\times 1}{V_m} = \underset{3N\times N}{C_{m,n}} \ \underset{N\times 1}{\Gamma_n} \tag{2.90}$$

For N total horseshoe vortices, there are also N collocation points, where the wall boundary conditions (i.e. flow-tangency) is enforced by the inner product $V \cdot \hat{n} = 0$, where V is the total velocity vector at the collocation point given by the sum of freestream V_∞ and the vortex-induced velocities, and $\hat{n}$ is the unit vector normal to the wing surface. It should be noted that the velocity vector obtained above has three components. Therefore, the formulation very general, allowing arbitrary geometries, such as swept wing, dihedral, multiple lifting surfaces and even vertical surfaces, with arbitrary kinematics, since the airframe can have quasi-steady motion (rolling, pitching and yawing with sideslip angle, for example).

At this point, a number of simplifications applicable to this work can be employed. For a single horizontal lifting surfaces, without dihedral, i.e. mostly contained in the xy-plane, at low angles of attack and no sideslip, it suffices to enforce the no-cross flow condition ($V \cdot \hat{n} = 0$) in the z-direction only. Therefore, only the third component of the induced velocities is considered (along the z-axis, or the unit vector k). This is done by selecting only the rows number 3, 6, 9, ... , $3N$ of $C_{m,n}$, such that the C_{m,n_k} matrix is $N \times N$. For low angles of attack, a small angles approximation is used and the following system of N algebraic equations is obtained:

$$\sum_{n=1}^{N} C_{m,n_k} (\Gamma_n) = V_\infty \left(\frac{\mathrm{d}f_c}{\mathrm{d}x} - \alpha \right)_m \quad , \quad m = 1, \ldots, N \tag{2.91}$$

where $\mathrm{d}f_c/\mathrm{d}x$ is the local slope of the camber line. For the purposes of this work, this parameter allows to apply flap deflections to the specific grid elements located near the trailing edge. For small flap deflections (less than 10 deg), the linearized relationship above is justified. Even though the wing angle of attack (α) is usually the

same for all panels, the relationship above can be used to apply geometric spanwise twist to the wing.

Given some angle of attack and flap deflection distribution along the span, the associated circulation vector can be obtained by solving the system of linear equations. From circulation, the dimensional lift can be obtained for each panel:

$$\Delta L_n = \rho V_\infty \Gamma_n \Delta b_n \quad , \quad n = 1, \ldots, N \tag{2.92}$$

where Δb_n is the panel bound vortex projection normal to the free stream. Total lift (L) for the wing is simply a summation of all N panels:

$$L = \sum_{n=1}^{N} \Delta L_n \quad , \quad n = 1, \ldots, N \tag{2.93}$$

For n_x chordwise panels and n_y spanwise panels used, $N = n_x \times n_y$. By summing the circulation contributions from each column of panels in the array (i.e. panels aligned chordwise), the $n_y \times 1$ vector of spanwise distribution of circulation Γ is obtained. This chordwise summation can be performed by premultiplying the vector Γ_n by a $n_y \times N$ sparse matrix consisting of zeros and ones, in order to select and sum the appropriate entries of Γ_n. The final Γ is a column vector with the circulation for each of the n_y spanwise stations, from which the spanwise distributions of lift per unit span (L') and local lift coefficient (C_L) can be readily obtained:

$$L' = \rho_\infty V_\infty \Gamma \tag{2.94}$$

$$L' = \frac{1}{2} \rho_\infty V_\infty^2 \, c(y) \, C_L \tag{2.95}$$

In the general case, $c(y)$ is a column vector describing the local airfoil chord at each of the n_y spanwise stations. Therefore, the $n_y \times 1$ vector of local lift coefficient (C_L)

is obtained by element-wise operations, or, equivalently, multiplying two diagonal matrices:

$$C_L = \frac{2L'}{\rho_\infty V_\infty^2 c(y)} = \frac{2}{\rho_\infty V_\infty^2} \mathrm{diag}\,(L') \left[\mathrm{diag}\Big(c(y)\Big)\right]^{-1} \tag{2.96}$$

The principles behind the classical VLM are simple, but extensive numerical manipulations are required to properly keep track of arbitrary geometry configurations and also to extract the required data in the post-processing step. Similar operations can be conducted to obtain distribution of downwash and induced drag, for example.

2.3.2 Helmholtz theorems, Kelvin's theorem and Kutta condition

The numerical procedures discussed so far inherently fulfill some fundamental theorems and conditions in fluid dynamics [91, 98], namely:

Helmholtz theorems:

1) The strength of a vortex filament is constant along its length;

2) A vortex filament cannot start or end in a fluid, hence it must form a closed path or extend to infinity;

3) The fluid that forms a vortex tube continues to form a vortex tube and the strength of the vortex tube remains constant as the tube moves about. Hence vortex elements (such as vortex lines, vortex tubes, vortex surfaces etc.) will remain vortex elements with time.

Kelvin's circulation theorem: it states that the circulation (Γ) is constant

along any closed curve in inviscid flow. Mathematically:

$$\frac{\mathrm{d}\Gamma}{\mathrm{d}t} = 0 \tag{2.97}$$

Kutta condition: it states that the flow must leave the airfoil at the trailing edge. Without enforcing this condition, the solution from potential flow is not unique. Each solution is associated with one specific location of the stagnation point. Kutta condition ties this location to the trailing edge. In other words, the flow must not go around the sharp trailing edge, which would require an infinite velocity. Therefore, the condition can be mathematically stated as: "the flow velocity at the trailing must be finite". From thin airfoil theory, it can be proved that this is equivalent to having no pressure jump at the trailing edge, which means that the circulation per unit length $\gamma(x)$ is zero at the trailing edge (T.E.):

$$\gamma_{TE} = 0 \tag{2.98}$$

Using the lumped-vortex element, the so-called 1/4-3/4 rule is merely a consequence of these conditions [98, page 114]. Hence, using this rule is numerically equivalent to enforcing the two-dimensional Kutta condition. When dealing with three-dimensional configurations (wings), the condition must be enforced along the trailing edge line (as opposed to a single point in the 2D case).

2.3.3 Choice of singularity

Up to this point, Laplace's equation has been solved using one type of singularity, namely the vortex (or vortex filaments, in 3D domains). More specifically, the horse-

shoe vortex has been used in both Lifting-Line and Vortex Lattice approaches (Fig. 2.12).

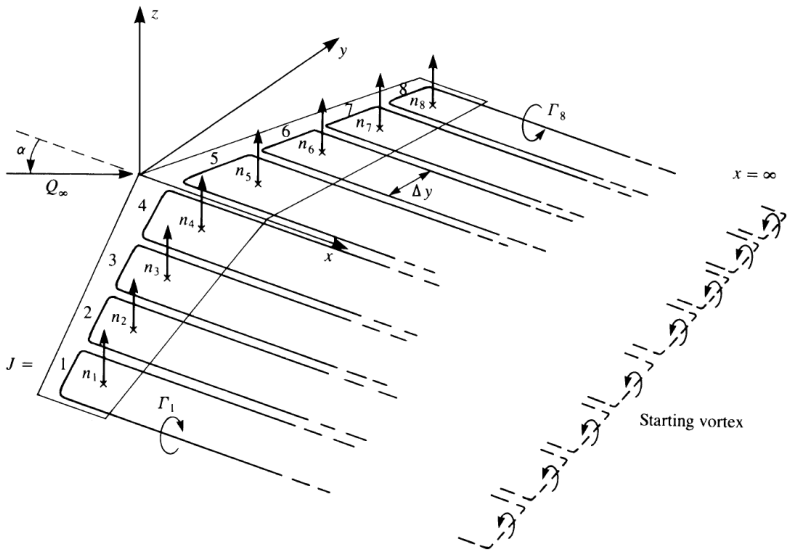

Figure 2.12: Horseshoe vortex lattice model. (Source: [98])

This approach is suitable for steady-state results, since the circulation values in the wake are constant and, therefore, can be modeled by a superposition of vortex filaments extending to infinity. Another vortex geometry commonly used is the vortex ring, which consists of a quadrilateral closed element with constant circulation. Each vortex ring has the same geometry as the wing, but is placed with an offset. The leading filament (i.e. frontal segment of the vortex ring) is placed at the quarter-chord line of the wing element (see Fig. 2.13). The collocation point is still at the center of the 3/4-chord line of each panel. The wake geometry is now also discretized. The wake rings have the same width as the rings on the wing, but they are free vortices, as opposed to the bound vortex rings placed on the wing. Therefore, the assumed planar wake is aligned to the freestream velocity. Once shed, the circulation for the wake

rings does not change with time, in accordance with Helmholtz theorem. Therefore, in steady-state conditions, the wake rings aligned in the streamwise direction (x-axis) must have the same circulation. As a result, it should be noted that the spanwise oriented (i.e. along y-axis) vortex lines of the adjacent vortex rings of the wake will cancel each other out and only a horseshoe-like vortex will remain.

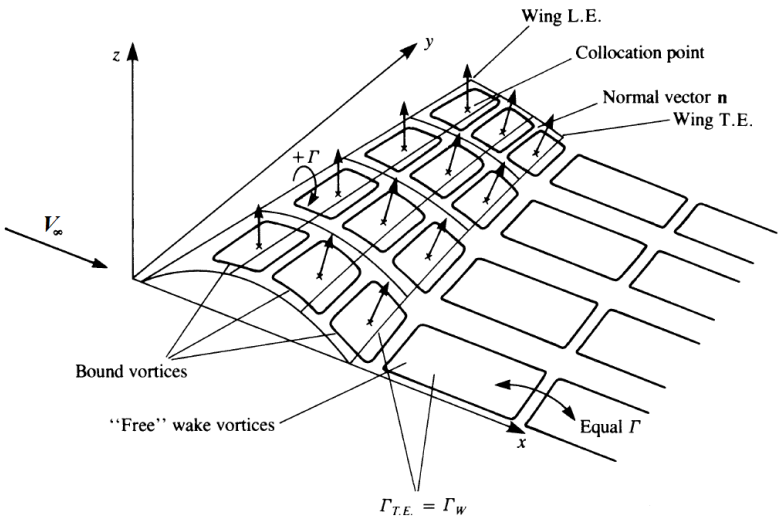

Figure 2.13: Vortex ring model for a thin lifting surface. (Source: [98])

Compared to the horseshoe formulation, the vortex ring model provides some advantages. For example, the bound vortex rings are placed along the camber line of the wing. Moreover, the vortex rings allow to align the wake to the freestream, whereas the horseshoe vortex approach assumes that the wake lies in the xy-plane. For planar wings (no camber) and low angles of attack, both singularities are practically equivalent in the steady-state case.

Another difference with respect to horseshoe vortices is the definition of local circulation. For the horseshoe, the circulation of the wing grid element is simply the

circulation of the associated vortex. For the vortex rings, the local circulation for the leading edge panels is equal to Γ_i, but for all the elements behind it is equal to the difference $\Gamma_i - \Gamma_{i-1}$. Here, i is the index of each panel in the chordwise direction, i.e. along the x-axis (Fig. 2.13).

It can be readily checked that horseshoe vortices and vortex rings fulfill Helmholtz theorems. In steady state conditions, the rate of change of circulation (Kelvin's theorem) is identically zero. The 2D Kutta condition is implied by the application of the 1/4 - 3/4 rule in both cases. For the 3D Kutta condition, the circulation must be zero at the trailing edge. Therefore, in steady-state conditions, all wake panels shed from a particular trailing-edge panel will have the same vortex strength, which is equal to the strength of the shedding panel. Hence:

$$\Gamma_w = \Gamma_{TE} \tag{2.99}$$

Although always present in actual flows, dissipation effects are not predicted by potential flow and can usually be neglected in high Reynolds flows, since the wake vortices quickly move away from the wing [104].

2.3.4 Augmenting the classical VLM with unsteadiness

In the previous section, a considerable effort was dedicated to elucidate the differences and similarities between horseshoe vortices and vortex rings. It was clear that both approaches are equivalent in quasi-steady conditions. However, the true advantage of vortex rings becomes evident when it is required to model unsteady aerodynamics. In this section, the classical VLM formulation is augmented with unsteady boundary

conditions, yielding the Unsteady Vortex Lattice Method (UVLM).

In the unsteady lifting-line, the unsteadiness was built into the airfoil behavior by indicial functions. The variation of airfoil lift was not a simple linear function of AOA anymore. It has internal dynamics represented by auxiliary states, in order to represent dynamic flap and gust inputs. For the UVLM, analytical results from 2D thin airfoil theory are not used at all. The unsteadiness is introduced by time-varying boundary conditions. In the present work, the main interest lies in modeling flap deflections, which effectively change the camber line on which the flow tangency conditions are enforced, but the approach could also handle arbitrary motions applied for each section, such as pitching, plunging and twisting.

Starting from a steady-state condition, a change in flap deflection causes an instantaneous variation in circulation along the wing panels. This variation is then transmitted to the wake panels, which in turn affect the wing elements. The information travels along the wake at freestream velocity V_∞. This dynamic behavior continues until a new steady-state condition is achieved. It should be clear now that the vortex rings approach is particularly amenable to the modeling of such propagations, as opposed to horseshoe vortices, whose trailing vortex legs extending to infinity have constant vortex strength. Therefore, a superposition of horseshoe vortices does not allow to model the dynamic changes in circulation that happen along the wake.

The algorithm for the UVLM is very similar to the classical VLM, but a few key differences are essential. The solution is based on time-stepping technique, and at the beginning of the motion only the wing-bound vortex rings exist (Fig. 2.14).

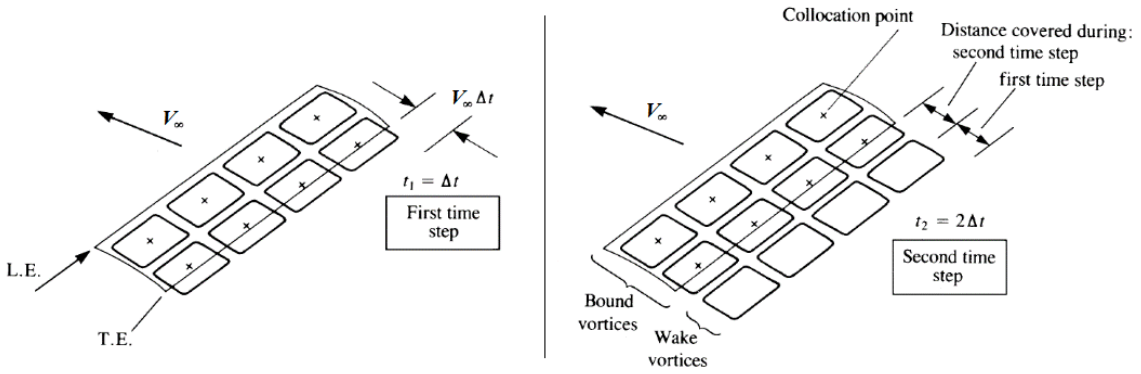

Figure 2.14: Initialization of UVLM algorithm. (Source: [98])

2.3.4.1 Initialization

The wing is assumed steady with no flow, so that no wake elements exist yet. Once accelerated to the desired airflow speed, the matrix of Aerodynamic Influence Coefficients can be computed. The Right-Hand Side (RHS) of Eq. 2.100, which consists of the non-penetration boundary conditions, is also computed. After solving for the circulation on the wing panels Γ_n, the instantaneous loads can be computed, just like in the classical VLM method.

$$\sum_{n=1}^{N} C_{m,n_k}(\Gamma_n) = V_\infty \left(\frac{\mathrm{d}fc}{\mathrm{d}x} - \alpha \right)_m \quad , \quad m = 1, \ldots, N \tag{2.100}$$

The largest difference is the wake shedding and convection. At the end of first iteration, the velocity flow field induced by the wing vortex rings at the corner points near the trailing edge is obtained (V_w). Using the Biot-Savart law, the velocity vector induced by the wing body on the wake (V_{bw}) and that induced by the wake on the wake itself (V_{ww}) can be computed:

$$V_w = V_{bw} + V_{ww} \tag{2.101}$$

For this first iteration $i = 1$, the wake does not exist yet, hence $V_{ww} = 0$. The first row of wake panels is shed by updating the position of these corner points using a simple time integration, as if they were free to float:

$$x_w^{i+1} = x_w^i + V_w^i dt \tag{2.102}$$

The superscript $(i+1)$ denotes next iteration, whereas i indicates current iteration. The geometry for each new wake ring is completely defined by the two corner points (x_w^n) in the trailing edge of the wing, plus their updated 3D positions (x_w^{n+1}). Each new wake vortex ring inherits the circulation from the wing panel immediately ahead, from which it was shed:

$$\Gamma_w^{i+1} = \Gamma_{TE}^i \tag{2.103}$$

This equation represents the unsteady equivalent of the Kutta condition. The circulations of the newly formed wake rings that will be used in the next iteration $(i+1)$ are equal to the circulations of the wing trailing edge in the previous iteration (i). If no variation occurs between iterations, a steady-state condition is reached and the conventional Kutta condition is recovered: $\Gamma_w = \Gamma_{TE}$, as presented in Eq. (2.99).

Although the Kutta condition is being extended to unsteady flows in this formulation, it is actually a concept based on steady flow conditions. For this reason, its applicability to unsteady flows is questionable for high values of reduced frequency k. In other words, under unsteady conditions, the flow might not leave the airfoil at the trailing edge point anymore. In the literature, the validity of the Kutta condition is usually accepted up to $k = 0.6$. Therefore, it can be safely used in this work, given that the expected reduced frequencies are below $k = 0.1$, as discussed in section . Ad-

ditional discussion on this topic is provided in [98, Section 13.11] and the references therein.

For the next iterations, the position of these wake rings will vary as they are convected away from the wing. However, even though they are free to float with the local velocity field, the vortex strength initially assigned (Γ_w^{i+1}) will not change, as dictated by Helmholtz theorem. Also, it should be pointed out that the vortex ring model inherently fulfills Kelvin's theorem [98, page 419]. In fact, the circulation of the wake rings are obtained without requiring application of $\mathrm{d}\Gamma/\mathrm{d}t = 0$.

2.3.4.2 Second iteration

Now, the recently generated vortex rings on the wake will require a re-evaluation of the boundary conditions at the collocation points. Now, the influence coefficients ($C_{m,nw}$) from the n_y wake rings can also be computed, since the geometry is completely known:

$$\sum_{n=1}^{N} C_{m,n_k}\left(\Gamma_n\right) + \sum_{n_w=1}^{N_w} C_{m,nw_k}\left(\Gamma_{w_{nw}}\right) = V_\infty \left(\frac{\mathrm{d}f_c}{\mathrm{d}x} - \alpha\right)_m, \quad m = 1, \ldots, N \tag{2.104}$$

where:

n is the index for the N vortex rings on the wing;

m is the index for the N collocation points (on the wing);

n_w is the index for the N_w vortex rings on the wake. For the second iteration ($i = 2$), there exist only one row of wake rings, generated at the end of the first iteration, so $N_w = n_y$. For the future iterations, the wake will grow, so that the number of wake rings at the i-th iteration is $N_w = n_y\,(i-1)$;

Γ_w is the circulation on the wake elements, known from the previous iteration;

C_{m,n_k} is the influence coefficient of the n-th wing ring on the m-th collocation point. The subscript k indicates that only the z-component is being considered in this analysis, as in the classical VLM;

C_{m,nw_k} is the influence coefficient of the n_w-th wake ring on the m-th collocation point;

$\mathrm{d}f_c/\mathrm{d}x$ is the spatial derivative of the camber line, which includes flap deflections, at the m-th collocation point;

α is the geometric angle of attack at the m-th collocation point.

The right-hand side of the system of equations (Eq. 2.104) is prescribed, so that the only unknown variables are the circulation for vortex ring elements on the wing (Γ_n). The new circulations induce a new velocity flowfield on the wake vortex ring corner points:

$$V_w = V_{bw} + V_{ww} \tag{2.105}$$

As before, V_{bw} is the velocity induced by all vortex rings from the wing, and V_{ww} is the velocity induced by all vortex rings from the wake. For the second iteration, a single row of wake elements exist. In Fig. 2.15, the vortex ring corner points represented by blue circles are free to float and their position is updated in every iteration. The points represented by red triangles are fixed, and coincide with the aft corner points of the last row of wing rings (i.e. at the trailing edge), from which the new wake elements are shed. The velocity vector induced at these points allows to update the spatial location of each corner of each wake element, by integrating the

velocity:

$$x_w^{i+1} = x_w^i + V_w^i \mathrm{d}t \tag{2.106}$$

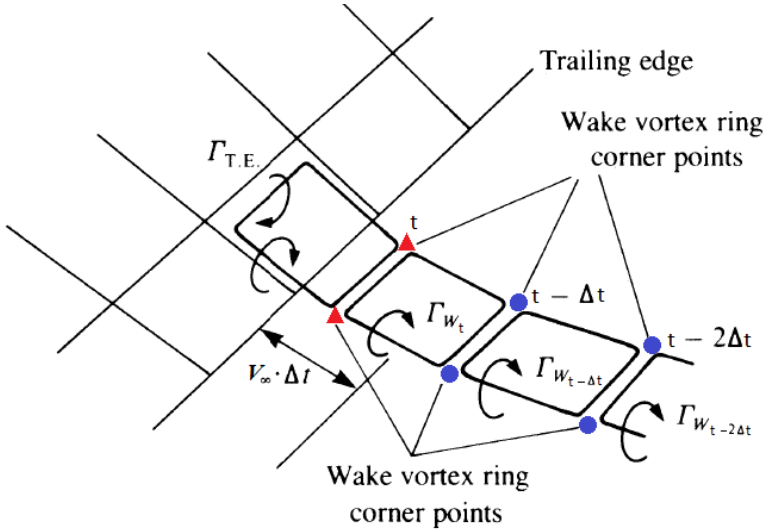

Figure 2.15: Wake shedding procedure at the trailing edge panels. (Source: [98])

This causes two effects:

1. The first row of wake elements is convected away from the wing, becoming the second row of elements for the next iteration. The value of circulation is kept constant (Helmholtz theorem);

2. A new row of wake elements is generated, similarly to the first iteration.

The value of circulation assigned to each new wake vortex ring is equal to the current circulation of the associated wing trailing edge element. At the end of the second iteration, there exist two rows of wake elements.

2.3.4.3 Next iterations: considerations about the wake

The procedure described above can be easily repeated and a new row of vortex rings will be added to the wake at each iteration. A schematic flowchart of the method is provide in Fig. 2.16.

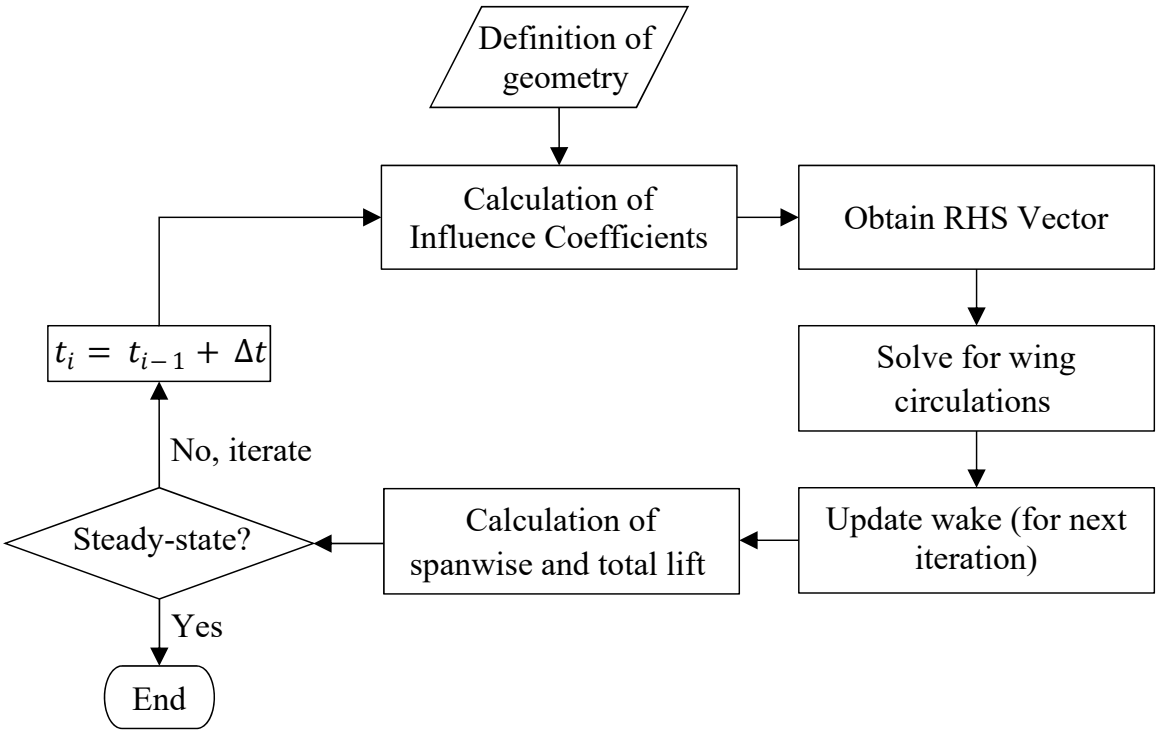

Figure 2.16: Schematic flowchart for the unsteady VLM.

For practical purposes, however, the wake cannot have an infinite number of vortex ring rows, so it must stop growing after reaching a reasonable length. Beyond this length, the wake rings have very little effect on the wing, such that the finite wake can be considered a good representation of the theoretically infinite wake. This length is a function of the wing aspect ratio and also error tolerance, so it must be defined on a case-by-case basis. It is suggested in [98] that four wingspans is usually a good initial estimate. In the present work, it was observed that the total wing C_L achieved steady-

state (accurate to 1%) with 16 rows of vortex rings in the wake, which corresponds to about two wingspans. The details about the discretization used in this work are given in section 2.3.5.

Even if the required length is obtained and the wake stops growing at each iteration, its geometry is still a function of the local velocity flow field, because the 3D position of its corner points are still updated at every iteration. Therefore, even after reaching the steady-state condition, the formulation of the influence coefficients from the wake (C_{m,nw_k}) is nonlinear and change at each iteration for dynamic inputs (such as flap deflections). In order to linearize the formulation, a *frozen wake* is assumed. This means that after reaching the trimmed, steady-state condition, the geometry of the wake is kept constant, while the values of circulation are normally convected from row to row at every iteration. This approach makes the coefficients C_{m,nw_k} constant and allows a linear, time-invariant state-space representation of the problem, as will be detailed in section 2.3.5.

For the Lifting-Line approaches (steady and unsteady) and also the steady VLM using horseshoe vortices, the wake was assumed flat. Another interesting feature of using vortex rings to discretize the wake is that the wake does not need to be assumed flat anymore. The wake shedding procedure allows the free wake rings to roll-up (Fig. 2.17), which remarkably yields a behavior closer to what is observed in real fluids.

2.3.4.4 Considerations about boundary conditions and constraints

The right-hand side (RHS) of Eq. 2.104 contains projections of different kinds of velocities at the N collocation points, except those induced by the vortex rings from

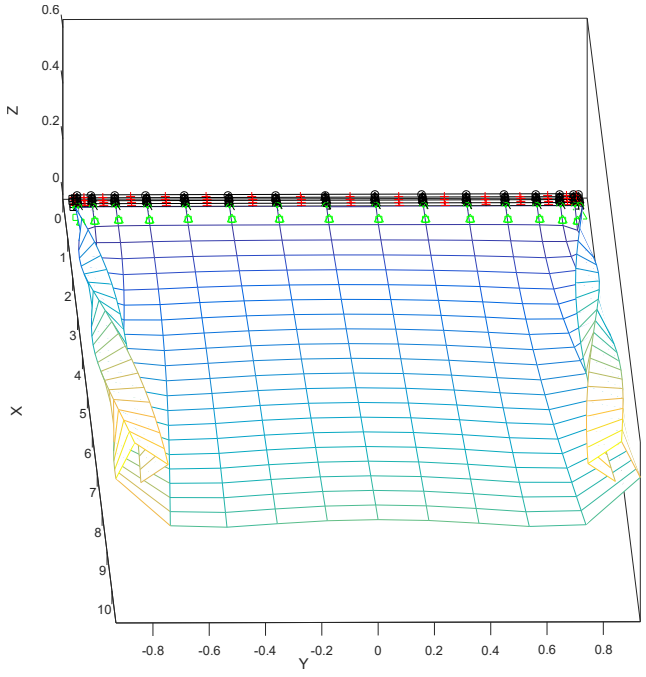

Figure 2.17: Wake roll-up in UVLM.

wing and wake. Therefore, such velocity components not related to vortex circulations will be referred to as non-circulatory velocities. Typically, these velocities include prescribed values, such as the freestream velocity, dynamic control surface deflection, but also exogenous velocities due to gusts, for example, all projected along the normal direction ($\hat{n}$) of each wing panel:

$$RHS = -\left(V_{\infty} + V_{deflection} + V_{gust}\right) \cdot \hat{n} \tag{2.107}$$

When these non-circulatory normal components are added to the velocities induced by all the vortex rings (along the normal direction as well), one should obtain zero at every collocation point in each panel. This is a representation of the non-penetration condition, or the wall boundary condition. Any flow velocity components remaining at the collocation points must then be tangent to the surface, hence the

boundary conditions is also called flow-tangency condition.

In this work, since the main interest is in the identification of aerodynamic modes, the wing can be assumed fixed in a wind tunnel for example, while dynamic flap inputs are applied. Hence, the wing is considered an inertial frame, which simplifies the formulation. For complete configurations in free-flight, the rotation rates of the wing body itself (when pitching, rolling and yawing) also induce local components for each wing panel, and the measurements taken with respect to the wing need to be converted to the inertial frame. Structurally, the wing is treated as a rigid body (no structural deformations). For a flexible airframe, the rate of change of structural deformation for the wing sections should also be included, caused mainly by bending and torsion. A detailed derivation for the more general case (flexible wing in free-flight) is presented in [98, 104].

Small angles of attack and flap deflection are also assumed, since the flow is potential (i.e. attached everywhere). The wing sections are assumed flat (i.e. zero camber) and the only variation in the panel's orientation is due to flap deflection. Moreover, for realistically achievable flap rates (i.e. no more than 100 deg/s), it can be checked that the velocities induced by dynamic flap deflection are negligible if compared to other components. For example, consider a panel at an incidence angle of 10 degrees, which can be a combination of angle of attack α and flap deflection δ_f (Fig. 2.18).

For the operating conditions from Table 2.1, the freestream velocity ($V_\infty = 10$

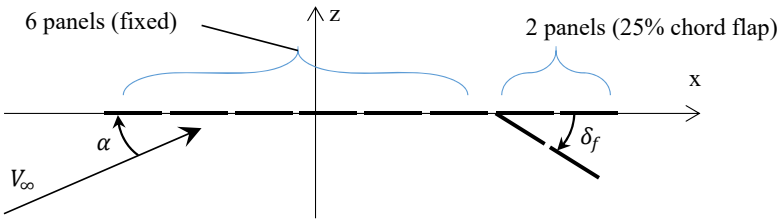

Figure 2.18: Schematic view of chordwise discretization.

m/s) projected along the normal vector of the panel can be approximated by:

$$V_1 = V_\infty \sin(\alpha + \delta_f) \cong V_\infty (\alpha + \delta_f) = (10 \text{ m/s})(10\,\pi/180) = 1.74 \text{ m/s} \tag{2.108}$$

The wing geometry is discretized with 8 chordwise panels. Since the flapped portion of the chord ($c = 0.30$ m) is 25%, the last two chordwise panels comprise the flaps. Considering the maximum flap actuation rate as $\omega = 100$ deg/s, the maximum linear velocity induced by flap motion occurs at the trailing edge and is given in absolute value by:

$$V_2 = \omega\,(c/4) = (100\,\pi/180 \text{ rad/s})(0.30 \text{ m}/4) = 0.13 \text{ m/s} \tag{2.109}$$

Therefore, the component due to the freestream velocity is much more important and the component due to flap motion can be considered negligible. The gust component is an upwash velocity w_g, perpendicular to the flight path, so the non-circulatory components are given by:

$$RHS = -V_\infty \hat{n} - V_{gust}\hat{n} = -V_\infty \sin\left(\alpha - \frac{\mathrm{d}f_c}{\mathrm{d}x}\right) - w_g \cos\left(\alpha - \frac{\mathrm{d}f_c}{\mathrm{d}x}\right) \tag{2.110}$$

Using small angles approximation:

$$RHS = V_\infty \left(\frac{\mathrm{d}f_c}{\mathrm{d}x} - \alpha\right)_m - w_g \quad , \quad m = 1, \ldots, N \tag{2.111}$$

where $\mathrm{d}f_c/\mathrm{d}x$ is the spatial derivative of the camber line. For the flat-plate airfoil assumption (Fig. 2.18), it is simply given by:

$$\frac{\mathrm{d}f_c}{\mathrm{d}x} = \begin{cases} 0 & \text{for panels 1 to 6} \\ -\delta_f & \text{for panels 7,8} \end{cases} \tag{2.112}$$

The formulation above allows to apply individual camber variations to each of the N grid elements of the wing. In practice, the number of trailing edge flaps n is much smaller than N, and several spatially adjacent grid elements will be associated to the same flap. Therefore, the input from a $n \times 1$ vector of flap deflections $\underline{\delta}_f$ has to be mapped into each of the N grid elements of the wing. This mapping is accomplished by premultiplying $\underline{\delta}_f$ by a large sparse matrix $N \times n$ consisting of zeros and ones.

2.3.4.5 Final considerations: time step, reference frames and flexible wing geometry

An overview of the Unsteady Vortex Lattice Method was provided in this section, with relatively simple boundary conditions. Because the circulation values of the wake in the previous iteration are used to compute wing circulations in the current iteration, the formulation is discrete-time. As such, the results depend strongly on the time-step (Δt) adopted. While the discretization of the wake in the spanwise direction is the same as the wing, the wake discretization on the streamwise direction depends on Δt. The streamwise length of each wake ring is approximately defined by the distance covered at each iteration: $\Delta x = V_\infty \Delta t$. Ideally, small Δt yields a more accurate representation of unsteady effects in time, but many rows of wake vortex

rings will be required to cover the desired wake length. In other words, the wake will grow very slowly. The larger the number of elements in the wake, the larger the matrix of influence coefficients. Therefore, there is a tradeoff on Δt. In this work, a value of 20 milliseconds was deemed fair to capture the required fast unsteady dynamics, while still yielding reasonably sized matrices.

Another assumption adopted throughout this work is that the wing is assumed rigid. For the UVLM, this means that the geometry of the wing rings and the 3D position of the collocation points do not change at each iteration. Consequently, the influence coefficients of the wing C_{m,n_k}, which map the velocities induced by wing rings on the collocation points, are constant. Therefore, a linear relationship can be obtained using the wing original geometry in a straightforward fashion.

If necessary, however, UVLM can easily incorporate the effect of large dynamic structural deflections by simply allowing the coefficients C_{m,n_k} to change between iterations. Of course, the resulting formulation is highly nonlinear and, for practical purposes, a linearization around the trimmed (deformed) condition can be obtained. This is equivalent to assume that the geometry variations around the deformed condition are small, which is usually the case for flight dynamics and control analysis of flexible airframes. One can think of this as a *frozen wing* assumption, similarly to the frozen wake assumption that allowed the wake influence coefficients C_{m,nw_k} to remain constant. As can be seen, UVLM provides a powerful framework to simulate complex scenarios with the benefits (and constraints) of a low-order, potential flow method.

2.3.5 Linearization of the UVLM

The general UVLM formulation is nonlinear, because of its dependence on the geometry of the wake after each time step. However, after shedding a wake, trimming it at an acceptable length and reaching steady-state conditions, the frozen wake assumption allows to linearize the UVLM formulation.

The equation for the nonlinear formulation for UVLM (Eq. 2.104) with the added input of vertical gusts w_g is given by:

$$\sum_{n=1}^{N} C_{m,n_k}\left(\Gamma_n\right) + \sum_{n_w=1}^{N_w} C_{m,nw_k}\left(\Gamma_{w_{nw}}\right) = V_\infty \left(\frac{\mathrm{d}f_c}{\mathrm{d}x} - \alpha\right)_m - w_g \tag{2.113}$$

The size of this system of equations depends on the discretization used. The following parameters define the geometry of the problem and the dimensions of related matrices:

$n_x = 8$ is the number of panels used to discretize the wing in the chordwise direction;

$n_{xw} = 16$ is the number of panels used to discretize the wake in the streamwise direction;

$n_y = 64$ is the number of panels used to discretize the wing in the spanwise direction;

Therefore, there are $N = n_x \times n_y = 8 \times 64 = 512$ wing panels, associated to N wing vortex rings and N collocation points. The spanwise discretization for the wake is equal to that used for the wing, thus there are $N_w = n_{xw} \times n_y = 16 \times 64 = 1024$ wake rings. Assuming frozen geometry, the influence coefficients can be arranged in constant matrices. The system of equations in (2.113) can be converted to matrix

format:

$$C_{mn}.\Gamma_b^{(i+1)} + C_{mn,w}.\Gamma_w^{(i+1)} = W_b^{(i+1)} \tag{2.114}$$

where:

The superscript "$(i+1)$" denotes current iteration;

C_{mn} is the 512×512 matrix of influence coefficients from the wing vortex rings to the collocation points;

$C_{mn,w}$ is the 512×1024 matrix of influence coefficients from the wake vortex rings to the collocation points;

$\Gamma_b^{(i+1)}$ is the 512×1 column vector of circulations for the wing rings, which from now on has a subscript "b" for wing body;

$\Gamma_w^{(i+1)}$ is the 1024×1 column vector of circulations for the wake rings;

W_b is the 512×1 column vector of vertical velocity components that must be induced by all vortices at the collocation points. The inputs to the system (flaps and gust) are embedded in this term:

$$W_b^{(i+1)} = V_\infty \left[\left(\frac{\mathrm{d}f_c}{\mathrm{d}x} \right)^{(i+1)} - \alpha^{(i+1)} \right] - w_g^{(i+1)} \tag{2.115}$$

The current wake circulation vector $\Gamma_w^{(i+1)}$ is known from the previous iteration and can be represented by:

$$\Gamma_w^{(i+1)} = C_b \Gamma_b^{(i)} + C_w \Gamma_w^{(i)} \tag{2.116}$$

where:

The superscript "(i)" denotes previous iteration;

$\Gamma_b^{(i)}$ and $\Gamma_w^{(i)}$ are the circulation vectors from the previous iteration;

C_b and C_w are very sparse constant convection matrices that extract the appropriate circulations from the previous iteration. Specifically:

C_b is a 2014×512 matrix of zeros and ones that takes the circulation from the last row of wing rings (i.e. in the trailing edge) to form the circulations on the first row of wake rings for the next iteration (wake shedding);

C_w is a 1024×1024 matrix that offsets the circulation in the first $(n_{xw} - 1)$ rows of wake rings (wake convection). The circulation from rows 1 to 15 (from i-th iteration) will become the circulation at rows 2 to 16 for $(i + 1)$-th iteration. The circulation values at the last row of wake rings is discarded.

A graphical representation of these sparse matrices is given in 2.19. In each case, the non-zero entries (i.e. ones) are represented by the blue line. The shedding matrix C_b has 64 non-zero (nz) entries, whereas the convection matrix C_w has 960 non-zero entries.

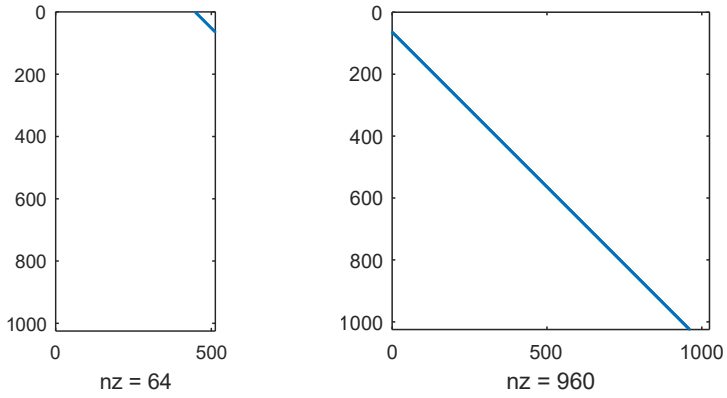

Figure 2.19: Graphical representation of sparse matrices C_b and C_w.

In order to obtain the instantaneous spanwise lift as the output of the model, it is necessary to use the unsteady version of the Kutta-Joukowski theorem (Eq. 2.66).

The equation for the circulation on the wing is known from Eq. (2.114), but the time derivative of the circulation is also required. By using a backward difference approximation, a third difference equation is obtained:

$$\dot{\Gamma}_b^{(i+1)} = \left(\Gamma_b^{(i+1)} - \Gamma_b^{(i)}\right)/\Delta t \tag{2.117}$$

The time step is denoted by Δt. From Eqs. (2.114), (2.116) and (2.117), a discrete-time LTI state-space formulation can be obtained:

$$x\left(k+1\right) = Ax\left(k\right) + Bu\left(k\right) \tag{2.118}$$

$$y\left(k\right) = Cx\left(k\right) + Du\left(k\right) \tag{2.119}$$

It should be noted that the system input $W_b^{(i+1)}$ is evaluated at the current time step $(i+1)$ instead of the usual previous time step (i). This requires a little more effort to put the system of difference equations into the state-space form given above. Substitute Eq. (2.116) into Eq. (2.114) and isolate current time step $(i+1)$ parameters to form the state x_1:

$$C_{mn}.\Gamma_b^{(i+1)} + C_{mn,w}.\left(C_b\Gamma_b^{(i)} + C_w\Gamma_w^{(i)}\right) = W_b^{(i+1)} \tag{2.120}$$

$$\underbrace{C_{mn}.\Gamma_b^{(i+1)} - W_b^{(i+1)}}_{x_1^{(i+1)}} = -C_{mn,w}.\left(C_b\Gamma_b^{(i)} + C_w\Gamma_w^{(i)}\right) \tag{2.121}$$

The state x_2 is obtained directly from Eq. (2.116):

$$\underbrace{\Gamma_w^{(i+1)}}_{x_2^{(i+1)}} = C_b\Gamma_b^{(i)} + C_w\Gamma_w^{(i)} \tag{2.122}$$

From the Eq. (2.117), isolate current timestep $(i+1)$ parameters to form the state x_3:

$$\underbrace{\Delta t.\dot{\Gamma}_b^{(i+1)} - \Gamma_b^{(i+1)}}_{x_3^{(i+1)}} = -\Gamma_b^{(i)} \tag{2.123}$$

In terms of the new states, the Eqs. (2.114), (2.116) and (2.117) become:

$$\begin{cases} x_1^{(i+1)} = -C_{mn,w}.\left(C_b\Gamma_b^{(i)} + C_w\Gamma_w^{(i)}\right) \\ x_2^{(i+1)} = C_b\Gamma_b^{(i)} + C_w\Gamma_w^{(i)} \\ x_3^{(i+1)} = -\Gamma_b^{(i)} \end{cases} \tag{2.124}$$

The expressions that define the states are:

$$\begin{cases} x_1^{(i+1)} = C_{mn}.\Gamma_b^{(i+1)} - W_b^{(i+1)} \\ x_2^{(i+1)} = \Gamma_w^{(i+1)} \\ x_3^{(i+1)} = \Delta t.\dot{\Gamma}_b^{(i+1)} - \Gamma_b^{(i+1)} \end{cases} \tag{2.125}$$

Eqs. (2.125) can be evaluated at the previous time step (i), yielding:

$$\begin{cases} x_1^{(i)} = C_{mn}.\Gamma_b^{(i)} - W_b^{(i)} \\ x_2^{(i)} = \Gamma_w^{(i)} \\ x_3^{(i)} = \Delta t.\dot{\Gamma}_b^{(i)} - \Gamma_b^{(i)} \end{cases} \tag{2.126}$$

From Eqs. (2.126), one can obtain $\Gamma_b^{(i)}$, $\Gamma_w^{(i)}$ and $\dot{\Gamma}_b^{(i)}$ as functions of states and input at previous time step (i):

$$\begin{cases} \Gamma_b^{(i)} = C_{mn}^{-1}.\left(x_1^{(i)} + W_b^{(i)}\right) \\ \Gamma_w^{(i)} = x_2^{(i)} \\ \dot{\Gamma}_b^{(i)} = \frac{\left(x_3^{(i)} + \Gamma_b^{(i)}\right)}{\Delta t} = \frac{x_3^{(i)}}{\Delta t} + \frac{C_{mn}^{-1}}{\Delta t}\left(x_1^{(i)} + W_b^{(i)}\right) \end{cases} \tag{2.127}$$

Substituting these results back into Eq. (2.124), the discrete-time state-space

equations for the states can be obtained:

$$\begin{cases} x_1^{(i+1)} = -C_{mn,w}C_bC_{mn}^{-1}x_1^{(i)} - C_{mn,w}C_wx_2^{(i)} - C_{mn,w}C_bC_{mn}^{-1}W_b^{(i)} \\ x_2^{(i+1)} = C_bC_{mn}^{-1}x_1^{(i)} + C_wx_2^{(i)} + C_bC_{mn}^{-1}W_b^{(i)} \\ x_3^{(i+1)} = -C_{mn}^{-1}x_1^{(i)} - C_{mn}^{-1}W_b^{(i)} \end{cases} \tag{2.128}$$

In order to obtain lift, the desired outputs are $\Gamma_b^{(i)}$, $\Gamma_w^{(i)}$ and $\dot{\Gamma}_b^{(i)}$. Therefore, the output equation of the system is given by Eq. (2.127). In matrix form, the discrete-time state-space formulation for the linearized version of UVLM is given by:

$$x^{(i+1)} = \begin{bmatrix} -C_{mn,w}C_bC_{mn}^{-1} & -C_{mn,w}C_w & [0] \\ C_bC_{mn}^{-1} & C_w & [0] \\ -C_{mn}^{-1} & [0] & [0] \end{bmatrix} x^{(i)} + \begin{bmatrix} -C_{mn,w}C_bC_{mn}^{-1} \\ C_bC_{mn}^{-1} \\ -C_{mn}^{-1} \end{bmatrix} W_b^{(i)} \tag{2.129}$$

$$y^{(i)} = \begin{bmatrix} C_{mn}^{-1} & [0] & [0] \\ [0] & [I] & [0] \\ C_{mn}^{-1}/\Delta t & [0] & [I]/\Delta t \end{bmatrix} x^{(i)} + \begin{bmatrix} C_{mn}^{-1} \\ [0] \\ C_{mn}^{-1}/\Delta t \end{bmatrix} W_b^{(i)} \tag{2.130}$$

where $[0]$ and $[I]$ are null and identity matrices of appropriate dimensions. For the UVLM, the discretization used was $n_x = 8$ (chordwise panels) and $n_y = 64$ (spanwise panels), so that the wing has $n_x \times n_y = 512$ vortex rings. For a time step of $\Delta t = 0.02$ s, it was observed that the wake required $n_{xw} = 16$ panels in the streamwise direction to achieve a steady-state error in total C_L of less than 1%, yielding $n_{xw} \times n_y = 1024$ vortex rings in the wake. The state vector in the UVLM contains bound circulations in the wing (Γ_b), their time derivatives ($\dot{\Gamma}_b$) and free circulations in the wake (Γ_w). Since each vortex ring is associated to one circulation value, the total number of states is: $(n_x \times n_y) + (n_x \times n_y) + (n_{xw} \times n_y) = 2048$. Once Γ_b, Γ_w and $\dot{\Gamma}_b$ are obtained, the

unsteady lift coefficient can be calculated along the wingspan [98, 105].

2.4 Verification of Aerodynamic Models

As any numerical algorithm, the routines developed in this work require verification against independent data. Because both methods (ULLT and UVLM) allow to predict unsteady, 3D behavior of flow, with application of flap inputs, a considerable number of verifications is required. Even though the methods have 3D capability, the 2D condition is an important preliminary test. By simply increasing the aspect ratio of the wing to very large values (AR=100 or 1000), while simultaneously reducing the spanwise discretization, the 2D behavior of a flat-plate airfoil can be numerically obtained. Therefore, the 2D tests serve to verify the behavior at the airfoil level, before applying to 3D flows around finite wings.

2.4.1 ULLT verification tests

For the ULLT, the test matrix is simplified, because the 2D behavior (both steady and unsteady) is automatically ensured by Wagner's function. In Fig. 2.20, the lift response due to a step input in flap deflection is presented. The 2D behavior of the ULLT is simulated by using a single flap along the span, and increasing the aspect ratio to AR=100. The thin airfoil response is obtained by simulating the state-space system presented in section 2.2.6 for a flap along 25% of the chord, and reflects the Wagner's function associated to a flap step input. For this flap geometry, thin airfoil theory predicts that the rate of change of lift coefficient (C_L) due to flap deflection

(δ_f) is:

$$C_{L\delta f} = \frac{\mathrm{d}C_L}{\mathrm{d}\delta_f} = 3.82/\mathrm{rad} \tag{2.131}$$

Therefore, in steady-state conditions and zero AOA, a flat plate generates a lift coefficient of 3.82 per radian of flap deflection. In the Fig. 2.20, the lift response for a unit step (in radians) input stabilizes at this value. The error between ULLT and thin airfoil theory is minimal (0.3%) and is due to 3D discretization and tip effects. It should be noted that, although the initial condition for simulation is zero, the lift response does not start at zero. Instead, it starts at a value which is approximately half of the steady state value. This is a consequence of the indicial step response (Wagner's function), which indeed does not start at zero. This nonzero initial response is also reflected in the fact that both LTI state-space realizations, for the airfoil (Eq. 2.59) and for the ULLT method (Eq. 2.86), have a nonzero direct transmission matrix D.

Regarding 3D flow, the steady-state case is verified against data from [106, page 172]. Specifically, the Induced Drag Factor (δ) is compared for different aspect ratios and taper ratios. This factor is inherently associated to the span efficiency factor (e):

$$C_{Di} = \frac{C_L^2}{\pi\, AR}\,(1+\delta) = \frac{C_L^2}{\pi\, AR\, e} \tag{2.132}$$

For an elliptical wing, $e = 1$, or, equivalently, $\delta = 0$. The induced drag factor can be obtained directly from the Fourier series coefficients (A_n) used to represent the circulation distribution in the general Lifting-Line problem:

$$\delta = \sum_{n=2}^{N} n \left(\frac{A_n}{A_1}\right)^2 \tag{2.133}$$

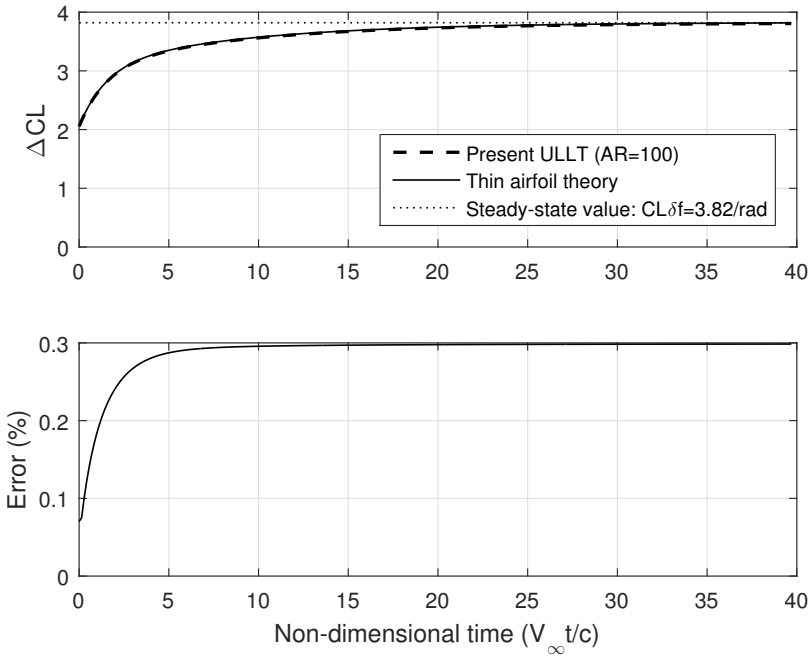

Figure 2.20: Lift response due to a step input in flap deflection.

More details are available in [91]. The comparison with results from McCormick [106] is given in Fig. 2.21. The number of spanwise stations used is $N = 200$. As can be observed, the results are identical.

2.4.2 UVLM verification tests

Initially, the steady-state behavior of the UVLM is verified with respect to flap deflection and variations in wing planform. Then, verifications in unsteady conditions are performed. For the 2D unsteady case, the present UVLM is compared to analytical results provided by Wagner's function and Theodorsen's theory. For the 3D case, the results are compared to numerical data provided by Katz and Plotkin [98].

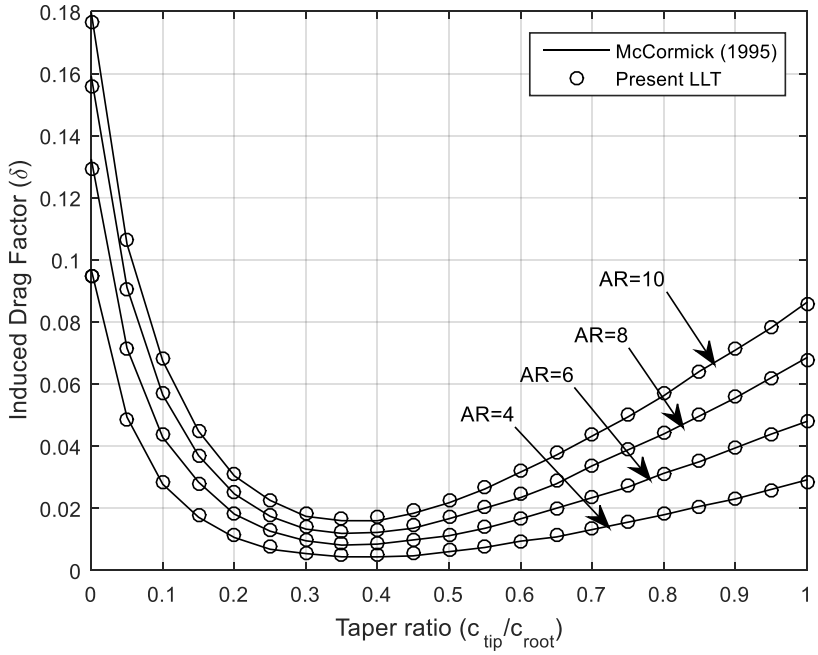

Figure 2.21: Verification of ULLT method for steady, 3D conditions.

2.4.2.1 Steady-state verification of VLM with respect to flap deflection

The verification with respect to flap inputs is carried out by comparing with results from another Vortex Lattice code widely used in the literature. Specifically, the Athena Vortex Latice (AVL) [107] will be used to verify the steady-state version of the UVLM algorithm developed in this work.

The same baseline configuration from Table 2.1 was loaded into AVL: rectangular wing, no camber, aspect ratio 6, with 8 trailing edge flaps (on 25% of the chord). The same discretization was used: $n_x = 8$ chordwise panels and $n_y = 64$ spanwise panels.

The variation in the spanwise distribution of lift coefficient due to a unit step input on flap deflection is presented in Fig. 2.22, where each plot represents one flap individually actuated. The results from the Lifting-Line Theory (steady-state version of ULLT) are also presented for completeness.

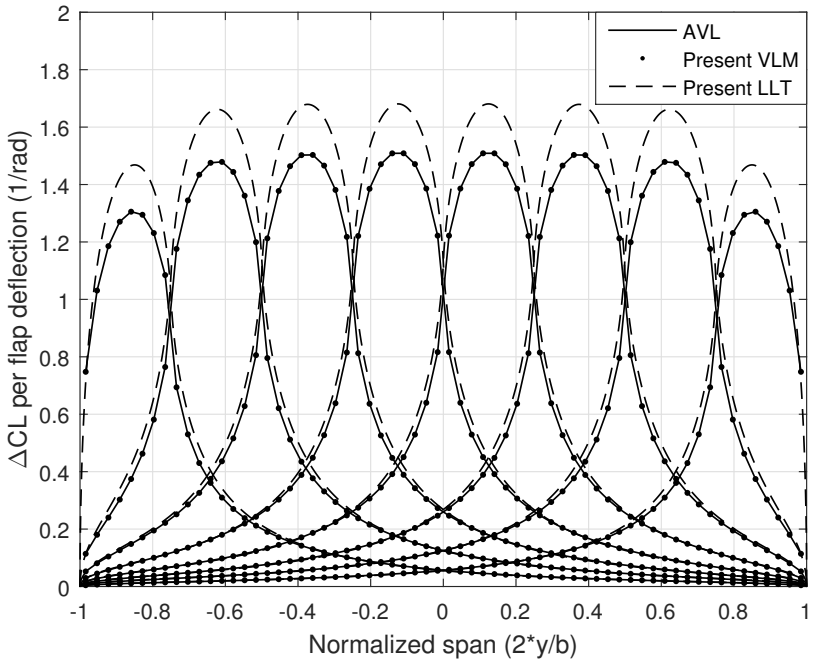

Figure 2.22: Spanwise variations of C_L for a unit step input applied to each of the 8 flaps individually.

The results from AVL and the present VLM are identical, which indicates that the steady-state results for the UVLM method are reliable. However, the comparison with Lifting-Line Theory (LLT) shows differences of up to 10%. The LLT was already checked in steady-state conditions, and the comparison with AVL shows that the present VLM is reliable as well. The differences, in this case, are due to two main causes: 2D modeling of flaps and representation of spanwise lift. Specifically:

1. The LLT models the 2D behavior of flaps correctly, but over predicts spanwise lift in general, and this tendency worsens for low aspect ratios [108, Chapter 3, page 149];

2. The VLM predicts spanwise lift well (for any aspect ratio), but under predicts

flap efficiency because of chordwise discretization.

Therefore, the true results probably lie in between the two models (LLT and VLM). The following discussion attempts to quantify the errors in each model, in order to determine which one is more accurate for the condition evaluated. The present LLT uses the correct value for $C_{L\delta f}$, which was supplied to the algorithm as 3.82/rad for a trailing edge flap occupying 25% of the chord. So, no errors in LLT are due to flap modeling.

Although equivalent to AVL results, VLM is known to depend on discretization. In the convergence analysis performed, it was observed that a mesh of 8×64 (chordwise x spanwise) elements provides errors in total C_L below 2%, for AOA=3 deg and zero flap deflections. The wing is planar (no camber, no dihedral) and unswept, so the effect of n_x in these conditions is negligible. In fact, even a single chordwise panel can provide high accuracy in such simple geometries [107]. The effect of n_y on total C_L is showed in Fig. 2.23.

The spanwise lift from VLM is then accurate within 2%. Better accuracy could be obtained with a cosine distribution of panels along the span. In this work, however, a uniform distribution was employed, since it simplifies the definition of flap geometries. The uniform distribution was also enforced in AVL in the comparison performed. For more complicated wing geometries, it is interesting to pursue more efficient vortex distributions (both spanwise and chordwise) in order to reduce the computational cost.

The 2% accuracy level described above, however, is not representative of the

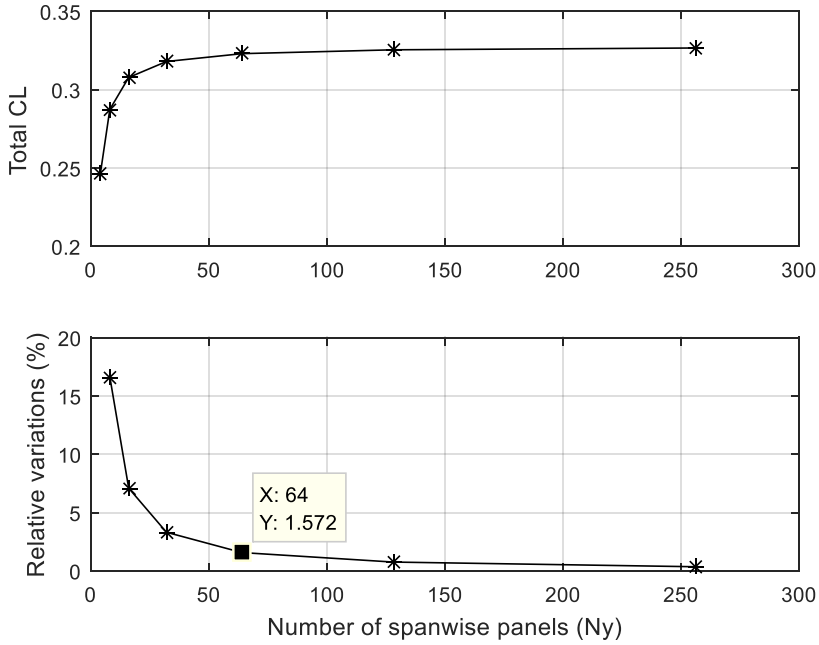

Figure 2.23: Effect of spanwise discretization on total C_L, for the present VLM.

steady-state condition with flaps deflected. In this case, there is a discontinuity in the airfoil camber at the hinge line. Therefore, the chordwise discretization n_x becomes important. In order to investigate how well the VLM is modeling the flap, the parameter $C_{L\delta f}$ is obtained from VLM, and then compared to the expected 2D value from thin airfoil theory. To effectively eliminate tip effects, an aspect ratio of AR=1000 was used, and a single spanwise panel was employed, i.e. $n_y = 1$. The total wing C_L was divided by the flap deflection (applied to all flaps simultaneously), and the chordwise discretization was tested for $n_x = [4, 8, 16, 32, 64]$. The results are presented in Fig. 2.24.

For low values of n_x, the VLM under predicts the flap efficiency, requiring many more chordwise panels ($n_x > 64$) to reach an error below 2%. It should be noted that the effects of 3D flow were removed by using AR=1000. Also, the VLM approach used

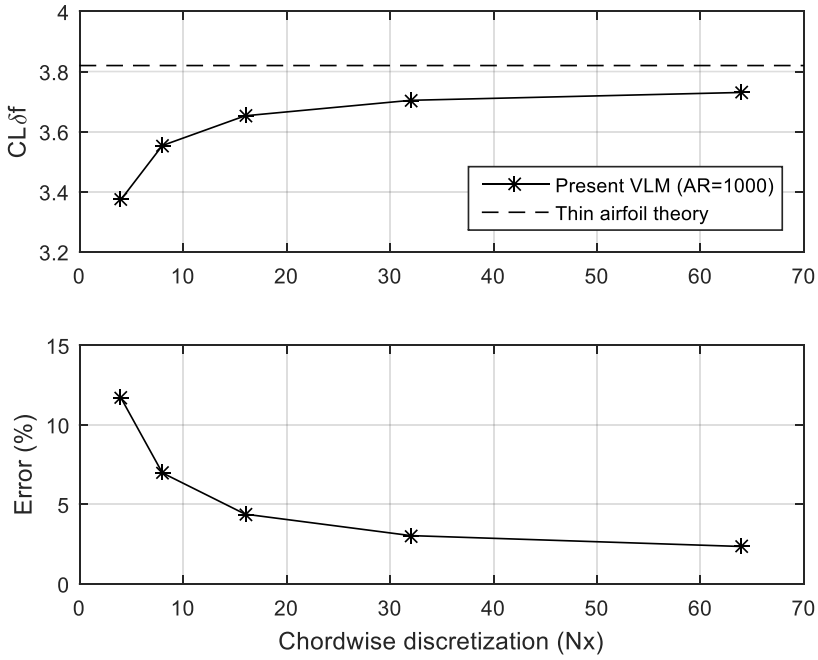

Figure 2.24: Error on the derivative $C_{L\delta f}$ due to chordwise discretization.

here is linear (small angles approximation is used), so these errors are not due to large flap deflections, and therefore are solely due to chordwise discretization limitations. For the purposes of this work, it was considered that using more than eight panels along the chord would require higher computational effort, for a relatively small improvement in accuracy. For $n_x = 8$, an error of 7% is expected in the airfoil lift due to flap deflection.

The results in Figs. 2.23 and 2.24 tried to quantify the error of VLM in the static influence functions from Fig. 2.22. It is clear that the VLM is underestimating the lift by:

1. Around 1.5% due to spanwise discretization ($n_y = 64$) alone. Because the flaps are not deflected, the chordwise discretization has practically no influence on this error, which is purely the error in representing the 3D flow effects (i.e. tip

effects).

2. About 7% due to chordwise discretization ($n_x = 8$) alone. In Fig. 2.24, the n_y discretization effects are numerically removed by using a very large aspect ratio (AR=1000).

Assuming these two errors are uncorrelated, they indicate that the VLM is under estimating spanwise lift by around 8.5%. However, these don't quite explain the 10% difference obtained in the static influence functions. The amount of lift over estimated by the Lifting-Line method can possibly explain the remaining difference.

In order to investigate the lift generation by the LLT, the following procedure was devised. First, using the same chordwise discretization ($n_x = 8$) for VLM, the aspect ratio of the wing was increased up to AR=1000, and both methods were evaluated. As shown in Fig. 2.25(a) (top plot), the parameter $C_{L\delta f}$ for the LLT converged to 3.82/rad (exact value from 2D thin airfoil theory), as expected, but the VLM converged to 3.56/rad, which represents a difference about 7% (Fig. 2.25(a), bottom plot). Note that the same value can be obtained from Fig. 2.24, by selecting $n_x = 8$. This lower value means that VLM is always modeling a less efficient flap. Now, if this value is supplied to LLT, then both algorithms will be employing the same 2D airfoil behavior, and any differences observed will be due to errors in the spanwise lift modeling. These results are plotted in Fig. 2.25(b). Now, $C_{L\delta f}$ converges to 3.56/rad in both methods (LLT and VLM), as expected. More importantly, it is clear that LLT and VLM provide equivalent results for $AR > 10$. In fact, LLT over estimates the total lift at lower aspect ratios, but only slightly. At $AR = 6$, it can be seen that

the relative difference is around 2% .

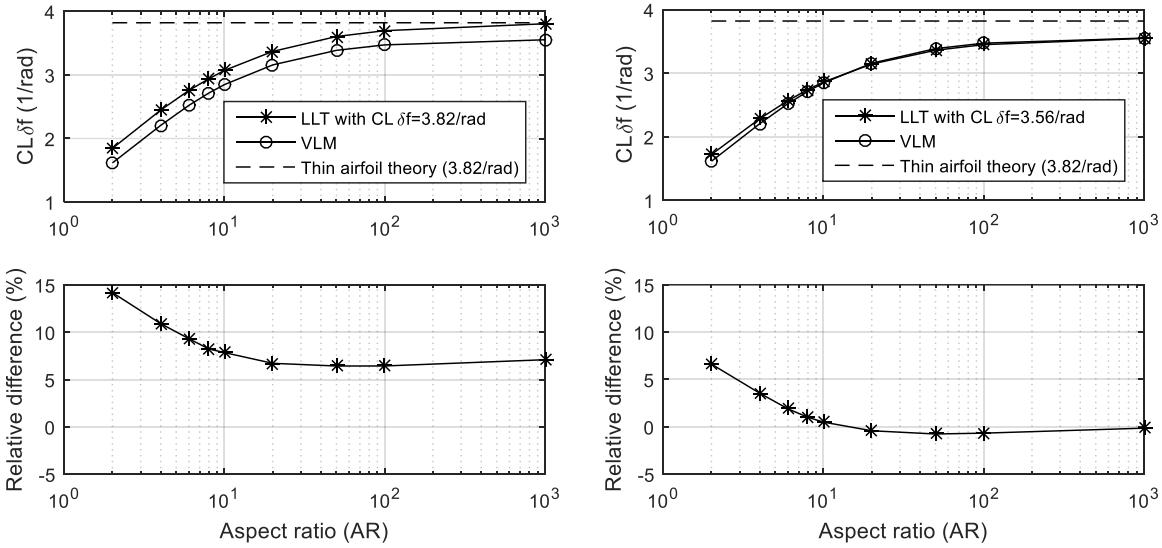

(a) $C_{L\delta f,\,2D}$=3.82/rad

(b) $C_{L\delta f,\,2D}$=3.56/rad

Figure 2.25: Derivative $C_{L\delta f}$ of rectangular wing vs. aspect ratio.

As a conclusion, the 10% error between LLT and VLM observed in the static influence functions (Fig. 2.22) is actually due to 8% under estimated lift by VLM, and 2% over estimated lift by LLT. This result might be unexpected, because LLT is often regarded as a low-accuracy method for moderate aspect ratios (such as AR=6), as compared to VLM. However, most comparisons in the literature are given with respect to angle of attack variations. Comparatively, the errors in lift slope ($C_{L\alpha}$) between LLT and VLM are much higher, as can be seen in Fig. 2.26, which also shows results from [108, page 150]. The relative difference shows in percentage how much lift the LLT over predicts, as compared to the VLM. It should be noted that the VLM results from [108] are actually referred to as Weissinger's method or extended LLT in that work, which are simply the VLM with unitary chordwise discretization

(as shown in Fig. 2.12). Therefore, $n_x = 1$ was used when generating results with the present VLM for comparison.

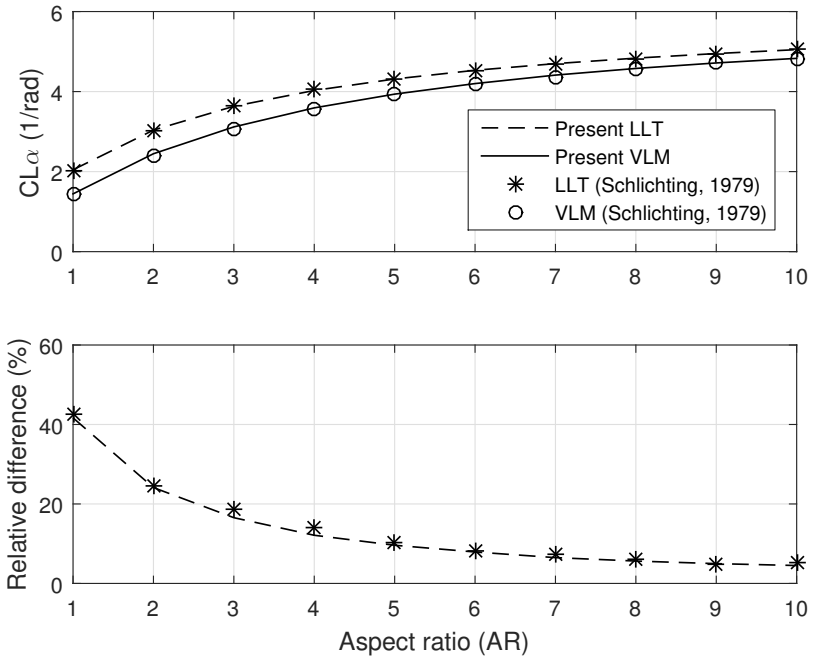

Figure 2.26: Lift slope $C_{L\alpha}$ of rectangular wing vs. aspect ratio.

2.4.2.2 Steady-state verification of VLM with respect to wing planform variation

The present VLM was also compared to experimental results. The lift slope ($C_{L\alpha}$) is computed for untapered wings, in different combinations of aspect ratio (AR) and sweep angle (Λ). The same chordwise ($n_x = 8$) and spanwise ($n_y = 64$) discretizations were kept in all cases. In Fig. 2.27, it can be seen that the VLM method agrees well to data from [98].

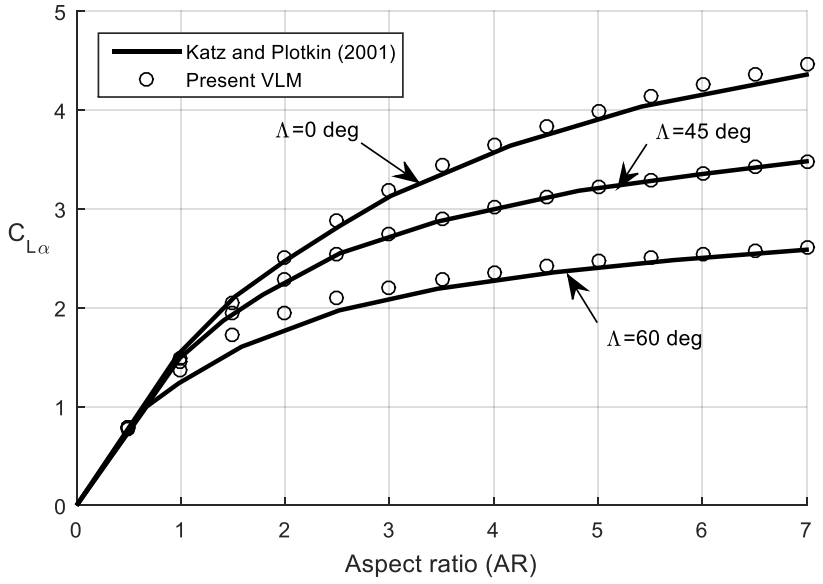

Figure 2.27: Lift slope $C_{L\alpha}$ of planar wings with different aspect ratios and sweep angles.

2.4.2.3 Unsteady verification of UVLM: 2D case using Wagner's function

While unsteady solutions for 3D flow conditions are scarce in the literature, it is possible to compare UVLM results in 2D flow conditions, for which analytical solutions from unsteady airfoil theory exist. Since the UVLM yields results in time-domain, a comparison with Wagner's function flows naturally. In this work, UVLM is used to obtain the lift build-up associated to a sudden acceleration of a flat plate with very large aspect ratio (AR=1000), which is effectively the same as a step input in angle of attack (Wagner's problem). Fig. 2.28 shows the results for a unit step input in AOA. The spanwise discretization was kept $n_y = 1$, to intentionally disregard any influence of 3D flow (tip effects), whereas the chordwise discretization (n_x) was varied.

It can be seen that the UVLM converges to Wagner's function exactly: increasing n_x, the error goes to zero. However, it is also necessary to define the time step (Δt).

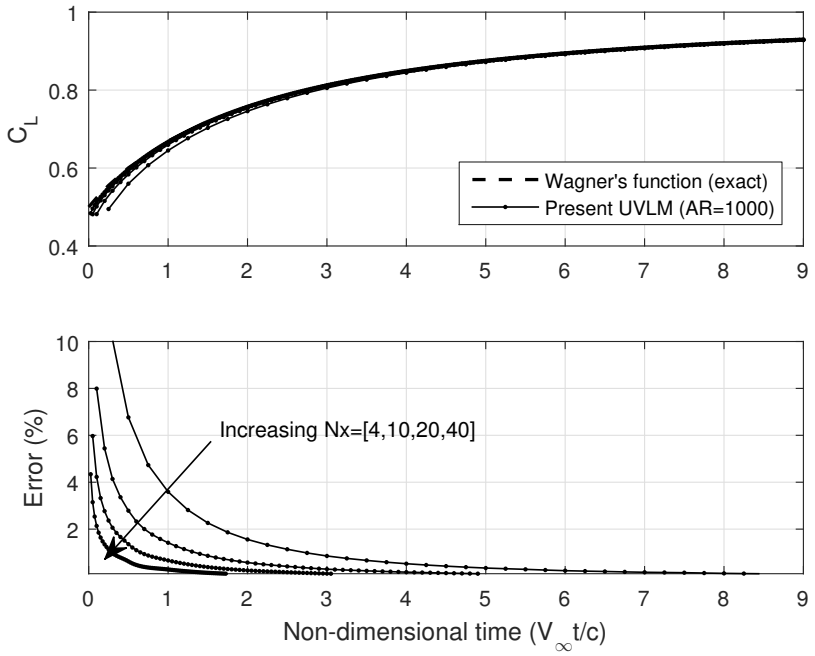

Figure 2.28: Unsteady lift for a flat plate, in response to a unit step input in AOA.

This parameter is intrinsically related to the discretization of the wake. The length of wake rings in the streamwise direction (Δx_w) is given by:

$$\Delta x_w = V_\infty \Delta t \tag{2.134}$$

Therefore, the simulation time step automatically sizes the wake vortex rings in the direction of the flow. A necessary condition for the UVLM to converge to Wagner's function is that the length of vortex rings in the wake (Δx_w) must be equal to those in the wing (Δx):

$$\Delta x = \frac{c}{n_x} = V_\infty \Delta t \tag{2.135}$$

From this condition, the time step is automatically defined by the chordwise discretization (n_x) used. In fact, the non-dimensional time step Δt_{ND} is given by:

$$\Delta t_{ND} = \frac{V_\infty}{c} \Delta t = \frac{1}{n_x} \tag{2.136}$$

In Fig. 2.28, it can be seen that the points are more closely spaced for higher Nx, which results in smaller non-dimensional time step. Some authors used this condition [104, 109], but there is no clear explanation of why $1/n_x$ was used as non-dimensional time-step. Since the last row of wake rings is shed from the wing trailing edge, its streamwise length must match the distance covered by the trailing edge during one iteration. If a larger (or smaller) time step is used, the vorticity would propagate along the wake faster (or slower) than the freestream velocity, affecting the results in unsteady conditions. A detailed discussion on this matter is given in [110]. Another relevant aspect that influences UVLM results is the chordwise location of the point where the wake is attached to the wing. The first row of wake rings must be placed at $\Delta x/4$ behind the trailing edge [104, 109, 110].

The analytical solution from Wagner assumes a flat wake. Therefore, the wake roll-up feature was disabled in the UVLM routine for this 2D verification, in order to yield a planar wake, aligned with freestream velocity, just like Wagner's and Theodorsen's theory. It should be noted that good accuracy is obtained even for low n_x discretization, as long as $1/n_x$ is used as non-dimensional time step.

One last comment regarding the representation of Wagner's function itself. In the ULLT formulation, the Wagner's function was approximated by a summation of two exponentials, and the final error was less than 1%. Values for these exponential parameters can be found in [90, 94]. However, for the accuracy level reported in Fig. 2.28, these approximations could not be used, otherwise the error curves become non-monotonic. A more accurate lookup table representation of Wagner's function was obtained by numerically evaluating its analytical formulation in terms of Bessel

functions [93, Section 5-7]. Hence, the Wagner's function used in Fig. 2.28 is regarded as *exact*, as opposed to an exponential approximation.

2.4.2.4 Unsteady verification of UVLM: 2D case with Theodorsen's function

The verification with Wagner's function generates the wake geometry for steady initial conditions. After shedding a wake, it is possible to obtain a linear, time-invariant, discrete-time model from UVLM, as in Eqs. (2.129)-(2.130). After converting these models to continuous-time, it is possible to simulate harmonic flap inputs for different reduced frequencies. The frequency response of UVLM models is compared to Theodorsen's results in Fig. 2.29, including non-circulatory effects.

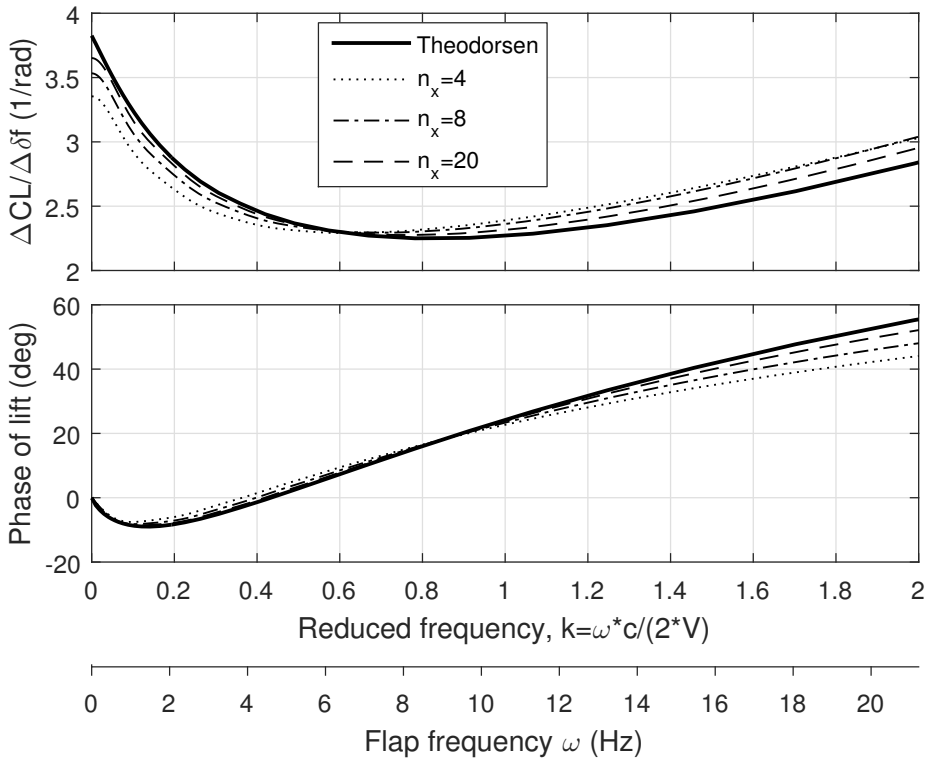

Figure 2.29: Convergence of present UVLM results to Theodorsen's function, as the chordwise discretization is increased.

The chordwise discretization is varied between $n_x = [4, 8, 20]$, whereas the wake length is defined by setting $n_{xw} = 20\, n_x$. It can be seen that, as the chordwise discretization is refined, the UVLM results converge to Theodorsen's theory, represented by the state-space model from Eqs. (2.48)-(2.50), including the non-circulatory lift from Eq. (2.51). In order to model the non-circulatory effects using UVLM, the velocity component induced by the flap rate on the collocation points ($V_{deflection}$) must also be considered when computing the RHS in Eq. (2.107). Since this component depends on $\dot{\delta}_f$, the flap rate also becomes an input to the system, but only for this verification test case. It should be noted that such measures are only necessary to

accurately model high reduced frequencies k. In fact, accurate results are obtained up to $k = 2$ in Fig. 2.29, which demonstrates the capabilities of UVLM. In this work, however, the range of reduced frequencies expected lies below $k = 0.1$, as discussed in Section 2.3.4.1. At these frequencies, the non-circulatory effects can be neglected.

From Fig. 2.29, it can be observed that the UVLM slightly under predicts the lift due to flap at low frequencies, and over predicts the lift for $k > 0.6$, where non-circulatory effects dominate. The magnitude results for $k = 0$ are very comparable to those in Fig. 2.24, for the same values of n_x. In other words, a coarse chordwise discretization represents a less efficient flap at low frequencies.

The time domain results associated to harmonic flap inputs at k=0.2, 0.4 and 0.8 are shown in Fig. 2.30, for $n_x = 20$. As the frequency increases, the slope of the major axis of the loop (left side) decreases, corresponding to attenuation in the lift magnitude shown in Fig. 2.29. Regarding phase, there is a phase lag at k=0.2, which becomes approximately zero at k=0.4, and then becomes phase lead at k=0.8. Therefore, the loop exhibits a counterclockwise direction at low reduced frequencies (k=0.2), and develops into a clockwise loop for higher frequencies (k=0.8).

The errors in maximum lift coefficient obtained using UVLM, with respect to Theodorsen's results, are presented in Fig. 2.31. The negative results for k=0.2 and k=0.4 correspond to UVLM results below Theodorsen's theory, whereas for k=0.8 the lift is over estimated. Overall, errors are of less than 5% should be expected when using at least 8 chordwise panels.

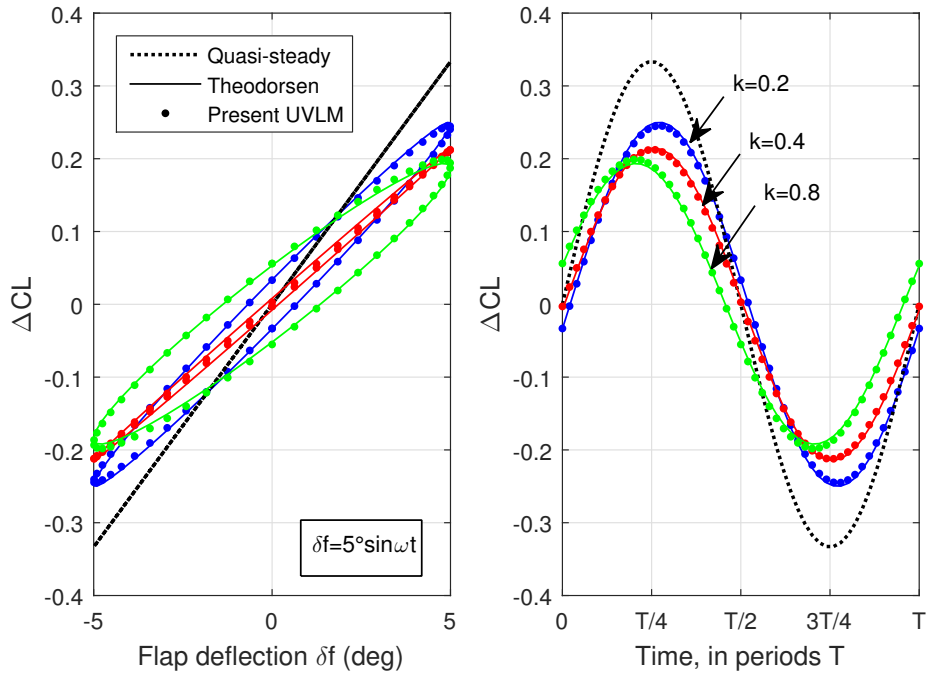

Figure 2.30: Unsteady lift for a harmonic flap oscillation in incompressible flow: vs flap angle (left) and vs time (right).

2.4.2.5 Unsteady verification of UVLM: 3D case

The verification of UVLM for finite wings was performed by comparison with numerical results provided by [98, page 430, Fig. 13.34]. These results represent the unsteady lift build up for rectangular wings of different aspect ratios that were suddenly set into forward motion at AOA=5 deg, i.e. sudden acceleration results (Fig. 2.32). The discretization used $n_x = 4$ chordwise panels, $n_y = 13$ spanwise panels, and a non-dimensional time-step of $\Delta t_{ND} = V_\infty \Delta t/c = 1/16$.

It can be seen that the present UVLM matches the numerical results from Katz and Plotkin [98] very accurately. Therefore, these results allowed verification of the present UVLM algorithm for the case of finite wings in unsteady conditions. Note,

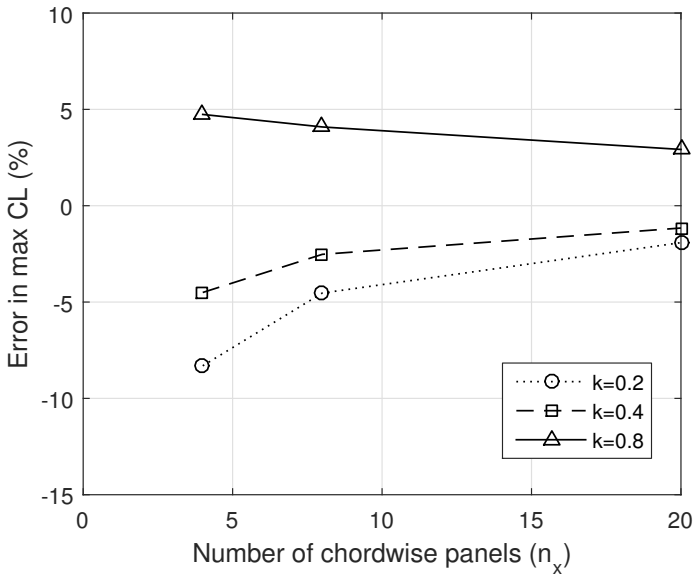

Figure 2.31: Error in maximum C_L obtained with UVLM during harmonic flap inputs.

that the non-dimensional time-step used is not equal to $1/n_x$. Therefore, the results for the infinite AR case are *not* expected to match Wagner's function well.

The exact role that the time step plays in UVLM formulation is still being investigated, with important findings being only recently reported [110]. For the present work, the most dramatic consequence of the time step used is the Nyquist frequency associated to the final discrete-time, LTI, state-space realization obtained for UVLM. For the modal analysis techniques that will be presented in Chapter 3, the eigenvalues of all relevant modes must lie below the Nyquist frequency.

For control synthesis in Chapter 5, a conversion from discrete-time to continuous-time will be eventually performed. In this case, one must keep in mind that the maximum reliable frequency (e.g. in the Bode plot or Singular Value plot) is the Nyquist frequency. Therefore, a tradeoff exists: for very small time step, the final

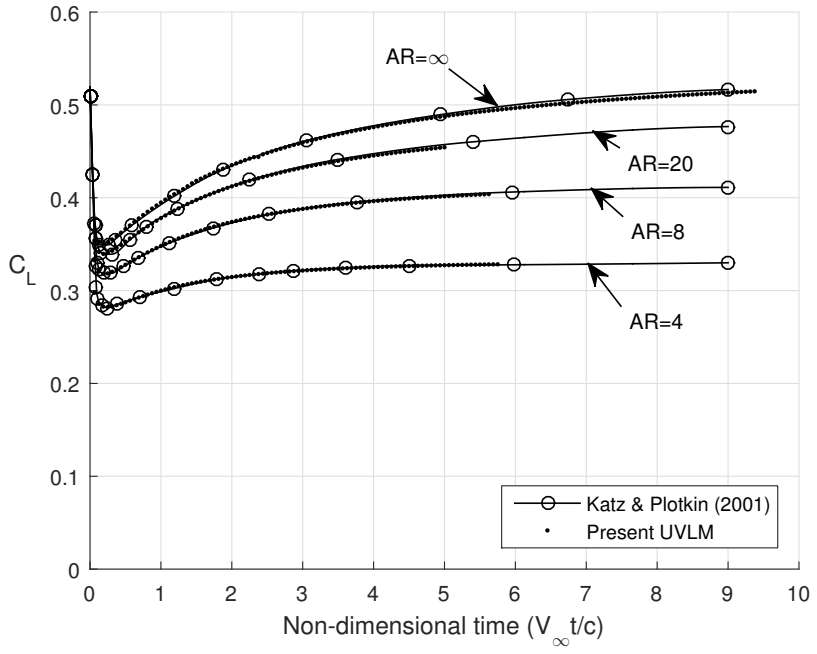

Figure 2.32: Unsteady lift response of flat plates to a 5 deg step input in AOA, for different aspect ratios.

discrete-system accurately describes the lift behavior at higher frequencies, but the wake will grow very slowly, requiring many vortex rings and increasing the computational cost considerably. For this work, a time-step of $\Delta t = 0.02$ s will be able to fulfill both requirements. For $V_\infty = 10$ m/s and $c = 0.3$ m, the associated non-dimensional time-step is $\Delta t_{ND} = V_\infty \Delta t / c = 10 \times (0.02/0.3) = 0.667$.

2.4.3 Comparison of nonlinear vs. linear UVLM formulations

In the previous sections, it was stated that the linearized formulation of UVLM from Eqs. (2.129)-(2.130) can be obtained when the wake geometry is assumed fixed. However, the validity of this assumption should be assessed. The linear and nonlinear

formulations are simulated for a harmonic input on flap 3, with amplitude $\delta_f = 5$ deg and $k = 0.47$. The lift coefficient results are plotted along span and along time in Fig. 2.33 (top left), along with the differences between the two formulations (bottom left). On the right, the results for a section located at the middle of the flap 3 are provided. The errors introduced by the linearization can be considered negligible. For lower reduced frequencies, these differences are expected to decrease even further.

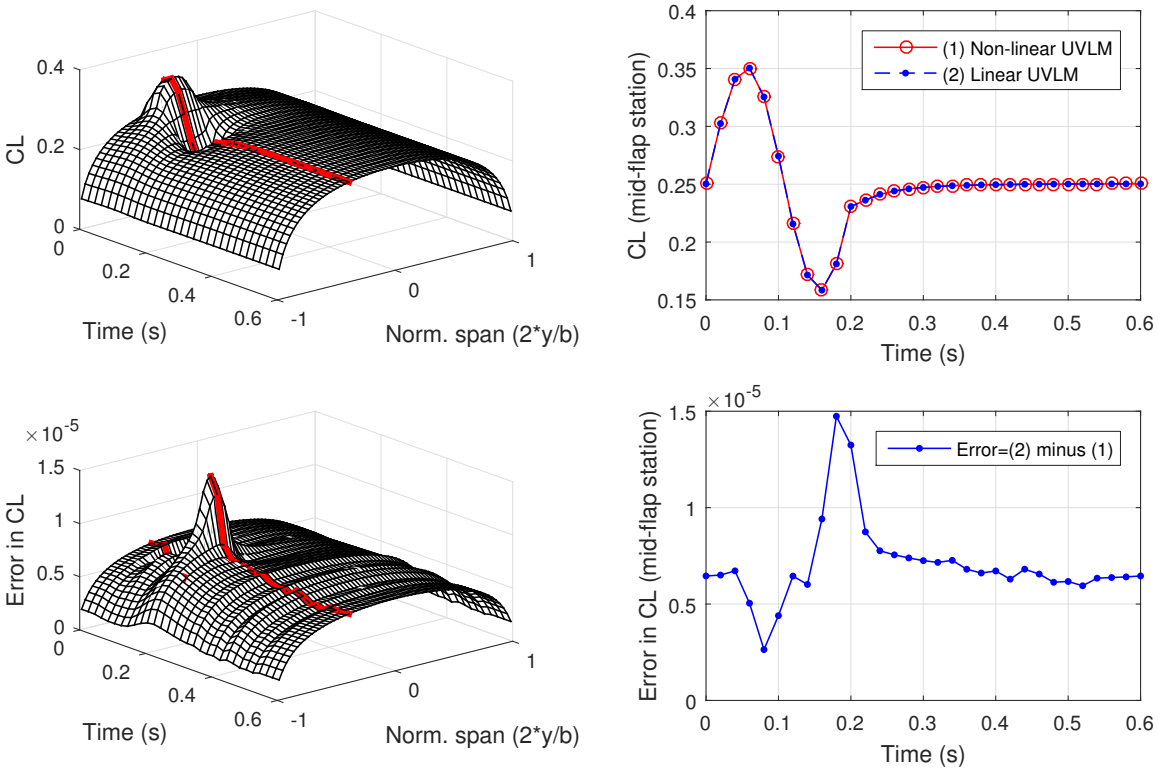

Figure 2.33: Comparison between nonlinear and linear UVLM formulations.

2.5 Assumptions and constraints

The two models presented previously (ULLT and UVLM) are capable of modeling the dynamic behavior of the spanwise lift distribution. Both approaches are based on

potential flow methods and, as such, share many assumptions:

- Flow is incompressible, irrotational and inviscid;
- Flow is attached everywhere, so low angles of attack and small flap deflections are assumed;
- Lifting surfaces are thin, hence airfoil thickness effects cannot be captured;
- For the unsteady case, both models assume that the wake vorticity travels at the free stream airspeed. For ULLT, this is embedded in Theodorsen's solution. For UVLM, this assumption is numerically enforced in the wake shedding and convection mechanism;
- Both models also assume that wake vorticity is constant along time, i.e. no vortex dissipation effects are modeled, although this could be incorporated into UVLM.

However, there are substantial differences as well. The Unsteady Lifting-Line Theory carries all the assumptions from Prandtl's classical Lifting-Line and from 2D unsteady thin airfoil theory (Wagner's and Theodorsen's theory). Regarding 3D behavior, vortex lattice methods are applicable to a broader range of configurations, as long as the incidence flow angles (angles of attack and sideslip) are low enough to ensure attached flow. A summary of the capabilities of the two methods is given in Table 2.2.

At the 2D level, Lifting-Line can be enhanced by using actual airfoil data, allowing representation of cambered airfoils and flaps, but it would require previous knowledge

Table 2.2: Comparison between capabilities of ULLT and UVLM.

Aspect	ULLT	UVLM
Wing planform	In-plane wings only, no sweep, moderate to high aspect ratios (AR 6 or higher)	Allows out-of-plane lifting surfaces (e.g. winglets, dihedral), sweep angle, any aspect ratio
Spatial discretization	Spanwise only	Chordwise and spanwise
Wake modeling	Flat wake	Allows wake roll-up

about the airfoil behavior, obtained from wind tunnel tests or CFD models. On the other hand, the camber effects can be automatically taken into account in Vortex Lattice, by placing vortex rings exactly at the camber line, but the accuracy of results depends on the chordwise discretization employed.

In order to obtain a linear formulation for the ULLT, the indicial functions were numerically approximated by a simpler function consisting of two exponential terms, with fit error below 1% (Fig. 2.6). Other than that, the Lifting-Line formulation is purely linear and was readily put into linear, time-invariant (LTI), state-space form. On the other hand, the UVLM provides a nonlinear formulation, due to the update of the wake geometry at every time-step. Under the assumption of frozen wake, a discrete-time LTI state-space formulation was obtained. It was shown that the errors introduced by this assumption are negligible (Fig. 2.33).

The two models also differ in terms of number of states required in the LTI state-space formulations. In this work, the ULLT uses $N = 200$ spanwise locations. Therefore, the total number of states for ULLT is $6N = 1200$. For the UVLM, the total

number of states is: $2(n_x \times n_y) + (n_{xw} \times n_y) = 2048$. While the number of states in the ULLT varies linearly with N, the number of states in the UVLM also depend on chordwise discretization along the wing (n_x) and wake (n_{xw}). Generally, in order to increase accuracy by using more vortices, it is necessary to refine the vortex spacing in both the spanwise and in the chordwise directions [107]. By increasing the chordwise spacing in the wing n_x, it is also necessary to increase the streamwise discretization along the wake (n_{xw}). Typical ratios between these parameters are:

$$\begin{aligned} 1/8 < \frac{n_x}{n_y} < 1/4 \\ 2 < \frac{n_{xw}}{n_x} < 10 \end{aligned} \tag{2.137}$$

Considering n_x and n_{xw} proportional to n_y, then the number of states for UVLM varies quadratically with the number of spanwise panels. These trends are shown in Fig. 2.34. The UVLM is represented as a region, that reflects the ranges in Eq. (2.137). Note that the number of states is given in a logarithmic scale.

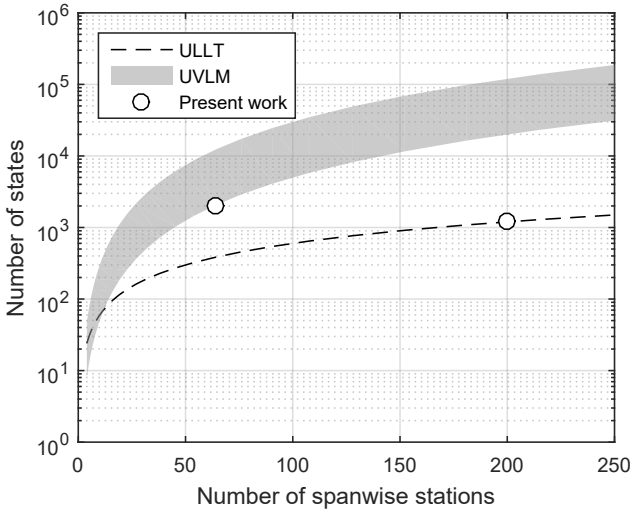

Figure 2.34: Size of LTI state-space models, as a function of spanwise discretization.

For spanwise discretizations between 30 and 170, the ULLT requires hundreds of states (100 up to 1000), whereas the UVLM would typically require thousands of states. It can be seen that UVLM can easily reach 10^5 states, if a refined discretization is used. A summary of the differences between the two LTI state-space models is given in Table 2.3.

Table 2.3: Comparison between state-space formulations of ULLT and UVLM.

Parameter	ULLT	UVLM
Temporal behavior	Continuous-time	Discrete-time
Typical number of states	100-1,000 (i.e. hundreds)	1,000-10,000 (i.e. thousands)
System inputs	Flap rate, vertical gust	Flap angle, vertical gust

Both models yield very large systems in terms of number of states. Since this work aims to synthesize controllers for lift distribution, it is not feasible to apply conventional controls to such a large LTI state-space systems. Therefore, it is necessary to apply model-order reduction techniques, which will be addressed in Chapter 3.

Despite the long list of assumptions, Lifting-Line and Vortex Lattice methods are used in a wide range of applications. In this work, both models are applicable to the baseline model used (rectangular wing, AR=6, with 8 uniform flaps). The reason for having both approaches available is to increase confidence in the results presented in this work.

One of the most relevant objectives in this work is to apply modal identification techniques and numerically obtain natural mode shapes for the spanwise lift distribution, also called aerodynamic modes. As will be seen in Chapter 4, both methods

(ULLT and UVLM) yield very similar mode shapes. Obtaining essentially the same mode shapes from two independent methodologies indicates that such results are reliable.

Chapter 3

Review of model order reduction methods

The LTI, state-space formulation obtained using the UVLM provides an efficient framework for quick simulations. However, the number of states in the model is very high (2048 states), which precludes the immediate application of conventional control techniques. In such cases, model order reduction methods become necessary. This Chapter presents an overview of model order reduction methods, including the Proper Orthogonal Decomposition (POD) and the Eigensystem Realization Algorithm (ERA). After presenting the main aspects of each method, the ERA is chosen as the preferred one, since it is also suitable for modal identification purposes. The ERA is applied to a simple cantilever beam example, in order to reduce the order of the original finite element model. By comparing the analytical eigenvalues and mode shapes with the numerical results from ERA, important conclusions are drawn regarding the usage of the algorithm and its limitations.

3.1 Introduction

The success of model-reduction methods largely depends on the characteristics of the system itself. The internal states most likely do not share the same level of importance in describing the system as a whole. Therefore, eigenanalysis techniques can be applied in order to select the most important modes, whereas the least relevant ones are discarded. The methods can be primarily separated into state-space-based and projection-based approaches.

3.1.1 State-space-based approaches: truncation and residualization

In this work, a state-space model describing the unsteady spanwise lift distribution is available, so that model order reduction can be achieved via truncation or residualization. A very lucid discussion is presented by Skogestad [111, Chapter 11]. Consider a stable linear system converted into modal canonical form. Since the fast modes quickly achieve zero, the system's response is dominated by the slow modes. A model truncation can be applied by keeping only the states associated with the smallest eigenvalues (in absolute value) in the diagonal A matrix, whereas the faster modes are simply disregarded. Because higher order modes also have a DC component, the truncation always causes an error at DC. This problem can be avoided by using the method of residualization of the less relevant states. In this case, the state equations of the faster modes are set to zero, from which one can obtain matrix relationships that enforce that the DC response matches that of the full-order model.

Therefore, truncation and residualization are the two main types of model-based order reduction approaches. The criteria of using the faster/slower modes, however, might not be the most appropriate sometimes. For example, a slow mode that is nearly unobservable should probably not be included in the reduced model. The same techniques given above (namely truncation and residualization) can be applied to a different state-space realization. Instead of using the modal canonical form, the balanced realization can be employed. In this particular realization, the Gramians (controllability and observability) are diagonal and equal, yielding the notable property that each state (or mode) is equally observable and controllable. The states kept in the reduced-order model are those associated with the higher Hankel Singular Values (HSV), which form the diagonal of the Gramians. This idea of balancing the contribution from each state was first introduced by Moore [28] and form the backbone of the main model-order reduction techniques used in the controls community.

The balanced truncation yields very efficient reduced-order models, but it requires the computation of Gramian matrices. While it is relatively straightforward to compute such matrices, the procedure becomes inefficient for large systems, with number of states in the order of 10^4 or more. Moreover, balanced truncation is restricted to stable, linear systems. Perhaps this explains why these techniques from the control theory community are not so popular in other fields, such as computational fluid dynamics [112, 113].

3.1.2 Projection-based approaches: POD, balanced POD and ERA

For some applications, such as the finite element method, the number of states is typically very large. The numerical model accurately represents the system behavior, but does not lend itself to other applications, such as optimization or control synthesis. Therefore, model-order reduction techniques are necessary. Even if a linear state-space formulation can be obtained, the system is very high-order, making it impractical to obtain its modal canonical or balanced realization. For other applications, the model might be non-linear or its analytical form might be unknown. For such cases, other techniques were developed, mostly based on projection methods.

The idea consists in projecting the system dynamics along specific directions. Depending on the choice of the basis used, the reduced-order model becomes more or less efficient. Among these techniques, Galerkin methods and Proper Orthogonal Decomposition (POD) are very common approaches. While Galerkin methods provide an analytical way to represent continuous operators as a truncated basis, POD is a numerical approach to model-order reduction. What follows next is a brief review of POD, and then a modified version called balanced POD is presented, which incorporates some degree of balancing to the final model. Finally, a different method called Eigensystem Realization Algorithm (ERA) is presented. ERA and balanced POD provide equivalent reduced-order models, but ERA is less computationally intensive. For this reason, only ERA results are presented in this work, but the balanced POD was used to check the ERA algorithm.

3.2 Proper Orthogonal Decomposition: fundamentals

Also known as Principal Component Analysis (PCA) and Karhunen-Loève Transform (KLT), POD can be described as a solution to the following problem: find a subspace approximating a given set of data in an optimal least-squares sense. This set of data (Y) can be generated from experiments or sampling data from simulations, if an analytical model is available. When cast into Lagrange multiplier formulation, the optimization problem is equivalent to solving the eigenvalue problem of the correlation matrix of the sampled data (YY^T). Because this matrix is symmetric and positive semi-definite, it can be decomposed as:

$$YY^T = Q\Lambda Q^{-1} = Q\Lambda Q^T \tag{3.1}$$

where Q is an orthogonal matrix with unit column vectors q_i (hence, Q is unitary) and Λ is a diagonal matrix of real numbers. Therefore:

$$YY^T Q = Q\Lambda \tag{3.2}$$

$$YY^T q_i = \lambda_i q_i \text{ , for } i = 1, 2, ..., N \tag{3.3}$$

From the spectral theorem, the eigenvalues are all positive and the eigenvectors are orthogonal. The most relevant directions are associated to the largest eigenvalues, and therefore must be included in the subspace. As more directions are added to the basis, the reduced-order representation gets closer to the original data. Hopefully, the eigenvalues exhibit fast decay in magnitude, so that a small basis can be used to

represent the data accurately enough. As one can observe, this problem is numerically equivalent to applying Singular Value Decomposition (SVD) to the original matrix of sampled data (Y):

$$Y = U\Sigma V^T \tag{3.4}$$

where U and V are unitary matrices of appropriate dimensions and Σ is a rectangular diagonal matrix of singular values σ_i. Taking the transpose to obtain YY^T, yields:

$$YY^T = U\Sigma V^T V_I \Sigma^T U^T = U\Sigma\Sigma^T U^T \tag{3.5}$$

$$YY^T U = U\Sigma\Sigma^T \tag{3.6}$$

$$YY^T u_i = \sigma_i^2 u_i \text{ , for } i = 1, 2, ..., N \tag{3.7}$$

The left singular vectors u_i (from SVD of Y) are exactly the eigenvectors q_i of YY^T, and the square of the singular values of Y are the eigenvalues of YY^T , i.e. $\sigma_i^2 = \lambda_i$. Therefore, POD is closely related to SVD, and from this point of view, POD has several advantages. It depends only on matrix operations, can be applied to either experimental data, or to data from simulations, from nonlinear or linear systems. In fact, even unstable systems can still generate simulation data for POD. The basis set obtained is always orthogonal, which represents the data provided in an efficient fashion. The volume of data can be reduced by using the method of snapshots [114], allowing application of POD even for very large systems. For the purposes of this work, the POD method described so far will be addressed as *snapshot POD*. A recent review on POD, from both a historical and mathematical points-of-view is presented in [115].

However, the method is not efficient for obtaining the modal characteristics of the system. The POD modes (left singular vectors from SVD) optimally approximate a given data set in the least-squares sense, but they are not designed to be the modes approximating the dynamics of the system that generated the given data set. In other words, the POD modes are generally not the same as system modes. Because of this fact, snapshot POD struggles to capture the system dynamics and the results are very dependent on the original data set used. Also, it is observed that, for some desired accuracy level, the reduced-order models generated from snapshot POD require many more modes than those produced by balanced truncation.

3.3 Balanced Proper Orthogonal Decomposition

In order to circumvent these deficiencies, several methods combining the ideas of POD and balanced truncation have been proposed, including [112]. Most notably, Rowley [113] developed and presented a method called balanced POD. The motivation for balanced POD is to provide some degree of balancing to POD by approximately computing Grammians from primal and adjoint systems simulations. For large systems, this is computationally more efficient than obtaining the exact matrices. Hence, balanced POD combines low computational cost from POD with approximate balancing of the states, yielding a much more efficient reduced-order model (i.e., fewer modes required for the same accuracy as snapshot POD). The drawback is that it requires data from adjoint simulation, which is not available from experiments. A comparison between POD and balanced POD is presented in [116]. A summary of the algorithm

is presented below [117]:

Step 1: Compute the generalized Hankel matrix. Initially, run impulse-response simulations of the so-called primal system (A, B, C, D) and collect (m_c+1) snapshots of states $x(k)$ in (m_cP+1) steps:

$$X = \begin{bmatrix} B & A^P B & A^{2P} B & \cdots & A^{m_c P} B \end{bmatrix} \tag{3.8}$$

where P is the sampling period. The matrix X is the impulse-response of the states, optionally downsampled for computational cost savings. Next, run impulse-response of the adjoint system:

$$z\left(k+1\right) = A^* z\left(k\right) + C^* v\left(k\right) \tag{3.9}$$

where the asterisk "$*$" stands for adjoint of a matrix (i.e. its conjugate transpose). Then, collect (m_o+1) snapshots of states $z(k)$ in (m_oP+1) steps:

$$Y = \begin{bmatrix} C^* & \left(A^*\right)^P C^* & \left(A^*\right)^{2P} C^* & \cdots & \left(A^*\right)^{m_o P} C^* \end{bmatrix} \tag{3.10}$$

Obtain the generalized Hankel matrix: $H = Y^* X$.

Step 2: Compute modes. Apply singular value decomposition to H:

$$H = U\Sigma V^* = \begin{bmatrix} U_1 & U_2 \end{bmatrix} \begin{bmatrix} \Sigma_1 & 0 \\ 0 & 0 \end{bmatrix} \begin{bmatrix} V_1^* \\ V_2^* \end{bmatrix} = U_1 \Sigma_1 V_1^* \tag{3.11}$$

where the diagonal matrix $\Sigma_1 \in R^{n_1 \times n_1}$ is invertible and includes all non-zero singular values of H, $n_1 = \mathrm{rank}\left(H\right)$ and $U_1^* U_1 = V_1^* V_1 = I_{n_1 \times n_1}$. Choose $r \leq n_1$. Let U_r and V_r denote the submatrices of U_1 and V_1 that include their first r columns, and Σ_r the

first $r \times r$ diagonal block of Σ_1. Calculate:

$$\Phi_r = X V_r \Sigma_r^{-\frac{1}{2}} \quad ; \quad \Psi_r = Y U_r \Sigma_r^{-\frac{1}{2}} \tag{3.12}$$

where the columns of Φ_r and Ψ_r are, respectively, the first r primal and adjoint modes of the original full-order system. The two sets of modes are bi-orthogonal: $\Psi_r^* \Phi_r = I_{r \times r}$.

Step 3: Project dynamics. The reduced-order model is obtained by projecting the full-order dynamics (A, B, C) into the directions given by Φ_r. Hence, the system matrices for the reduced-order model are:

$$A_r = \Psi_r^* A \Phi_r \; ; \; B_r = \Psi_r^* B \; ; \quad C_r = C \Phi_r \tag{3.13}$$

More details on the balanced POD method are given in [113, 117].

3.4 Eigensystem Realization Algorithm (ERA)

Although primarily developed for the modal identification of large flexible structures [118], the Eigensystem Realization Algorithm is particularly suitable for model order reduction. It is known to produce approximately balanced realizations [119, 120] and does not depend on adjoint simulations, being therefore applicable to experimental data. If a model is available, simulation data can be used as well. It works for both discrete and continuous time models [121, 122]. Due to its simplicity and efficiency, this algorithm has become the main approach in experimental modal identification. The basic formulation is in time-domain, but it has been extended to frequency

domain [123] and to time-varying systems [122]. The algorithm has been proved to provide essentially the same reduced-order models as the balanced POD method, without requiring adjoint simulations [117].

In this work, a numerical model is available from the UVLM formulation, therefore ERA and balanced POD can be applied. Since they are essentially different ways to achieve the same reduced-order model, one serves as a check to verify the implementation of the other. A summary of the algorithm is presented below [117]:

Step 1: Construct the generalized Hankel matrix. First, run impulse-response simulations of the full-order system for $(m_c + m_o)P + 2$ steps. The integers m_c and m_o, respectively, reflect how much effect is taken for considering controllability and observability, and P is the sampling period.

Next, arrange the snapshots of the outputs y in the following pattern:

$$\begin{aligned}(CB,\ \ CAB,\ \ CA^{P}B,\ \ CA^{P+1}B,\ \ \ldots,\ \ CA^{m_cP}B,\ \ CA^{m_cP+1}B,\ldots,\\ CA^{(m_c+m_o)P}B,\ \ CA^{(m_c+m_o)P+1}B)\end{aligned} \tag{3.14}$$

The terms CA^kB are called Markov parameters, which are $(m \times p)$ matrices corresponding to slices of the 3D impulse response matrix $(m \times p \times N)$ along the temporal dimension. In this work, the impulse response is calculated for $N = 200$ time steps, at 50 Hz (associated to the discrete time-step of 0.02 s from UVLM), and controllability and observability are equally taken into consideration (i.e. $m_c = m_o$). Now, construct

the generalized Hankel matrix $H \in \mathbb{R}^{m(m_o+1)\times p(m_c+1)}$:

$$H = \begin{bmatrix} CB & CA^P B & \cdots & CA^{m_c P} B \\ CA^P B & CA^{2P} B & \cdots & CA^{(m_c+1)P} B \\ \vdots & \vdots & \ddots & \vdots \\ CA^{m_o P} B & CA^{(m_o+1)P} B & \cdots & CA^{(m_c+m_o)P} B \end{bmatrix} \tag{3.15}$$

Step 2: Compute SVD of H (exactly as in balanced POD), to obtain:

$$H = U\Sigma V^* = \begin{bmatrix} U_1 & U_2 \end{bmatrix} \begin{bmatrix} \Sigma_1 & 0 \\ 0 & 0 \end{bmatrix} \begin{bmatrix} V_1^* \\ V_2^* \end{bmatrix} = U_1 \Sigma_1 V_1^* \tag{3.16}$$

where U_r and V_r denote the submatrices of U_1 and V_1 that include their first r columns, and Σ_r the first $r \times r$ diagonal block of Σ_1, with r chosen such that $r \leq \text{rank}\,(H)$.

Step 3: Obtain the reduced matrices:

$$A_r = \Sigma_r^{-\frac{1}{2}} U_r^* H' V_r \Sigma_r^{-\frac{1}{2}} \tag{3.17}$$

$$B_r = \text{the first } p \text{ columns of } \Sigma_r^{\frac{1}{2}} V_r^* \tag{3.18}$$

$$C_r = \text{the first } m \text{ rows of } U_r \Sigma_r^{\frac{1}{2}} \tag{3.19}$$

where H' represents a shifted Hankel matrix:

$$H' = \begin{bmatrix} CAB & CA^{P+1} B & \cdots & CA^{m_c P+1} B \\ \vdots & \vdots & \ddots & \vdots \\ CA^{m_o P+1} B & CA^{(m_o+1)P+1} B & \cdots & CA^{(m_c+m_o)P+1} B \end{bmatrix} \tag{3.20}$$

More details regarding this method are provided in [118] and [120, Section 10.5].

Step 4: Convert the system into modal canonical form:

Assume that the state matrix A_r has a complete set of linearly independent eigenvectors $v_1, v_2, \ldots, v_r$ and therefore form a non-singular matrix $V = \begin{bmatrix} v_1 & v_2 & \cdots & v_r \end{bmatrix}$, with corresponding eigenvalues $\lambda_1, \lambda_2, \ldots, \lambda_r$, which are not necessarily distinct. Applying the similarity transform $x_r(k) = Vz(k)$, the reduced-order system can be put into modal canonical form:

$$\begin{cases} z(k+1) = \Lambda z(k) + V^{-1} B_r u(k) \\ y(k) = C_r V z(k) \end{cases} \tag{3.21}$$

where $z(k)$ is the new state vector of modal coordinates and Λ is a diagonal matrix of eigenvalues defined as:

$$\Lambda = V^{-1} A_r V = \begin{bmatrix} \lambda_1 & & & \\ & \lambda_2 & & \\ & & \ddots & \\ & & & \lambda_r \end{bmatrix} \tag{3.22}$$

The diagonal matrix Λ contains the information of modal damping rates and damped natural frequencies. The matrix $V^{-1}B_r$ defines the initial modal amplitudes and the matrix $\Phi = \text{real}(C_r V)$ defines the mode shapes ϕ_i at the sensor points. It should be noted that the eigenvectors v_i of the state matrix depend on the coordinate system used, but the mode shapes ϕ_i are always the same.

3.5 Example: application to a Finite Element Model of a cantilever beam

This section presents the results obtained from the application of ERA to a model of a simple structure, namely a cantilever beam in bending. Since the analytical solution to this problem is known, it is possible to compare the true eigenvalues (natural frequencies) and eigenvectors (modes shapes) to the numerical results provided by ERA. Therefore, this example serves as a validation test for the model-order reduction routines developed in this work. Additionally, it provides valuable insight regarding the algorithm and familiarization with the limitations related to the modal identification process. After that, in Chapter 4, it will be possible to apply the same routines to aerodynamic models, for which analytical solutions are not available from theory.

3.5.1 State-space formulation

The FEM discretization for a Bernoulli-Euler beam is calculated according to [124, Chapter 6] and also [125, Chapter 10]. Using the typical cubic polynomials approach to describe the bending displacement along each beam element, the following element stiffness and mass matrices are obtained:

$$K_e = \frac{2EI}{L^3}\begin{bmatrix} 6 & 3L & -6 & 3L \\ 3L & 2L^2 & -3L & L^2 \\ -6 & -3L & 6 & -3L \\ 3L & L^2 & -3L & 2L^2 \end{bmatrix}, \quad M_e = \frac{\rho AL}{420}\begin{bmatrix} 156 & 22L & 54 & -13L \\ 22L & 4L^2 & 13L & -3L^2 \\ 54 & 13L & 156 & -22L \\ -13L & -3L^2 & -22L & 4L^2 \end{bmatrix} \tag{3.23}$$

where:

- L is the length of each element ($= L_b/N$, i.e. length of beam L_b divided by the number of elements N);
- EI is the flexural stiffness;
- ρ is the material density;
- A is the area of the cross-section (assumed rectangular);
- $m = \rho A$ is the mass per unit length.

The numerical values considered in this example for each variable are provided in Table 3.1.

Table 3.1: Geometric and material properties for the beam.

Property	Value
Beam length, L_b	1.00 m
Section width, b	0.02 m
Section thickness, h	0.001 m
Section area, $A = b \times h$	2×10^{-5} m
Area moment of inertia, $I = (\frac{1}{12})bh^3$	1.6667×10^{-12} m^4
Young's modulus (E)	71 GPa
Density, ρ	2700 kg/m^3
Mass per unit length, $m = \rho \times A$	0.054 kg/m

Each beam element has two vertices at its boundaries, also called *nodes* in the context of FEM. Each node has two degrees of freedom: vertical displacement and rotation. Since adjacent beam elements share two degrees of freedom, assembly of the element matrices (K_e, M_e) into system matrices (K, M) is carried out by adding the terms corresponding to the same degrees of freedom. In this example, a beam of unit length ($L = 1$ m) is considered, discretized with $N = 20$ elements, i.e. 21 nodes. Therefore, there are initially 42 DOF in the system. By application of boundary

conditions for a cantilever beam, the displacement and slope at the first node are zero. Hence the first and second rows and columns are removed from the system matrices, yielding 40×40 matrices for K and M.

The system of equations of motion associated to the beam is given by:

$$[M]\ddot{q} + [C]\dot{q} + [K]q = f \tag{3.24}$$

where:

- q is a $2n \times 1$ (40×1) column vector of nodal degrees of freedom for the system, $q = [w_1 \quad \theta_1 \quad w_2 \quad \theta_2 \quad \dots \quad w_{20} \quad \theta_{20}]^T$, where w_i and θ_i are, respectively, the bending displacement and slope at the i-th node. Note that $w_0 = \theta_0 = 0$, as per boundary conditions for a cantilever beam;
- f is $2n \times 1$ (40×1) column vector of inputs, with pointwise forces and moments applied at the nodes;
- $[C]$ is a proportional damping matrix introduced to represent viscous damping and numerically enforce stability of the system: $[C] = 10^{-4}([M] + [K])$;
- $\dot{q}$ and $\ddot{q}$ are, respectively, the first and second time derivatives of q.

By choosing $\{q, \dot{q}\}$ as state variables, the system of ordinary differential equations (ODE) above admits the following state-space realization:

$$\begin{cases} \dot{x} = Ax + Bu \\ y = Cx \end{cases} \tag{3.25}$$

The state matrix A is a 80×80 matrix and the input matrix B is an 80×40 matrix,

given by:

$$\begin{bmatrix} \dot{q} \\ \ddot{q} \end{bmatrix} = \begin{bmatrix} [0]_{2n} & [I]_{2n} \\ -M^{-1}K & -M^{-1}C \end{bmatrix} \begin{bmatrix} q \\ \dot{q} \end{bmatrix} + \begin{bmatrix} [0]_n \\ M^{-1} \end{bmatrix} u \tag{3.26}$$

where $[0]_{2n}$ denotes a $2n \times 2n$ null matrix and $[I]_{2n}$ is the identity matrix of order $2n = 40$. The input u is a column vector with $p = 40$ inputs, i.e. discrete forces and moments at each of the 20 nodes. Since we are particularly interested in mode shapes in terms of displacements, the output of the system is given by a column vector of $m = 20$ outputs. Therefore, the output matrix C is a 20×80 sparse matrix of zeros and ones, that selects only the displacements w_i from the state vector.

3.5.2 ERA results and analysis

The FEM model from Eq. (3.26) was used to generate simulated impulse response data at 200 Hz, which was provided to the ERA. The plot of the first 20 singular values of the Hankel matrix H is given in Fig. 3.1. Relatively small singular values can be safely discarded. Therefore, a number of 8 states were kept in the reduced-order model.

The modal identification results are presented in Fig. 3.2. The location of the eigenvalues in the s-plane is provided in Fig. 3.2(a). The eight eigenvalues obtained from the ERA approximate very closely the first eight eigenvalues of the system. The mode shapes obtained from ERA are shown in Fig. 3.2(b), normalized such that the maximum absolute deflection is equal to one. Since the eigenvalues appear as complex conjugate pairs, each pair is associated to one natural frequency ω_n and one mode shape ϕ. The natural frequency is simply the magnitude of each eigenvalue.

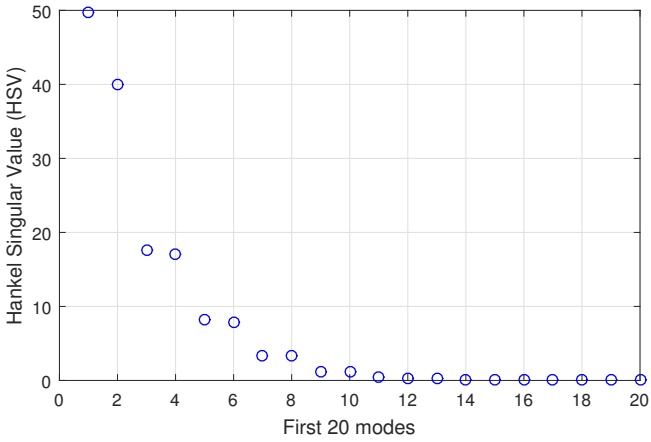

Figure 3.1: Hankel Singular Value magnitudes for model order selection.

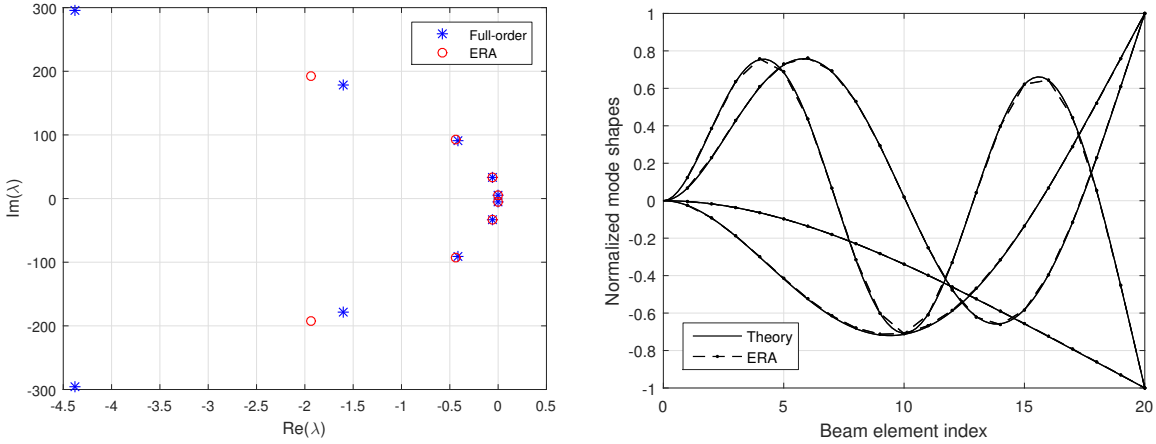

(a) Location of eigenvalues in the s-plane.

(b) Normalized mode shapes.

Figure 3.2: Modal identification results for a cantilever beam.

The analytical natural frequencies for a cantilever beam in bending are obtained from the solutions of the following equation [125]:

$$1 + \cos(\beta L_b)\cosh(\beta L_b) = 0 \tag{3.27}$$

where L_b is the beam length and each root β is related to a natural frequency ω_n by:

$$\omega_n = \beta^2\sqrt{\frac{EI}{m}} \tag{3.28}$$

A numerical comparison for the first 4 natural frequencies is given in Table 3.2.

The results from the full-order model (FEM) are essentially the same as those from theory, indicating that the spatial discretization used in the FEM (20 elements) is producing converged results for these modes. This is important when comparing the ERA to theory, because the numerical results provided by the ERA can only be as accurate as those from the FEM.

Table 3.2: Comparison of natural frequencies ω_n, in rad/s.

Mode	Theory	Full-order model (FEM)	Reduced-order model (ERA)	ERA error (%)
1	5.2048	5.2048	5.2051	0.004
2	32.618	32.618	32.691	0.222
3	91.332	91.333	92.954	1.776
4	178.97	178.99	191.97	7.261

The mode shapes obtained with ERA essentially coincide with the theoretical shapes (Fig. 3.2(b)). Specific details about the analytical equations describing the theoretical shapes can be obtained from [125, Chapter 8].

3.5.3 Impulse response sampling requirements

Up to this point, no explanation was given for the specific sampling rate used (200 Hz). The results from the ERA depend strongly on the simulated impulse response data used to obtain the Markov parameters, which form the generalized Hankel matrix (Eq. 3.15). More specifically, the ERA results depend not only on the sampling frequency (f_s), but also on the number of samples (N) used in the impulse response.

Intuitively, a smaller time step Δt is necessary to capture the dynamics of faster modes in the simulated data. At the same time, a sufficiently large number of samples is required to cover at least one cycle of the slowest mode, i.e. the first mode. The

period T_1 for the first mode is given by:

$$T_1 = \frac{2\pi}{\omega_{n,1}} = \frac{2\pi}{5.2048 \text{ rad/s}} = 1.2 \ s \tag{3.29}$$

Then, the number of samples N is defined in terms of T_1 and the sampling frequency f_s:

$$N = \frac{T_1}{\Delta t} = (T_1)\left(\frac{1}{\Delta t}\right) = 1.2\, f_s \tag{3.30}$$

If a high sampling rate is used, but not enough samples are collected, the identification of the lower order modes will be affected. On the other hand, if the sampling frequency is excessively high, the number of samples will be large, yielding very large Hankel matrices. Therefore, the important question is: what is the minimum sampling frequency f_s required to properly identify the first n modes? The following discussion will show the importance of this parameter in the modal identification results.

From the Nyquist-Shannon sampling theorem, a sampling rate of $f_s = 1/\Delta t$ allows unambiguous reconstruction of signals with frequencies up to the Nyquist frequency $f_N = 1/(2\Delta t)$. For illustration purposes, consider the Bode diagram (magnitude only) of the SISO model whose input is the vertical force at the free-end of the beam, and the output is the bending displacement at the tip (Fig. 3.3). This model is simply a selection of the appropriate input/output pair from the 20×40 MIMO system (Eq. 3.26). Although the FEM model for the beam is MIMO, the resonance peaks occur at the same natural frequencies for any combination of input and output. Therefore, the natural frequencies for the beam correspond to the resonance peaks in this plot.

If we are interested in the first 4 modes, we must be able to reconstruct frequencies

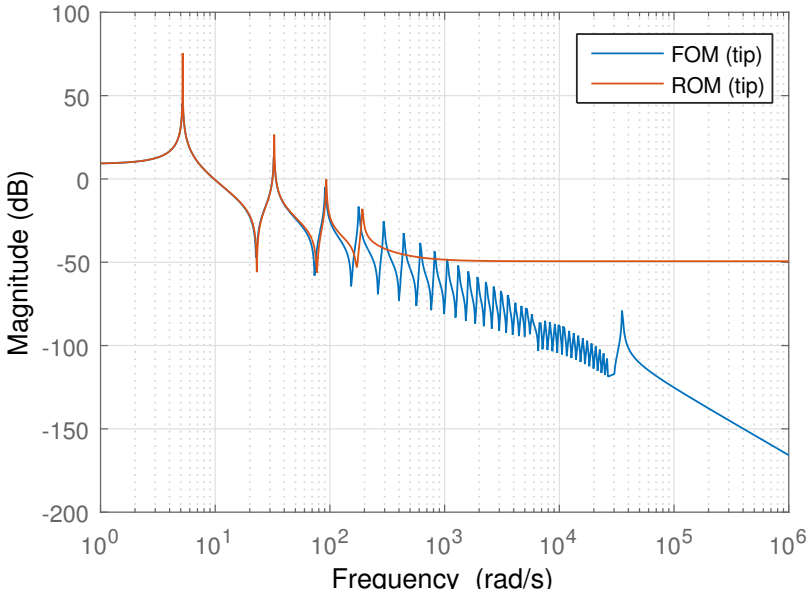

Figure 3.3: Frequency response between displacement (output) and force (input), both at tip.

up to 179 rad/s = 28.5 Hz (fourth peak in Fig. 3.3). Hence, one might suggest a minimum sampling rate of $f_s = 2 \times 179 = 358$ rad/s = 57 Hz for the simulated data. However, this frequency does not satisfy the sampling theorem, because the unit impulse input will excite all natural frequencies of the system (i.e. all 40 modes from the full-order model). Therefore, there will exist frequency content above 179 rad/s in the impulse response. When the simulation data is sampled at this lower frequency (358 rad/s), the higher order natural frequencies become aliased, generating additional frequency components that do not correspond to actual system dynamics. According to [121, Chapter 2], if the ERA is applied to aliased data, some aliased frequencies might be identified in lieu of the true modes, depending on the relative magnitudes of peaks between aliased modes and true modes in the Power Spectrum Density (PSD).

In order to reduce or eliminate aliasing, one can:

1) apply a low-pass anti-aliasing filter to the system output before the sampling takes place; or

2) choose a significantly higher Nyquist frequency (oversampling).

The cutoff frequency for the anti-aliasing filter is ideally chosen as the Nyquist frequency, but all filters will always cause some distortion close to the cutoff frequency. In order to avoid distortion in the bandwidth of interest, a higher Nyquist frequency (f_N) is selected. A higher f_N also simplifies the filter design, because it reduces the requirements for a sharp transition band.

The second approach consists in sampling the signal at a much higher rate, without filtering. A Nyquist frequency f_N at least 10 times greater than the highest frequency of interest is suggested in [121]. This procedure preserves a wider range of frequencies and pushes the aliasing boundary to higher order modes, which are naturally more attenuated. Aliased frequencies will still exist in the frequency response, but they are now related to high order modes, thus reducing the magnitude of these "non-physical" peaks in the frequency response. As a net result, the ERA is able to select the true peaks (actual modes) up to a higher bandwidth. For experimental data, oversampling also improves the signal-to-noise ratio.

For the present example, we are interested in 4 modes, so the recommended Nyquist frequency for oversampling is $f_N = 10 \times 28.5 = 285\ Hz$, with the sampling rate $f_s = 2f_N = 570$ Hz. The problem with this approach is that such a high frequency will generate excessively large matrices and require more computational effort. The recommended oversampling factor of 10 is actually indicated for exper-

imental data. For simulation data without added noise, such as in the case of this work, it was observed that a lower factor around 3 to 5 times the highest frequency of interest suffices. This is more clearly observed in a so-called stabilization diagram, a plot showing how the identified eigenvalues change as a function of the number of modes kept in the reduced model.

In Fig. 3.4, the ERA results are compared to the first 10 true eigenvalues, which are known from the full-order model (FOM). The ERA is applied to impulse responses generated with different sampling rates, namely 50, 100, 200 and 400 Hz.

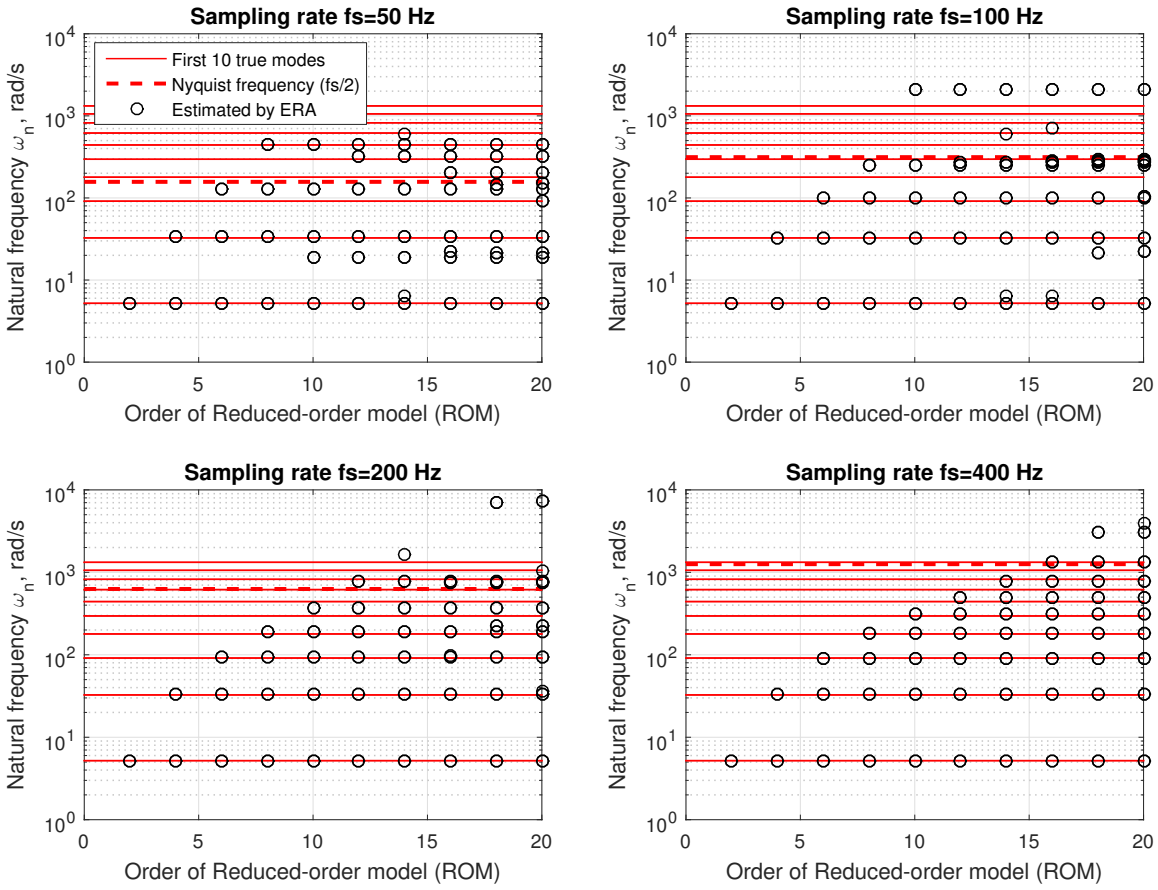

Figure 3.4: Stabilization diagrams for different sampling rates.

When 2 states are kept in the reduced-order model (ROM), the estimated A matrix

is 2×2 and the eigenvalues provided by the ERA should be one complex conjugate pair associated to the first mode. The absolute value of the eigenvalues is the natural frequency for the first mode. When 4 states are kept, the two pairs of eigenvalues should provide the natural frequencies for the first 2 modes. This initial tendency is observed in all plots (i.e. for all sampling rates used). However, for 50 Hz, the ERA results quickly lose accuracy for 6 or more states kept in the ROM. Note that the natural frequency for the 3$^{\text{rd}}$ mode is below the Nyquist frequency associated to 50 Hz, and there is no noise in the data. This loss of accuracy is purely related to the presence of aliased frequencies in the simulation data, since no anti-aliasing filter was used. It should also be noted that, if additional states are kept in the ROM (e.g. for 10 or more states), these aliased frequencies are eventually captured. This is denoted by the data points between the first 2 horizontal lines (first 2 modes) in the top left plot of Fig. 3.4 ($f_s = 50$ Hz). These points are clearly associated to frequencies that do not exist in the original system.

For 100 Hz, the ERA is accurate up to the 3$^{\text{rd}}$ mode (6 states kept in the ROM). For 200 Hz, the accuracy is acceptable up to 4$^{\text{th}}$ (8 states in the ROM). Increasing the sampling rate to 400 Hz, the results are accurate up to 5$^{\text{th}}$ mode (10 states kept in the ROM). It should be noted that the presence of aliased frequencies in the ERA results (i.e. data points in between actual modes) is effectively eliminated at 400 Hz. The aliased frequencies still exist in the range between zero and the Nyquist frequency, but they are now related to higher order modes, hence they are attenuated as compared to the first 10 actual modes of interest.

Table 3.3 compares different sampling frequencies ($f_s = 50$ Hz, 100 Hz, 200 Hz,

400 Hz), Nyquist frequency ($f_N = f_s/2$) and the maximum natural frequency accurately estimated. From these results, an estimate is obtained for the oversampling factor required to accurately identify the first few modes, ranging from 3.5 to 4.8. For example, an oversampling factor of 4.2 would provide accurate results for the first 5 modes. Therefore, the oversampling factor of 10 suggested by [121] was too conservative for this example, where simulation data without added noise are used. In experimental applications, anti-aliasing filters are always employed, and a higher sampling rate improves the signal-to-noise ratio of the measurements. However, since the natural frequencies are unknown, it is still necessary to perform an analysis (such as a stabilization diagram) to separate the true modes from aliased frequencies and noise modes. For a sufficiently high sampling rate and adequate anti-aliasing filtering, the true structural modes stabilize at very specific frequencies, just like in Fig. 3.4, whereas aliased modes and noise modes oscillate and might eventually disappear.

Table 3.3: Estimated oversampling factor necessary for the first 5 modes.

Sampling frequency (f_s), Hz	Nyquist frequency ($f_N = f_s/2$), rad/s	Highest mode accurately estimated, ω_n in rad/s	Estimated oversampling factor (f_N/ω_n)
50	157.1	2^{nd} mode, $\omega_n = 32.6$	4.8
100	314.2	3^{rd} mode, $\omega_n = 91.3$	3.4
200	628.3	4^{th} mode, $\omega_n = 179$	3.5
400	1257	5^{th} mode, $\omega_n = 296$	4.2

The inaccuracies in eigenvalues are naturally reflected in the estimated mode shapes, which will deviate from the theoretical shapes. However, the error in mode shapes was much less sensitive to low sampling rates than the error in eigenvalues. In other words, even when considerable errors exist for the identified natural frequency

(e.g. 50% or more), the associated mode shape is still close to the theoretical shapes. If not enough samples from the impulse response are used, the complex pair of eigenvalues for the first mode degenerates into 2 real eigenvalues (with one of them being possibly unstable). Even in this case, it was observed that the associated mode shape would still be close to the theoretical shape.

In the results from ERA presented in Fig. 3.2, a sample frequency of $f_s = 200$ Hz and number of samples N=200 were used. It was possible to obtain the 4^{th} natural frequency with a 7.3% error. Increasing f_s to 400 Hz and N to 400 yielded a 1.7% error, but required much more computational time for a relatively small improvement.

3.6 Chapter summary

The Eigensystem Realization Algorithm (ERA) can be used as a model order reduction method, but is also suitable for modal identification. The ERA provides approximately balanced realizations, without requiring computation of Gramian matrices (as balanced truncation requires). The results from ERA are theoretically equivalent to those from balanced POD, but ERA is more computationally efficient because it does not require simulations of an adjoint system.

Although the procedure for the ERA is computationally simple and relatively straightforward, the final results depend on proper choice of some parameters, namely the sampling frequency f_s, the number of samples in the impulse response, and the number of modes kept in the reduced-order model. These parameters depend on the modal behavior of the system, which is usually unknown at first. Therefore, some

iterative procedure or fine tuning is required.

Aliasing distortions affect the signals at frequencies below the Nyquist limit even in noise-free data. Therefore, if no anti-aliasing filter is employed in the simulation, the choice of sampling frequency involves a tradeoff between the amount of aliasing tolerated and computational cost.

At this point, it is clear that the ERA results depend on the characteristics of the system and the parameters selected by the operator (sampling rate, number of samples). The methodology developed for the cantilever beam in this section will be useful when dealing with the modal identification of the aerodynamic model, which is the subject of the next chapter.

Chapter 4

Modal identification of aerodynamic systems

The concept of decomposing the behavior of an aerodynamic system into eigenmodes has been investigated for the last three decades, mainly motivated by the benefits that modal decomposition provided to other fields (e.g. structural dynamics). The early works in this field followed the exact same steps of structural modal decomposition.

In [126], a linearized version of the unsteady vortex lattice method was derived and applied to airfoils and 3D wings. The state-space discrete-time system was transformed into modal canonical form and truncated, by keeping only the slowest modes in the reduced-order model. To account for the effect of the truncated modes in the steady-state response, a static correction term was added, which is common practice in structural systems. To ensure accurate results, the number of states (model order) for the flow around a wing was reduced from 480 to no less than 40. This reduction enabled substantial savings in computational effort, but 40 states is still relatively

high for controls applications. These results pointed to some of the difficulties in applying modal decomposition to aerodynamic systems (also observed in the present work):

- The eigenvalues are closely spaced in the frequency range (as opposed to well-spaced eigenvalues in structural systems), which makes it difficult to select the relevant modes based on temporal bandwidth alone.

- Applying truncation to the modal canonical realization does not work well for aerodynamic systems. While the slowest modes are precisely the most relevant ones in structural systems, this is not necessarily true for unsteady flows. This fact motivated the use of balanced realizations, which allow more efficient selection of relevant modes, as explained in Chapter 3.

Despite these difficulties, model order reduction based on modal decomposition can still be applied, assuming the model can be linearized. A review on the types of flow models and eigenanalysis results is given in [127, 128]. More efficient tools for model order reduction of a vortex lattice model were tested in [129, 130], including POD, balanced truncation, and ERA, which were presented in Chapter 3. These methods became the standard tools used in model order reduction for aerodynamic systems, while each one has its own advantages. A recent comparison between these methods was presented in [131].

The previous works were mainly interested in obtaining a reduced-order model to reduce the computational effort required to analyze an unsteady flow model. A small subset of these works presented the modal parameters for the aerodynamic model,

but only in terms of root locus plots of the eigenvalues. No information is provided about the natural modal shapes associated with the dominant modes. In the present work, not only the eigenvalues and aerodynamic mode shapes are presented, but also a physical interpretation is provided for each aerodynamic mode.

In this chapter, the main results from modal identification of the wing are presented in terms of eigenvalues and mode shapes obtained from both aerodynamic models, namely ULLT and UVLM. Additionally, time-domain simulations for the spanwise lift are provided for two situations: when the initial lift distribution applied is aligned to the system mode shapes, and when it is not. These results will clearly show the modal behavior of the system. Finally, mode shapes for different wing planforms (tapered and swept) are presented.

4.1 Modal identification from UVLM

Consider the baseline configuration with 8 trailing edge flaps uniformly distributed along the span. Recall from Chapter 2 that the wing is discretized using with $n_y = 64$ spanwise panels and $n_x = 8$ chordwise panels. Using the Unsteady Vortex Lattice Method (UVLM) with the assumption of frozen wake geometry, a discrete-time, state-space model is obtained. There are 8 inputs associated with the flaps, and 64 outputs where the local lift coefficient is computed. The model, however, is high order due to the 2048 states necessary to capture the effects of unsteady aerodynamics. When the ERA is applied to reduce the model order, it is necessary to define the truncation level, i.e. how many states (or modes) will be kept in the reduced-order model. From

the plot of Hankel Singular Values (HSV), shown in Fig. 4.1, it can be seen that the first 16 HSV are relatively larger than the others. This suggests that 16 modes are able to accurately represent the original system. Thus, let us select 16 modes, and then proceed with the eigenvalue analysis of the resulting reduced-order system.

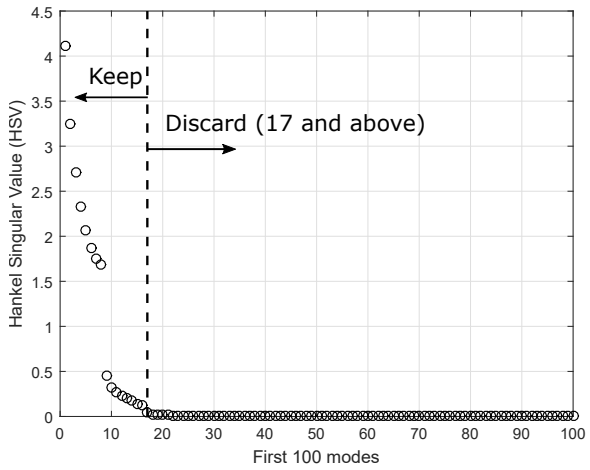

Figure 4.1: Hankel Singular Values (HSV) of the first 100 modes, for a wing with 8 flaps.

4.1.1 Eigenvalue analysis

In Fig. 4.2, the 2048 eigenvalues from the full-order model are shown against the 16 eigenvalues identified using the ERA. In Fig. 4.2(a), the eigenvalues of the discrete-time system are shown in the z-domain. The models can be converted to continuous-time by applying a Tustin transformation, yielding the root locus in the s-domain shown in Fig. 4.2(b). The z-domain eigenvalues lie inside the unit circle, whereas the s-domain eigenvalues lie in the left half s-plane, indicating inherent stability for both models (full-order and reduced-order). These plots are similar to those provided by Hall (1994) in [126], which is most likely the first report of eigenvalues of unsteady

flow around a three-dimensional wing using a vortex lattice model.

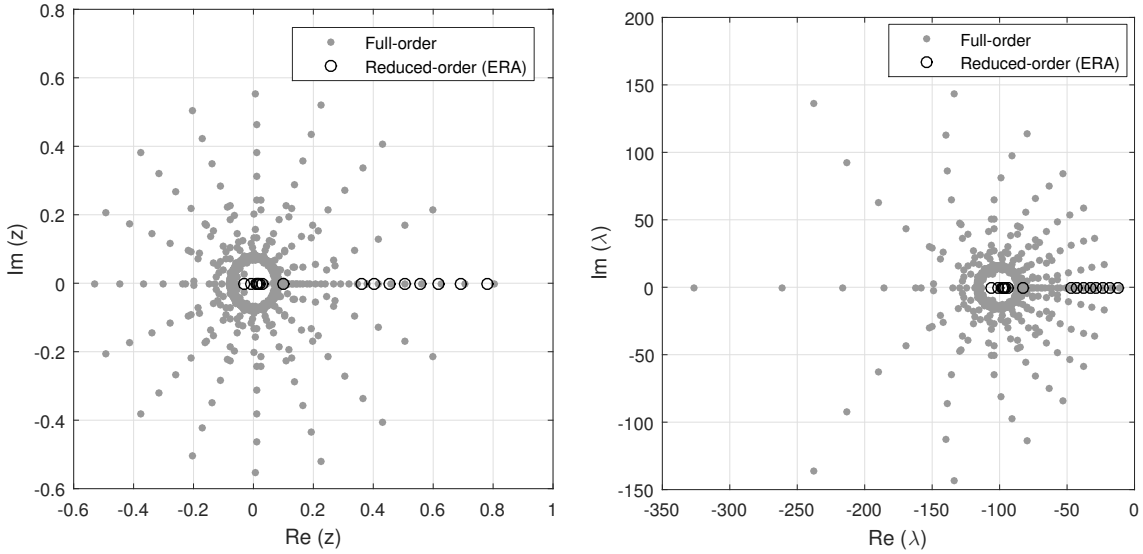

(a) z-domain (b) s-domain

Figure 4.2: Eigenvalues of vortex lattice model of unsteady flow around a 3D wing featuring 8 uniform trailing edge flaps, with 16 modes kept in the reduced-order model.

The most relevant eigenvalues selected by the ERA form a dominant branch along the real axis. In the s-domain, these eigenvalues are real and negative, i.e. the dominant modes exhibit non-oscillatory behavior (exponential decay), which is typical from indicial functions describing lift changes in unsteady aerodynamics. The eigenvalues for the full-order model exhibit a radial pattern. The number of branches is associated with the number of rows of vortex rings used to spatially discretize the wake in the streamwise direction. As more modes are included in the reduced-order model, the ERA automatically selects eigenvalues from the outer regions, in addition to those in the dominant branch. For illustration purposes, the root loci for 128 and

256 modes are shown in Fig. 4.3. From these plots, it is clear that the poles located in the outer region are more relevant than those in the inner region of the plot.

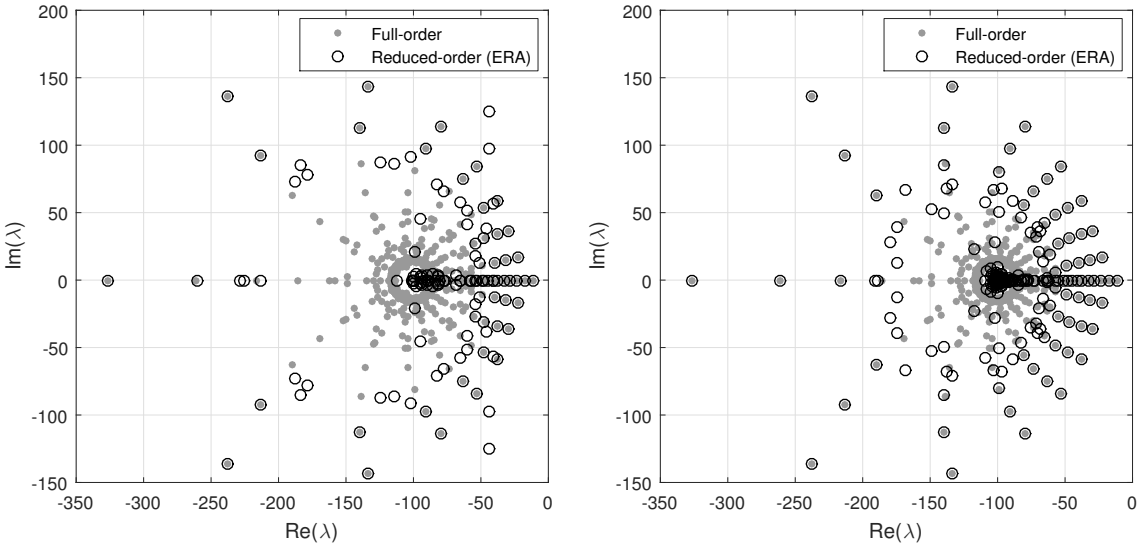

(a) 128 modes kept

(b) 256 modes kept

Figure 4.3: Eigenvalues of vortex lattice model of unsteady flow around a 3D wing featuring 8 uniform trailing edge flaps, s-domain only.

It should be noted that the modes are not chosen by magnitude of eigenvalues, as is common practice with structural systems. In the simpler modal truncation approach, the slowest modes are kept, whereas the fastest (i.e. larger eigenvalue magnitude, in absolute value) are truncated. In the present case, we are dealing with approximately balanced truncations, as provided by ERA. Therefore, the relevant modes are selected by the magnitude of Hankel Singular Values (HSV), i.e. these modes are the ones that exhibit better observability and controllability simultaneously. This explains the eigenvalue selection pattern observed previously.

Finally, it should be observed that the center of the array in the z-plane ($z = 0$)

is mapped to $s = -100$ in the s-plane. This is due to the bilinear transform (Tustin's method) used to convert the model from discrete-time to continuous-time, and the time step used to generate the full-order model ($T = 0.02$ s). The mapping $z = e^{sT}$ can be inverted to yield a first order approximation:

$$s = \frac{1}{T}\log z \approx \frac{2}{T}\frac{(z-1)}{(z+1)} \tag{4.1}$$

Therefore, for $T = 0.02$ s and $z = 0$, then $s = -100$. The time step also defines the maximum temporal frequency that can be resolved. In this case, the Nyquist frequency is $(1/T)/2 = 25$ Hz= 157.1 rad/s.

4.1.2 Aerodynamic mode shape analysis

The number of modes selected previously (16 modes) was based on the HSV plot from Fig. 4.1. The mode shapes associated with the first 12 modes are presented in Fig. 4.4. These shapes represent the spanwise distribution of local lift coefficient associated with each mode. The amplitudes were normalized to the range $[-1, +1]$, whereas the spanwise coordinate y was normalized as $\bar{y} = y/(b/2) = 2y/b$, yielding $\bar{y} = -1$ for the left wingtip and $\bar{y} = 1$ for the right wingtip.

Immediately, a serious problem with shapes 9 to 12 can be observed. These shapes exhibit unnatural breaks and do not even fulfill the boundary conditions, such that the lift distribution must reach zero at the wingtips. This condition is required to avoid singularities represented by infinite downwash velocities induced at these points. Clearly, these shapes are simply numerical results from ERA that do not correspond to actual mode shapes.

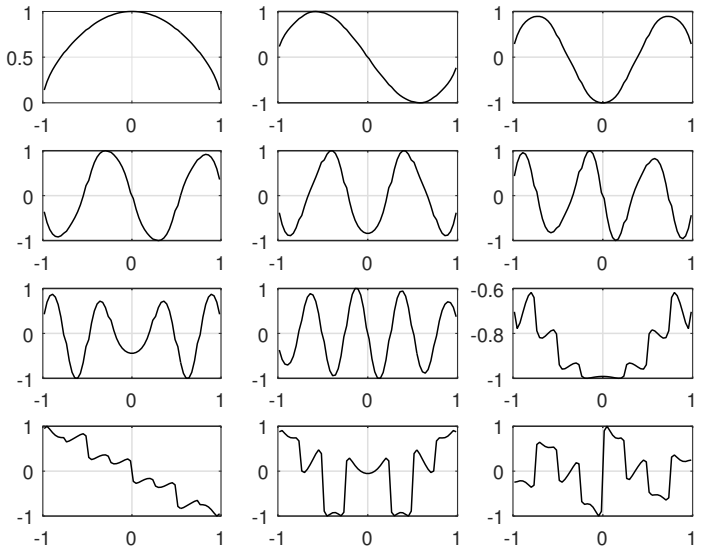

Figure 4.4: Normalized mode shapes for the first 12 modes, ordered from left to right, top to bottom (wing with 8 flaps).

A plausible explanation for this effect lies in the fact that the system is being excited with spatially distributed actuators (flaps). Following a terminology from the field of smart structures, a distributed actuator is said to have a spatial aperture. In the ERA, the data is generated by applying impulse inputs to each input channel. Since each of the 8 flaps occupies 1/8=12.5% of the wingspan, one should not expect to excite high spatial frequencies. Specifically with this set of actuators, the minimum wavelength that can be excited is about 25% of the wingspan, which corresponds to 4 cycles per span (i.e. the 8-th mode shape). Consequently, we should not rely on the eigenvalues associated with modes 9 through 16. In fact, a closer inspection on the root locus of the 16 eigenvalues in the reduced-order model (Fig. 4.2) shows that the first 8 modes are somewhat isolated from the other 8 modes.

One way to avoid this problem is to simply truncate at the first 8 modes, if the reduced model still provides a reasonable accuracy level. If higher-order modes

(beyond 8) need to be properly identified, then it is necessary to change the inputs of the system. It should be noted that, for any system in general, changing the inputs (or the B matrix) does not modify the modal behavior, i.e. the A matrix is unchanged. However, it does change the controllability properties of each mode. Intuitively, flaps with smaller apertures would allow us to excite higher spatial frequencies. Therefore, suppose the number of flaps is increased from 8 to 16. The Hankel Singular Values (HSV) for the first 100 modes are then shown in Fig. 4.5, which suggests that 32 modes should be kept in the reduced-order model.

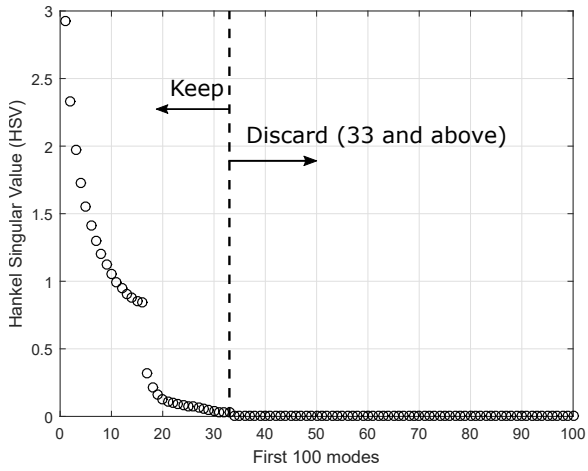

Figure 4.5: Hankel Singular Values (HSV) of the first 100 modes, for a wing with 16 flaps.

Because now there are 16 flaps uniformly distributed across the span, it is possible to properly identify the first 16 modes. In the plots of eigenvalues in Fig. 4.6, the same branch of dominant eigenvalues can be observed with the first 16 modes, whereas the last 16 modes (not identifiable) form a cluster near $z = 0$ (or $s = -100$).

The normalized mode shapes obtained for the first 20 modes are plotted in Fig. 4.7. As expected, now the first 16 modes seen acceptable, since they lie well within the

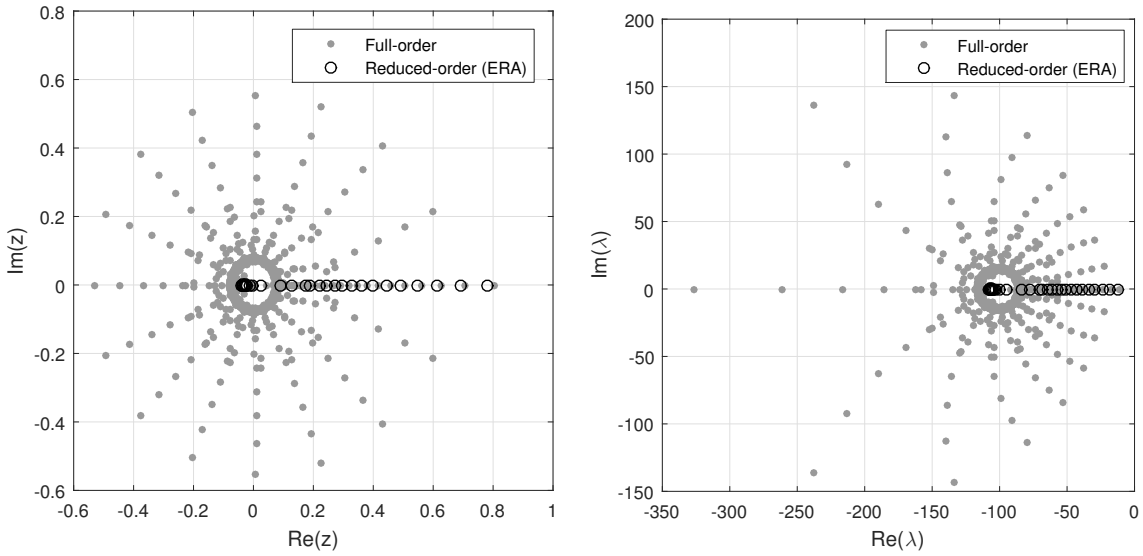

(a) z-domain (b) s-domain

Figure 4.6: Eigenvalues of vortex lattice model of unsteady flow around a 3D wing featuring 16 uniform trailing edge flaps, with 32 modes kept in the reduced-order model.

identification range. The lower order mode shapes exhibit zero lift at the wingtips without abrupt breaks. However, as we move to higher orders, such as modes 13 through 16, the identified shapes deteriorate. For mode 17 and beyond, the shapes become unreliable again.

The previous observations show that for N spanwise flaps, one can expect to properly identify only the first N modes. The size of the flaps could be reduced further, until eventually reaching the spanwise discretization limit. Since the wing is discretized with $n_y = 64$ panels in the spanwise direction, this is the maximum number of flaps that can be represented.

Making a comparison with a Finite Element Model for a simply supported beam,

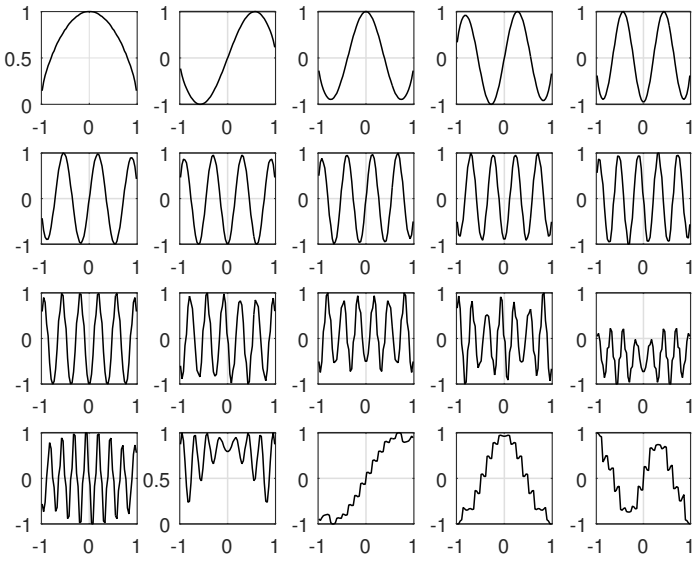

Figure 4.7: Normalized mode shapes for the first 20 modes, ordered from left to right, top to bottom (wing with 16 flaps).

excitation loads can be applied at the boundaries of each element (i.e. at the nodes), such as pointwise forces and moments. Therefore, the maximum mode order identifiable is only limited by the beam spatial discretization itself. For the aerodynamic case (3D wing), the equivalent situation consists in applying individual flap inputs to each of the spanwise panels, in order to excite the lift distribution in a pointwise way. Assuming 64 uniformly distributed spanwise panels, one should expect to identify up to 64 modes (assumed similar to sine functions). In order to represent this situation, a new aerodynamic model was synthesized, now using 64 spanwise flaps as inputs. For comparison purposes with the previous figure, only the first 20 modes are shown in Fig. 4.8.

All modes shown are very smooth, without breaks and exhibit zero lift at the wingtips. However, it can be seen that for modes 16-20 some peaks are not well

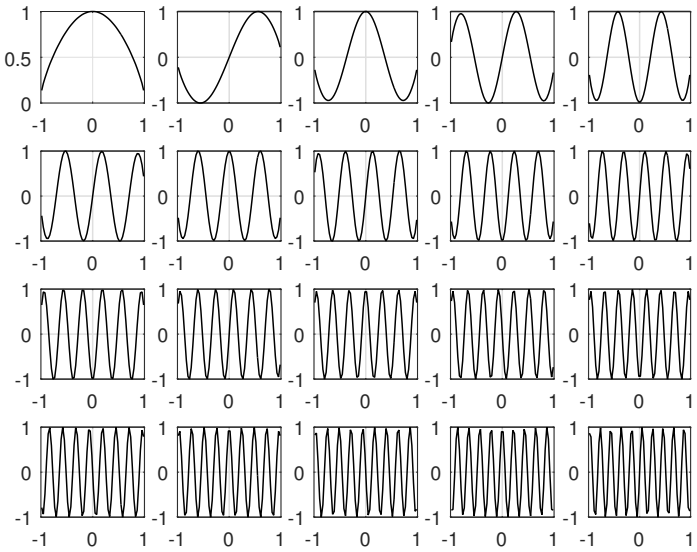

Figure 4.8: Normalized mode shapes for the first 20 modes, ordered from left to right, top to bottom (wing with 64 flaps).

captured due to spatial discretization limitations, since the lift profile is sampled at 64 points along the wingspan. Also, for the purposes of the following discussion, assume that the mode shapes can be approximated by sine functions. Then, using the Nyquist-Shannon sampling theorem, the maximum spatial frequency that can be properly represented is 32 cycles/span, i.e. 64 modes. As the mode order increases towards this limit, the identified shapes become distorted by the peaks and valleys eventually missed due to low spatial discretization. For illustration purposes, the modes 33 through 64 are shown in Fig. 4.9. Despite the distortions, no spatial aliasing occurs.

4.1.3 Final mode shapes and eigenvalues from UVLM

After applying individual inputs to each of the 64 panels along the wingspan, it was possible to obtain reliable mode shapes and the associated eigenvalues. The first 4

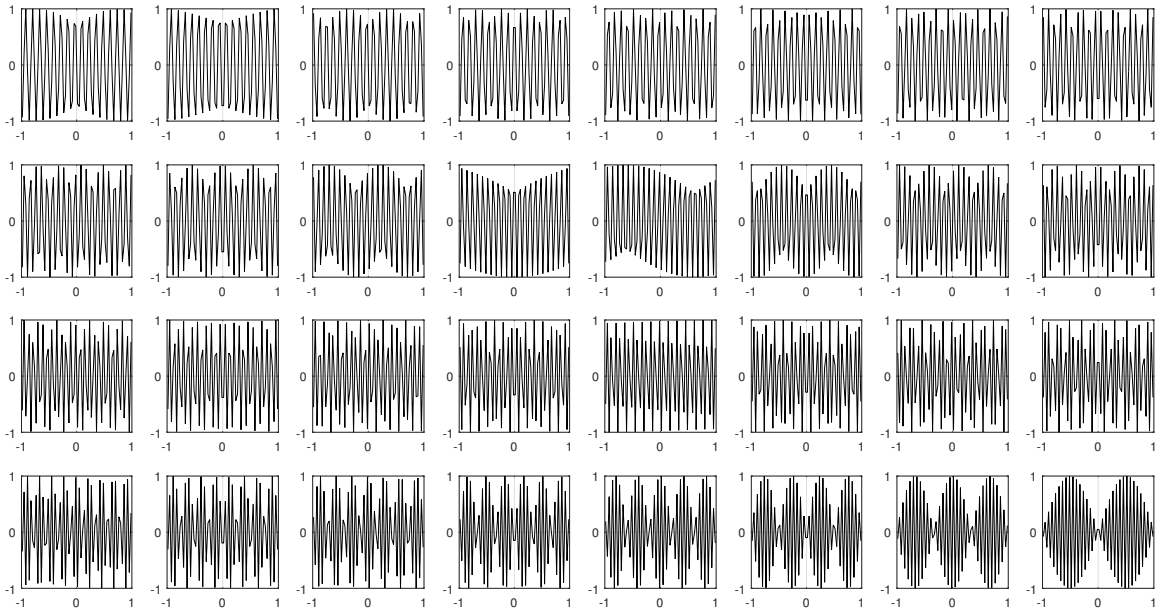

Figure 4.9: Normalized mode shapes for the modes 33 through 64, ordered from left to right, top to bottom (wing with 64 flap inputs along the span).

normalized aerodynamic mode shapes are presented in Fig. 4.10 in terms of local lift coefficient along the span. Interestingly, the mode shapes are very smooth and resemble sine functions, but they are not sinusoidals, which are shown for comparison in the same figure. Moreover, it can be mathematically verified that these aerodynamic mode shapes are not orthogonal to each other.

This is in stark contrast with structural mode shapes. Most structural systems with simple boundary conditions are self-adjoint. As a consequence, the mode shapes are not only orthogonal to each other, but also form a complete set in the sense of Parseval [1]. In practical terms, any piecewise smooth function representing the structural deformation can be properly described by a linear superposition of structural mode shapes. As the number of modes included in the formulation is increased, the error between the original function and the series necessarily goes to zero.

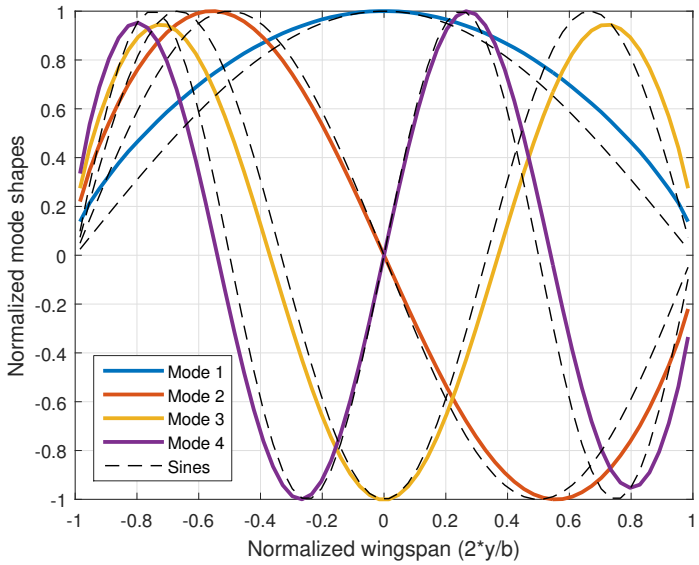

Figure 4.10: Normalized aerodynamic mode shapes for the first 4 modes.

With respect to eigenvalues, structural systems usually exhibit natural frequencies sparsely distributed along the spectrum of frequencies (see Tab. 3.2), whereas the aerodynamic eigenvalues observed above are much closer to each other. The root locus of the first 16 modes, associated with the smooth shapes, is shown in Fig. 4.11, whereas the numerical values are given in Table 4.1.

Table 4.1: Eigenvalues for the first 16 modes identified by ERA.

Modes 1-4	Modes 5-8	Modes 9-12	Modes 13-16
-18.3190	-46.6904	-67.1108	-82.2805
-26.0646	-52.4386	-71.3124	-85.4669
-33.5223	-57.7156	-75.2232	-88.4462
-40.4165	-62.5935	-78.8733	-91.2356

4.2 Limits in identifiability

From the previous section it was is clear that the modal identification process has some limitations, which are inherent to the spatial-temporal discretization used to

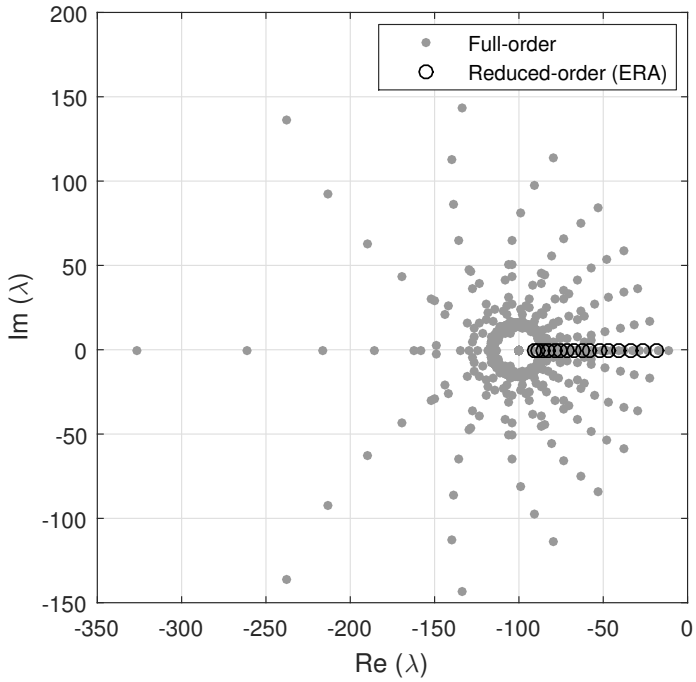

Figure 4.11: Final root locus of 16 modes identified by ERA.

represent the aerodynamic model. At this point, it is helpful to summarize such limitations:

- Spatial aperture of control input: using distributed actuators with finite aperture, it is only possible to provide excitation up to some spatial frequency. For N uniformly distributed flaps, up to N modes can be estimated.

- Temporal discretization limit (Nyquist frequency): the discrete-time system used in this work has a time step of 20 milliseconds. Therefore, the Nyquist frequency is 25 Hz = 157.1 rad/s, and the modes kept in the reduced-order model must have temporal frequencies preferably well below this limit. Note that the eigenvalues for the first 16 modes are below this limit, as shown in Fig. 4.11 and Table 4.1.

- Spatial discretization limit: for $n_y = 64$ spanwise panels, one can theoretically reproduce up to 32 cycles/span (i.e. 64 modes). This is the equivalent of the Sampling Theorem in the spatial domain.

In this work, the most critical limitation is the spatial aperture of the actuators, which distorted the higher order modes, as shown in Fig. 4.4 (for 8 flaps along the span) and in Fig. 4.7 (for 16 flaps). To circumvent this limitation, the aperture of the actuator was reduced. After obtaining the reduced-order model (with the required number of modes), the system inputs can be manipulated in terms of the B matrix. For example, suppose one requires a reduced-order model with only 8 modes included. For modal identification purposes, at least 16 uniform flaps are necessary to properly excite up to the 8-th mode. After applying ERA, the reduced-order model has the following dimensions: A matrix [8×8], B matrix [8×16], C matrix [64×8]. However, 8 flaps would suffice for control requirements, as will be detailed in Chapter 5. Therefore, the adjacent pairs of columns of the B matrix can be added (or merged), so that the final model has only 8 uniform flaps as inputs.

The number of actuators along the span must be increased for modal identification, which reduces the actuator spatial aperture and enables excitation of higher order modes. After obtaining reliable shapes, the actuators can be merged into groups by combining the corresponding columns in the B matrix, which reduces the number of actuators to the amount required for shape control. This numerical procedure ensures that the modal properties of the reduced-order model were properly identified up to the required spatial bandwidth, and closely represent those of the full-order model,

while keeping the minimum number of flaps for controls.

It should be observed that changing the inputs of the system (by adding or removing flaps, or changing their spatial aperture) does not change the modal behavior of the system (eigenvalues and mode shapes). However, the system inputs are intrinsically related to the quality of the modal identification results. Moreover, even though the B matrix does not change the modal parameters of the system, it does affect the controllability of each mode. Different flap configurations yield different degrees of controllability over the modes. In Chapter 5, this concept is used to obtain an optimal set of flap apertures that maximizes a given controllability metric.

Note that two different flap configurations are used in this work, for different purposes. For best modal identification results, it was necessary to employ 64 flaps uniformly distributed along the span, which represents the maximum density allowed by the spatial discretization used. For controls purposes, only 8 flaps are required to control 8 modes. As will be seen in Chapter 5, the 8 modes of interest are fully controllable with any set of 8 flaps. However, it will be shown in section 5.3.1 that the flap dimensions can be designed to maximize their effect on the first 8 modes, in the sense of singular values of the MIMO system.

4.3 Modal identification from ULLT

In this section, the modal identification results from ULLT are compared to those from UVLM, which were presented in section 4.1. Since the two aerodynamic models were obtained independently, this comparison can be useful to validate the aerodynamic

eigenvalues and mode shapes presented in this work.

The same limitations in modal identification discussed in section 4.2 for the UVLM were also observed for the ULLT. The final mode shapes identified depend strongly on the spatial aperture of the excitation provided. By reducing the size of the actuators down to the discretization limit, very smooth mode shapes were obtained. The spanwise discretization used in the ULLT was $N = 64$ stations, which is the same used in the UVLM. A comparison between mode shapes from ULLT and UVLM is provided in Fig. 4.12. Only slight differences exist near the wingtips, which can be explained by the fact the Lifting-Line methods tend to overpredict lift near the wingtips, as compared to Vortex Lattice methods. Although obtained from two completely independent models, the shapes are remarkably similar. This fact supports the reliability of the results and indicates that such shapes can indeed be used to represent the spatial behavior of the unsteady flow around a 3D wing.

The root locus plot of the eigenvalues obtained from ULLT is shown in Fig. 4.13. As discussed in Chapter 2, there are 2 auxiliary states for each station, required to model Wagner's functions in the state-space format. These states are associated with 2 bundles of 64 poles located at $\lambda = -3.71$ and $\lambda = -22.2$ in the root locus. Another set of 64 poles can be associated with each Fourier coefficient in the unsteady Lifting-Line formulation, starting at $\lambda = -43.44$ towards negative infinity. Finally, one integrator is required for each station to convert flap rate into flap deflection, which corresponds to a bundle of 64 poles at the origin. Except for these poles at $\lambda = 0$, the eigenvalues of the full-order model are negative real, i.e. lie along the negative real-axis, just like the dominant branch in the UVLM model.

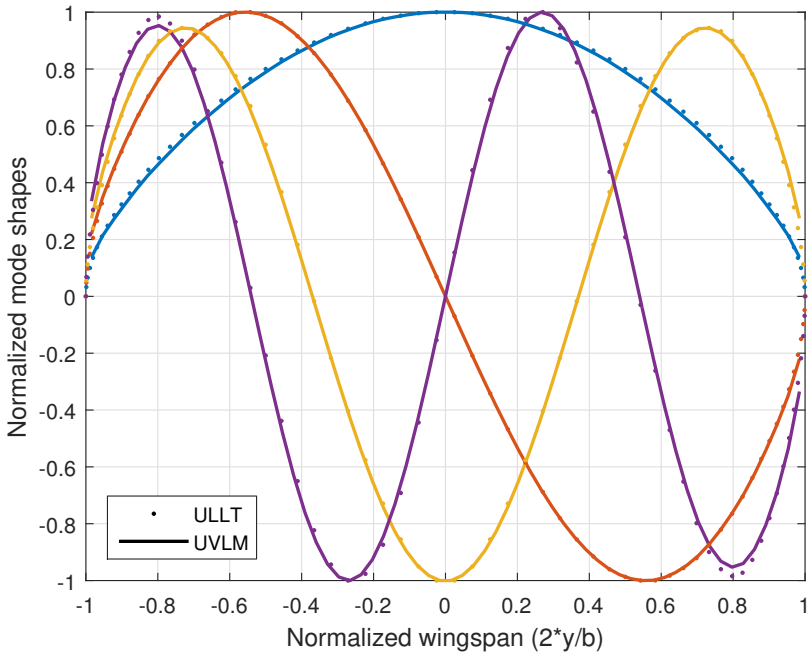

Figure 4.12: Comparison of mode shapes obtained from UVLM and ULLT, for the first 4 modes.

However, the poles at the origin add more complexity to the analysis. Because the full-order plant is only marginally stable, some of the tools typically employed in model order reduction cannot be used. For example, the computation of exact balanced realizations (e.g. see Matlab® function `balreal.m`) is restricted to fully stable plants. On the other hand, it is still possible to apply ERA to the plant. As shown in Fig. 4.13, the most relevant eigenvalues selected by ERA are precisely those at origin. After those are included, the selection pattern continues from right to left. Recall from Chapter 2 that these integrators are present in the formulation because the input to the ULLT model is flap rate. As shown in Eq. (2.49), the effects of flap rate are required to model a portion of circulatory lift due to quasi-steady flap inputs (δ_{qs}).

Additionally, the presence of repeated eigenvalues makes it difficult, if not impossible, to obtain a modal canonical realization for the full-order plant (e.g. see Matlab® function `canon.m`). Because of these difficulties with ULLT, and given that the spatial-temporal behavior of both models (ULLT and UVLM) are very comparable, the UVLM is chosen as the preferred method for the next steps in this work. From this point on, it should be assumed that the aerodynamic model being discussed is that obtained from UVLM.

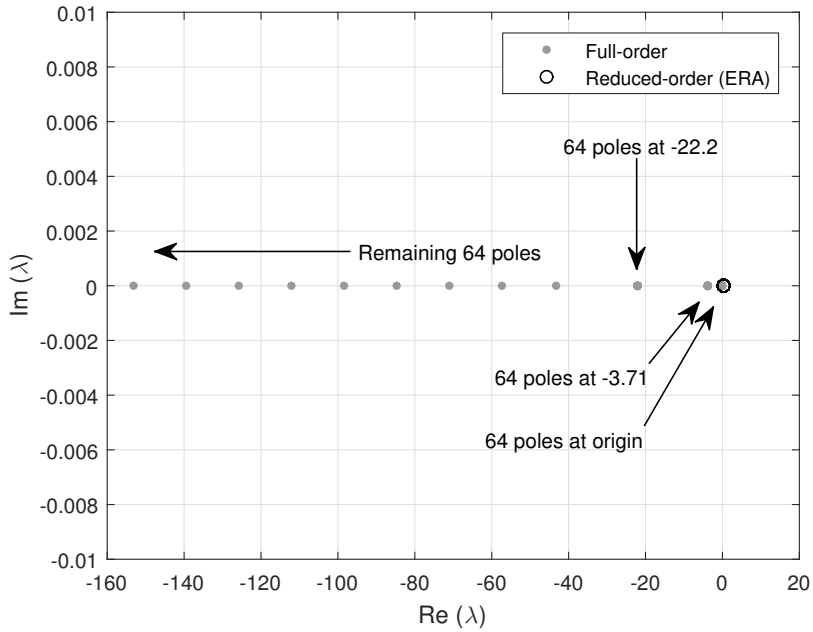

Figure 4.13: Eigenvalues of unsteady flow around a 3D wing, obtained from ULLT, with 8 modes kept in the reduced-order model.

4.4 Physical interpretation of aerodynamic modes

In most works dealing with modal representation of fluids, the combination of mode shapes reproduces the original system behavior. However, a physical interpretation

for each individual mode is usually not provided. In the present work, each mode is in fact a preferred aerodynamic shape that the wing naturally favors. For example, if some disturbance in the lift distribution profile is applied to the wing, and is spatially similar to the N-th natural shape, it is expected that the system's response will be in terms of the N-th mode alone. In other words, the disturbance magnitude will decay exponentially at a rate given by the N-th eigenvalue, and no other mode shapes will be present in the response. In Fig. 4.14, the full-order aerodynamic model is simulated for different initial lift distributions applied (i.e. no external inputs applied).

In the first case, the lift distribution applied is equal to the first mode shape, scaled by a factor of 0.05 (see top left plot). As a consequence, only the first mode is excited and the system's response is completely described by this mode alone. The output y can be expanded in terms of the normalized mode shapes at each time step, so that the shape coefficients can be obtained over time. As expected, only the first shape coefficient is nonzero (top right plot), and its value starts at 0.05 and decays to zero. The plot of shape coefficients along time provide information regarding the spatial content of the plant response. Similar results are obtained for the second mode (plots in the middle row). Finally, any linear superposition of these shapes only excites the associated modes. In the bottom row, a sum of first and second mode shapes is provided. As expected, only these 2 shape coefficients are nonzero, with the first mode decaying slower than the second mode. It should be noted that these are simulations of the full-order model (i.e. with 2048 modes), even though the mode shapes were obtained from the reduced-order model. This is an indication that the identified shapes are indeed the modes of the original (full-order) model, as

originally desired.

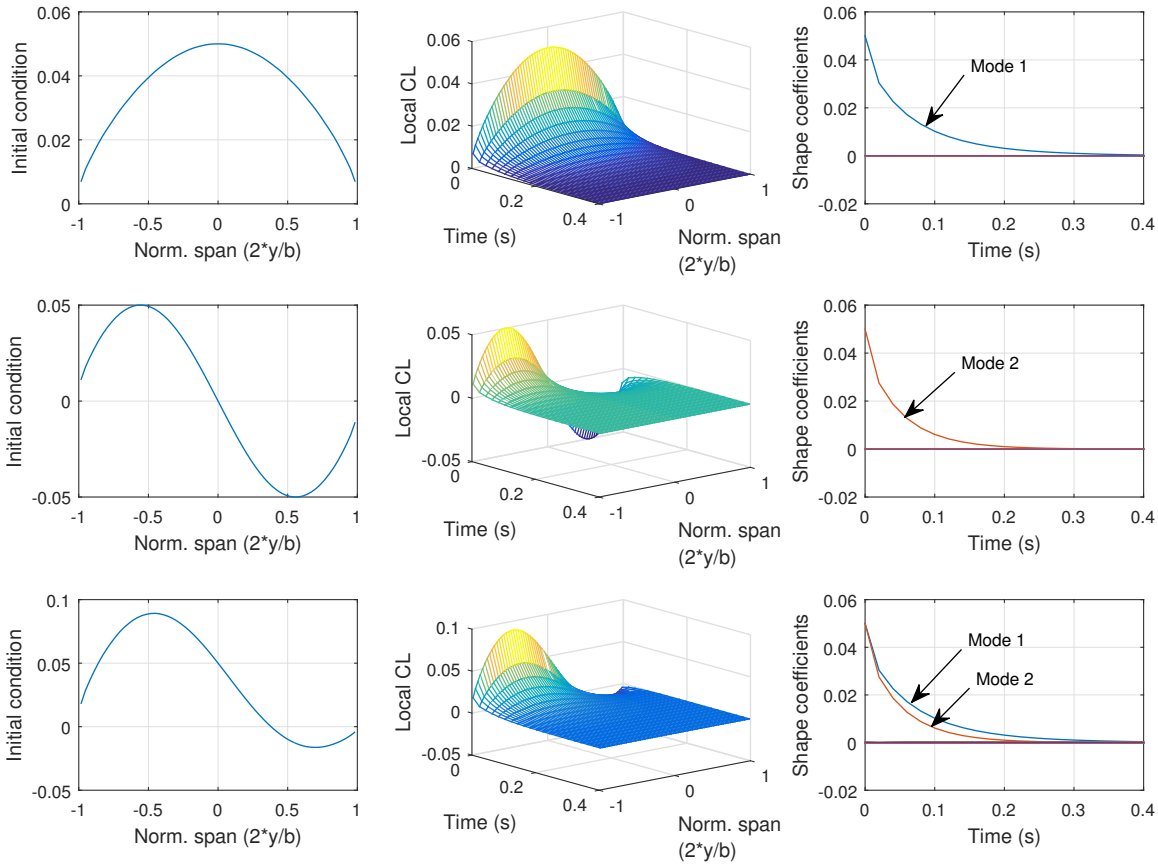

Figure 4.14: Spatial-temporal behavior of spanwise lift distribution when the initial condition is a superposition of mode shapes.

On the other hand, if the disturbance cannot be exactly described in terms of a finite superposition of modes (e.g. a cosine distribution or a uniform distribution), then all modes are excited. In practice, the higher order modes decay so fast that they cannot be visualized. This can be shown in a simulation environment. Shortly after the beginning of the simulation, the disturbance in lift distribution is re-shaped into a combination of the first few modes, which decay exponentially. Simulation results are presented in Fig. 4.15 for three initial lift distributions: uniform, linearly varying, and cosine. Note that these distributions are not feasible in reality (because the lift

must be zero at the wing tips), but they can be numerically simulated. After the first time step (20 ms), the wing quickly enforces the zero lift condition at the tips. Also, the higher order shape coefficients become practically zero and the response is dominated by lower order modes, indicating that a reduced-order model is capable of reproducing the behavior of the full-order system. In the plots of shape coefficients over time, the spatial content of the plant response can be observed. The lower order of the mode is linked to the slower decay of the associated shape coefficient. It should also be noted that a symmetric distribution (such as the constant lift distribution) excites only symmetric modes (1^{st}, 3^{rd}, etc.), whereas anti-symmetric distributions (such as linearly varying and cosine) excite only anti-symmetric modes (2^{nd}, 4^{th}, etc.).

4.5 Effects of varying wing planform on the mode shapes and eigenvalues

The fact that the mode shapes presented so far are similar to sinusoids might provide a misleading idea that the modes for lift distributions are close to sinusoids for every aerodynamic configuration. For comparison purposes, the aerodynamic mode shapes for wing planforms other than rectangular are presented in this section. In Fig. 4.16, the first four mode shapes for the rectangular wing (already presented earlier) are compared to the mode shapes for tapered and swept planforms.

Additionally, the exact sines are also shown in the same plot, so that a better idea of the differences can be obtained. The wingspan (1.8 m) and the chord length at the

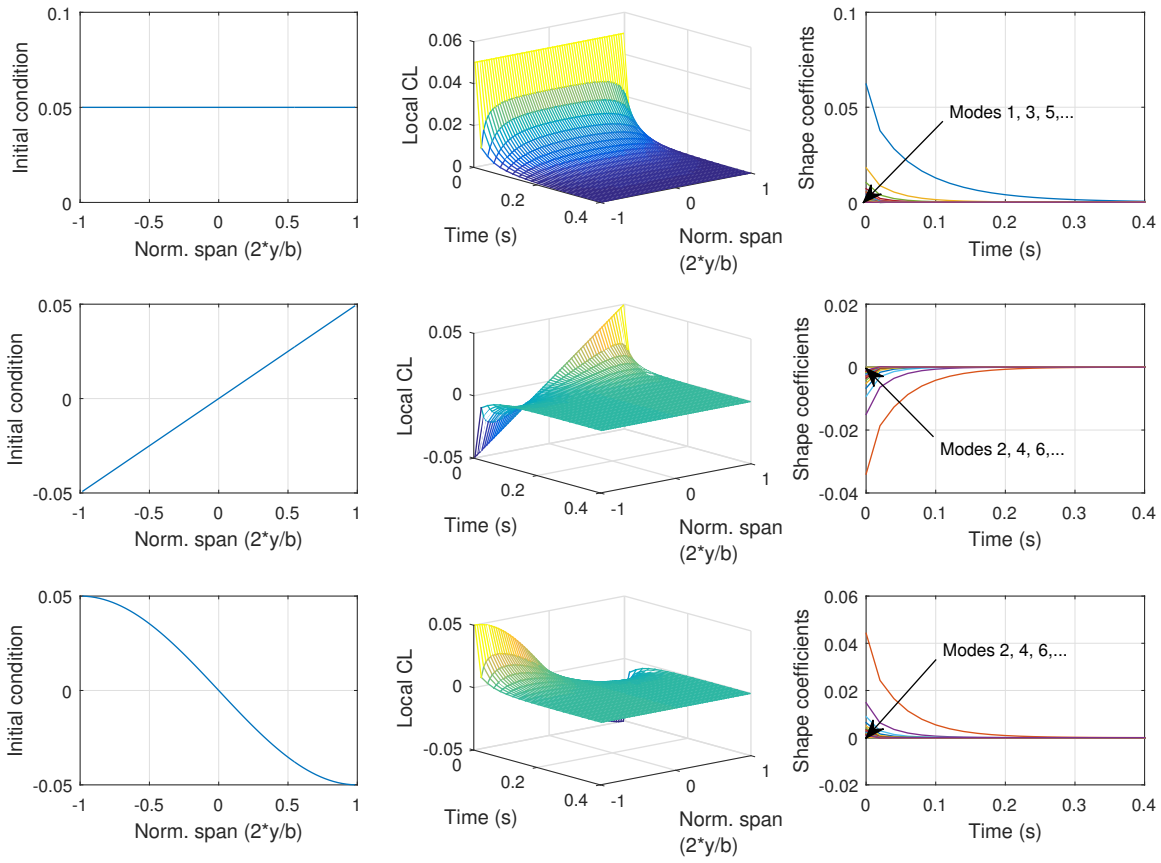

Figure 4.15: Spatial-temporal behavior of spanwise lift distribution when the initial condition cannot be described by a superposition of mode shapes.

wing root (0.3 m) were kept constant in all configurations. In fact, the rectangular wing yields mode shapes close to sines. The second configuration has taper ratio 0.4 and zero sweep angle at the quarter-chord line, whereas the third planform has a 30 deg sweep angle with taper ratio unity. For the tapered and swept wings, there exists a discontinuity in the first derivative of the symmetric shapes. This can be attributed to a discontinuity in the distribution of chord lengths along the span. It should be noted that the output of the system is given in terms of lift coefficient, which is proportional local lift per unit span divided by local chord. If the system output was given in terms of dimensional lift (per unit span), then there would be no

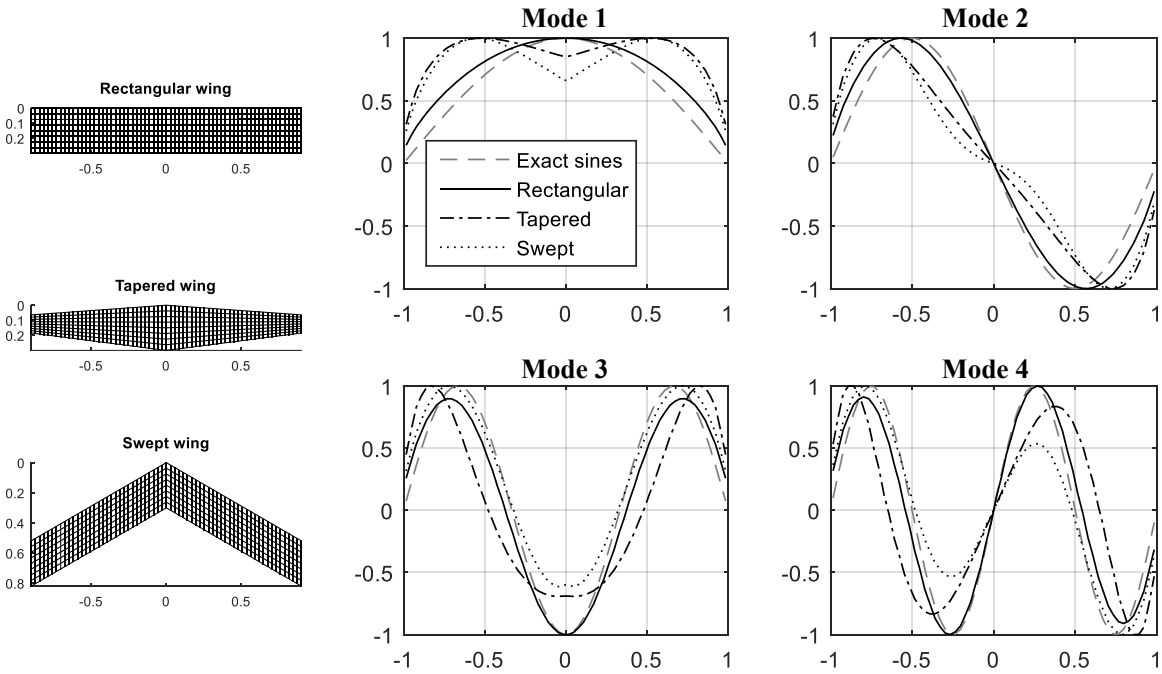

Figure 4.16: First four mode shapes along normalized wing span, for different wing planforms.

such discontinuities, since the distribution of lift should exhibit smooth transitions along the span. Whether the mode shapes are represented in terms of dimensional lift or lift coefficient, is purely an arbitrary choice from the point of view of modal identification. These are simply different ways of representing the same behavior of the system.

Regarding the eigenvalues, the root loci for the full-order models varied only slightly between these configurations, and are omitted here. The dominant branch of eigenvalues selected for the reduced-order model is still along the real, negative axis for all configurations. Eventually, complex conjugate pairs are selected for the swept wing configuration, but only after the 4^{th} mode. Despite their oscillatory nature, the associated modes are heavily damped (damping ratio above 0.95) and therefore it

is difficult to visualize any oscillations. In essence, the non-oscillatory, exponential decay is observed for all relevant modes of the configurations presented.

4.6 Chapter summary

This chapter presented modal identification results for both aerodynamic models (UVLM and ULLT), which are capable of describing the unsteady lift distribution along the wing span. The Eigensystem Realization Algorithm (ERA) was used as a model order reduction method, but is also suitable for modal identification.

The modal identification for the aerodynamic model yielded very different results as compared to usual modal analysis for structural systems. For the aerodynamic system, the eigenvalues are much closer to each other in the frequency range, and the Hankel Singular Values do not decay in magnitude as fast as structural eigenvalues (see section 3.5). Moreover, the relevant aerodynamic eigenvalues are usually negative real and exhibit exponential decay, as opposed to the oscillatory behavior from structural eigenvalues that usually appear in complex conjugate pairs. Nevertheless, a threshold for the most relevant modes can still be selected in terms of Hankel Singular Values (HSV).

Limitations on the spatial-temporal discretization of the model affect the reliability of the modal identification results. Specifically, the spatially distributed actuators (flaps) precluded proper excitation of modes with higher spatial frequency. As a rule of thumb, if the identification of the first N mode shapes is required, then at least $2N$ uniformly distributed flaps must be employed. The smaller the aperture of the

actuators used, the higher the order of modes that can be identified. Therefore, it is necessary to increase the number of actuators along the span, perform modal identification and model reduction, and then merge the columns of the B matrix to reduce the number of actuators. This process will be detailed in Section 5.3.1.

The aerodynamic mode shapes obtained from UVLM and ULLT are remarkably similar, but the two methods yielded different eigenvalues and root loci. Both methods have similar spatial-temporal behavior, but the UVLM provides a fully stable plant, with non-repeated eigenvalues. Therefore, the results from UVLM were selected for the subsequent steps in this work.

Chapter 5

Spatial control of spanwise lift distribution

This chapter explores the controllers synthesized for gust alleviation. The output of the reduced-order model is still given as local lift coefficient, which is then expanded in terms of basis functions to yield shape coefficients as outputs. Some considerations for selecting a threshold for model truncation are also provided. Next, the *spatial part of the controller* is designed, i.e. the number of flaps, as well as their size, and location along the wingspan are defined. This MIMO system is purely temporal with reduced dimension, hence suitable for control synthesis. Initially, a Liner Quadratic Tracker (LQT) with full state feedback is designed to track any set of N shape coefficients, while alleviating load variations caused by a discrete gust with a '1-cos' profile. The gust is modeled as a spatially uniform, 1D, vertical velocity field, but its magnitude varies along time. Since measuring the N shape coefficients is very challenging, it is shown that a Luenberger observer can be used to estimate these coefficients, but it

requires that the gust profile along time is known. For practical applications, the gust magnitude is an exogenous (unknown) input, therefore a special observer structure is used. As will be shown, the Unknown Input Observer (UIO) decouples the state estimation process from the gust input.

5.1 Model output expansion into mode shapes

Recall the discrete-time, reduced-order model, converted to modal coordinates, as obtained from ERA in Eq. (3.21), repeated here for convenience:

$$\begin{cases} z(k+1) = \Lambda z(k) + V^{-1} B_r u(k) \\ y(k) = C_r V z(k) = \Phi z(k) \end{cases} \tag{5.1}$$

In this formulation, the inputs and outputs are the same as the original full-order system. The inputs are 8 flap deflections and the outputs are 64 spanwise local lift coefficient measurements. The order of the reduced-order model is chosen as $r = 8$ (an explanation for this truncation level chosen is given in section 5.2). Therefore, the modal coordinate vector $z(k)$ has 8 states.

In order to enforce some desired lift distribution, the usual approach is to control the variables in the system's output vector $y(k)$. However, this is not practical for distributed parameters systems. Instead of controlling each pointwise local lift coefficient, the present work adopts a spatially distributed shape control approach, typically applied to the control of flexible structures [1, 132]. Assuming that the system output y (lift distribution) can be spatially described as a superposition of basis functions ψ_i, then the problem consists in controlling the coefficients c_i that multiply

each function:

$$y(x,t) = \sum_{i=1}^{\infty} c_i(t)\psi_i(x) = c_1(t)\psi_1(x) + c_2(t)\psi_2(x) + \dots \tag{5.2}$$

Exact representations will depend on the output shape desired and the set of basis functions $\Psi = [\psi_1, \psi_2, \dots]$ chosen to represent this shape. Thus, zero error might not be possible with a finite number of shapes, but a sufficiently accurate representation of the output $y(x,t)$ might be possible with a finite number of basis functions. Therefore, for practical applications the series is usually truncated at N terms. The main advantage is that controlling N shape coefficients will provide a better spatial representation of the system output than controlling N points scattered along the span. Truncating Eq. (5.2) at N terms yields:

$$\begin{aligned} y(x,t) = \sum_{i=1}^{N} c_i(t)\psi_i(x) &= c_1(t)\psi_1(x) + c_2(t)\psi_2(x) + \dots \\ &+ c_N(t)\psi_N(x) = \Psi \begin{bmatrix} c_1(t) \\ c_2(t) \\ \vdots \\ c_N(t) \end{bmatrix} = \Psi\, c(t) \end{aligned} \tag{5.3}$$

Note that, after choosing the basis set Ψ, the spatial portion of the output becomes known and the output $y(x,t)$ depends only on the vector of shape coefficients $c(t)$. Therefore, the output of the state-space formulation obtained previously can be described by $c(t)$. Pre-multiplying the output equation by Ψ^+ (Moore-Penrose pseudoinverse) yields:

$$\begin{cases} \dot{z}(t) = \Lambda z(t) + V^{-1} B_r u(t) \\ c(t) = \Psi^+ y(t) = \Psi^+ \Phi z(t) \end{cases} \tag{5.4}$$

where the system was converted to continuous-time for convenience. The matrix $(\Psi^{+}.\Phi)$ projects the contributions of each modal coordinate into the shape coefficients. Although different possibilities exist, a natural choice for the basis functions ψ_i are the system eigenfunctions ϕ_i, also known as mode shapes. This particular choice $(\Psi = \Phi)$ enables significant simplifications in the state-space formulation above, in the sense that the output matrix becomes the identity matrix: $\Psi^{+}\,\Phi = \Psi^{+}\,\Psi = I$. The vector of shape coefficients $c(t)$ become exactly the modal coordinates $z(t)$, i.e. the system outputs become equal to the system states.

It should be noted that the number of basis functions included in the truncated representation (N) is equal to the order of the reduced-order model (r). If compared to the original full-order model (obtained from UVLM), the resulting state-space formulation is remarkably simple:

1) The state matrix is an 8-by-8 diagonal matrix of the first 8 eigenvalues;

2) The input matrix is also 8-by-8 matrix, mapping the effects of 8 flaps on the 8 shape coefficients;

3) The output matrix is an 8-by-8 identity matrix.

5.2 Threshold for model truncation

Several criteria can be used to define how many modes should be included in the truncated representation of the plant. The number of modes r included in the low-order model from Eq. (5.1) directly affects the control task. For example:

1) r defines the relative accuracy of the reduced-order, as compared to the original

full-order model;

2) r defines the number of mode shapes used to expand the system output;

3) r also defines the number of independent control inputs required, in order to track any reference given in terms of the shape coefficients.

Therefore, each of these aspects can become a criterion for the truncation level required. The first aspect listed above can be evaluated by comparing the Singular Value plots of the full-order and reduced-order models. The singular values for $r = 8$ (i.e. 8 modes kept) are shown in Fig. 5.1. The truncated representation with 8 modes closely approximates the frequency response of the full-order model. In this figure, note the Nyquist frequency of 157.1 rad/s, associated to the inherent time step of 0.02s used in the formulation of the aerodynamic model, as obtained in Eq. (4.1). The infinity-norm of the difference between the two models can be used as an objective criterion for model accuracy.

The second aspect listed above is closely related to the concept of required spatial bandwidth. The first few aerodynamic mode shapes have low spatial frequency, in the sense of cycles along the wingspan (see Fig. 4.8 or 4.10). With more mode shapes included, it may be possible to represent more abrupt spanwise variations in lift profile.

Suppose we desire to change the lift distribution from the initial profile (given by a rectangular wing, aspect ratio 6, at 3 deg AOA and zero flap deflections) into an elliptical distribution, i.e. same total lift redistributed in an elliptical fashion, as shown in Fig. 5.2(a). Ideally, the difference ΔC_L between these two profiles (solid line in Fig. 5.2(b)) should be perfectly modeled by the reduced-order, output expanded

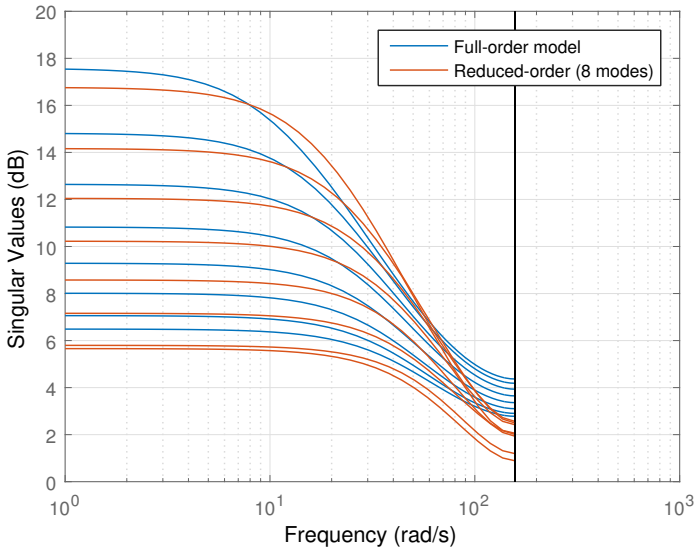

Figure 5.1: Comparison of singular values between full-order and reduced-order models.

system derived previously. In practice, this difference can be closely approximated (in a least squares sense) using the first 8 mode shapes, as represented by the dashed line in Fig. 5.2(b). The differences between the two shapes in Fig. 5.2(b) can be quantified by the Integrated Mean Square Error (IMSE), defined as:

$$IMSE = \frac{\int_{-1}^{1} (y - y_{fit})^2 \mathrm{d}x}{\int_{-1}^{1} y^2 \mathrm{d}x} \tag{5.5}$$

For $r = 8$, the IMSE becomes less than 5%. The IMSE values obtained for different values of r are shown in Fig. 5.3. Beyond $r = 8$, the IMSE does not change significantly. Therefore, the control task can provide a criterion for spatial bandwidth, hence becoming a criterion for selecting the truncation level r. This approach is typically used in structural shape control [1, 132].

Finally, the third and last aspect listed above is related to the number of actuators required to drive the shape coefficients to any desired combination, in the sense of

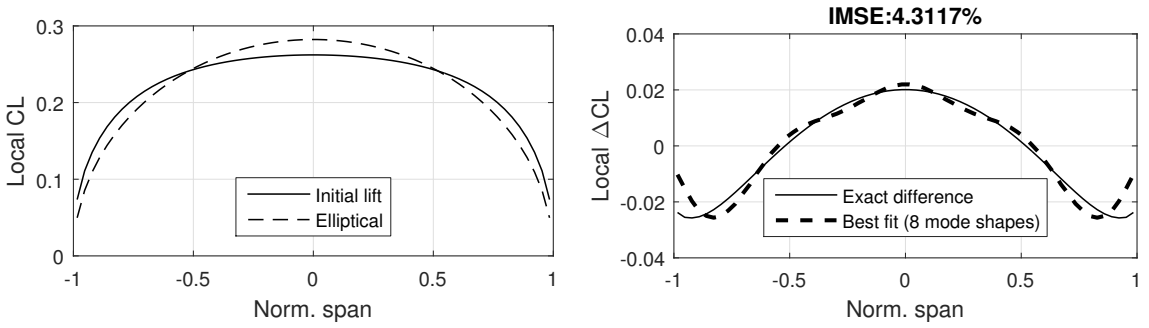

(a) (b)

Figure 5.2: Example of shape control task to define the required spatial bandwidth.

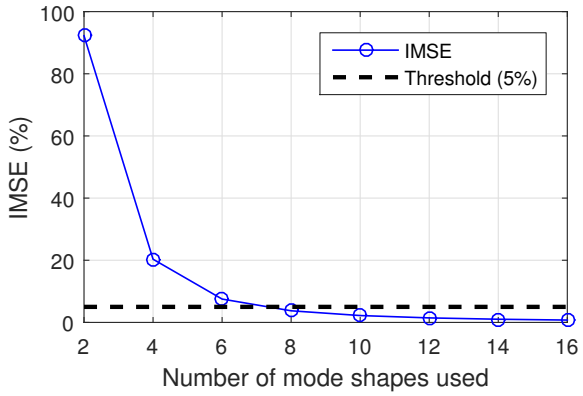

Figure 5.3: Variation of the Integrated Mean Square Error (%) with the number of modes shapes employed in the approximation.

reference tracking. The shape control task requires as many system inputs as outputs. Therefore, if the number of actuators available is relatively low, then it becomes a limiting factor in the truncation threshold as well, because we cannot perform shape control with more shapes than actuators. In the present work, the criterion adopted was that the IMSE be less than 5%, when seeking an elliptical lift distribution from the initial trimmed condition. Hence, the order of the truncated plant was chosen as $r = 8$.

5.3 Spatial-temporal controller synthesis

The shape control of Distributed Parameter Systems (DPS) typically involve actuators (transducers) which exhibit both spatial and temporal dynamics. The spatial and temporal dynamics of such distributed actuators can usually be assumed separable in space and time [1]:

$$u(x,t) = \Lambda(x)\, u(t) \tag{5.6}$$

where $\Lambda(x)$ describes the transducer's spatial aperture and $u(t)$ describes the transducer's temporal dynamics. Such actuators are referred to as degenerate [133]. This is the case of the flaps and the spanwise lift distribution considered in this work. Until now, the flaps were simply considered as uniformly distributed along the wingspan, in all state-space models presented so far. Pre-defining a uniform distribution is equivalent to assigning the spatial aperture $\Lambda(x)$. However, changing the distribution of flaps effectively changes the controllability properties and the closed-loop performance of the system. Therefore, designing the spatial aperture of the actuators is important. Although both spatial and temporal parts of the controller can be synthesized simultaneously, in the present work the spatial part is designed *first* [1, 134]. The spatial design of the controller yields the actuators apertures that best couple into the mode shapes of the system. Then, the spatial part is fixed and the model becomes purely temporal, allowing conventional MIMO techniques to be used to design temporal controllers.

5.3.1 Spatial design of the controller

The spatial design consists in defining the number, location, and aperture of the actuators. The number of actuators must be the same as the number of mode shapes (from Section 5.2, $r = 8$), so that any combination of shape coefficients can be effectively tracked. The problem now is how to obtain an aerodynamic model that can handle different flap distributions. Such model could be used to quantify the coupling between different flap distributions and the system mode shapes. From the linearized model obtained from UVLM, it is possible to generate a full-order state-space model that takes independent flap deflections from each one of the 64 spanwise station as inputs. In the state-space structure obtained from UVLM, the B matrix is now 2048×64, and the system can be converted to continuous-time for convenience, yielding:

$$\begin{cases} \dot{x} = Ax + Bu \\ \\ y = Cx \end{cases} \tag{5.7}$$

Since the spanwise discretization used in the UVLM is uniform, models with different flap distributions can be obtained by suitably combining the columns of the B matrix. For example, merging the columns in groups of 8 adjacent columns recreates the model with uniform distribution of 8 flaps. This can be achieved by post-multiplying the 2048×64 B matrix by a conveniently built 64×8 sparse matrix, whose entries are either 0 or 1. By allowing interpolation between the 64 columns of the B matrix, actuator discretizations better than 1/64 of the wingspan can be obtained. The same methodology explored in Chapters 3 and 4 can be applied to

reduce the order of the model, while keeping 64 flap inputs:

$$\begin{cases} \dot{x}(t) = A_r x(t) + B_r u(t) \\ y(t) = C_r x(t) \end{cases} \tag{5.8}$$

where A_r is 8×8 diagonal, B_r is 8×64 and C_r is the 8×8 identity matrix. The system output is given in terms of shape coefficients. Depending on how the columns of the matrix B_r are combined, different degrees of coupling to the system's mode shapes are obtained. By merging the columns of B_r into 8 groups, the system inputs is reduced to 8 flaps and the associated Transfer Function Matrix $G(s)$ correlates the inputs $u(s)$ to the shape coefficients $c(s)$, in the frequency domain:

$$c(s) = G(s)\, u(s) \tag{5.9}$$

Evaluating $G(s)$ at $s = 0$ yields an 8×8 matrix G_0 whose singular values provide a measure of the coupling between the flap deflections and the shape coefficients in steady-state conditions. The singular value decomposition of this matrix is given by:

$$G_0 = U \Sigma V^T \tag{5.10}$$

where U and V are, respectively, left and right singular vectors for the corresponding singular values of G_0 contained in Σ. As the ratio of maximum and minimum singular values of G_0 (i.e. its condition number) approaches 1, then each mode shape becomes equally attainable. Therefore, the condition number can be used as a criterion to screen candidate flap distributions.

The effort in screening distributions with several inputs can be reduced by using input/output coupling operators [1, 135]. This technique involves expressing the

singular value decomposition of G_0 in terms of an input/output factorization:

$$G_0 = U\Sigma V^T = EF \tag{5.11}$$

$$E = U\Sigma^{1/2} \tag{5.12}$$

$$F = \Sigma^{1/2}V^T \tag{5.13}$$

where the matrix F transforms the input to the gain space of the singular values, and the matrix E transforms from gain space to output shape space. Each column of F is the contribution of the corresponding actuator, from the input (control) space to the gain space. Therefore, the 2-norm of the i-th column of F can be thought of as a measure of the i-th actuator's contribution to controlling all 8 shapes:

$$\|z_i\|_2 = \|F_i\|_2 \tag{5.14}$$

If the input coupling operator $\|z_i\|_2$ is the same for each actuator, then all actuators participate equally over the entire spatial bandwidth of the shape control task. Other criteria can also be chosen, such as a decoupled output space (when the matrix U of left singular vectors becomes the identity matrix) or maximizing the minimum singular value (S.V.) of G_0, which ensures that all shapes are achievable with low control requirements. Additional details about these criteria can be found in [1]. In the present work, the four criteria were tested as cost functions for a constrained nonlinear optimization algorithm in Matlab®. The results are summarized in Table 5.1.

Since the flap distribution results are symmetric with respect to the wing root, only the results for a half-wing are presented, i.e. 4 flaps, from the wing tip (left

Table 5.1: Optimal flap distribution results, for different screening criteria.

Distribution/criterion	Flap aperture on half wing (% of semi-span, from tip to root)				Cond. number	Min. S.V.
I-Minimum cond. number	25.00	25.22	24.99	24.79	3.2862	0.3433
II-Balanced participation	27.82	24.15	24.12	23.91	3.5503	0.3133
III-Decoupled output space	23.29	25.06	25.83	25.82	3.6207	0.3156
IV-Maximize minimum S.V.	25.00	25.02	25.34	24.63	3.2864	0.3434

column) to the wing root (right column). The flap aperture results are given in terms of percentage of semi-span, so that the values add to 100% in each row. The associated input coupling operators are presented in Fig. 5.4. It is clear that the different criteria yield very similar distributions. The results vary only slightly from a uniform distribution of flaps. The exactly uniform distribution yields condition number 3.3142 (only slightly higher than distribution I) and minimum singular value 0.3407 (only slightly lower than distribution IV). It should be pointed out that small variations in flap size lead to large variations in condition number. In section 5.4.4, it will be shown that variations of 12.5% (of semi-span) in some of the flaps yield condition numbers above 20. However, one might already expect that the condition number is greatly dependent on the actuator apertures. What perhaps is surprising in these results is the fact that the same distribution (uniform) essentially combines all of the interesting features presented above. For this reason, a uniform flap distribution is chosen for the spatial design. It should be noted that this analysis is only valid for the baseline model defined in Fig. 2.1, which is a rectangular wing. As shown in Section 4.5, other wing planforms have different mode shapes, for which the optimum flap distribution will be different.

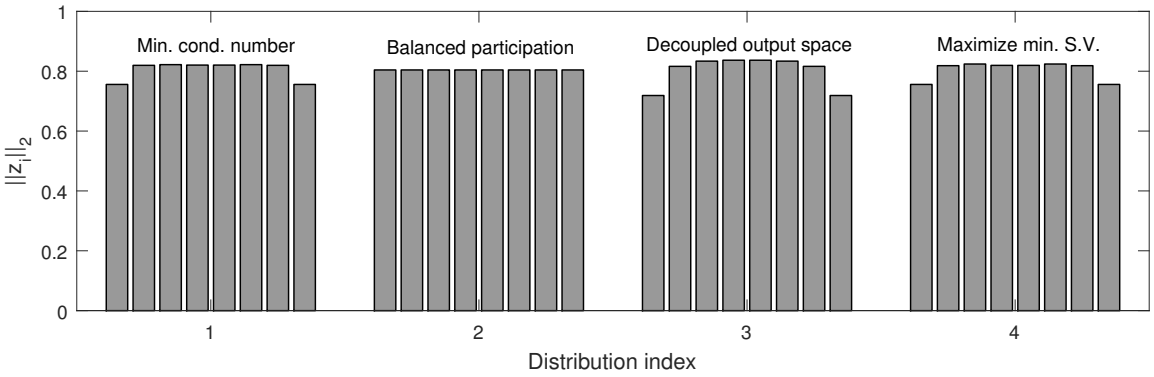

Figure 5.4: Input coupling operators for flap distributions I-IV.

5.3.2 Design of temporal controllers

After designing the spatial part of the controller, in terms of flap apertures, the model becomes purely temporal and suitable for conventional MIMO control techniques, as already presented in Eq. (5.4). In this work, only discrete gusts are simulated and the measurement noise in the system outputs is not considered at this point. Therefore, only deterministic approaches are used.

The different control approaches are detailed and presented in the following sections. First, a Linear Quadratic Tracker (LQT) using full state feedback is employed for shape control, i.e. to achieve and maintain a desired lift distribution, represented by a set of 8 shape coefficients. Then, a deterministic state observer (Luenberger observer) is added, in order to allow estimation of the shape coefficients from practical measurements. The load alleviation capability of the controller is evaluated for the case of discrete gusts ('1-cos' profile).

Although the Luenberger observer works well, it assumes knowledge of all inputs and outputs. However, the gust magnitude is an exogenous input and is not generally

known *a priori*. Therefore, a new observer structure is used to estimate not only the states, but also the gust magnitude over time. The so-called Unknown Input Observer (UIO) decouples the estimation of states from the unknown input, allowing application of control laws without knowledge of the gust profile ahead of time.

It should be noted that the discrete gust could be interpreted as an input disturbance to the plant. However, it cannot be simply rejected by the controller, because it is a low-frequency disturbance. Therefore, its frequency bandwidth lies close to the tracking bandwidth. It would be possible to track commands and reject disturbances, but these requirements must lie in regions well separate in the frequency spectrum.

5.4 Shape control problem

In this section, the capabilities of the LQ tracker are explored, still assuming that full state feedback is available. Some relevant aspects of shape control are shown before moving towards gust alleviation task, which is the final objective of this work.

5.4.1 Open-loop simulation

In order to provide some insight about the linear state-space model obtained in Eq. (5.4), the results for a unit step of 5 deg applied to the second flap (located at the left wingtip) are presented in Fig. 5.5. The second flap lies between -0.75 and -0.50 of normalized span.

The plot on the top shows the temporal evolution of the 8 states (shape coefficients) after the flap input at t=0.1s. All coefficients exhibit a non-oscillatory behav-

ior, typical of 1st-order systems with different time constants, as we should expect from the real negative eigenvalues. Note that a simple linear model 20.2/(s+20.2) for each flap actuator is included to avoid unrealistically high flap temporal rates. For any given time, a set of 8 shape coefficients can be used to reconstruct the lift profile by means of Eq. (5.3). The reconstructed lift distribution for t=1s (i.e. steady-state condition) is shown in the bottom plot (solid line). The dashed line plot is the influence function associated to the second flap, already given in Fig. 2.2, and represents the steady-state change in lift as given by the full-order model, whereas the solid line is how the reduced-order model perceives this change. In other words, the solid line is a truncated representation of the dashed line, in terms of 8 mode shapes.

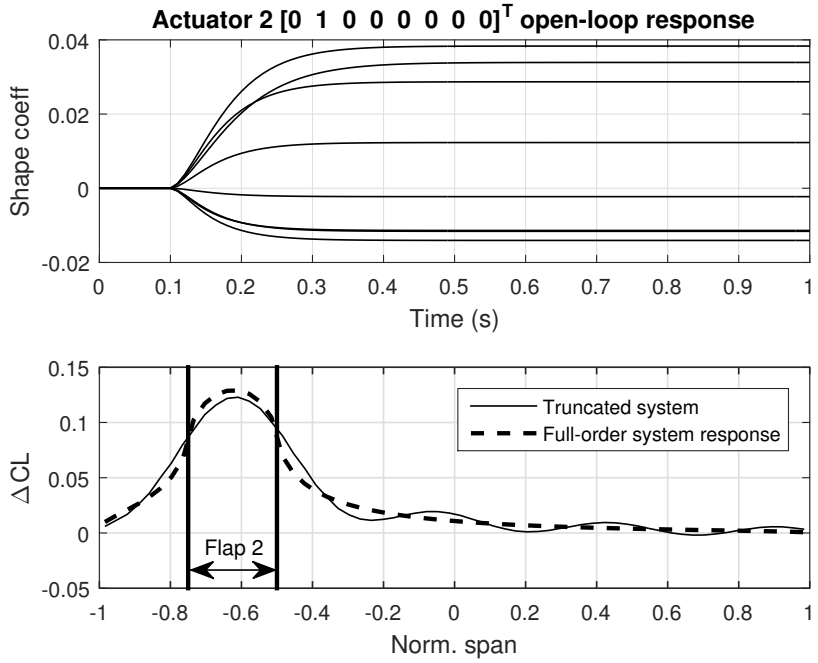

Figure 5.5: Open-loop response to a 5 degree input in flap 2.

A critical point is that the solid line plot does not occur in reality. The deflection of a single flap cannot induce such spanwise oscillations in lift. This is merely the

effect of representing the system output as a truncated expansion into mode shapes. Clearly, using only 8 shapes, it is not possible to replicate the full-order response exactly. This simplified representation, however, is low order and can be used to generate control inputs in closed-loop. Similar results were obtained for the other flaps as well.

5.4.2 Linear Quadratic Tracker formulation

Recall from Eq. (5.4) that, after expanding the output into mode shapes, the state-space system has 8 inputs, 8 states and 8 outputs:

$$\begin{cases} \dot{x} = Ax + Bu \\ \\ y = Cx \end{cases} \tag{5.15}$$

For command following, typical strategies for zero steady-state errors include integral control, in which the difference between desired and current outputs become additional states in the augmented system. This methodology is more robust to plant uncertainties, but requires extra states (as many as the outputs that we wish to track). Another methodology is the feedforward control, which consists in modifying the control input as $u = -Kx + \bar{N}r$, where the matrix $\bar{N}$ is carefully selected and pre-multiplies the reference signal r. This approach does not require adding extra states and will be used in this section for its simplicity.

Suppose that r is the reference that we wish to track. The control problem is to design a control law, depending on x and r, so that the closed-loop system is stable and the tracking error $e(t) = r - y(t)$ tends to zero as $t \to \infty$. In steady-state

conditions, one should have:

$$\begin{cases} \dot{x}_{ss} = Ax_{ss} + Bu_{ss} = 0 \\ \\ y_{ss} = Cx_{ss} = r \end{cases} \tag{5.16}$$

Which is equivalent to solving the equation:

$$\begin{bmatrix} A & B \\ \\ C & 0 \end{bmatrix} \begin{bmatrix} x_{ss} \\ \\ u_{ss} \end{bmatrix} = \begin{bmatrix} 0 \\ \\ r \end{bmatrix} = \begin{bmatrix} 0 \\ \\ I \end{bmatrix} r \tag{5.17}$$

where 0 and I are, respectively, the null and identity matrices of size 8×8. Since the number of inputs and outputs is the same, then the matrix on the left hand side in Eq. (5.17) is square. Assuming this matrix is also nonsingular, then this equation can be solved for any arbitrary reference r:

$$\begin{bmatrix} x_{ss} \\ \\ u_{ss} \end{bmatrix} = \begin{bmatrix} A & B \\ \\ C & 0 \end{bmatrix}^{-1} \begin{bmatrix} 0 \\ \\ I \end{bmatrix} r = \begin{bmatrix} N_x \\ \\ N_u \end{bmatrix} r \tag{5.18}$$

From Eq. (5.18), the matrices N_x and N_u are obtained. Now, let $\Delta x = x - x_{ss}$, $\Delta u = u - u_{ss}$ and $\Delta y = y - Cx_{ss} = y - r$. By subtracting Eq. (5.16) from Eq. (5.15), a differential equation for Δx is obtained:

$$\begin{cases} \Delta\dot{x} = A\Delta x + B\Delta u \\ \\ \Delta y = C\Delta x \end{cases} \tag{5.19}$$

A control law $\Delta u = -K\Delta x$ that stabilizes this system (i.e. $\Delta x \to 0$ as $t \to \infty$)

will also ensure $y \to r$:

$$\begin{aligned} \Delta u &= -K\Delta x \\ u - u_{ss} &= -K(x - x_{ss}) \\ u - N_u r &= -K(x - N_x r) \\ u &= -Kx + (N_u + KN_x)r \\ u &= -Kx + \bar{N}r \end{aligned} \tag{5.20}$$

where $\bar{N} = N_u + KN_x$. The same gain K obtained for a Linear Quadratic Regulator (LQR) in terms of Δx can be used to ensure zero steady-state error $e(t) = y(t) - r$, in terms of x. Hereafter, this approach is called Linear Quadratic Tracker (LQT), but it is also known as reference input tracking using feedforward control [136] or set point tracking with full state feedback [137]. The closed-loop system is given by:

$$\begin{cases} \dot{x} = (A - BK)x + \bar{N}r \\ y = Cx \end{cases} \tag{5.21}$$

It should be noted that both approaches (integral control and feedforward control) require only controllability of the original system, i.e. (A, B) controllable. The gain K is obtained from LQR synthesis, with weighting matrices Q and R chosen such that a variation of 0.1 in shape coefficient (states) is equally penalized as flap deflections of 10 degrees (inputs), i.e.:

$$\begin{aligned} Q &= \text{diag}(q),\ q_i = \frac{1}{(0.1)^2},\ i = 1, \ldots, 8 \\ R &= \text{diag}(r),\ r_i = \frac{1}{[10(\pi/180)]^2},\ i = 1, \ldots, 8 \end{aligned} \tag{5.22}$$

The controller developed in this section will be used to command and achieve

lift distributions in section 5.4. Specifically, the closed-loop results using the LQT approach from above will be presented in section 5.4.3.

5.4.3 Linear Quadratic Tracker results

In this section, the Linear Quadratic Tracker (LQT) with full state feedback is synthesized. At this point, it is assumed that all states are known and that the outputs of the system are shape coefficients, as in Eq. (5.4). Therefore, the LQT is able to achieve and maintain any desired set of 8 shape coefficients, which can be used to reconstruct the desired lift distribution profiles along time. As an example, a unit step input is applied to the second shape coefficient, yielding the results in Fig. 5.6.

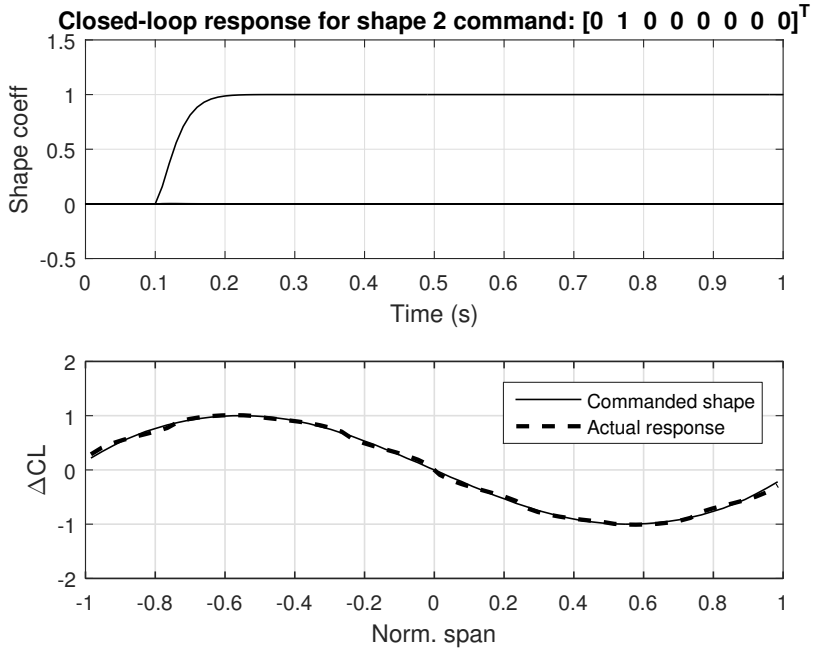

Figure 5.6: Closed-loop response to a unit step command for the second shape coefficient.

It can be seen that the shape coefficient associated with the second shape is the

only one excited, while the others remain at zero. All flaps are deflected according to the control law, in order to yield a spanwise lift variation very similar to the second mode shape. The bottom plot presents the steady-state results of lift coefficient variations along the span. The solid line plot represents the commanded shape, whereas the dashed line shows the actual lift distribution from the full-order model.

It should be emphasized that the reduced-order model is capable of representing the first 8 mode shapes (or any combination of them) exactly. From the point of view of the controller (based on the reduced-order model), the second mode shape commanded in Fig. 5.6 is obtained exactly. However, as explained in the previous section, the actual plant responds with all modes, hence generating slightly different results (dashed line). Nevertheless, the actual plant response is very close to the ideal shapes, because the actuator apertures were specifically designed to maximize control authority over the first 8 mode shapes.

5.4.4 Relevance of spatial design

In the previous sections, it was explained that many advantages arise when the basis set chosen to expand the system output is the same as the system mode shapes. Moreover, it was shown that the actuator distribution can be spatially designed to best couple to these shapes. In order to illustrate the benefits of such design, the closed-loop performance of the chosen design (uniform flaps, labeled as distribution 1) will be compared to two non-optimal distributions, shown in Fig. 5.7.

The metrics already discussed in section 5.3.1 were also used in this comparison.

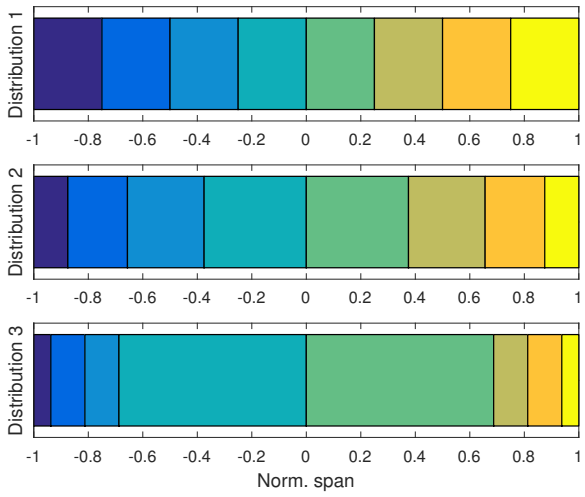

Figure 5.7: Spanwise flap apertures for distributions 1-3.

The condition number and minimum singular value are given in Table 5.2, and the associated input coupling operators are shown in Fig. 5.8. Each distribution yields a different system realization, because the B matrix is specific for each flap configuration. From the condition number results, it is clear that the plant becomes highly directional when the distribution deviates from uniform. Also, the minimum singular value (S.V.) for the system becomes extremely small in non-optimal distributions, indicating that a large control gain will be required for some of the actuators, i.e. large flap deflections.

Table 5.2: Comparison between uniform flaps and two other flap distributions.

Distribution/criterion	Flap aperture on half wing (% of semi-span, from tip to root)				Cond. number	Min. S.V.
1 (uniform flaps)	25.00	25.00	25.00	25.00	3.492	0.3549
2	12.50	21.88	28.13	37.50	20.44	0.0701
3	6.250	12.50	12.50	68.75	1437	0.0014

From the point of view of controllability, all three cases are fully controllable, but some modes will require much more control effort than others. In order to compare

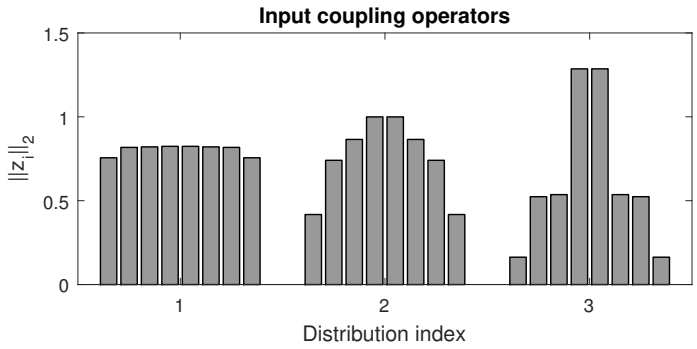

Figure 5.8: Input coupling operators for flap distributions 1-3.

the closed-loop performance, the LQ tracker was synthesized for each system using the same weighting matrices Q and R to penalize the states and controls, respectively, as given in Eq. (5.22).

The control task chosen consists in achieving and maintaining the third mode shape (arbitrarily scaled to 0.05 in amplitude), with results shown in Fig. 5.9. At the top plots, it can be seen that all reduced-order models predict that the third shape coefficient becomes 0.05, while all the others remain at zero, as desired (1^{st} row of plots). However, the LQ tracker has different gains for each model, yielding different control inputs (2^{nd} row of plots). Since the commanded shape is symmetric, the flaps are also deflected symmetrically, hence only 4 flap deflections are discernible in the plots. For distribution 1, the actual plant achieves a response very close to the ideal shape, and requires small flap deflections for that (less than 2 deg). For distribution 2, the flap deflections are still relatively small (less than 3 deg). However, the steady-state response of the full plant is very different from the desired shape. For distribution 3, the deflections for some flaps become unrealistically large, and reflect the high directionality of the plant in this case. When applied to the actual plant

(full-order, linear model), these inputs predict a steady-state profile very different from mode shape number 3. Note that any flap configuration between distributions 2 and 3 could easily generate deflections that violate the boundaries of aerodynamic linearity.

Moreover, the large flap deflections also affect the actuator rate requirements. For distributions 1, 2 and 3, the peak rates were, respectively, 135 deg/s (for flaps 2 and 6), 160 deg/s (for flaps 1 and 8) and 30084 deg/s (for flaps 1 and 8). Therefore, a proper spatial design ensures that lower actuator rates will be required, as compared to a non-optimal distribution. If the spatial design is disregarded, the flap distribution used becomes very inefficient in generating the required lift profiles.

In summary:

- As far as the reduced-order model is concerned, perfect tracking of any of the 8 mode shapes is always possible, independently of flap spatial design, but it might result in large flap amplitudes, which cause the actual plant response to deviate significantly from the reduced-order prediction;
- If flap apertures are properly designed, then we maximize the influence of flaps on the 8 first mode shapes (in the sense of the metrics presented in Section 5.3.1), yielding relevant consequences:
    1. This approach decreases the amplitude of flap deflections required for any control task defined in terms of 8 first shape coefficients;
    2. It also naturally reduces the excitation of higher order modes (i.e. modes 9 and above) in the full-order model. Thus, the actual plant response

becomes similar to that predicted using the reduced-order model;

3. Since the two responses become similar, then the actual plant is also able to closely track each of the 8 mode shapes independently, or any linear combination of such modes.

Therefore, any temporal controller based on the reduced-order model will be successful (when applied to the full-order plant) only if the spatial part of the controller is properly designed first. This is a crucial point in the present work.

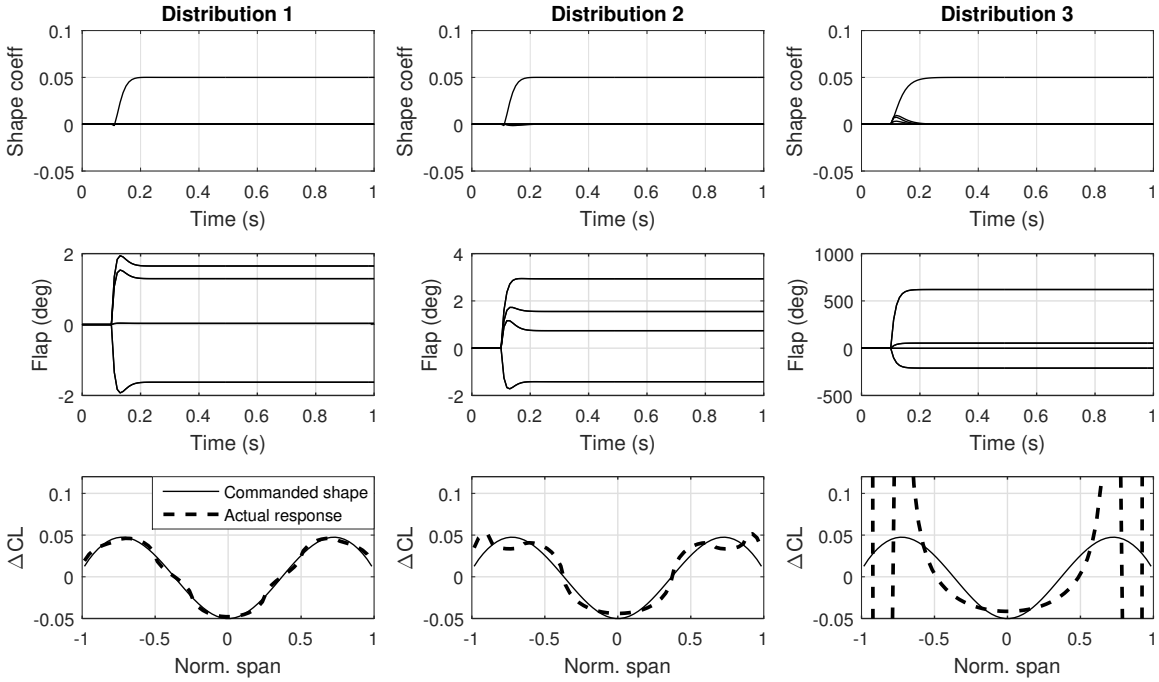

Figure 5.9: Closed-loop response of distributions 1-3.

5.4.5 Tracking elliptical lift distribution

From the previous section, it is clear that a properly designed distribution of flaps is required to closely track each of the mode shapes, while requiring small flap inputs.

With the spatial-temporal controller completely synthesized, the performance of the closed-loop system can be investigated.

This section addresses the performance benefits that can be obtained from the unsteady aerodynamic model, as compared to the simpler quasi-steady model, which is much easier to obtain. To investigate this, recall the shape control task of achieving and maintaining an elliptical spanwise lift distribution, as presented in Fig. 5.2. The reference vector of shape coefficients that best approximates the ideal differences is given by:

$$r = [0.0056 \quad 0 \quad -0.0199 \quad 0 \quad -0.0085 \quad 0 \quad -0.0046 \quad 0]^T \tag{5.23}$$

Since we are dealing with symmetric shapes in this case, all coefficients related to anti-symmetric modes shapes (2^{nd}, 4^{th}, 6^{th} and 8^{th}) are zero. This set of shape coefficients was used as a command input for the LQ tracker, with same weighting matrices Q and R as defined in Eq. (5.22). The results can be observed in Fig. 5.10, for shape coefficients (top left) and flap inputs (bottom left) plotted over time. The open-loop response is obtained by simply commanding the desired flap deflections as fast as possible (step input commanded), as if such deflections were calculated from a quasi-steady model. Clearly, the controller based on the unsteady aerodynamic model provided control inputs that accelerated the response in closed-loop. Although this result is expected, this simple example shows that active control for gust alleviation will benefit from an unsteady aerodynamics model. The input provided by the quasi-steady model required about 200 milliseconds of additional time to reach steady-state (for the slowest mode). This example also complements the discussion from Section

2.1 about the inadequacy of the quasi-steady model for closed-loop tracking of lift distributions.

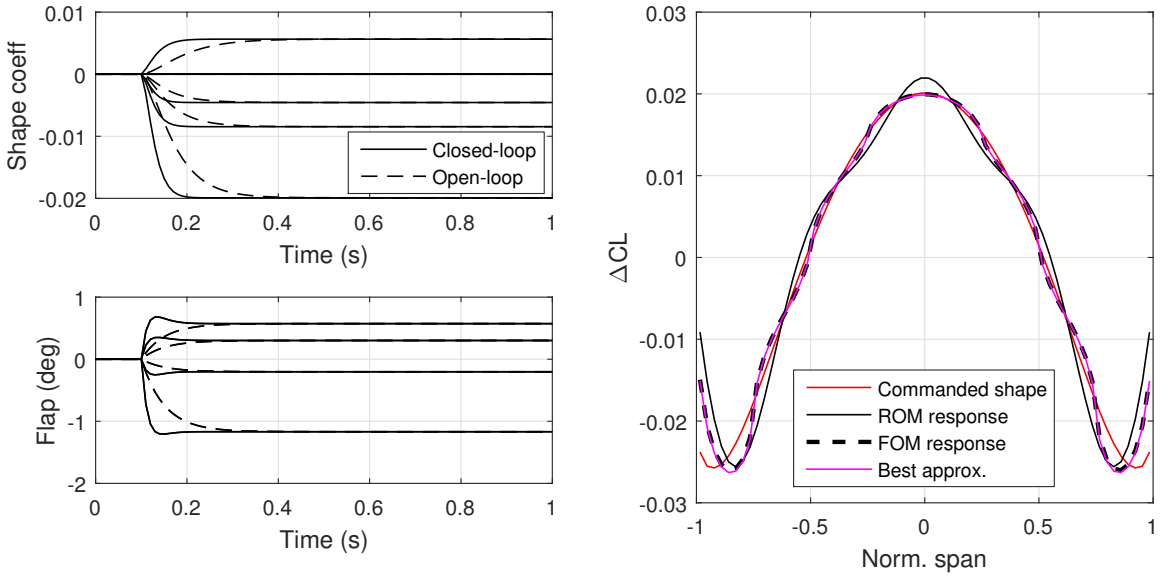

Figure 5.10: Closed-loop response when commanding an elliptical lift distribution.

Perhaps the most unexpected result lies in the plot on the right, which presents the final lift distribution profile achieved (i.e, for t=1s). Note that this result is given in terms of ΔC_L, since the aerodynamic model provides the changes around the initial trimmed condition (i.e. initial profile + ΔC_L = elliptical). The curve in red is the shape desired, i.e. the exact difference between the elliptical and initial profiles. This red shape is expanded into mode shapes, yielding the coefficients in Eq. (5.23) and the representation truncated at 8 modes ("ROM response"), which was already shown in Fig. 5.2. However, as explained earlier, this truncated representation does not occur in reality. It is merely a band-limited representation, as seen by the controller. As a matter of fact, the controller inputs are actually applied to the full-order plant, yielding a different steady-state profile ("FOM response"). The "ROM response" has

an IMSE of 4.31%, as already shown in Fig. 5.2, whereas the "FOM response" has an IMSE of 1.48%. The difference is that previously we were fitting the desired shape with 8 mode shapes, which is a simplified (truncated) version of the plant, but useful for defining spatial bandwidth requirements. In reality, the system's response contains all mode shapes. Even though these additional shapes (modes 9 and higher) are not being directly controlled, they respond to flap inputs and contain a DC component (i.e. steady-state). For this reason, the actual shape obtained is closer to the desired profile than initially predicted.

However, there is no guarantee that the steady-state deflections generated by the controller (based on 8 modes) actually yield the minimum error with respect to the desired shape. The optimal values of steady-state deflections can be obtained by expanding the desired shape into the influence functions, given in Fig. 2.2. Then, using these new deflections, the best approximation is obtained ("Best approx.", in Fig. 5.10). Note that this computation provides the best final condition, but it does not say how to move the system from the initial to the final state.

On the other hand, the dynamic model not only enables controller synthesis, but also generates very good steady-steady signals, i.e. very similar to the *best* set of flap deflections that provide the minimum amount of error (in a least squares sense). In fact, the plots "FOM response" and "Best approx." practically coincide. In other words, the truncated model is as good in generating steady-state inputs (that minimize the error to some desired shape) as the best approximation derived from the full-order system, with the advantage that it is possible to generate dynamic control inputs to move the system to the desired final state.

5.4.6 Relevance of expansion into mode shapes

At this point, it should be clear that the entire methodology is based on the fact that the mode shapes ϕ_i were chosen as the set of functions ψ_i for expansion. A pertinent question that arises is: can we choose a different set Ψ? If a different set is chosen (e.g. sine functions), it is still possible to re-run the design steps and find a new flap distribution that best couples to this new set of functions, according to one of the design criteria (e.g. minimum condition number).

If a different expansion basis is chosen, then the C matrix of the system presented in Eq. (5.4) is not identity anymore. However, if the functions ψ_i are linearly independent, then the matrix $(\Psi^{+}.\Phi)$ is still an 8×8 full column rank matrix and the observability properties of the system are preserved. Therefore, the LQ tracker can be synthesized and would still predict exact tracking of each set of 8 shape coefficients.

Note that this matrix multiplication is simply the projection of the set of system mode shapes Φ onto the set Ψ, which was chosen. If these sets are different, some information will be lost in the projection. In other words, if we take the resulting 8×8 matrix C, and then pre-multiply it by Ψ, we do not recover Φ exactly. In the extreme case, if the set Ψ is orthogonal to Φ, all information is lost, i.e. the matrix C becomes a null matrix. These projection errors are propagated to the controller, generating sub-optimal inputs.

As a consequence of this difference, the steady-state errors in the actual plant response will be relatively larger when these new shapes (e.g. sines) are commanded, even if the flaps were optimized for them. Therefore, choosing the mode shapes as

the set for the expansion yields a closed-loop model with better tracking capabilities.

5.5 Gust Load Alleviation problem

The problem of gust alleviation is considered for the case of discrete gusts, specifically the '1-cos' pattern. For actual applications, measuring the states is a major difficulty because these are shape coefficients that multiply aerodynamic modes. Measuring the lift distribution and then expanding into the mode shapes is not a viable option, since this would require a large number of pressure sensors on the wing surface. This section deals with the estimation of these shape coefficients from practical measurements. The closed-loop performance of the controller with a state observer is also evaluated against discrete gusts.

5.5.1 State observer by output injection

Since measuring the states is not always feasible, a state observer is usually required for practical applications. In the present work, the Luenberger observer is used:

$$\begin{cases} \dot{\hat{x}} = A\hat{x} + Bu + L(y - C\hat{x}) \\ \\ u = -K\hat{x} \end{cases} \tag{5.24}$$

where L is the observer gain and $(C\hat{x} - y)$ is the output prediction error or innovation. The dynamics of the error $e = x - \hat{x}$ is given by:

$$\dot{e} = Ae + LC(x - \hat{x}) = (A - LC)e \tag{5.25}$$

If the observer gain L can be designed so that $(A - LC)$ is stable (i.e. all its eigenvalues lie in the LHP), then $e \to 0$ exponentially. The observer eigenvalues can

be placed arbitrarily if and only if the pair (A, C) is observable. In matrix form, the closed-loop observer is given by:

$$\begin{bmatrix} \dot{e} \\ \dot{\hat{x}} \end{bmatrix} = \begin{bmatrix} A - LC & 0 \\ LC & A - BK \end{bmatrix} \begin{bmatrix} e \\ \hat{x} \end{bmatrix} + \begin{bmatrix} 0 \\ B \end{bmatrix} u \tag{5.26}$$

In order to simulate gust inputs, the B matrix must be modified to accept not only 8 flap inputs, but also one vertical gust input. This can be easily implemented in the UVLM model. The gust input u_{gust} is assumed to be uniform in space, i.e. the same value affects all points of the wing at the same time. Moreover, the Linear Quadratic Tracker formulation developed in section 5.4.2 can also be added, in order to track a desired lift distribution while actively reducing the effect of gusts. The final system is given by:

$$\begin{bmatrix} \dot{e} \\ \dot{\hat{x}} \end{bmatrix} = \begin{bmatrix} A - LC & 0 \\ LC & A - BK \end{bmatrix} \begin{bmatrix} e \\ \hat{x} \end{bmatrix} + \begin{bmatrix} 0 \\ B \end{bmatrix} u + \begin{bmatrix} 0 \\ B_g \end{bmatrix} u_{gust} + \begin{bmatrix} 0 \\ B\bar{N} \end{bmatrix} r \tag{5.27}$$

where B_{gust} is an 8×1 gust input matrix, $\bar{N}$ is the gain matrix presented in Eq. (5.20), and r is the reference set of 8 shape coefficients desired. It should be noted that u in Eq. (5.27) represents the flap deflections commanded, if any. The term Bu is only included for completeness, being considered zero in the subsequent gust analyses. Also note that the C matrix used in this formulation is *not* the 8×8 identity matrix anymore, since this would simply yield shape coefficients as outputs. The C matrix is defined and derived in the next section.

5.5.2 Observability of aerodynamic shape coefficients

The mode shapes were provided in Chapter 4 (see Figs. 4.8 or 4.10). It is known that the spanwise lift distribution in terms of local lift coefficient (C'_L) can be reconstructed reasonably well by Eq. (5.3), repeated here for convenience:

$$C'_L = \sum_{i=1}^{N} c_i(t)\psi_i(\bar{y}) = \frac{L'}{q_\infty c(\bar{y})} \tag{5.28}$$

where the local airfoil chord $c(\bar{y})$ is constant for rectangular wing, hence $c(\bar{y}) = c$. Note also that the spatial dependence of the functions ψ_i is given in terms of normalized spanwise coordinate $\bar{y}$. The total wing lift (L) is given by the integral of the lift per unit span (L') from wingtip to wingtip:

$$L = \int_{-b/2}^{b/2} L' \mathrm{d}y = \frac{b}{2}\int_{-1}^{1} L' \mathrm{d}\bar{y} \tag{5.29}$$

where the normalized wingspan coordinate is given by $\bar{y} = y/(b/2) = 2y/b$. Substituting Eq. (5.28) into Eq. (5.29) yields total lift as a function of shape coefficients:

$$L = \frac{1}{2} q_\infty S \int_{-1}^{1} C'_L \mathrm{d}\bar{y} \tag{5.30}$$

$$L = \frac{1}{2} q_\infty S \int_{-1}^{1} \sum_{i=1}^{N} c_i(t)\psi_i(\bar{y}) \mathrm{d}\bar{y} \tag{5.31}$$

$$L = \sum_{i=1}^{N} c_i(t) \left(\frac{1}{2} q_\infty S \int_{-1}^{1} \psi_i(\bar{y}) \mathrm{d}\bar{y} \right) = \sum_{i=1}^{N} c_i(t)\Omega_i \tag{5.32}$$

where the reference wing area is given by $S = b\,c$. The term inside the parentheses can be numerically evaluated, yielding a constant scalar Ω_i for each mode shape. Therefore, the total lift at any time t is given simply by the linear combination of $c_i(t)$, weighted by Ω_i. For the operating conditions and geometry given in Table 2.1,

one obtains:

$$\Omega = [\Omega_1 \quad \Omega_2 \quad \dots \quad \Omega_8] = [23.72 \quad 0 \quad 5.550 \quad 0 \quad 3.005 \quad 0 \quad 1.955 \quad 0] \tag{5.33}$$

It is clear that only the symmetric mode shapes (1^{st}, 3^{rd}, etc.) contribute to changes in the total lift of the wing, since the integral in Eq. (5.32) is zero for anti-symmetric mode shapes. On the other hand, the anti-symmetric modes generate a rolling moment M_x, which is given by the integral of the local lift (L') multiplied by the arm, i.e. spanwise coordinate y:

$$M_x = -\int_{-b/2}^{b/2} L' y \mathrm{d}y = -\left(\frac{b}{2}\right)^2 \int_{-1}^{1} L' \bar{y} \mathrm{d}\bar{y} \tag{5.34}$$

The negative sign accounts for the convention in flight dynamics (positive M_x means right wing down). It is possible to estimate the total rolling moment (M_x) by adding the contribution of each mode:

$$M_x = -q_\infty c \left(\frac{b}{2}\right)^2 \int_{-1}^{1} C'_L \bar{y} \mathrm{d}\bar{y} \tag{5.35}$$

$$M_x = -q_\infty c \left(\frac{b}{2}\right)^2 \int_{-1}^{1} \left(\sum_{i=1}^{N} c_i(t)\psi_i(\bar{y})\right) \bar{y} \mathrm{d}\bar{y} \tag{5.36}$$

$$M_x = \sum_{i=1}^{N} c_i(t) \left(-q_\infty c \left(\frac{b}{2}\right)^2 \int_{-1}^{1} \psi_i(\bar{y}) \bar{y} \mathrm{d}\bar{y}\right) = \sum_{i=1}^{N} c_i(t) \Upsilon_i \tag{5.37}$$

The terms inside the parentheses can be numerically evaluated, yielding a constant scalar Υ_i for each mode shape:

$$\Upsilon = [\Upsilon_1 \quad \Upsilon_2 \quad \dots \quad \Upsilon_8] = [0 \quad 10.79 \quad 0 \quad 4.242 \quad 0 \quad 2.494 \quad 0 \quad 1.693] \tag{5.38}$$

Clearly, only the anti-symmetric shapes (2^{nd}, 4^{th}, etc.) contribute to M_x. In flight dynamic applications, the total lift L and total rolling moment M_x can be measured

using inertial sensors [138, 139]:

$$L = -ma_z \cos\alpha + (ma_x - T)\sin\alpha \tag{5.39}$$

$$M_x = I_{xx}\dot{p} + qr(I_{zz} - I_{yy}) - I_{xz}(\dot{r} + pq) \tag{5.40}$$

where: a_x and a_z are specific forces, as measured by accelerometers along x-axis and z-axis, respectively; m is the aircraft mass; α is the angle of attack; T is engine thrust; (p, q, r) are rotation rates (roll, pitch, yaw) in body axes; (I_{xx}, I_{yy}, I_{zz}) are the moments of inertia around the body axes; and I_{xy} is the product of inertia in the xy-plane. Therefore, L and M_x can easily be measured in real-time for control applications. Assuming low angles of attack ($\alpha \approx 0$) and pure rolling motion ($q = r = 0$), then total lift is obtained from a single vertical accelerometer ($L = -ma_z$) and total rolling moment is obtained from a single gyro ($M_x = I_{xx}\dot{p}$), upon temporal differentiation of the roll rate p. On the other hand, if the wing is constrained (e.g. in a wind tunnel setup), then the lift and rolling moment could be directly measured as the shear force and bending moment at the root. In any case, the metrics required to ensure observability of all modes of interest are available.

Now, instead of having shape coefficients c_i as model outputs, it is possible to have a new C matrix, given by:

$$C = \begin{bmatrix} \Omega \\ \Upsilon \end{bmatrix} = \begin{bmatrix} 23.72 & 0 & 5.550 & 0 & 3.005 & 0 & 1.955 & 0 \\ 0 & 10.79 & 0 & 4.242 & 0 & 2.494 & 0 & 1.693 \end{bmatrix} \tag{5.41}$$

Therefore, observability of the symmetric modes is guaranteed by the first output (L) and observability of the anti-symmetric modes is provided by the second output (M_x).

5.5.3 Structural loading as a function of shape coefficients

Similarly to the cases of total lift (L) and total rolling moment (M_x), the knowledge of shape coefficient values over time allows one to reconstruct the load, shear force and bending moment along the entire wingspan, at all times. The load is given precisely by the lift per unit span (L'), already defined in Eq. (5.28). Integration of the load yields the shear force and integration of V along the span yields the bending moment:

$$\mathrm{d}V/\mathrm{d}y = L' \tag{5.42}$$

$$\mathrm{d}M/\mathrm{d}y = V \tag{5.43}$$

Therefore, the load (L'), shear force (V) and bending moment (M) can be obtained as:

$$L'(\bar{y}) = q_\infty c C'_L(\bar{y}) \tag{5.44}$$

$$V(\bar{y}) = \begin{cases} q_\infty c \left(\dfrac{b}{2}\right) \displaystyle\int_{-1}^{\bar{y}} C'_L(\bar{y}_0)\mathrm{d}\bar{y}_0, & \text{for} \quad -1 \leq \bar{y} < 0 \\ -q_\infty c \left(\dfrac{b}{2}\right) \displaystyle\int_{\bar{y}}^{1} C'_L(\bar{y}_0)\mathrm{d}\bar{y}_0, & \text{for} \quad 0 < \bar{y} \leq 1 \end{cases} \tag{5.45}$$

$$M(\bar{y}) = \begin{cases} q_\infty c \left(\dfrac{b}{2}\right)^2 \displaystyle\int_{-1}^{\bar{y}} C'_L(\bar{y}_0)\,(\bar{y} - \bar{y}_0)\mathrm{d}\bar{y}_0, & \text{for} \quad -1 \leq \bar{y} < 0 \\ q_\infty c \left(\dfrac{b}{2}\right)^2 \displaystyle\int_{\bar{y}}^{1} C'_L(\bar{y}_0)\,(\bar{y}_0 - \bar{y})\mathrm{d}\bar{y}_0, & \text{for} \quad 0 < \bar{y} \leq 1 \end{cases} \tag{5.46}$$

where $\bar{y}_0$ is simply a dummy variable of integration. In the derivation above, the integration is carried out separately for each half of the wing. This choice was made to avoid handling of point loads at the wing root. For symmetric modes, a vertical point force is required to balance the loading, whereas a point moment is required to achieve static equilibrium for anti-symmetric modes. Therefore, the wing is a rigid structure, constrained in rotation and translation at the wing root station. The sign

convention used was such that positive bending moments cause compression on top of the structure and positive shear force rotate the element in a clockwise fashion. The distributions associated to each normalized aerodynamic mode shape (i.e. amplitude scaled to $[-1, +1]$) are presented in Fig. 5.11.

The load L' is simply the mode shape (C'_L) scaled by $q_\infty c = 18.38$, according to Table 2.1. Note that the relationships involving derivatives of these quantities in Eqs. (5.42)-(5.43) are respected. Additionally, for the symmetric mode shapes, there exists one discontinuity at $\bar{y} = 0$ in shear force, due to the vertical force required for balance (which is equal to the total lift L associated). For the anti-symmetric modes, the discontinuity occurs in bending moment, due to a reaction moment $\bar{y} = 0$ required to balance the load (which is equal to the total rolling moment M_x associated). Interestingly, the magnitude of these "jumps" are given by the parameters Ω_i and Υ_i, as shown in Eq. (5.41).

In section 5.5.2, it was assumed that the measurements were taken at the wing root. The plots in Fig. 5.11 condense information for all points of the wing, including the wing root. This can be very helpful if a particular sensor (e.g. for bending moment) is located at one specific station along the wing, e.g. $\bar{y} = 0.5$. Then, it is possible to collect the weights in the plots of bending moment at $\bar{y} = 0.5$, for each mode shape. This set of 8 scalars can be appended as a third row to the C matrix in Eq. (5.41), and now the system would have three outputs: total lift, total rolling moment, and bending moment at $\bar{y} = 0.5$. The extra output can be useful for improving the estimation of shape coefficients via observers, for example. This strategy does not require any changes to the original aerodynamic model and illustrates the

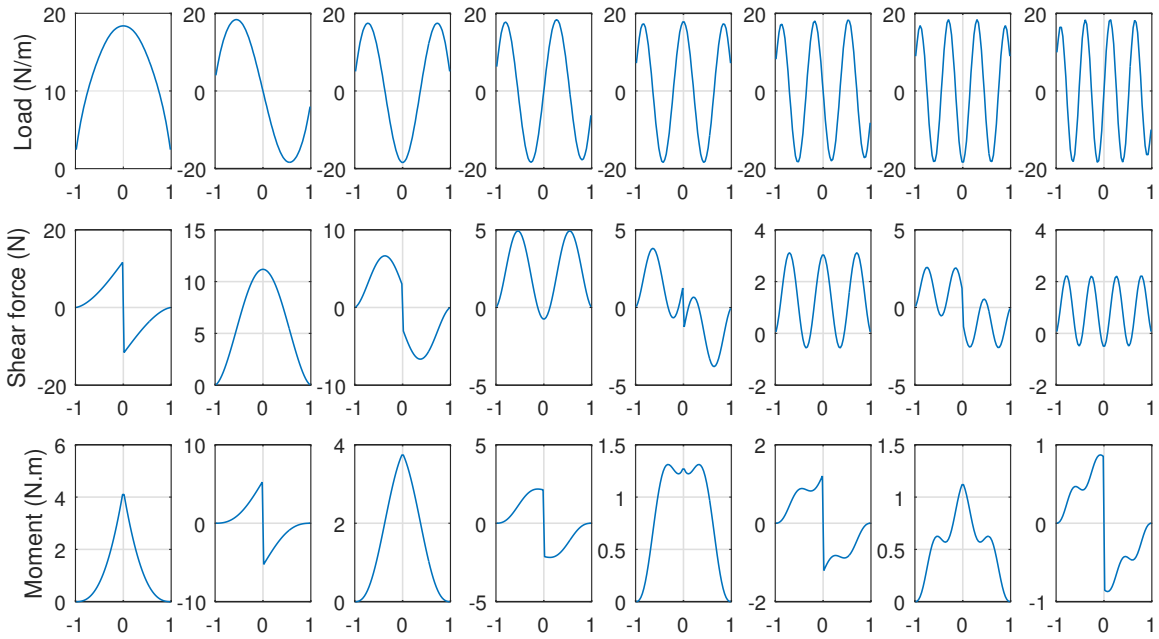

Figure 5.11: Distribution of load, shear stress, and bending moment along normalized span, associated with each of the 8 aerodynamic mode shapes.

power of the modal decomposition techniques for shape control applications.

5.5.4 Gust load alleviation results

The Luenberger observer is used to obtain estimates for the shape coefficients over time, while the wing suffers the influence of a discrete gust with a '1-cos' profile. The gust magnitude along time $u_g(t)$ is prescribed as:

$$u_g(t) = \begin{cases} 0, & \text{for } \; t < t_0 \\ \dfrac{A_{gust}}{2}\left[1 - \cos\dfrac{2\pi}{T_{gust}}(t - t_0)\right], & \text{for } \; t_0 \leq t \leq T_{gust} + t_0 \\ 0, & \text{for } \; t > T_{gust} + t_0 \end{cases} \tag{5.47}$$

where $A_{gust} = -1$ m/s is the gust amplitude, $T_{gust} = 0.5$ s is the period or duration of the gust and $t_0 = 0.1$ s is the time when the gust starts. It should be noted that

these gust parameters were arbitrarily chosen, and the resulting loads are related to this specific gust profile. For certification purposes, the gust parameters must be "tuned" for each aircraft, in order to define the critical excitation that maximizes the load variations in the airframe. More details are provided in [34]. Since the main objective here is to present a general methodology for shaping lift distribution during gust loads, the arbitrary parameters defined for Eq. (5.47) suffice. The open-loop results are presented in Fig. 5.12 (left side).

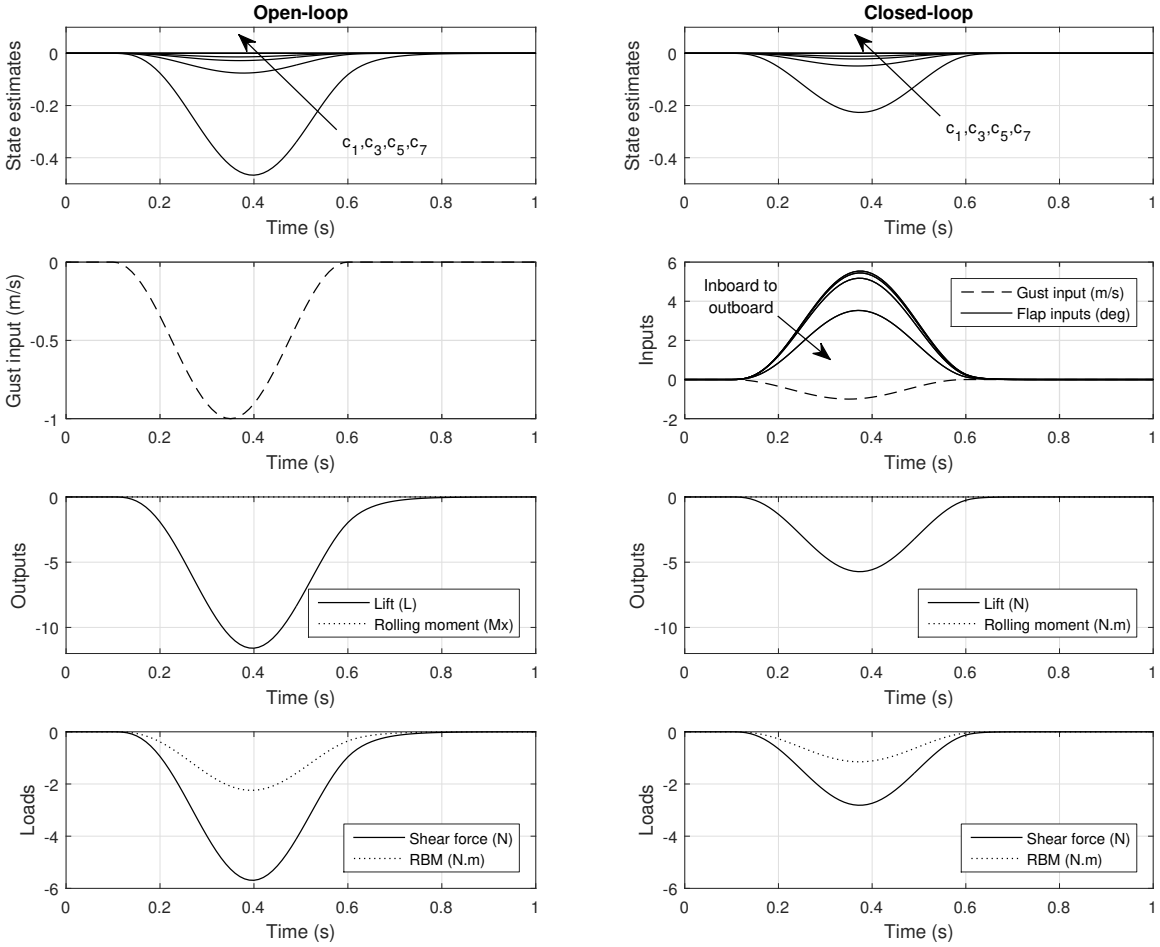

Figure 5.12: System response to '1-cos' discrete gust in open-loop (left) and closed-loop (right).

In the results shown, the observer has already converged at $t = 0$. The gust input from Eq. (5.47) takes place from $t = 0.1$ s until $t = 0.6$ s, reaching maximum magnitude of 1 m/s (downward) at $t = 0.35$ s. The outputs measured were total lift (L) and total rolling moment (M_x), as presented in section 5.5.2. It should be noted that the input is symmetric (uniform gust), therefore only the symmetric mode shapes are excited, and the four shape coefficients associated to anti-symmetric mode shapes (i.e. c_2, c_4, c_6, c_8) remain at zero at all times. Also, since the gust is symmetric, right and left wings experience the same loads in absolute values, but due to sign convention, the shear force will have opposite signs on each side of the wing. As an example, the loads at the root of the left wing over time are also presented (bottom plots). The maximum loads obtained were -5.69 N in shear force at the wing root and -2.24 N.m for root bending moment (RBM).

The results in closed-loop are presented in Fig. 5.12 (right side), with flap inputs generated by the controller. All 8 flaps are deflected, but symmetrically, hence only 4 lines are discernible in the inputs plot. The inboard pairs of flaps (i.e. near the wing root) deflected more than the outboard pairs (i.e. near the wing tips), as indicated by the arrow in the inputs plot. In terms of maximum absolute loads, the shear force was reduced to -2.81 N (i.e. decreased by 51%), whereas the RBM was reduced to -1.15 N.m (i.e. decreased by 49%). The flap rates associated with the closed-loop performance are shown in Fig. 5.13. The level of load attenuation achieved is intrinsically related to the control effort required. Using the weighting matrices Q and R defined in Eq. (5.22), the maximum flap rate was kept below 35 deg/s. In order words, a better load alleviation could be obtained, but it would require higher

actuator rates and deflections.

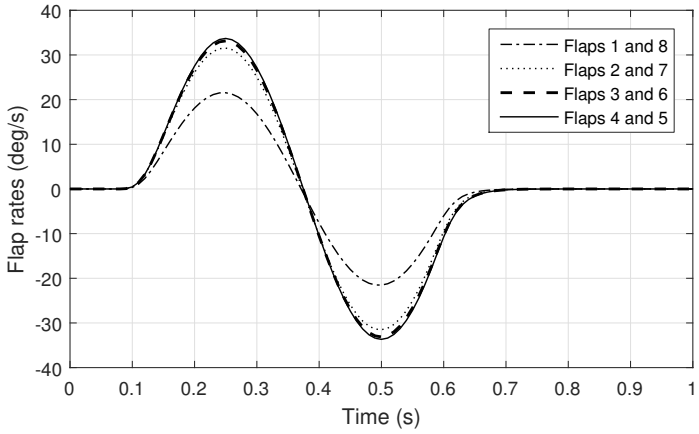

Figure 5.13: Flap rates associated with the closed-loop response to the '1-cos' discrete gust.

As mentioned in section 5.5.3, the modal decomposition of aerodynamic loads also allow reconstruction of the spanwise distributions of shear force and bending moment during the maneuver. The open-loop results for the gust input are also presented in Fig. 5.14, where the load variations are provided along the normalized span (-1 to +1) and also time (0s to 1s). Moreover, each column shows the individual contribution of the modes that play a role in the response (i.e. symmetric modes), in terms of shear force (plots at the top) and bending moment (plots at the bottom). The final loads at any desired location are simply given by the superposition of these modes.

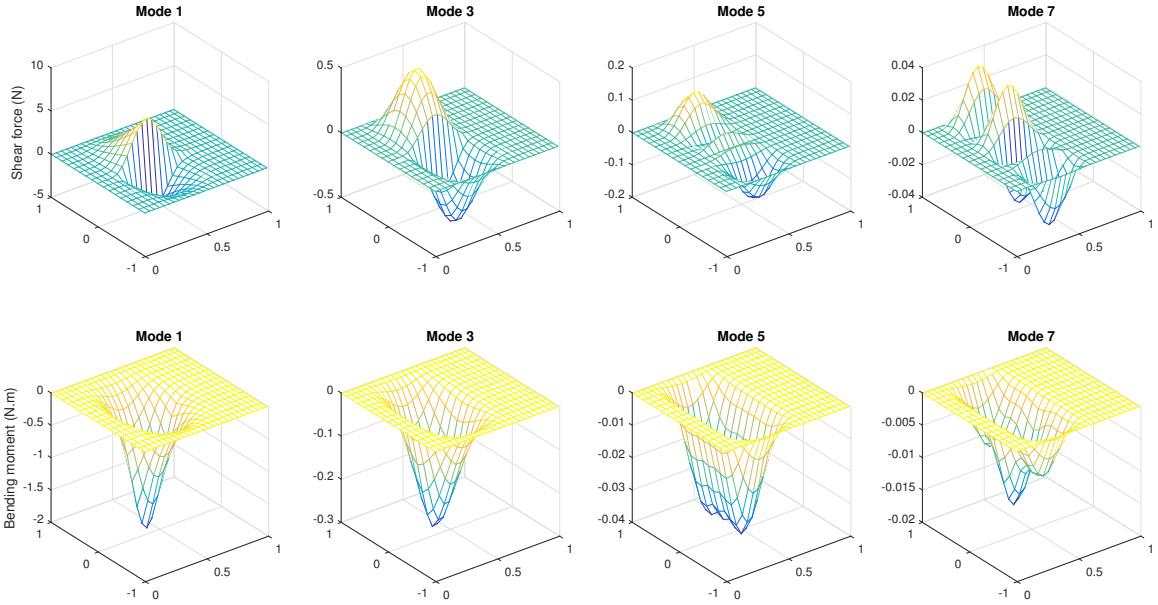

Figure 5.14: Spatio-temporal distribution of loads, due to each symmetric mode.

5.6 Gust Load Alleviation problem, with gust estimation

A new problem arises because the Luenberger observer from section 5.5.1 requires that all inputs and outputs are provided, including exogenous inputs (such as the gust magnitude). Therefore, in order to estimate the shape coefficients, the gust magnitude over time was assumed known in the previous sections. However, measuring the gust field might be as cumbersome as measuring the lift distribution in the first place [57, 61]. In the present work, this problem is avoided by means of a special structure observer, namely the Unknown Input Observer (UIO), which provides state estimates in the presence of unknown inputs. The UIO decouples the plant disturbance inputs from the state estimation process [140], and is largely employed in fault detection and isolation algorithms [141, 142].

5.6.1 Theory and design of Unknown Input Observer (UIO)

The scheme proposed by Chen, Patton and Zhang [140] is closely followed in this section. The aerodynamic model with flaps and gust inputs belong to a class of systems with an *additive* unknown disturbance term in the state-space formulation:

$$\begin{cases} \dot{x}(t) = Ax(t) + Bu(t) + B_g u_g(t) \\ y(t) = Cx(t) \end{cases} \tag{5.48}$$

where $x(t) \in \mathbb{R}^n$ is the state vector, $y(t) \in \mathbb{R}^m$ is the output vector, $u(t) \in \mathbb{R}^p$ is the known input vector (flap deflections) and $u_g(t) \in \mathbb{R}$ is the unknown input or disturbance vector (gust magnitude). By definition, an observer is defined as an unknown input observer for the system described in Eq. (5.48), if its state estimate error vector $e(t) = x(t) - \hat{x}(t)$ approaches zero asymptotically, regardless of the presence of the unknown input (disturbance) in the system. Now, consider the following structure for a full order UIO:

$$\begin{cases} \dot{z}(t) = Fz(t) + TBu(t) + Ly(t) \\ \hat{x}(t) = z(t) + Hy(t) \end{cases} \tag{5.49}$$

where $\hat{x}(t) \in \mathbb{R}^n$ is the vector of states estimates, $z(t) \in \mathbb{R}^n$ is the state vector of the full order observer, and F, T, L, H are matrices to be designed for achieving unknown input decoupling. When the observer in Eq. (5.49) is applied to the system in Eq. (5.48), the estimation error $e(t)$ can be expanded as:

$$\begin{aligned} \dot{e}(t) = {} & (A - HCA - L_1C)e(t) + [(A - HCA - L_1C) - F]z(t) \\ & + [(A - HCA - L_1C)H - L_2]y(t) \\ & + [I - HC - T]Bu(t) + (I - HC)B_g u_g(t) \end{aligned} \tag{5.50}$$

where:

$$L = L_1 + L_2 \tag{5.51}$$

Note that if the following relations hold:

$$(I - HC)B_g = 0 \tag{5.52}$$

$$T = I - HC \tag{5.53}$$

$$F = A - HCA - L_1 C \tag{5.54}$$

$$L_2 = FH \tag{5.55}$$

Then the dynamics of the estimate error is reduced to:

$$\dot{e}(t) = Fe(t) \tag{5.56}$$

The error dynamics becomes independent of all other signals, but the error e itself. If all the eigenvalues of F are stable, then the error $e(t)$ will approach zero asymptotically, regardless of the unknown input u_g. Therefore, the state estimation becomes decoupled from the disturbance input. The design procedure of this observer consists in solving Eqs. (5.52)-(5.55), while ensuring that all eigenvalues of F are stable. The necessary and sufficient conditions for the system in Eq. (5.49) to be an UIO for the system defined in Eq. (5.48) are:

1. $\text{rank}(CB_g) = \text{rank}(B_g)$
2. (C, A_1) is a detectable pair, where $A_1 = A - B_g \left[(CB_g)^T CB_g \right]^{-1} (CB_g)^T CA$

If the first condition is not met, then an UIO does not exist. Otherwise, the

following observer matrices can be computed:

$$H = B_g \left[(CB_g)^T CB_g \right]^{-1} (CB_g)^T \tag{5.57}$$

$$T = I - HC \tag{5.58}$$

$$A_1 = TA \tag{5.59}$$

From Eq. (5.54), $F = TA - L_1C = A_1 - L_1C$. Therefore, in order to stabilize F, it is necessary to adequately choose the matrix L_1, assuming the pair (C, A_1) is at least detectable. If the pair (C, A_1) is observable, then a proper gain L_1 can be designed via pole placement. If the pair (C, A_1) is not observable, but it is detectable, then the observable canonical decomposition of the system must be obtained:

$$PA_1P^{-1} = \begin{bmatrix} A_{11} & 0 \\ A_{12} & A_{22} \end{bmatrix} \tag{5.60}$$

$$CP^{-1} = \begin{bmatrix} C^* & 0 \end{bmatrix} \tag{5.61}$$

where P is the similarity transformation matrix, $A_{11} \in \mathbb{R}^{n_1 \times n_1}$, $C^* \in \mathbb{R}^{m \times n_1}$, n_1 is the rank of the observability matrix for (C, A_1), and (C^*, A_{11}) is observable. This decomposition can be obtained using Matlab® function `obsvf.m`. The n_1 eigenvalues of $(A_1 - L_p^1 C^*)$ can be assigned using pole placement, from which the gain L_p^1 is obtained. The gain L_1 can be calculated from:

$$L_1 = P^{-1} L_p = P^{-1} \left[(L_p^1)^T (L_p^2)^T \right]^T \tag{5.62}$$

The $(n - n_1)$ eigenvalues of A_{22} are stable, but can not be moved. Therefore, the gain matrix L_p^2 can be any $(n - n_1) \times m$ matrix (e.g. zeros). With these results, the

last two observer matrices are computed:

$$F = A_1 - L_1 C \tag{5.63}$$

$$L = L_1 + L_2 = L_1 + FH \tag{5.64}$$

More details about the observer design can be found in [143]. In matrix form, the open-loop observer is given by:

$$\begin{aligned} \begin{bmatrix} \dot{e} \\ \dot{z} \end{bmatrix} &= \begin{bmatrix} F & 0 \\ 0 & F \end{bmatrix} \begin{bmatrix} e \\ z \end{bmatrix} + \begin{bmatrix} 0 & 0 \\ TB & L \end{bmatrix} \begin{bmatrix} u \\ y \end{bmatrix} \\ \begin{bmatrix} e \\ \hat{x} \end{bmatrix} &= \begin{bmatrix} I & 0 \\ 0 & I \end{bmatrix} \begin{bmatrix} e \\ z \end{bmatrix} + \begin{bmatrix} 0 & 0 \\ 0 & H \end{bmatrix} \begin{bmatrix} u \\ y \end{bmatrix} \end{aligned} \tag{5.65}$$

The same control gain K designed using LQR techniques can be used in conjunction with UIO. The input u is now divided into $u_c = -K\hat{x}$, generated by the controller, and u_p, which are manual flap commands (or "pilot" inputs):

$$u = u_c + u_p \tag{5.66}$$

$$u_c = -K\hat{x} = -Kz - KHy \tag{5.67}$$

When substituted into Eq. (5.49), gives:

$$\begin{cases} \dot{z}(t) = (F - TBK)z(t) + TBu_p(t) + (L - TBKH)y(t) \\ \hat{x}(t) = z(t) + Hy(t) \end{cases} \tag{5.68}$$

which yields the following closed-loop equations for the UIO:

$$\begin{aligned} \begin{bmatrix} \dot{e} \\ \dot{z} \end{bmatrix} &= \begin{bmatrix} (F - TBK) & 0 \\ 0 & (F - TBK) \end{bmatrix} \begin{bmatrix} e \\ z \end{bmatrix} + \begin{bmatrix} 0 & 0 \\ TB & (L - TBKH) \end{bmatrix} \begin{bmatrix} u_p \\ y \end{bmatrix} \\ \begin{bmatrix} e \\ \hat{x} \end{bmatrix} &= \begin{bmatrix} I & 0 \\ 0 & I \end{bmatrix} \begin{bmatrix} e \\ z \end{bmatrix} + \begin{bmatrix} 0 & 0 \\ 0 & H \end{bmatrix} \begin{bmatrix} u_p \\ y \end{bmatrix} \end{aligned} \tag{5.69}$$

where u_p denotes manually commanded flap deflections, if present. Finally, it should be noted that the tracking capability from section 5.4.2 can be added by modifying the control input to $u_c = -K\hat{x} + \bar{N}r$, yielding the new equations:

$$\begin{cases} \dot{z}(t) = (F - TBK)z(t) + TBu_p(t) + (L - TBKH)y(t) + TB\bar{N}r \\ \\ \hat{x}(t) = z(t) + Hy(t) \end{cases} \tag{5.70}$$

or, equivalently, the closed-loop equations for the UIO, with LQ tracker:

$$\begin{bmatrix} \dot{e} \\ \\ \dot{z} \end{bmatrix} = \begin{bmatrix} (F - TBK) & 0 \\ \\ 0 & (F - TBK) \end{bmatrix} \begin{bmatrix} e \\ \\ z \end{bmatrix} + \begin{bmatrix} 0 & 0 & 0 \\ \\ TB & (L - TBKH) & TB\bar{N} \end{bmatrix} \begin{bmatrix} u_p \\ \\ y \\ \\ r \end{bmatrix}$$

$$\begin{bmatrix} e \\ \\ \hat{x} \end{bmatrix} = \begin{bmatrix} I & 0 \\ \\ 0 & I \end{bmatrix} \begin{bmatrix} e \\ \\ z \end{bmatrix} + \begin{bmatrix} 0 & 0 & 0 \\ \\ 0 & H & 0 \end{bmatrix} \begin{bmatrix} u_p \\ \\ y \\ \\ r \end{bmatrix} \tag{5.71}$$

This formulation allows estimation of the shape coefficients, while commanding desired lift distributions and simultaneously alleviating the loads caused by an unknown gust. In the Luenberger observer, there is usually a reasonable amount of design freedom that can be explored towards making the observer error insensitive to some of the inputs. The UIO takes advantage of this design freedom to converge regardless of some of the inputs. As a limitation, the maximum number of disturbances that can be decoupled cannot be larger than the number of the independent measurements [140]. It is also possible to estimate the gust magnitude over time, according to the following relation:

$$\hat{u}_g = (CB_g)^+ \left[\dot{\hat{y}} - CA\hat{x} - CBu \right] \tag{5.72}$$

where "+" denotes the pseudo-inverse of the matrix, and $\dot{\hat{y}}$ is the numerical derivative of the output estimation

5.6.2 Gust load alleviation results, with Unknown Input Observer (UIO)

The UIO structure presented in Eq. (5.69) is used to estimate the gust magnitude and the shape coefficients over time, for the same discrete gust already presented in section 5.5.4. The results obtained with UIO are presented as dot markers in Fig. 5.15, where they are superimposed on those results already given in Fig. 5.12 for the Luenberger observer. Once the observer converges, the results are practically identical, but now the gust input is not assumed known *a priori*.

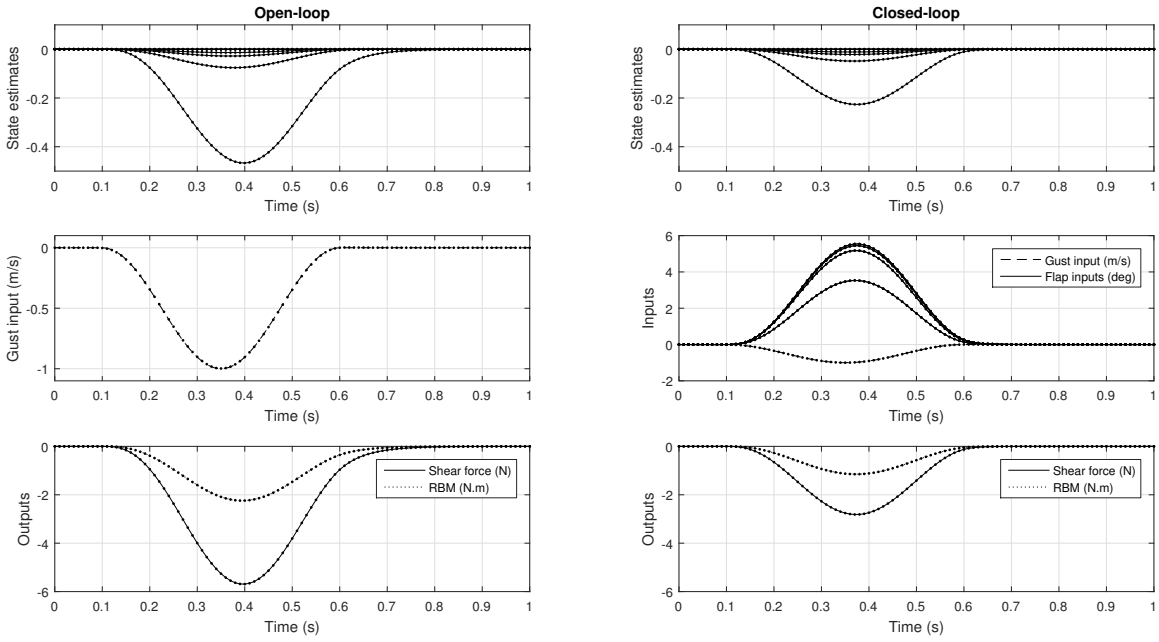

Figure 5.15: System response to '1-cos' discrete gust in open-loop (left) and closed-loop (right), using Unknown Input Observer (UIO).

The differences between the estimated gust magnitude and the actual gust profile used in the simulation are plotted in Fig. 5.16. It should be noted that the error in the gust estimation is practically negligible (less than 0.004 m/s) during the entire gust disturbance. This approach is extremely interesting, since it avoids the necessity of measuring the flow field ahead of the wing using a LIDAR system, for example. In the present work, the gust field is assumed uniform in space, therefore one variable suffices to describe the gust over time. More complex, spatially-varying gust fields could also be estimated, if additional independent measurements are available. For example, one extra bending moment sensor at some spanwise location would allow estimation of one additional unknown input, so that two inputs could be used to model the gust field. In this case, the gust could admit one value for each side of the wing, as opposed to one value for all points in space, or the gust magnitude can vary linearly along the span.

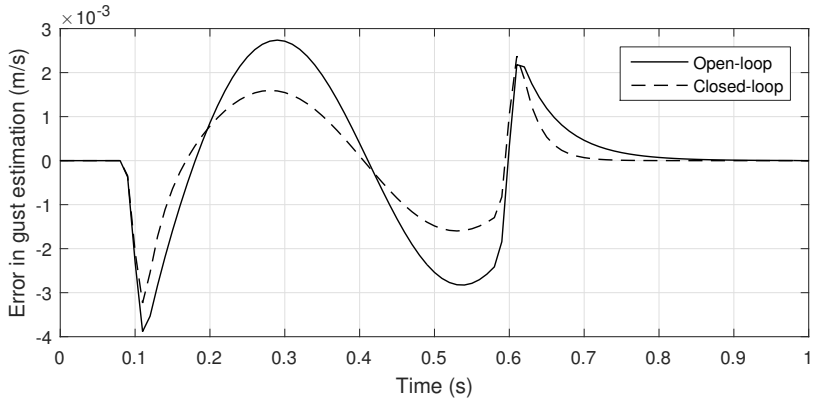

Figure 5.16: Error in gust magnitude estimation using Unknown Input Observer (UIO).

5.7 Chapter summary

This chapter builds upon the results from the previous chapters and deals with the core objective of this dissertation, i.e. controlling the distribution of loads along the wingspan. After identifying the eigenvalues and mode shapes in Chapter 4, there were some additional steps necessary in order to achieve a model suitable for shape control. First, it was necessary to define the set of expansion functions Ψ, which is used to represent the lift distribution. It was shown that choosing the system eigenfunctions as Ψ yields simplifications in the model. Second, it was necessary to define a threshold for model truncation, i.e. the number of modes that would be kept in the reduced-order model. Among the many criteria that can be employed, the IMSE was intuitive and simple to implement. When commanding an elliptical lift distribution, it was shown that 8 mode shapes would provide sufficient spatial bandwidth, in the sense that the IMSE was less than 5%.

In order to properly track 8 shape coefficients, it is necessary to have 8 independent control effectors (flaps). Additionally, the location and size of these flaps affect the performance of the final controller. The problem of defining these parameters was denoted as the spatial design of the controller. Using constrained nonlinear optimization, it was found that a uniform flap distribution was remarkably close to the optimal results, according to 3 different metrics. After fixing the spatial aperture of the actuators, the final state-space realization of the system was obtained and temporal controllers were designed.

Initially, a Linear Quadratic Tracker was designed to follow a reference set of 8

shape coefficients, assuming full state feedback was available. This simple formulation was used to assess the effect of two non-optimal flap distributions on the performance of the LQT. As a result, it was found that the uniform distribution allowed to reduce the flap deflections and rate requirements.

For the gust alleviation problem, the aerodynamic model input was augmented with a gust input. The observability of states was investigated and it was determined that a single accelerometer can be employed to observe the states associated with symmetric modes, whereas a gyrometer provides estimates for the coefficients associated with anti-symmetric modes. Interestingly, this result does not depend on the number of modes kept in the reduced-order model. Assuming that the gust profile over time is known, then a Luenberger observer can be used to estimate all shape coefficients.

The normalized aerodynamic mode shapes were converted into spanwise loads, including shear force and bending moment distributions. Therefore, if the shape coefficients are estimated, it is possible to reconstruct these loads over time, for all stations of the wing. Alternatively, this information can be used to model additional sensors along the span, in order to improve observability of the shape coefficients. Finally, the modal components of shear force and bending moment distributions can be used to design weighting matrices for the LQT that penalize the loads across all sections more equally. In the results showed in this chapter, all shape coefficients were penalized equally, and the loads were simply a consequence. The largest shear forces and bending moments were generated at the wing root. By properly designing the weights, it is possible to penalize each mode differently, in order to distribute the

load more evenly along the span.

The Luenberger observer required knowledge of the gust profile over time. In order to circumvent this limitation, the Unknown Input Observer (UIO) was used. It was shown that the special structure of this observer decouples the state estimation from the exogenous input. The closed-loop system allowed alleviation of loads caused by unknown gust inputs, while estimating the loads distributions over time. Optionally, the system can also admit a reference set of 8 shape coefficients, in order to track a desired lift distribution. The main limitation of the UIO is that only a subset of the inputs can be decoupled from the state estimation. Specifically, the number of independent measurements available must not be less than the number of exogenous inputs.

Chapter 6

Conclusions and future work

This chapter concludes this dissertation. Initially, the summary of the research is presented in section 6.1, and then the main contributions of this work are emphasized in section 6.2. Finally, the suggestions for future work are provided in section 6.3.

6.1 Summary

This work presented a novel methodology to control the wing spanwise lift distribution, based on techniques typically used for shape control of flexible structures. The unsteady aerodynamics of the wing was modeled using Unsteady Lifting-Line Theory (ULLT) and Unsteady Vortex Lattice Method (UVLM). Although based on potential flow, these methods provided a good trade-off between model accuracy and computational burden. Both models yielded a linear, state-space model, for which the inputs are trailing edge flap deflections, uniformly distributed along the span, whereas the outputs are local lift coefficient sampled along the span. Both models are capable of

modeling the spatial-temporal behavior of the lift distribution. However, even for reasonable spatial discretizations, these models yielded hundreds (ULLT) or thousands (UVLM) of states, which are not amenable for controller synthesis.

The model-order was reduced using the Eigensystem Realization Algorithm (ERA), which is also suitable for modal identification. Regarding the modal parameters identified, both models (ULLT and UVLM) yielded essentially the same mode shapes. Moreover, the dominant eigenvalues lie along the negative real axis for both cases. Since similar modal identification results were obtained from two independent models, this is an indication that the results are reliable.

Once the aerodynamic mode shapes were obtained, the output of the reduced-order model was expanded as a linear superposition of these shapes, yielding shape coefficients as outputs. Some of the most relevant criteria used to define a threshold for model truncation were discussed. In this work, the Integrated Mean Square Error (IMSE) with respect to a desired shape was used to determine the minimum number of mode shapes required. For the control task of achieving an elliptical lift distribution, it was found that 8 mode shapes would yield an IMSE less than 5%. Using more than 8 shapes would not improve the shape representation significantly.

In this work, the controller was assumed separable in space and time, i.e. the controller implemented for shape control consisted of a spatial part and a temporal part. The spatial part was designed first and consisted in obtaining the location and apertures of the flaps that best couple into the aerodynamic mode shapes. Different criteria for evaluating candidate actuator distributions were presented, namely minimal condition number, balanced participation, decoupled output space and maxi-

mization of the minimum singular value. The flap distribution was designed according to each of these criteria. Interestingly, the optimal results from these different criteria are quite similar to a uniform distribution. In other words, the uniform distribution essentially provides all of the features listed in the criteria above. For this reason, this particular actuator distribution was chosen and a purely temporal MIMO system was obtained, mapping 8 flap deflections into 8 shape coefficients.

Once the spatial design is defined, the temporal part of the controller can be designed. A Linear Quadratic Tracker using full state feedback was synthesized for shape control, enabling tracking of any set of 8 shape coefficients. Moreover, this controller was used to show the relevance of the spatial design of flaps. When non-optimal flap distributions are used, the response from the actual plant (full-order model) deviates significantly from that predicted by the reduced-order model. Moreover, the inputs generated by the controller require large flap deflections and high actuator rates.

For actual applications, however, measuring the system states (shape coefficients) is not feasible. It was shown that the shape coefficients for any number of modes kept in the reduced-order model can be obtained via state observer (Luenberger observer). All symmetric modes are observable from a single accelerometer sensor placed at the wing root, whereas a rate gyro can provide angular acceleration, from which all anti-symmetric aerodynamic modes are observable. From flight dynamics equations, it is possible to measure in-flight total lift and total rolling moment using an inertial unit (3-axes accelerometers and 3-axes gyrometers). Therefore, this methodology can be easily extended for general flight conditions.

For gust alleviation assessment, the input vector was augmented with gust magni-

tude. The gust was assumed vertical and uniform at all points in space. The Linear Quadratic Tracker and state observer were used to demonstrate closed-loop behavior under the influence of a discrete gust ('1-cos' profile). The simulation results indicated that the controller synthesized, based on the truncated model representation, is effective in reducing the gust loads (shear force and bending moment at the wing root) by 50%, as compared to the open-loop case. The loads could be reduced even further, but it would require higher flap rates. In the simulations performed with gusts, the control effort was penalized such that the flap rates were kept below 35 deg/s.

The Luenberger observer assumed that all inputs (flaps and gust magnitude) and all outputs (total lift and total rolling moment) were known. However, for practical applications, measuring the gust magnitude over time is very challenging. To avoid this requirement, the Unknown Input Observer (UIO) was used. It was shown that the special structure of this observer decouples the state estimation from the exogenous input. If an UIO exists, it will converge and yield state estimates, regardless of the unknown gust input. The main limitation is that the number of independent measurements available as system outputs must not be less than the number of exogenous inputs expected.

6.2 Key contributions of this work

6.2.1 Development of unsteady aerodynamic models

The first challenge in this work was modeling the unsteady aerodynamic flow around a 3D wing, with moving control surfaces. The Lifting-Line augmented with Wagner's theory was the first approach adopted (ULLT), followed by the Vortex Lattice method with finite wake history (UVLM). These two models provided an adequate trade-off between accuracy and computational cost. Other methods, such as Navier-Stokes equations, would also be able to model unsteadiness and would improve accuracy, but with prohibitive computational costs, mainly due to the moving flaps, which would require unsteady analysis with a moving mesh geometry.

6.2.2 Modal identification of aerodynamic modes

This work presents the dominant eigenvalues and mode shapes associated to unsteady flow around a 3D wing. The results were obtained using two independent models, namely the Unsteady Lifting-Line Theory (ULLT) and the Unsteady Vortex Lattice Method (UVLM). As discussed in Chapter 4, the aerodynamic mode shapes were compared and found to be identical. The dominant eigenvalues also lie in the negative real axis for both methods. In the literature survey conducted, there were no references to purely aerodynamic mode shapes. Therefore, it is believed that the aerodynamic shapes presented in this work are a new result, that should be explored to simplify the spatial control of distributed aerodynamic systems. Moreover, it was observed that these aerodynamic modes retain some of the fundamental concepts

of modal decomposition theory. In contrast to structural systems, the aerodynamic shapes are not orthogonal to each other, and the aerodynamic eigenvalues are located very close to each other in the frequency spectrum. Nevertheless, it was possible to obtain these modal parameters using the Eigensystem Realization Algorithm (ERA).

6.2.3 Spatial design of actuators

It was shown in Section 5.4.4 that properly sized flaps are crucial to achieve shape control. The response of the full-order plant can always be represented as a superposition of its eigenfunctions or mode shapes, regardless of the flap distribution. However, if the flaps are spatially designed to strongly couple to those shapes (in the sense of the metrics presented in Section 5.3.1), then a number of advantages can be obtained. First, the flap deflections and rates required will be reduced, as compared to a non-optimal flap distribution used in the same shape control task (see Fig. 5.9). Second, the actual plant response will be very close to that predicted by the truncated plant. Since the controller is based on the truncated representation, the controller will also work well when applied to the full-order plant. Third, by maximizing the projection of input signals (flap deflections) onto the first 8 modes, this approach naturally reduces the excitation of higher order modes. Finally, this methodology yields an elegant solution to incorporate several control surfaces into the lift distribution problem, such as the VCCTEF [69, 70], shown in Fig. 1.6.

6.2.4 Observability of aerodynamic modes

Another relevant result presented in this study is that all aerodynamic shape coefficients can be inferred from simple measurements. More specifically, the symmetric modes are observable from some symmetric metric, such as total wing lift, or vertical acceleration, whereas the anti-symmetric modes can be observed using rolling moment or roll rate measurements. It was shown that this result does not depend on the number of modes kept in the reduced-order model. This methodology can be easily expanded to experiments in wind tunnel or wings in free-flight.

6.2.5 Decoupling of gust input in the state estimation

A large amount of effort in this work was devoted to obtain a methodology that could be used in practical applications. For this reason, the observability of aerodynamic shape coefficients was analyzed and guaranteed from feasible measurements. Similarly, it was shown that a Luenberger observer would require knowledge of all inputs and outputs. If exogenous inputs are present, such as gusts, then it would be necessary to measure the gust field ahead of the wing in real-time. In order to avoid this requirement, a new observer structure is used. The Unknown Input Observer (UIO) decouples the state estimation process from the gust inputs. The results from the UIO are essentially identical to those obtained with the Luenberger observer, for which the gust temporal profile was assumed known.

6.2.6 Controller synthesis for Distributed Parameter Systems

The methodology developed in this work can be applied to synthesize spatial-temporal controllers for distributed systems in general, including non-self-adjoint cases. For many systems of interest, it is not possible to obtain the modal parameters analytically, thus requiring numerical approaches such as the Finite Element Method. The methodology can still be applied even if the full-order model is nonlinear, but there are two main requirements. First, it must be possible to approximate the system behavior using a state-space representation, which is obtained by the ERA. Second, the input-output behavior of the system must be adequately described by a subset of states, which is crucial for efficient reduced order models. In other words, the plot of Hankel Singular Values (HSV) obtained from ERA must decay in magnitude relatively fast, as shown in Fig. 4.1. Finally, these shape control techniques are typically applied to self-adjoint systems, which have orthogonal mode shapes. In this work, it was also shown that the orthogonality of the shapes is not a requirement for shape control.

6.3 Recommendations for future work

This work presented novel results for lift distribution control using shape control concepts. Still, there are several improvements that could be implemented in the future. The first natural extension of this work consists in applying the methodology

to a complete aeroelastic system, i.e. adding structural dynamics to the unsteady aerodynamics model. Typically, aeroelastic mode shapes are described as structural deformations in bending or torsion. However, the description depends entirely on the output of the model used in the modal identification algorithm. If the local lift coefficient at each station is appended to the structural deformation, as one long output vector, then the aeroelastic mode shapes identified will also describe the lift distribution associated to each mode. In other words, one could implement shape control in terms of structural deformation, in terms of lift distribution profile, or a combination of both. This approach will certainly be interesting to a Very Flexible Aircraft (VFA), which features significant interaction between aerodynamics and structures [66, 78, 82, 83].

Once a complete aeroelastic model is obtained, the critical gust parameters defined in [34] should be investigated, in order to determine the gust temporal profile that causes the maximum structural loads. In this work, the wing was considered a rigid body. For this reason, the gust peak was arbitrarily chosen as -1 m/s, since this parameter makes little difference for a rigid wing. The load reduction ratios obtained would be very similar, regardless of the gust magnitude. For a flexible wing, however, there is a critical gust length, which is related to the frequency of excitation. This particular gust profile usually excites the first structural mode (in bending or torsion), which significantly increases the loads. Shorter gust lengths cause higher frequency inputs, which are naturally filtered by the structure. For longer gust lengths, the excitation frequency is lower, i.e. away from the first resonance peak, which causes lower loads.

The present work investigated the control of lift distribution, which generates shear force and bending moment loads. However, the torsional loads caused by pitching moment distribution along the span can be relevant as well. The UVLM could be used to model pitching moment variations along the wingspan, provided that the chordwise discretization is reasonably refined (e.g. 16 panels or more). Therefore, the distribution of pitching moment could also be controlled, in addition to lift distribution. This approach would also allow computation of the torsional moments at any station of interest along the wing, and then use this output in the cost function of the controller synthesis. A similar argument for spanwise drag distribution would yield control of in-plane bending moment and shear force. However, unsteady modeling of drag using UVLM is a challenge that only recently has been addressed [98, 104, 109].

In order to improve the reliability of the modal identification results, it would be interesting to perform modal identification using high-order CFD (e.g. Navier-Stokes equations). The advantages of computational methods lie in the application of the excitation at any desired point, and measurements at virtually any points of interest. However, it would be very difficult to validate computational results without an experimental database, and the computational cost could be prohibitive. Another possibility is to directly perform experimental modal identification of the aerodynamic modes, in a wind tunnel. In this case, the main challenge would be how to design an excitation system to apply pointwise loads aerodynamically, such as a local gusts at any spanwise station, or several flaps along the span with very small spanwise apertures. Moreover, the measurement of unsteady lift along the entire span would also be very difficult, because it requires a high number of pressure sensors distributed

along the top and bottom surfaces of the wing.

The experimental setup required for modal identification is much more complicated than that required for validation of controllers. The simple measurements at the wing root (shear force and bending moment) would suffice to estimate all shape coefficients and the gust magnitude using the Unknown Input Observer (UIO) approach.

Another possibility to extend this work is to investigate the estimation problem with non-uniform gusts along the span. This problem is relevant to high aspect ratio vehicles, since it is difficult to ensure that all points of the wing are subject to the same gust magnitude at a given time. The UIO can be used to estimate the parameters that model this spatial variation of the gust along the span. For example, the uniform gust only requires one parameter (gust magnitude), but the gust might vary linearly along the span, thus requiring two parameters over time to entirely describe the gust field. Decomposing the unknown gust profile in the sense of a Fourier series would also be possible, with each Fourier coefficient being a time-varying unknown input. However, this approach would require as many independent measurements as the number of elements in the truncated Fourier series.

The methodology presented herein yields a purely temporal MIMO system, enabling application of modern control techniques that are usually not applicable to spatial-temporal systems. Therefore, robust controllers can easily be explored. For future developments, continuous gusts (turbulence) can also be studied. In this case, it would be interesting to make the controller robust to this high frequency disturbance. Moreover, the closed-loop system can be designed to be robust to any modeling

errors induced by the model-order reduction.

Finally, it was clear that the performance of the actuators can significantly constrain the performance of a gust alleviation system. In this work, the actuators were assumed linear and were limited to low deflection rates via proper weighting matrices Q and R. The effect of saturations in flap deflection and rates can be investigated using Model Predictive Control (MPC). If the actuators are able to work at maximum operating rates, it is expected that the load alleviation capability of the controller would be improved.

Appendices

Appendix A

Equivalence between the convolution integral and Duhamel's integral

Method 1: Consider a linear system, whose representation in Laplace domain is $G(s)$, relating the output $Y(s)$ to the input $U(s)$:

$$Y(s) = G(s)U(s) \tag{A.1}$$

For an impulse input, $U(s) = 1$, the impulse response $H(s)$ is given by $H(s) = G(s)$. Also, for a step impulse $U(s) = 1/s$, the step response $A(s)$ is given by $A(s) = G(s)/s$. Hence, the impulse and step responses are related by $A(s) = H(s)/s$ in the frequency-domain.

Now, apply Laplace transform to the convolution formulation:

$$\mathcal{L}\{y(t)\} = \mathcal{L}\left\{\int_0^t f(\tau)h(t-\tau)\mathrm{d}\tau\right\} = F(s)H(s) \tag{A.2}$$

where h(t) is the impulse response and f(t) is any arbitrary input, both in time-domain. Use the fact that $A(s) = H(s)/s$:

$$\mathcal{L}\{y(t)\} = sF(s)(\frac{H(s)}{s}) = sF(s)A(s) \tag{A.3}$$

From the Laplace transform for time-derivative, obtain an expression for $s.F(s)$:

$$\mathcal{L}\left\{\frac{\mathrm{d}f(t)}{\mathrm{d}t}\right\} = sF(s) - f(0) \tag{A.4}$$

$$sF(s) = \mathcal{L}\{f'(t)\} + f(0) \tag{A.5}$$

Then:

$$\mathcal{L}\{y(t)\} = \mathcal{L}\{f'(t)\}A(s) + f(0)A(s) \tag{A.6}$$

$$\mathcal{L}\{y(t)\} = \mathcal{L}\{f'(t)\}\mathcal{L}\{A(t)\} + f(0)\mathcal{L}\{A(t)\} \tag{A.7}$$

Apply inverse Laplace transform, and use the convolution formulation once more:

$$y(t) = \int_0^t \frac{\mathrm{d}f(\tau)}{\mathrm{d}\tau}A(t-\tau)\mathrm{d}\tau + f(0)A(t) \tag{A.8}$$

Method 2:

Find a relationship between the indicial (step) response $A(t)$ and the system's impulse response $h(t)$. First, apply Laplace transform to the time-derivative of $A(t)$:

$$\mathcal{L}\{A'(t)\} = sA(s) - A(0) = s\frac{H(s)}{s} - A(0) = H(s) - A(0) \tag{A.9}$$

Apply inverse Laplace transform:

$$A'(t) = h(t) - A(0)\mathcal{L}^{-1}\{1\} = h(t) - A(0)\delta(t) \tag{A.10}$$

$$h(t) = A'(t) + A(0)\delta(t) \tag{A.11}$$

where $\delta(t)$ is the Dirac delta. Substitute in the convolution integral formulation:

$$\begin{aligned} y(t) &= \int_0^t f(\tau)h(t-\tau)\mathrm{d}\tau \\ &= \int_0^t f(\tau)A'(t-\tau)\mathrm{d}\tau + A(0)\int_0^t f(\tau)\delta(t-\tau)\mathrm{d}\tau \end{aligned} \tag{A.12}$$

Now, use:

$$A'(t-\tau) = \frac{\mathrm{d}A(t-\tau)}{\mathrm{d}(t-\tau)} = \frac{\mathrm{d}A(t-\tau)}{\mathrm{d}\tau}\frac{\mathrm{d}\tau}{\mathrm{d}(t-\tau)} = -\frac{\mathrm{d}A(t-\tau)}{\mathrm{d}\tau} \tag{A.13}$$

$$\int_0^t f(\tau)\delta(t-\tau)\mathrm{d}\tau = \int_0^t f(\tau)\delta(\tau-t)\mathrm{d}\tau = f(t) \tag{A.14}$$

Yielding:

$$y(t) = -\int_0^t f(\tau)\frac{\mathrm{d}A(t-\tau)}{\mathrm{d}\tau}\mathrm{d}\tau + A(0)f(t) \tag{A.15}$$

Integrate by parts:

$$y(t) = -f(\tau)A(t-\tau)|_{\tau=0}^t + \int_0^t \frac{\mathrm{d}f(\tau)}{\mathrm{d}\tau}A(t-\tau)\mathrm{d}\tau + A(0)f(t) \tag{A.16}$$

$$y(t) = -f(t)A(0) + f(0)A(t) + \int_0^t \frac{\mathrm{d}f(\tau)}{\mathrm{d}\tau}A(t-\tau)\mathrm{d}\tau + A(0)f(t) \tag{A.17}$$

$$y(t) = \int_0^t \frac{\mathrm{d}f(\tau)}{\mathrm{d}\tau}A(t-\tau)\mathrm{d}\tau + f(0)A(t) \tag{A.18}$$

Therefore, Duhamel's integral and convolution integral are equivalent concepts. For another derivation of Duhamel's integral, see Ref. [93, Appendix C].

Bibliography

[1] J. E. Hubbard. *Spatial Filtering for the Control of Smart Structures: An Introduction*. Springer, 2009. doi:10.1007/978-3-642-03804-4.

[2] C. L. Nickol. Technologies and concepts for reducing the fuel burn of subsonic transport aircraft. In *NATO AVT-209 Workshop on Energy Efficient Technologies*, 2012.

[3] W. R. Graham, C. A. Hall, and M. V. Morales. The potential of future aircraft technology for noise and pollutant emissions reduction. *Transport Policy*, 34:36–51, 2014.

[4] European Commission. European Aeronautics: A Vision for 2020, Office for Official Publications of the European Communities, Luxembourg, ISBN 92-894-0559-7, 2001.

[5] European Commission. Flightpath 2050: Europes Vision for Aviation, Publications Office of the European Union, Luxembourg, ISBN 978-92-79-19724-6, 2011.

[6] B. M. Yutko, N. Titchener, C. Courtin, M. Lieu, L. Wirsing, J. Tylko, J. T. Chambers, T. W. Roberts, and C. S. Church. Conceptual design of a D8 commercial aircraft. In *17th AIAA Aviation Technology, Integration, and Operations Conference*, page 3590, 2017.

[7] D. L. Huff. Nasa glenns contributions to aircraft engine noise research. *Journal of Aerospace Engineering*, 26(2):218–250, 2012.

[8] Y. Liu, A. Elham, P. Horst, and M. Hepperle. Exploring vehicle level benefits of revolutionary technology progress via aircraft design and optimization. *Energies*, 11(1):166, 2018. doi:10.3390/en11010166.

[9] G. Bezos-O'Connor, M. Mangelsdorf, C. Nickol, H. Maliska, A. Washburn, and R. Wahls. Fuel efficiencies through airframe improvements. In *3rd AIAA Atmospheric Space Environments Conference*, page 3530, 2011.

[10] M. K. Bradley, C. K. Droney, and T. J. Allen. Subsonic ultra green aircraft research. Phase 2. Volume 1: Truss braced wing design exploration. 2015.

[11] M. Drela. Development of the D8 transport configuration. In *29th AIAA Applied Aerodynamics Conference*, page 3970, 2011.

[12] M. K. Bradley and C. K. Droney. Subsonic ultra green aircraft research: Phase 2. Volume 2: Hybrid electric design exploration. 2015.

[13] E. M. Greitzer, P. Bonnefoy, E. DelaRosaBlanco, C. Dorbian, M. Drela, D. Hall, R. Hansman, J. Hileman, R. Liebeck, J. Levegren, *et al.* N+3 aircraft concept designs and trade studies. Volume 1. Technical Report NASA/CR-2010-216794/VOL1, 2010.

[14] M. M. D'Angelo, J. Gallman, V. Johnson, E. Garcia, J. Tai, and R. Young. N+3 small commercial efficient and quiet transportation for year 2030-2035. Technical Report NASA/CR2010-216691, 2010.

[15] International Air Transport Association. IATA technology roadmap. Technical report, 2013. Available online: `http://www.iata.org/whatwedo/environment/Documents/technology-roadmap-2013.pdf` (accessed: 28 Jan 2019).

[16] J. Xu. *Aircraft design with active load alleviation and natural laminar flow.* PhD thesis, Stanford University, 2012.

[17] J. Xu and I. Kroo. Aircraft design with active load alleviation and natural laminar flow. *Journal of Aircraft*, 51(5):1532–1545, 2014. `doi:10.2514/1.C032402`.

[18] M. K. Bradley and C. K. Droney. Subsonic Ultra Green Aircraft Research: Phase I Final Report. Technical Report NASA/CR-2011-216847, 2011.

[19] C. Rossow, M. Hepperle, and H. von Geyr von Schweppenburg. *The 1g-wing, Visionary Concept Or Naive Illusion?* DLR, Deutsches Zentrum für Luft- und Raumfahrt, 2016.

[20] M. Karpel. Design for active flutter suppression and gust alleviation using state-space aeroelastic modeling. *Journal of Aircraft*, 19(3):221–227, 1982. `doi:10.2514/3.57379`.

[21] M. D. Olson. Finite elements applied to panel flutter. *AIAA Journal*, 5(12):2267–2270, 1967. `doi:10.2514/3.4422`.

[22] M. D. Olson. Some flutter solutions using finite elements. *AIAA Journal*, 8(4):747–752, 1970. `doi:10.2514/3.5751`.

[23] T. Theodorsen. General theory of aerodynamic instability and the mechanism of flutter. Technical Report NACA-ARR-1935, 1935.

[24] E. G. Broadbent. *Flutter prediction in practice.* North Atlantic Treaty Organization, Advisory Group for Aeronautical Research and Development, 1956.

[25] E. Albano and W. P. Rodden. A doublet-lattice method for calculating lift distributions on oscillating surfaces in subsonic flows. *AIAA Journal*, 7(2):279–285, 1969. doi:10.2514/3.5086.

[26] K. Roger. Airplane math modeling methods for active control design. Technical Report AGARD-CP-288, 1977.

[27] M. Karpel. *Design for Active and Passive Flutter Suppression and Gust Alleviation*. PhD thesis, Stanford University, 1980.

[28] B. Moore. Principal component analysis in linear systems: Controllability, observability, and model reduction. *IEEE transactions on automatic control*, 26(1):17–32, 1981. doi:10.1109/TAC.1981.1102568.

[29] O. Sensburg, J. Becker, H. Lusebrink, and F. Weiss. Gust load alleviation on Airbus A300. In *International Council of the Aeronautical Sciences*, number ICAS 82-2.1.1, 1982.

[30] D. McLean. Gust-alleviation control systems for aircraft. In *Proceedings of the Institution of Electrical Engineers*, volume 125, pages 675–685. IEE, 1978. doi:10.1049/piee.1978.0159.

[31] R. A. Prasad. *Application of optimal control to structural load alleviation control systems*. PhD thesis, Loughborough University of Technology, 1980.

[32] D. McLean and R. Prasad. A structure load alleviation control system for a large aircraft. *Transactions of the Institute of Measurement and Control*, 2(1):25–37, 1980. doi:10.1177/014233128000200104.

[33] B. Liebst, W. Garrard, and J. A. Farm. Design of a multivariable flutter suppression/gust load alleviation system. *Journal of Guidance, Control, and Dynamics*, 11(3):220–229, 1988. doi:10.2514/3.20297.

[34] Federal Aviation Administration (FAA), U.S. Department of Transportation. Advisory Circular 25.341-1, Subject: Dynamic Gust Loads, Date: 12/12/14.

[35] S. Gage. Creating a unified graphical wind turbulence model from multiple specifications. In *AIAA Modeling and simulation technologies conference and exhibit*, page 5529, 2003. doi:10.2514/6.2003-5529.

[36] C. D. Regan and C. V. Jutte. Survey of applications of active control technology for gust alleviation and new challenges for lighter-weight aircraft. Technical Report NASA/TM-2012-216008, NASA Dryden Flight Research Center, Edwards, CA, USA, 2012.

[37] F. M. Hoblit. *Gust loads on aircraft: concepts and applications*. American Institute of Aeronautics and Astronautics, 1988.

[38] T. L. Lomax. *Structural loads analysis for commercial transport aircraft: theory and practice*. American Institute of Aeronautics and Astronautics, 1996.

[39] J. Arnold and J. Dempster. Flight test evaluation of an advanced stability augmentation system for the B-52 aircraft. *Journal of Aircraft*, 6(4):343–348, 1969. doi:10.2514/3.44062.

[40] P. Burris and M. Bender. Aircraft load alleviation and mode stabilization (LAMS): B-52 system analysis, synthesis, and design. Technical Report AFFDL-TR-68-161, 1969.

[41] J. Wykes. Structural dynamic stability augmentation and gust alleviation of flexible aircraft. In *5th Annual Meeting and Technical Display*, page 1067, 1968. doi:10.2514/6.1968-1067.

[42] T. Disney. C-5A active load alleviation system. *Journal of Spacecraft and Rockets*, 14(2):81–86, 1977. doi:10.2514/3.57164.

[43] J. Johnston. Accelerated development and flight evaluation of active controls concepts for subsonic transport aircraft. Volume 1: Load alleviation/extended span development and flight tests. Technical Report NASA CR 159097, 1979.

[44] R. F. O'Connell. Design, development and implementation of an active control system for load alleviation for a commercial transport airplane. Technical report, Advisory Group for Aerospace Research and Development (AGARD), 1980.

[45] H. Hoenlinger, H. Zimmermann, O. Sensburg, and J. Becker. Structural aspects of active control technology. In *AGARD Conference Proceedings*, number 18. AGARD, 1995.

[46] R. Britt, J. Volk, D. Dreim, and K. Applewhite. Aeroservoelastic characteristics of the B-2 bomber and implications for future large aircraft. Technical report, Northrop Grumman Corp., 2000.

[47] S. Hecker and K.-U. Hahn. Advanced gust load alleviation system for large flexible aircraft. In *1st CEAS European Air and Space Conference*, number CEAS-2007-110, pages 523–530, 2007.

[48] M. Alam, M. Hromcik, and T. Hanis. Active gust load alleviation system for flexible aircraft: Mixed feedforward/feedback approach. *Aerospace Science and Technology*, 41:122–133, 2015. doi:10.1016/j.ast.2014.12.020.

[49] H. Hesse and R. Palacios. Dynamic load alleviation in wake vortex encounters. *Journal of Guidance, Control, and Dynamics*, 39(4):801–813, 2016. doi:10.2514/1.G000715.

[50] A. Wildschek, T. Haniš, and F. Stroscher. L_∞-optimal feedforward gust load alleviation design for a large blended wing body airliner. *Progress in flight dynamics, guidance, navigation, control, fault detection, and avionics*, 6:707–728, 2013. doi:10.1051/eucass/201306707.

[51] A. Wildschek, Z. Bartosiewicz, and D. Mozyrska. A multi-input multi-output adaptive feed-forward controller for vibration alleviation on a large blended wing body airliner. *Journal of Sound and Vibration*, 333(17):3859–3880, 2014. doi:10.1016/j.jsv.2014.04.021.

[52] Y. Zhao, C. Yue, and H. Hu. Gust load alleviation on a large transport airplane. *Journal of Aircraft*, 53(6):1932–1946, 2016. doi:10.2514/1.C033713.

[53] A. Mangalam, S. Mangalam, and P. Flick. Unsteady aerodynamic observables for gust load alleviation. In *49th AIAA/ASME/ASCE/AHS/ASC Structures, Structural Dynamics, and Materials Conference*, page 1725, 2008. doi:10.2514/6.2008-1725.

[54] K. T. Magar, G. W. Reich, A. M. Pankonien, and B. Smyers. Active gust alleviation using artificial hair sensors and feedforward control. In *AIAA Guidance, Navigation, and Control Conference*, page 1485, 2017. doi:10.2514/6.2017-1485.

[55] J. C. Ellsworth. Dynamic leading edge stagnation point determination utilizing an array of hot-film sensors with unknown calibration. In *55th AIAA Aerospace Sciences Meeting*, page 0250, 2017. doi:10.2514/6.2017-0250.

[56] K. T. Magar, A. M. Pankonien, G. W. Reich, and R. V. Beblo. Aerodynamic parameter prediction via artificial hair sensors with signal power in turbulent flow. *AIAA Journal*, 57(3):898–903, 2019. doi:10.2514/1.J057632.

[57] D. C. Soreide, R. K. Bogue, L. Ehernberger, and H. R. Bagley. Coherent LIDAR turbulence measurement for gust load alleviation. In *Optical Instruments for Weather Forecasting*, volume 2832, pages 61–76. International Society for Optics and Photonics, 1996. doi:10.1117/12.258887.

[58] S. M. Hannon, H. R. Bagley, and R. K. Bogue. Airborne doppler lidar turbulence detection: ACLAIM flight test results. *Proceedings of SPIE - The International Society for Optical Engineering*, 1999. doi:10.1117/12.351378.

[59] D. C. Soreide, R. K. Bogue, L. Ehernberger, S. M. Hannon, and D. A. Bowdle. Airborne coherent LIDAR for advanced in-flight measurements (ACLAIM) flight testing of the LIDAR sensor. In *9th Aviation, Range and Aerospace Meteorology*. American Meteorological Society, 2000.

[60] N. P. Schmitt, W. Rehm, T. Pistner, P. Zeller, H. Diehl, and P. Navé. The awiator airborne lidar turbulence sensor. *Aerospace Science and Technology*, 11(7-8):546–552, 2007. doi:10.1016/j.ast.2007.03.006.

[61] G. J. Rabadan, N. P. Schmitt, T. Pistner, and W. Rehm. Airborne lidar for automatic feedforward control of turbulent in-flight phenomena. *Journal of Aircraft*, 47(2):392–403, 2010. doi:10.2514/1.44950.

[62] H.-G. Giesseler, M. Kopf, P. Varutti, T. Faulwasser, and R. Findeisen. Model predictive control for gust load alleviation. *IFAC Proceedings Volumes*, 45(17):27–32, 2012. doi:10.3182/20120823-5-NL-3013.00049.

[63] J. Zeng, B. Moulin, R. D. Callafon, and M. Brenner. Adaptive feedforward control for gust load alleviation. *Journal of Guidance, control, and dynamics*, 33(3):862–872, 2010. doi:10.2514/1.46091.

[64] N. Fezans, H.-D. Joos, and C. Deiler. Gust load alleviation for a long-range aircraft with and without anticipation. *CEAS Aeronautical Journal*, pages 1–25, 2019. doi:10.1007/s13272-019-00362-9.

[65] R. M. Hueschen. Development of the Transport Class Model (TCM) aircraft simulation from a sub-scale Generic Transport Model (GTM) simulation. Technical Report NASA/TM2011-217169, 2011.

[66] S. Haghighat, H. H. T. Liu, and J. R. RA Martins. Model-predictive gust load alleviation controller for a highly flexible aircraft. *Journal of Guidance, Control, and Dynamics*, 35(6):1751–1766, 2012. doi:10.2514/1.57013.

[67] N. Fezans and H.-D. Joos. Combined feedback and LIDAR-based feedforward active load alleviation. In *AIAA Atmospheric Flight Mechanics Conference*, page 3548, 2017. doi:10.2514/6.2017-3548.

[68] N. Nguyen, U. Kaul, S. Lebofsky, E. Ting, D. Chaparro, and J. Urnes. Development of variable camber continuous trailing edge flap for performance adaptive aeroelastic wing. SAE Technical Paper 2015-01-2565, 2015. doi:10.4271/2015-01-2565.

[69] S. Lebofsky, E. Ting, K. V. Trinh, and N. T. Nguyen. Optimization for load alleviation of truss-braced wing aircraft with variable camber continuous trailing edge flap. In *33rd AIAA Applied Aerodynamics Conference*, page 2723, 2015. doi:10.2514/6.2015-2723.

[70] Y. Ferrier, N. T. Nguyen, E. Ting, D. Chaparro, X. Wang, C. C. de Visser, and Q. P. Chu. Active gust load alleviation of high-aspect ratio flexible wing aircraft. In *AIAA Guidance, Navigation, and Control Conference*, page 0620, 2018. doi:10.2514/6.2018-0620.

[71] T. E. Noll, J. M. Brown, M. E. Perez-Davis, S. D. Ishmael, G. C. Tiffany, and M. Gaier. Investigation of the Helios prototype aircraft mishap. volume i. mishap report. 2004.

[72] T. E. Noll, S. D. Ishmael, B. Henwood, M. E. Perez-Davis, G. C. Tiffany, J. Madura, M. Gaier, J. M. Brown, and T. Wierzbanowski. Technical findings, lessons learned, and recommendations resulting from the Helios prototype vehicle mishap. In *UAV Design Processes/Design Criteria for Structures*, 2007.

[73] D. K. Schmidt and D. L. Raney. Modeling and simulation of flexible flight vehicles. *Journal of Guidance, Control, and Dynamics*, 24(3):539–546, 2001. doi:10.2514/2.4744.

[74] M. J. Patil and D. H. Hodges. Flight dynamics of highly flexible flying wings. *Journal of Aircraft*, 43(6):1790–1799, 2006. doi:10.2514/1.17640.

[75] C. M. Shearer and C. E. Cesnik. Nonlinear flight dynamics of very flexible aircraft. *Journal of Aircraft*, 44(5):1528–1545, 2007. doi:10.2514/1.27606.

[76] M. J. Patil, D. H. Hodges, and C. E. S. Cesnik. Nonlinear aeroelasticity and flight dynamics of high-altitude long-endurance aircraft. *Journal of Aircraft*, 38(1):88–94, 2001. doi:10.2514/2.2738.

[77] M. J. Patil and D. H. Hodges. On the importance of aerodynamic and structural geometrical nonlinearities in aeroelastic behavior of high-aspect-ratio wings. *Journal of Fluids and Structures*, 19(7):905–915, 2004. doi:10.1016/j.jfluidstructs.2004.04.012.

[78] C. E. S. Cesnik, P. J. Senatore, W. Su, E. M. Atkins, and C. M. Shearer. X-HALE: a very flexible unmanned aerial vehicle for nonlinear aeroelastic tests. *AIAA Journal*, 50(12):2820–2833, 2012. doi:10.2514/1.J051392.

[79] F. Afonso, J. Vale, É. Oliveira, F. Lau, and A. Suleman. A review on non-linear aeroelasticity of high aspect-ratio wings. *Progress in Aerospace Sciences*, 89:40–57, 2017. doi:10.1016/j.paerosci.2016.12.004.

[80] J. Murua, R. Palacios, and J. Graham. Open-loop stability and closed-loop gust alleviation on flexible aircraft including wake modeling. In *53rd AIAA/ASME/ASCE/AHS/ASC Structures, Structural Dynamics and Materials Conference*, page 1484, 2012. doi:10.2514/6.2012-1484.

[81] M. Dillsaver, C. Cesnik, and I. Kolmanovsky. Gust load alleviation control for very flexible aircraft. In *AIAA Atmospheric Flight Mechanics Conference*, page 6368, 2011. doi:10.2514/6.2011-6368.

[82] R. G. Cook, R. Palacios, and P. Goulart. Robust gust alleviation and stabilization of very flexible aircraft. *AIAA Journal*, 51(2):330–340, 2013. doi:10.2514/1.J051697.

[83] R. J. Simpson, R. Palacios, H. Hesse, and P. Goulart. Predictive control for alleviation of gust loads on very flexible aircraft. In *55th AIAA/ASMe/ASCE/AHS/SC Structures, Structural Dynamics, and Materials Conference*, page 0843, 2014. doi:10.2514/6.2014-0843.

[84] Y. Wang, A. Wynn, and R. Palacios. Nonlinear aeroelastic control of very flexible aircraft using model updating. *Journal of Aircraft*, 55(4):1551–1563, 2017. doi:10.2514/1.C034684.

[85] E. Livne. Active flutter suppression - plans for assessing the technologys state of the art. *Joint advanced materials and structures center of excellence technical review. Seattle, WA*, 2014.

[86] J. Fuller. Evolution of airplane gust loads design requirements. *Journal of Aircraft*, 32(2):235–246, 1995. doi:10.2514/3.46709.

[87] T. Kim. System identification for coupled fluid-structure: Aerodynamics is aeroelasticity minus structure. *AIAA Journal*, 49(3):503–512, 2011. doi:10.2514/1.J050245.

[88] E. H. Dowell and D. Tang. *Dynamics of very high dimensional systems*. World Scientific Publishing Company, 2003. doi:10.1142/5346.

[89] H. Wagner. Über die entstehung des dynamischen auftriebes von tragflügeln. *ZAMM-Journal of Applied Mathematics and Mechanics/Zeitschrift für Angewandte Mathematik und Mechanik*, 5(1):17–35, 1925.

[90] J. G. Leishman. Unsteady lift of a flapped airfoil by indicial concepts. *Journal of Aircraft*, 31(2):288–297, 1994.

[91] J. D. Anderson Jr. *Fundamentals of aerodynamics*. McGraw-Hill, 5th edition, 2010.

[92] J. J. Bertin and R. M. Cummings. *Aerodynamics for Engineers*. Pearson, 6th edition, 2013.

[93] R. L. Bisplinghoff, H. Ashley, and R. L. Halfman. *Aeroelasticity*. Dover Publications, 1996.

[94] R. T. Jones. Operational treatment of the non-uniform lift theory in airplane dynamics. Technical Report NACA-TN-667, 1938.

[95] W. P. Jones. Aerodynamic forces on wings in non-uniform motion. Technical Report ARC-RM-2117, 1945.

[96] G. J. Leishman. *Principles of helicopter aerodynamics*. Cambridge university press, 2006.

[97] S. C. Jensen, G. D. Jenney, and D. Dawson. Flight test experience with an electromechanical actuator on the F-18 systems research aircraft. In *19th Digital Avionics Systems Conference*. IEEE, 2000. doi:10.1109/DASC.2000.886914.

[98] J. Katz and A. Plotkin. *Low-speed aerodynamics*. Cambridge university press, 2nd edition, 2001.

[99] M. Drela. Integrated simulation model for preliminary aerodynamic, structural, and control-law design of aircraft. In *40th Structures, Structural Dynamics, and Materials Conference and Exhibit*, 1999. doi:10.2514/6.1999-1394.

[100] J. Boutet and G. Dimitriadis. Unsteady lifting line theory using the Wagner function. In *55th AIAA Aerospace Sciences Meeting*, 2017. doi:10.2514/6.2017-0493.

[101] T. Liu, S. Wang, X. Zhang, and G. He. Unsteady thin-airfoil theory revisited: Application of a simple lift formula. *AIAA Journal*, 53(6):1492–1502, 2015. doi:10.2514/1.J053439.

[102] J. A. Cole, M. D. Maughmer, G. Bramesfeld, and M. Kinzel. A practical application of an unsteady formulation of the Kutta-Joukowski theorem. In *35th AIAA Applied Aerodynamics Conference*, 2017. doi:10.2514/6.2017-3904.

[103] R. M. Cummings, W. H. Mason, S. A. Morton, and D. R. McDaniel. *Applied computational aerodynamics: A modern engineering approach*. Cambridge university press, 2015.

[104] J. Murua. *Flexible Aircraft Dynamics with a Geometrically-Nonlinear Description of the Unsteady Aerodynamics*. PhD thesis, Imperial College London, 2012.

[105] B. K. Stanford and P. S. Beran. Analytical sensitivity analysis of an unsteady vortex-lattice method for flapping-wing optimization. *Journal of Aircraft*, 47(2):647–662, 2010. doi:10.2514/1.46259.

[106] B. W. McCormick. *Aerodynamics, Aeronautics and Flight Mechanics*. John Wiley & Sons, 1995.

[107] M. Drela and H. Youngren. AVL 3.36 User Primer, 2017. http://web.mit.edu/drela/Public/web/avl/ (Last retrieved: 28 Jan 2019).

[108] H. T. Schlichting and E. A. Truckenbrodt. *Aerodynamics of the Airplane*. McGraw-Hill, 1979.

[109] R. J. S. Simpson, R. Palacios, and J. Murua. Induced-drag calculations in the Unsteady Vortex Lattice Method. *AIAA Journal*, 51(7):1775–1779, 2013. doi:10.2514/1.J052136.

[110] B. T. Roesler and B. P. Epps. Discretization requirements for vortex lattice methods to match unsteady aerodynamics theory. *AIAA Journal*, 56(6):2478–2483, 2018. doi:10.2514/1.J056400.

[111] S. Skogestad and I. Postlethwaite. *Multivariable feedback control: analysis and design*, volume 2. Wiley, New York, 2007.

[112] K. Willcox and J. Peraire. Balanced model reduction via the proper orthogonal decomposition. *AIAA Journal*, 40(11):2323–2330, 2002. doi:10.2514/2.1570.

[113] C. W. Rowley. Model reduction for fluids, using balanced proper orthogonal decomposition. *International Journal of Bifurcation and Chaos*, 15(03):997–1013, 2005. doi:10.1142/S0218127405012429.

[114] L. Sirovich. Turbulence and the dynamics of coherent structures. parts i-iii. *Quarterly of Applied Mathematics*, 45(3):561–590, 1987.

[115] R. Pinnau. Model reduction via proper orthogonal decomposition. In *Model Order Reduction: Theory, Research Aspects and Applications*, pages 95–109. Springer, 2008. doi:10.1007/978-3-540-78841-6_5.

[116] A. C. Or, J. L. Speyer, and J. Kim. Reduced balancing transformations for large nonnormal state-space systems. *Journal of Guidance, Control and Dynamics*, 35(1):129–137, 2012. doi:10.2514/1.53777.

[117] Z. Ma, S. Ahuja, and C. W. Rowley. Reduced-order models for control of fluids using the Eigensystem Realization Algorithm. *Theoretical and Computational Fluid Dynamics*, 25(1-4):233–247, 2011. doi:10.1007/s00162-010-0184-8.

[118] J. N. Juang and R. S. Pappa. An eigensystem realization algorithm for modal parameter identification and model reduction. *Journal of Guidance, Control and Dynamics*, 8(5):620–627, 1985. doi:10.2514/3.20031.

[119] W. Gawronski. *Balanced control of flexible structures*, volume 211. Springer, 2006. doi:10.1007/3-540-76017-2.

[120] J. N. Juang and M. Q. Phan. *Identification and control of mechanical systems*. Cambridge University Press, 2001. doi:10.1017/CBO9780511547119.

[121] R. S. Pappa. Eigensystem realization algorithm user's guide for VAX/VMS computers. NASA-TM-109066, NASA Langley Research Center, 591 p., May 1994.

[122] M. Majji, J. N. Juang, and J. L. Junkins. Time-varying Eigensystem Realization Algorithm. *Journal of Guidance, Control and Dynamics*, 33(1):13–28, 2010. doi:10.2514/1.45722.

[123] J.-N. Juang and H. Suzuki. An eigensystem realization algorithm in frequency domain for modal parameter identification. *Journal of Vibration, Acoustics, Stress, and Reliability in Design*, 110(1):24–29, 1988. doi:10.1115/1.3269475.

[124] W. Weaver Jr., S. P. Timoshenko, and D. H. Young. *Vibration problems in engineering*. John Wiley & Sons, 1990.

[125] L. Meirovitch. *Fundamentals of vibrations*. McGraw-Hill, 2001.

[126] K. C. Hall. Eigenanalysis of unsteady flows about airfoils, cascades, and wings. *AIAA Journal*, 32(12):2426–2432, 1994. doi:10.2514/3.12309.

[127] E. H. Dowell, K. C. Hall, and M. C. Romanowski. Eigenmode analysis in unsteady aerodynamics: Reduced order models. *Applied Mechanics Reviews*, 50(6):371–386, 1997. doi:10.1115/1.3101718.

[128] E. Dowell, K. Hall, J. Thomas, R. Florea, B. Epureanu, and J. Heeg. Reduced order models in unsteady aerodynamics. In *40th Structures, Structural Dynamics, and Materials Conference and Exhibit*, page 1261, 1999. doi:10.2514/6.1999-1261.

[129] D. Tang, D. Kholodar, J.-N. Juang, and E. H. Dowell. System identification and proper orthogonal decomposition method applied to unsteady aerodynamics. *AIAA Journal*, 39(8):1569–1576, 2001. doi:10.2514/2.1482.

[130] J.-N. Juang, D. Kholodar, and E. H. Dowell. System identification of a vortex lattice aerodynamic model. *AIAA Journal*, 40(6):1187–1196, 2002. doi:10.2514/2.1770.

[131] E. Gillebaart and R. De Breuker. Reduced-order modeling of continuous-time state-space unsteady aerodynamics. In *53rd AIAA Aerospace Sciences Meeting*, page 0260, 2015. doi:10.2514/6.2015-0260.

[132] J. E. Hubbard. Dynamic shape control of a morphing airfoil using spatially distributed transducers. *Journal of Guidance, Control, and Dynamics*, 29(3):612–616, 2006. doi:10.2514/1.15196.

[133] A. G. Butkovskiy. *Structural Theory of Distributed Systems*. Ellis Horwood, 1983.

[134] S. E. Burke and J. E. Hubbard. Shape control of distributed parameter systems: Modeling and performance analysis. In *American Control Conference*, pages 1552–1557. IEEE, 1990. doi:10.23919/ACC.1990.4790997.

[135] K. D. Minto and T. Knack. Input-output oriented computation algorithms for the control of large flexible structures. In *NASA Workshop on Computational Aspects in the Control of Flexible Systems*, July 1988.

[136] P. Y. Li. Reference input tracking: Feedforward control. In *ME 8281 - Advanced Control Systems - Course Notes, Chapter 9*. University of Minnesota, 2006.

[137] R. H. Kwong. Control design for set point tracking. In *ECE410F Control Systems - Course Notes, Chapter 5*. University of Toronto, 2008.

[138] B. L. Stevens, F. L. Lewis, and E. N. Johnson. *Aircraft control and simulation: dynamics, controls design, and autonomous systems*. John Wiley & Sons, 2015. doi:10.1002/9781119174882.

[139] E. A. Morelli and V. Klein. *Aircraft System Identification: Theory and Practice*. Sunflyte Enterprises, Williamsburg, VA, 2 edition, 2016.

[140] J. Chen, R. J. Patton, and H.-Y. Zhang. Design of unknown input observers and robust fault detection filters. *International Journal of Control*, 63(1):85–105, 1996. doi:10.1080/00207179608921833.

[141] J. Chen and R. J. Patton. *Robust model-based fault diagnosis for dynamic systems*, volume 3. Springer Science & Business Media, 2012. doi:10.1007/978-1-4615-5149-2.

[142] M. Witczak. Fault diagnosis and fault-tolerant control strategies for non-linear systems. *Lecture Notes in Electrical Engineering*, 266:375–392, 2014. doi:10.1007/978-3-319-03014-2.

[143] J. Chen. *Robust residual generation for model-based fault diagnosis of dynamic systems*. PhD thesis, University of York, 1995.